

**CONTROLLED NUCLEIC ACID DELIVERY USING
PHOTO-RESPONSIVE POLYMERIC FORMULATIONS**

by

Chad T. Greco

A dissertation submitted to the Faculty of the University of Delaware in partial fulfillment of the requirements for the degree of Doctor of Philosophy in Chemical Engineering

Summer 2017

© 2017 Chad T. Greco
All Rights Reserved

**CONTROLLED NUCLEIC ACID DELIVERY USING
PHOTO-RESPONSIVE POLYMERIC FORMULATIONS**

by

Chad T. Greco

Approved: _____
Abraham M. Lenhoff, Ph.D.
Chair of the Department of Chemical & Biomolecular Engineering

Approved: _____
Babatunde A. Ogunnaike, Ph.D.
Dean of the College of Engineering

Approved: _____
Ann L. Ardis, Ph.D.
Senior Vice Provost for Graduate and Professional Education

I certify that I have read this dissertation and that in my opinion it meets the academic and professional standard required by the University as a dissertation for the degree of Doctor of Philosophy.

Signed:

Millicent O. Sullivan, Ph.D.
Professor in charge of dissertation

I certify that I have read this dissertation and that in my opinion it meets the academic and professional standard required by the University as a dissertation for the degree of Doctor of Philosophy.

Signed:

Thomas H. Epps, III, Ph.D.
Professor in charge of dissertation

I certify that I have read this dissertation and that in my opinion it meets the academic and professional standard required by the University as a dissertation for the degree of Doctor of Philosophy.

Signed:

Robert E. Akins, Ph.D.
Member of dissertation committee

I certify that I have read this dissertation and that in my opinion it meets the academic and professional standard required by the University as a dissertation for the degree of Doctor of Philosophy.

Signed:

Wilfred Chen, Ph.D.
Member of dissertation committee

I certify that I have read this dissertation and that in my opinion it meets the academic and professional standard required by the University as a dissertation for the degree of Doctor of Philosophy.

Signed:

April M. Kloxin, Ph.D.
Member of dissertation committee

ACKNOWLEDGMENTS

I'd like to start by thanking my advisors, Prof. Millicent O. Sullivan and Prof. Thomas H. Epps, III, for their mentorship throughout graduate school. Both of you have taught me so much about research, science, collaboration, mentoring, writing, and communication. In particular, I especially thank Prof. Sullivan for teaching me how to organize my thoughts and hypotheses into a reasoned and compelling story. Furthermore, I especially thank Prof. Epps for teaching me to think critically and instilling in me a drive to be better. Working with both of you has provided me with numerous lessons that I believe will give me a leg up over my colleagues throughout my entire career.

I'd also like to thank my committee members, Prof. Robert E. Akins, Prof. Wilfred Chen, and Prof. April M. Kloxin, for their support of my studies. Each of you provided me with valuable insights into my project at various points along the way. Moreover, I appreciate your willingness to take time out of your busy schedules to help me progress through the different stages of graduate school and challenge my ideas during committee meetings.

Of course, I'd like to thank all the students in the Sullivan and Epps groups for their friendship and scientific discussions. I owe a lot to everyone who shared an office with me, especially those who were present for most/all of my time here including Dr. Morgan Urello, Erik Munsell, and Rashida Ruddock. You've listened to my (sometimes crazy) ideas and tolerated my random discussions about life for many years now. I'd like to acknowledge Prof. Matthew Green and Dr. Abbygail Foster for

mentoring me as a first year student. I also thank Dr. Tiffany Suekama for working with me on various aspects of the project and for providing guidance. Furthermore, I appreciate everyone's questions and comments during group meetings, which truly helped me become a better scientist and communicator.

Additionally, I'd like to thank two undergraduate students that have worked with me for a few years, Jason Andrechak and Victoria Muir. As much as you think I may have taught you, I'm confident that I learned even more from both of you. Training, mentoring, and collaborating with you has been the highlight of my graduate school experience. The past few years reminded me of my passion for teaching and taught me a lot about leadership and working with others. I look forward to seeing what both of you accomplish in your careers.

Also, I'd like to acknowledge other scientists and staff members who have helped me throughout my graduate school career. I thank Dr. Chandran Sabanayagam for training me how to conduct FCS experiments. I also appreciate Dr. Lynn Opdenaker's help with flow cytometry data collection. Moreover, I thank Dr. Mark Villamil for training me how to use the fluorometer and Stefanie Berges for helping me with challenges related to flow cytometry. I especially thank the Kloxin group for coordinating the usage of their 365 nm laser with me. Also, I'd like to thank Kathie Young, who has made jumping through all the hoops of gradation more manageable.

I'd like to acknowledge the encouragement from and good times with all my friends over the last five years. I was fortunate enough to be able to spend significant time with friends from high school, college, and graduate school. I would not have survived this journey without our shared experiences, laughs, and trips. I cannot mention everyone by name, but you know who you are.

I'd especially like to thank Lilly for supporting me every day and for providing the love that helped keep me going when I would get frustrated. Much of my experience in graduate school was shaped by you, and I'm a much better person for it. You were often my escape from the struggles of research, and I can't thank you enough for everything that you have done for me.

Most importantly, I'd like to acknowledge my family. Daniel, Tyler, and Kyle, watching you grow up and accomplish so much over the course of my time in graduate school has inspired me to pursue my passions and overcome any challenge I face with even greater vigor. All of my grandparents have supported me in everything I do and their faith in me has pushed me to strive for excellence. Finally, Mom and Dad, your love and guidance have made my entire career possible. I know that both of you will always be in my corner. I dedicate this dissertation to you.

TABLE OF CONTENTS

LIST OF TABLES	xv
LIST OF FIGURES	xvii
ABSTRACT	xxxix

Chapter

1	INTRODUCTION AND MOTIVATIONS	1
1.1	Nucleic Acid Delivery	1
1.1.1	siRNA enables gene silencing	2
1.2	Delivery Vehicles	4
1.2.1	Polyplexes.....	5
1.3	Controlling Binding vs. Release	5
1.3.1	Stimuli-responsive materials	7
1.3.1.1	Biological stimuli-responsive nanocarriers	8
1.3.1.2	Externally-triggered nanocarriers	10
1.3.2	Mixed block copolymer formulations	12
1.3.3	Incorporation of anionic excipients	13
1.4	Spatiotemporal Control over Gene Expression	16
1.4.1	Applications in regenerative medicine: coronary artery bypass grafting	18
1.5	Gene Silencing Dynamics and Dosing Regimens	19
1.6	Novel Photo-Responsive Block Copolymer.....	21
1.6.1	Polymer synthesis and characterization.....	22
1.6.2	Properties of siRNA/mPEG- <i>b</i> -P(APNBMA) polyplexes.....	27
1.6.2.1	siRNA binding and polyplex formation	28

1.6.2.2	Physical characterization and stability of polyplexes...	29
1.6.2.3	UV-induced unpackaging.....	35
1.6.2.4	Cellular uptake.....	39
1.6.2.5	NIH/3T3 cell viability	41
1.6.2.6	Gene silencing capacity of photo-responsive polyplexes.....	42
1.6.3	Summary of the synthesis and preliminary characterization of the photo-responsive BCP	44
1.7	Dissertation Overview	45
REFERENCES.....		49
2	CHARACTERIZATION TECHNIQUES.....	67
2.1	Gel Electrophoresis	67
2.2	Dynamic Light Scattering (DLS)	69
2.3	Fluorescence Correlation Spectroscopy (FCS)	72
2.4	Flow Cytometry.....	75
2.5	Western Blotting.....	79
2.6	Immunocytochemistry (ICC).....	82
2.7	Reverse Transcription Quantitative Polymerase Chain Reaction (RT-qPCR)	85
REFERENCES.....		90
3	siRNA RELEASE: MECHANISTIC UNDERSTANDING AND SPATIOTEMPORAL CONTROL.....	93
3.1	Introduction	93
3.2	Materials and Methods	96
3.2.1	Materials	96
3.2.2	Preparation of siRNA/mPEG- <i>b</i> -P(APNBMA) nanocarrier.....	97
3.2.3	Cell culture	98
3.2.4	<i>In vitro</i> cell transfection.....	98
3.2.5	Spatiotemporal control over gene silencing	99
3.2.6	GAPDH protein knockdown	99
3.2.7	GAPDH mRNA knockdown	100
3.2.8	Characterizing siRNA release	101
3.2.9	FRET efficiencies in aqueous solutions	102
3.2.10	FRET: flow cytometry.....	102
3.2.11	FRET: confocal microscopy.....	103

3.2.12	Intracellular FCS	104
3.3	Results and Discussion	104
3.3.1	Spatiotemporal control over gene silencing	104
3.3.2	Tuning gene silencing through light dosage and concentration effects	109
3.3.3	Modeling the gene silencing process.....	116
3.3.4	Controlling siRNA release	119
3.3.5	Monitoring polyplex structural changes.....	123
3.3.6	Detection of intracellular siRNA release.....	130
3.4	Conclusions	132
REFERENCES	134
4	MIXED POLYMER NANOCARRIERS AND KINETIC MODELING TO PREDICT DOSING	140
4.1	Introduction	140
4.2	Materials and Methods	143
4.2.1	Materials	143
4.2.2	Formulation of siRNA nanocarriers	144
4.2.3	Ethidium bromide exclusion assay	145
4.2.4	Cell culture and transfection.....	145
4.2.5	Protein knockdown analysis	146
4.2.6	Cellular uptake.....	147
4.2.7	Light-induced siRNA release	148
4.2.8	Kinetic modeling	148
4.2.9	Polyplex size determination	148
4.2.10	Zeta potential analysis	149
4.2.11	mRNA knockdown analysis	149
4.3	Results	150
4.3.1	siRNA binding efficiencies	150
4.3.2	Tuning gene silencing.....	151
4.3.3	Calculating siRNA availability to predicting gene silencing	154
4.3.3.1	Cellular uptake of polyplexes	156
4.3.3.2	Photo-triggered siRNA release.....	157
4.3.3.3	Predicting gene silencing using kinetic modeling	158

4.3.4	Dynamic silencing response	158
4.3.4.1	Dosing regimens and dynamic silencing response with multiple siRNA treatments	161
4.4	Discussion.....	162
4.5	Conclusions	170
REFERENCES		172
5	INCORPORATION OF ANIONIC EXCIPIENTS FOR IMPROVED THERANOSTICS	178
5.1	Introduction	178
5.2	Materials and Methods	183
5.2.1	Materials	183
5.2.2	Preparation of nanocarriers.....	184
5.2.3	Cell culture	185
5.2.4	<i>In vitro</i> cell transfection.....	185
5.2.5	GAPDH protein knockdown	185
5.2.6	Polyplex size determination using fluorescence correlation spectroscopy (FCS)	186
5.2.7	Serum and storage stability assay	187
5.2.8	Heparin-induced siRNA release	187
5.2.9	RNAi modeling	187
5.2.10	FRET-based polyplex disassembly	188
5.2.11	Flow cytometry to detect FRET-based polyplex disassembly ..	188
5.2.12	Cryogenic transmission electron microscopy (cryo-TEM) imaging of nanocarriers	188
5.3	Results and Discussion	189
5.3.1	Formulation of PAA-containing polyplexes	189
5.3.2	Gene silencing of PAA-containing polyplexes	190
5.3.3	Serum and storage stability	193
5.3.4	Heparin-induced siRNA release and cellular uptake.....	197
5.3.5	Predicting gene silencing <i>via</i> siRNA release assays	201
5.3.6	Incorporation of quantum dots: selective siRNA release	203
5.3.7	QD-based FRET analyses of polyplex unpackaging.....	206
5.3.8	Cryo-TEM imaging of QD-containing polyplexes.....	209
5.3.9	Incorporation of UCNPs.....	212
5.4	Conclusions	214

REFERENCES	216
6 HYBRID FORMULATIONS FOR ATTENUATING MALADAPTIVE RESPONSES IN HUMAN AORTIC ADVENTITIAL FIBROBLASTS	222
6.1 Introduction	222
6.2 Materials and Methods	225
6.2.1 Materials	225
6.2.2 Formulation of siRNA nanocomplexes	227
6.2.3 Cell culture	227
6.2.4 <i>In vitro</i> cell transfection.....	228
6.2.5 Protein knockdown analysis	228
6.2.6 RNAi modeling	229
6.2.7 Immunocytochemistry (ICC).....	230
6.2.8 mRNA knockdown analysis	231
6.2.9 Cell Proliferation	231
6.3 Results and Discussion	232
6.3.1 Hybrid nanocomplexes enable on/off control over gene silencing.....	232
6.3.2 Characterization of hybrid nanocomplexes	235
6.3.3 Gene silencing dynamics following a single siRNA dose.....	238
6.3.4 Gene silencing dynamics following a double dose of siRNA...	241
6.3.5 Gene silencing affects myofibroblast differentiation (α SMA protein expression)	242
6.3.6 Gene silencing affects myofibroblast differentiation (α SMA mRNA expression)	247
6.3.7 Attenuation of cellular proliferation following gene silencing .	249
6.3.8 Cell density effects on CDH11 knockdown	251
6.3.9 Gene knockdown in rabbit aortic fibroblasts.....	254
6.4 Conclusions	257
REFERENCES	259
7 CONCLUSIONS AND FUTURE DIRECTIONS	266
7.1 Dissertation Summary	266
7.1.1 siRNA release: mechanistic understanding and spatiotemporal control (Chapter 3)	267

7.1.2	Mixed polymer nanocarriers and kinetic modeling to predict dosing (Chapter 4)	268
7.1.3	Incorporation of anionic excipients for improved theranostics (Chapter 5).....	269
7.1.4	Hybrid formulations for attenuating maladaptive responses in human aortic adventitial fibroblasts (Chapter 6)	270
7.2	Recommendations for Future Work	271
7.2.1	Direct extensions of recent work	271
7.2.1.1	<i>In vivo</i> rabbit models	271
7.2.1.2	Incorporation of upconverting nanoparticles.....	273
7.2.2	Modifications to the polymer structure	275
7.2.2.1	Altering the <i>o</i> -NB functional moiety in the monomer	276
7.2.2.2	Changing the hydrophilic block	279
7.2.3	Endosomal escape: mechanistic understanding and strategies for enhancement	281
7.2.3.1	Mechanistic understanding of cellular uptake, endosomal escape, and polyplex fate	281
7.2.3.2	Strategies for overcoming limitations related to endosomal escape	284
7.2.4	Co-cultures and other anionic theranostic cargo	286
7.2.4.1	Cell co-cultures.....	286
7.2.4.2	Anionic cargos.....	288
7.2.5	Summary of recommended future directions	289
	REFERENCES	290
Appendix		
A	SUPPORTING INFORMATION FOR CHAPTER 3	296
B	SUPPORTING INFORMATION FOR CHAPTER 4	299
C	SUPPORTING INFORMATION FOR CHAPTER 5	301
D	SUPPORTING INFORMATION FOR CHAPTER 6	304
	REFERENCES	310

E	TEXT AND FIGURE REPRINT PERMISSIONS	311
---	---	-----

LIST OF TABLES

Table 1.1:	Characterization of mPEG- <i>b</i> -P(Boc-APNBMA) _n using ¹ H NMR spectroscopy and SEC.	27
Table 3.1:	Representative estimation of the number of siRNAs per mPEG- <i>b</i> -P(APNBMA) polyplex. The number of fluorescent particles (raw data) was computed by the ZEN 2010 software on the basis of the value of the autocorrelation function at $\tau = 0$ s. The dilution factor was estimated on the basis of the concentrations of siRNAs that were added during sample preparation. The relative number of particles was calculated by multiplying the number of particles (raw data) by the dilution factor. The normalized number of particles was computed by dividing the relative number of particles by 2.7 (relative number of polyplexes).	123
Table 5.1:	Estimated number of PAA polymer chains per polyplex in various formulations.	200
Table A.1:	Representative calculation of the normalized mRNA expression level (<i>m</i>) of a test sample relative to the untreated control. The values were computed using Equations 2.12 and 2.13, as described in detail in Chapter 2 (section 2.7).	296
Table A.2:	The raw values of the ratios between the intensities of the acceptor and donor peaks (I_{665}/I_{560}) of three independent samples from Figure 3.9B (prior to normalization).	297
Table B.1:	Raw values of polyplex diameters and the calculation of the average and standard deviation for each mixed polymer formulation. These values are plotted in Figure 4.5.	299
Table B.2:	Raw values of polyplex zeta potentials and the calculation of the average and standard deviation for each mixed polymer formulation. These values are plotted in Figure 4.5.	300

Table D.1: Average size and zeta potential of the hybrid lipid-polymer nanocomplexes. The average nanocomplex diameter was determined using fluorescence correlation spectroscopy (FCS). The average zeta potential was determined using a Brookhaven Instruments (Brookhaven, CT) ZetaPALS, and each sample was measured with 3 runs of 10 cycles. Results are reported as the mean and standard deviation of data obtained from three independent experiments. 306

Table D.2: Sequences of custom-designed siRNA sequences that target IL1 β in rabbits. The siRNA was purchased in duplex form from MilliporeSigma (Darmstadt, Germany). 309

LIST OF FIGURES

- Figure 1.1: Schematic of the RNAi mechanism. This figure was adapted with permission from K.A. Whitehead, R. Langer, D.G. Anderson, Knocking down barriers: advances in siRNA delivery, *Nat. Rev. Drug Discov.* 8(2) (2009) 129-138.¹³ Copyright 2009, Rights Managed by Nature Publishing Group..... 3
- Figure 1.2: siRNA polyplexes must satisfy seemingly contradictory demands of remaining stable extracellularly but disassembling intracellularly. The competing requirements of siRNA binding vs. release are some of the most significant challenges hindering the translation of siRNA nanocarrier systems. 7
- Figure 1.3: Different stimuli that have been used in biomaterials to gain better control over nucleic acid binding vs. release. This figure was adapted with permission from Y. Lu, W.J. Sun, Z. Gu, Stimuli-responsive nanomaterials for therapeutic protein delivery, *J. Control. Release* 194 (2014) 1-19.50 Copyright 2014 Elsevier B.V. All rights reserved. 8
- Figure 1.4: Overview of three of the main strategies (stimuli-responsive materials, mixed BCP formulations, and incorporation of anionic excipients) used to enhance control over siRNA binding vs. release. Ultimately, a combination of these three distinct strategies may provide the best opportunity to improve gene silencing efficiencies and gain precise control over nucleic acid activity. 15
- Figure 1.5: Depiction of a coronary artery bypass graft. The autologous vein graft is placed to bypass the blockage and is sutured to the coronary artery at anastomoses. Current therapeutic approaches lack the spatial control needed to reduce maladaptive responses in the anastomoses ('on') while avoiding off-target effects in the rest of the graft conduit ('off'). The cartoon of the graft was adapted from: <http://www.mobilevascular.com/bypass-surgery.html>. (March 17, 2017)..... 19
- Figure 1.6: Overview of the synthetic scheme of mPEG-*b*-P(APNBMA)_n..... 24
- Figure 1.7: Size exclusion chromatograms of mPEG-*b*-P(Boc-APNBMA)_n..... 25

Figure 1.8: ^1H NMR spectroscopy of Boc-APNBMA monomer (top) in CDCl_3 , mPEG- <i>b</i> -P(Boc-APNBMA) _n (middle) in CDCl_3 , and mPEG- <i>b</i> -P(APNBMA) _n (bottom) in $\text{DMSO-}d_6$.	26
Figure 1.9: Characterization of siRNA/mPEG- <i>b</i> -P(APNBMA) _n polyplexes. Representative siRNA mobility assay in 4 wt% agarose gels stained with ethidium bromide. Polyplexes were prepared with (A) mPEG- <i>b</i> -P(APNBMA) _{7.9} and (B) mPEG- <i>b</i> -P(APNBMA) _{23.6} . Lane 1 of both gels is siRNA alone (N/P = 0) while the remaining lanes show siRNA complexed with polymer at varied N/P ratios. Tabulated values indicate percentages of free siRNA based on ImageJ analysis of the free siRNA band.	29
Figure 1.10: Polyplex characterization using DLS. (A) D_H of polyplexes determined at various N/P ratios. (B) Representative D_H of polyplexes prepared at N/P ratio of 4 following a 1 h or a 3 h incubation in 20 mM HEPES (pH = 6; black), Opti-MEM (gray), or PBS containing 150 mM NaCl (diagonal lines). siRNA/PEI polyplexes also were incubated in PBS for 1 h for comparison.	30
Figure 1.11: Heparin displacement of (A) siRNA/mPEG- <i>b</i> -P(APNBMA) _{23.6} polyplexes (N/P ratio of 4), and (B) siRNA/PEI polyplexes (N/P ratio of 6) incubated in the presence of increasing amounts of heparin. (C) Quantification of free siRNA in siRNA/mPEG- <i>b</i> -P(APNBMA) _{23.6} polyplexes (black) and siRNA/PEI polyplexes (white) based on gel image analysis using ImageJ.	33
Figure 1.12: Gel mobility shift and nuclease stability analyses of siRNA polyplexes. (A) Stability of free siRNA and siRNA/mPEG- <i>b</i> -P(APNBMA) _{23.6} polyplexes against serum-mediated disassembly. Free siRNA and siRNA/mPEG- <i>b</i> -P(APNBMA) _{23.6} polyplexes prepared at N/P ratios of 2, 4, 6, and 8 were analyzed in the presence (+) or absence (-) of serum. (B) Stability of free siRNA and siRNA polyplexes (N/P ratio of 4) against RNase A-mediated degradation. Free siRNA and siRNA/mPEG- <i>b</i> -P(APNBMA) _{23.6} polyplexes were treated with RNase A (+) or RNase A-free (-) buffers, the nuclease reactions were terminated, and the polyplexes were either disassembled in SDS (+) or left intact (-).	35

Figure 1.13: UV absorbance spectral changes of (A) mPEG- <i>b</i> -P(APNBMA) _{23.6} and (B) siRNA/mPEG- <i>b</i> -P(APNBMA) _{23.6} polyplexes following exposure to UV irradiation (365 nm, 200 W/m ²) for 0 (black), 5 (red), 10 (orange), 20 (green), 40 (blue), or 60 (purple) min. Normalized absorbance (filled squares) at 316 nm for (C) mPEG- <i>b</i> -P(APNBMA) _{23.6} and (D) siRNA/mPEG- <i>b</i> -P(APNBMA) _{23.6} polyplexes as a function of UV irradiation time. The log of the normalized intensity, for which the red dashed line indicates an exponential decay fit to the normalized intensity. Error bars represent the standard deviation determined from the mean of three independent absorbance measurements.	37
Figure 1.14: (A) Electrophoretic gel migration patterns of siRNA/mPEG- <i>b</i> -P(APNBMA) _{23.6} polyplexes after exposure to UV irradiation (365 nm, 200 W/m ²) for varying periods of time. Free siRNA is shown for comparison. (B) Quantification of ethidium bromide fluorescence in the siRNA band using ImageJ analysis software.	38
Figure 1.15: Representative fluorescence microscopy images showing the internalization of siRNA polyplexes in NIH/3T3 cells. siRNA was labeled with YOYO-1 iodide (green); the nucleus was stained with Hoechst (blue). Cells transfected with siRNA/mPEG- <i>b</i> -P(APNBMA) _{23.6} polyplexes for (A) 1 h, and (B) 3 h. Arrows indicate punctate polyplex structures, and the scale bar represents 25 μm and applies to all images.	40
Figure 1.16: Cellular uptake of fluorescently-labeled siRNA complexes quantified using flow cytometry. Lipofectamine RNAiMax assemblies (black); mPEG- <i>b</i> -P(APNBMA) _{23.6} polyplexes (light gray). The mean fluorescence intensity (MFI, arbitrary units) of the cells that had internalized lipoplexes or polyplexes was quantified. Each data point represents the mean ± standard deviation for a total of three separately prepared samples. An asterisk indicates a statistically significant difference at a given time point between the mPEG- <i>b</i> -P(APNBMA) _{23.6} polyplexes and the Lipofectamine lipoplexes (p < 0.001).	41
Figure 1.17: Cell viabilities 48 h after polyplex treatment, UV exposure, or the combination of polyplexes and UV exposure as measured by the AB assay. Percent viabilities are relative to untreated cells. Each data point represents the mean ± standard deviation for a total of at least three separately prepared and analyzed samples. The untreated control sample is shown in black.	42

Figure 1.18: Western blot analysis of NIH/3T3 cell extracts collected 48 h post-transfection. Cells were treated with GAPDH targeted siRNA/mPEG- <i>b</i> -P(APNBMA) _{23.6} polyplexes with (+) or without (-) UV exposure (20 min), or with Lipofectamine lipoplexes containing either non-targeting or GAPDH targeting siRNAs.....	44
Figure 1.19: Overview of the topics of each data chapter.	46
Figure 2.1: Representative micrograph of an agarose gel loaded with siRNA samples and pre-stained with ethidium bromide.....	69
Figure 2.2: Comparison of diffusive properties and correlation functions of small and large particles. The smaller particles diffuse more quickly, resulting in more rapid fluctuations in light intensity and shorter correlation times.	71
Figure 2.3: Schematic of a typical FCS experimental setup. The excitation light (green) is directed to the sample and excites the fluorophores in the confocal volume. The resulting emission signal (red) is transmitted through a dichroic mirror. Before reaching the detector, the light is passed through a bandpass filter and pinhole that exclude all light that is outside the designated wavelength range or is not from the confocal volume, respectively.....	73
Figure 2.4: Representative two-dimensional dot plot of forward vs. side scattered intensity. 85.5% of the detected particles were designated to be considered live cells (within the 6-sided polygon gate). The gate was applied to this population due to the specimen's large size (indicated by high forward scattering) and fairly complex morphology (indicated by medium-high side scattering). The remaining 14.5% of particles were determined to be either dead cells (slightly smaller size and more complex morphology) or cell debris/other macromolecular species (much smaller size and less complex morphology).	77
Figure 2.5: Representative compensation matrix and compensated histogram distributions of FRET intensities. The APC and PE channels primarily detected signals from individual fluorophores (control samples) and the PE-Texas Red channel primarily detected the signal attributed to FRET. After compensation, the distributions of the control samples (blue is donor fluorophore and red is acceptor fluorophore) had the same median fluorescence intensity as the distribution of untransfected cells (black). The compensation procedure allowed the true FRET signal (purple) to be isolated while taking signal spillover into account.....	79

Figure 2.6:	Representative image of a western blot membrane following the addition of a chemiluminescent substrate. Nine different protein samples were analyzed, and the resulting bands can be quantified to determine the protein content in each sample.	82
Figure 2.7:	Representative ICC micrographs. F-Actin was stained with Phalloidin-660 (magenta), α SMA was stained with rabbit α SMA-targeting primary antibodies and secondary goat anti-rabbit AF488-labelled secondary antibodies (green), and nuclear DNA was stained with Hoechst 33258 (blue).	84
Figure 2.8:	Representative amplification curves for test and control samples. The housekeeping gene test samples had C_q values of ~ 11 , and the targeted gene test samples had C_q values of ~ 24 . All NTC and NRT control samples had C_q values that were much greater than the corresponding test samples, indicating that contamination was not a significant factor in this experiment.	89
Figure 3.1:	On/off spatiotemporal control over nanocarrier disassembly to modulate expression of an exogenous gene. (A) Schematic of polyplex self-assembly and light-induced polymer charge reversal to release the siRNA. (B and C) Wide-field view of circular patterning in GFP expression. Cells were transfected with (B) GFP pDNA/Lipofectamine 2000 lipoplexes and GFP-targeting siRNA/mPEG- <i>b</i> -P(APNBMA) polyplexes or (C) GFP pDNA/Lipofectamine 2000 lipoplexes and no siRNA. A circular photomask was applied prior to 20 min of 365 nm light irradiation. The dashed red line represents the edge of the photomask, and the scale bars represent 1 mm and apply to both images.	106
Figure 3.2:	Zoomed-in view of line-patterning of GFP expression with cell-to-cell resolution. (A) NIH/3T3 cells were co-transfected with pDNA/Lipofectamine 2000 and GFP-targeting siRNA/mPEG- <i>b</i> -P(APNBMA), and half of the plate was covered with a photomask prior to 20 min of 365 nm light irradiation. (B and C) Phase contrast microscopy (left) and fluorescence microscopy (right) images of NIH/3T3 cells. (B) Cells were treated with GFP pDNA/Lipofectamine 2000 lipoplexes and no siRNA or (C) GFP pDNA/Lipofectamine 2000 and non-targeting siRNA/mPEG- <i>b</i> -P(APNBMA) and irradiated with 365 nm light for 20 min. The scale bars represent 250 μ m and apply to all images.	107

Figure 3.3: On/off spatiotemporal control over expression of an exogenous gene in human aortic adventitial fibroblast (AoAF) cells using mPEG-*b*-P(APNBMA) polyplexes. Phase contrast microscopy (left) and fluorescence microscopy (right) images were taken 24 h post-transfection. Cells were co-transfected with GFP DNA and GFP-targeting siRNA and either (A) covered with a photomask or (B) left unmasked. The covered and unmasked cells were exposed to 10 min of 365 nm light irradiation. The scale bars represent 250 μ m and apply to all images..... 109

Figure 3.4: Tunable protein silencing of model exogenous and endogenous genes in NIH/3T3 cells. (A) A panel of representative microscopy images of GFP expression in cells following treatment with GFP-targeting siRNA/ mPEG-*b*-P(APNBMA) polyplexes and exposure to 365 nm light for varying lengths of time. The scale bars represent 250 μ m and apply to all images. (B) The overall intensities of representative fluorescence microscopy images (panel A) were quantified using ImageJ software, and values were normalized to the intensity of cells that were not treated with GFP-targeted siRNA. (C) Representative western blot analyses and quantification of GAPDH protein expression levels as a function of irradiation time. Cells were treated with 20 nM siRNA polyplexes and subsequently exposed to 365 nm light for varying lengths of time. Data represent the GAPDH protein expression levels relative to the levels of the loading control β -actin, normalized to the native protein levels in controls with no siRNA treatment. Results are shown as the mean \pm standard deviation of data obtained from three independent experiments. (D) Western blot analysis of GAPDH protein knockdown using extended incubation periods (48 h or 96 h) prior to cell lysis. Cells were treated with GAPDH-targeting siRNA that was packaged with mPEG-*b*-P(APNBMA) or Lipofectamine RNAiMAX. (E) Western blot analysis of GAPDH protein knockdown following treatment with mPEG-*b*-P(APNBMA) polyplexes and irradiation for 20 min. 111

Figure 3.5: Cellular uptake and gene silencing efficiencies of mPEG-*b*-P(APNBMA) polyplexes over a range of siRNA concentrations. (A) Cells were incubated in polyplex solutions formulated with Dy647-labeled siRNA at concentrations of 0 nM (black), 20 nM (red), 30 nM (green), or 40 nM (blue) siRNA, and cellular fluorescence was measured using flow cytometry. (B) The mean fluorescence intensity per cell (from panel A) was computed. (C) Cells were treated with varying siRNA polyplex concentrations and subsequently exposed to 365 nm light for 0 min (dark gray bars) or 20 min (white bars). Data represent the GAPDH protein expression levels relative to the levels of the loading control β -actin, normalized to the native protein levels in controls with no siRNA treatment. Results are shown as the mean \pm standard deviation of data obtained from three independent experiments. 113

Figure 3.6: qPCR analyses of GAPDH mRNA silencing as a function of irradiation time and siRNA concentration. (A) Cells were treated with 20 nM siRNA polyplexes and then exposed to 365 nm light for varying lengths of time. (B) Cells were treated with varying siRNA polyplex concentrations and then exposed to 365 nm light for 0 min (dark gray bars) or 20 min (white bars). Data represent the GAPDH mRNA expression levels relative to β -actin mRNA levels, normalized to the native levels in controls with no treatment siRNA treatment. Results are reported as the mean \pm standard deviation of data obtained from three independent replicates. 116

- Figure 3.7: Mass action kinetic model that predicts GAPDH silencing following siRNA release from mPEG-*b*-P(APNBMA) polyplexes. (A) The set of equations (3.1-3.3) was solved using differential equation solver ode45 in MATLAB and plotted up to 96 h post-transfection. All concentrations were normalized to 100 at the time of transfection. The terms k_{mRNA} , k_{siRNA} , and k_{prot} are the rate constants for the production of mRNA, siRNA, and protein, respectively. The terms $k_{\text{m,deg}}$, $k_{\text{s,deg}}$, and $k_{\text{p,deg}}$ are the rate constants for the degradation of mRNA, siRNA, and protein, respectively. Degradation rate constants were computed on the basis of the component half-lives reported in literature,^{40, 44, 45} and production rate constants were fit to ensure mRNA and protein steady-state values were reached in the absence of siRNA. (B) Model predictions of protein silencing efficiencies of mPEG-*b*-P(APNBMA) polyplexes following irradiation with 365 nm light for varying lengths of time. Predictions from the kinetic model (blue bars) were computed on the basis of siRNA release data in Figure 3.8C (blue bars). These values were compared to experimental data (red bars) from Figure 3.4C. 119
- Figure 3.8: Representative gel mobility shift and fluorescence correlation spectroscopy (FCS) analyses of light-induced siRNA release. (A) Gel electrophoresis data from polyplex solutions with varying SDS and light dosages. (B) Normalized autocorrelation functions of polyplex solutions with varying light dosages as follows: 0 min (black), 10 min (red), 20 min (yellow), and 40 min (green) all at SDS S/P of 15; 0 min at SDS S/P of 200 (blue); free siRNA (gray). (C) Quantification of siRNA released on the basis of gel mobility studies (black) and FCS (gray). Polyplexes were pre-incubated in solutions containing no SDS (S/P of 0; diamonds) or SDS at S/P of 15 (triangles). Results are shown as the mean \pm standard deviation of data obtained from three independent samples..... 121
- Figure 3.9: Fluorescence emission spectra of polyplexes undergoing FRET as a function of irradiation time. (A) Polyplexes were formed with equal molar ratios of donor and acceptor fluorophore-labeled siRNA molecules and exposed to varying dosages of 365 nm light as follows: 0 min (black), 2.5 min (red), 5 min (orange), 10 min (green), 20 min (blue), 40 min (purple). (B) Normalized ratio between the intensities of the acceptor and donor peaks (I_{665}/I_{560}) of three independent samples for each time point. The lines connecting data points are to guide the eye..... 125

- Figure 3.10: Representative flow cytometry data showing the intracellular FRET signal following 365 nm light irradiation of transfected NIH/3T3 cells. The fluorescence signals from cells treated with no siRNA (black), Dy547-siRNA (blue), Dy647-siRNA (red), or Dy547- and Dy647-siRNA (purple) over a series of varying irradiation times were quantified by the mean fluorescence intensity (MFI) per cell. Results are shown as the mean \pm standard deviation of data obtained from three independent experiments, and the compensation matrices are reported in Figure A.1 in Appendix A. 127
- Figure 3.11: Normalized FRET efficiencies as a function of mPEG-*b*-P(APNBMA) polyplex exposure to 365 nm light irradiation. FRET efficiencies of polyplexes in solution were measured through fluorescence spectroscopy (gray diamonds), and cellular FRET efficiencies were measured *via* flow cytometry (black squares) or confocal microscopy (white triangles). In solution, normalized FRET efficiencies were computed from the ratio between the donor and acceptor peaks for polyplexes. In cells, the normalized FRET efficiencies were determined from the fluorescence intensities attributed to FRET after accounting for both autofluorescence and donor/acceptor bleed-through signals. Results are shown as the mean \pm standard deviation of data obtained from three independent experiments, and the raw values for FRET in solution as measured by fluorescence spectroscopy are recorded in Table A.2 in Appendix A. 128
- Figure 3.12: Confocal microscopy images and colocalization quantification of intracellular FRET as a function of irradiation time. (A) Selectively exciting the donor fluorophore produced fluorescence signals unique to the donor (green) and acceptor (red) fluorophores. The overlay of these two images is displayed as yellow. The scale bar represents 25 μ m and applies to all images. (B) Quantification of micrographs using the Manders' correlation coefficient to compute the fraction of polyplexes undergoing FRET. Results are reported as the mean \pm standard deviation of data obtained from 30 randomly chosen cells per sample..... 129
- Figure 3.13: Normalized FCS autocorrelation functions showing the intracellular diffusion patterns of siRNA molecules following 365 nm light irradiation. Cells were treated with 365 nm light for 0 min (red), 5 min (orange), 10 min (green), or 20 min (blue) after the delivery of labeled polyplexes. The arrow indicates an inflection point in the 20 min irradiation autocorrelation function..... 132

- Figure 4.1: Ethidium bromide exclusion analyses of mPEG-*b*-P(APNBMA) polyplexes. The polyplex composition is defined as the ratio of mPEG-*b*-P(APNBMA)_{7,9}/mPEG-*b*-P(APNBMA)_{23,6} polymers, on a molar basis of cationic amine groups. (A) Representative gel electrophoresis images of polyplexes formed at varying total N/P ratios with different polymer compositions. (B) Quantification of the gel electrophoresis images in (A) calculated from ImageJ analysis of siRNA band intensities. Results are shown as the mean ± standard deviation of data obtained from three independent experiments. 151
- Figure 4.2: GAPDH protein silencing efficiencies of mPEG-*b*-P(APNBMA) polyplexes. The polyplex composition is defined as the ratio of mPEG-*b*-P(APNBMA)_{7,9}/mPEG-*b*-P(APNBMA)_{23,6} polymers, on a molar basis of cationic amine groups. Cells were treated with 20 nM siRNA polyplexes formed at an N/P ratio of 4, irradiated with 365 nm light for 10 min, and lysed for western blot analysis 48 h post-transfection. Polyplexes are formed from various ratios of mPEG-*b*-P(APNBMA)_{7,9}/mPEG-*b*-P(APNBMA)_{23,6} polymers on a fixed molar basis of cationic amine groups. Data represent the GAPDH protein expression levels relative to the levels of the loading control β-actin, normalized to the native protein levels in controls with no siRNA treatment. Results are shown as the mean ± standard deviation of data obtained from three independent experiments. An asterisk indicates a statistically significant difference in silencing from the 50/50 composition ($p < 0.05$). 153
- Figure 4.3: Western blot analysis of GAPDH protein levels following polyplex treatment without 365 nm light irradiation. Polyplexes were formed at a total N/P of 4, with different polymer compositions of mPEG-*b*-P(APNBMA)_{7,9}/mPEG-*b*-P(APNBMA)_{23,6}, on a molar basis of cationic amine groups. The cell extract was collected 48 h post-transfection. Relative band intensities were quantified on the basis of the change in GAPDH protein expression levels relative to the band intensity of the loading control, β-actin. These values were normalized to the native levels in controls with no treatment. No significant knockdown was exhibited in any samples in the absence of 365 nm irradiation. 154

- Figure 4.4: siRNA release and cellular uptake analyses to predict gene silencing using kinetic modeling. (A) Schematic of important biological barriers that determine the level of gene silencing, as estimated through the kinetic model. (B) Cellular uptake levels as a function of polyplex composition as measured by flow cytometry. The mean fluorescence intensity (MFI) per cell was normalized to the MFI for the 0/100 polyplexes. (C) Light-triggered release of siRNA from polyplexes following incubation in SDS solutions (S/P ratio of 2.5) and irradiation with 365 nm light for 10 min. The solutions were analyzed by gel electrophoresis analyses. (D) Kinetic modeling predictions of gene silencing on the basis of siRNA availability estimates from siRNA release and cellular uptake data. The predicted level of protein knockdown (red diamonds) was compared to the experimentally determined values from Figure 4.2 (blue bars). Results for all plots are shown as the mean \pm standard deviation of three independent samples..... 155
- Figure 4.5: Average zeta potentials (light blue, associated with primary y-axis) and diameters (pink, associated with secondary y-axis) of polyplexes with varying compositions. Polyplexes were formed at a total N/P of 4, with different polymer compositions of mPEG-*b*-P(APNBMA)_{7.9}/mPEG-*b*-P(APNBMA)_{23.6}, on a molar basis of cationic amine groups. Results are shown as the mean \pm standard deviation of data obtained from three independent measurements. 157
- Figure 4.6: (A & C) Kinetic models predict the dynamic nature of the GAPDH silencing process with a single dose (A) and double dose (C) of siRNA. Initial protein and mRNA concentrations were normalized to 100. A dose of siRNA was introduced 3.5 h after each transfection, which corresponds to the time of 365 nm light treatment. (B & D) Cells were lysed at 48 h or 75 h following either a single dose (B) or double dose (D) of siRNA, respectively. GAPDH mRNA and protein expression levels were determined through qPCR and western blot experiments, respectively. Model predictions of mRNA (green) and protein (orange) expression levels at the end points of 48 h and 75 h are presented as solid bars; experimental values are presented as diagonal striped bars. Experimental values are shown as the mean \pm standard deviation of data obtained from three independent samples... 160

- Figure 4.7: Representative western blot used to analyze GAPDH protein levels following a double dose delivery of polyplexes. Cells were transfected for 3 h with mPEG-*b*-P(APNBMA)_{7,9}/mPEG-*b*-P(APNBMA)_{23,6} polyplexes (50/50) containing GAPDH-targeting siRNA and irradiated 0.5 h later with 365 nm light for 10 min. A second transfection was performed 28 h after the first transfection, and the cell extract was collected 75 h after the first transfection (47 h after the second transfection). Relative band intensities were quantified on the basis of GAPDH protein expression levels and normalized to the band intensity of the loading control, β -actin. These values then were normalized to the native levels in controls with no treatment. No significant knockdown was noted without 365 nm light exposure. However, GAPDH protein levels were reduced to ~15% with 365 nm light treatment following the double dosing schedule, as compared to a minimum achievable reduction of ~30% after a single dose. 162
- Figure 4.8: GAPDH protein silencing efficiencies of mPEG-*b*-P(APNBMA)/siRNA polyplexes. Polyplexes were formed at a total N/P of 4, with different polymer compositions of mPEG-*b*-P(APNBMA)_{7,9}/mPEG-*b*-P(APNBMA)_{23,6} (blue bars) or with mPEG-*b*-P(APNBMA)_{16,6} (orange bar). Cells were treated with 20 nM siRNA polyplexes, irradiated with 365 nm light for 10 min, and lysed for western blot analysis 48 h post-transfection. Data represent the GAPDH protein expression levels relative to the levels of the loading control β -actin, normalized to the native protein levels in controls with no siRNA treatment. Results are shown as the mean \pm standard deviation of data obtained from three independent experiments. An asterisk indicates a statistically significant difference in silencing from the 50/50 composition ($p < 0.05$). 170
- Figure 5.1: Cartoon schematic of mPEG-*b*-P(APNBMA) siRNA polyplexes (A) without PAA or QDs and (B) with PAA and QDs. Following polyplex formation, the formulations were treated with a photo-stimulus to trigger unpackaging of siRNA. The incorporation of the excipients resulted in enhanced and selective release of siRNA. 183
- Figure 5.2: Representative ethidium bromide exclusion analyses of various formulations. Control polyplexes were formed at various N/P ratios with mPEG-*b*-P(APNBMA) and siRNA. Different formulations were made by substituting siRNA with 240 kDa PAA at various weight ratios while keeping the amount of mPEG-*b*-P(APNBMA) unchanged. Polyplex solutions were examined *via* gel electrophoresis. 190

- Figure 5.3: Silencing efficiency fold change of mPEG-*b*-P(APNBMA)/PAA ternary siRNA polyplexes. siRNA was substituted with PAA on a weight percent basis, and the molecular weight of PAA was varied. Cells were treated with 20 nM siRNA polyplexes, irradiated with 365 nm light for 10 min, and lysed for western blot analysis at 48 h post-transfection. Data represent the fold change in GAPDH protein silencing efficiency (on a per μg of siRNA basis) of each formulation relative to polyplexes without PAA (fold change = 1). Results are shown as the mean of data obtained from three independent experiments. 192
- Figure 5.4: Representative western blot analysis of GAPDH protein levels following treatment with various mPEG-*b*-P(APNBMA)/240 kDa PAA siRNA formulations at an N/P ratio of 4 in the absence of light irradiation. The cell extract was collected 48 h post-transfection. Relative band intensities were quantified on the basis of the change in GAPDH protein expression levels relative to the band intensity of the loading control, β -actin. These values were normalized to the native levels in controls with no treatment. 192
- Figure 5.5: Serum stability of mPEG-*b*-P(APNBMA)/240 kDa PAA and PEI siRNA polyplexes, based upon analysis of polyplex size following exposure to 100% FBS for various lengths of time at 37 °C. The nanocarriers that were not exposed to FBS (0 h) were stored in the formulation buffer, HEPES buffer, at 37 °C prior to analysis. Average polyplex diameters were computed from FCS analyses. Results are shown as the mean \pm standard deviation of data obtained from three independent experiments. An asterisk indicates a statistically significant difference between polyplex sizes after exposure to FBS ($p < 0.05$). 194

- Figure 5.6: Polyplex stability in serum-containing media and following storage for one week. The silencing efficiencies of (A) mPEG-*b*-P(APNBMA)/PAA (30/70, 240 kDa) ternary siRNA polyplexes and (B) PEI/siRNA polyplexes were analyzed. Transfections were conducted in either OptiMEM (serum-free) or DMEM containing 10% FBS. Polyplexes were incubated for either 30 min or 1 week prior to transfection. Cells were treated with 20 nM siRNA polyplexes, irradiated with 365 nm light for 10 min, and lysed for western blot analysis at 48 h post-transfection. Data represent the fold change in GAPDH protein silencing efficiency (on a per μg of siRNA basis) of each sample relative to polyplexes without PAA (red dashed line). Results are shown as the mean \pm standard deviation of data obtained from three independent experiments. An asterisk indicates a statistically significant difference between a given sample and polyplexes incubated for 30 min prior to transfection in serum-free media ($p < 0.05$). 195
- Figure 5.7: Heparin-induced siRNA release from mPEG-*b*-P(APNBMA)/PAA ternary siRNA polyplexes. siRNA was substituted with PAA on a weight percent basis, and the molecular weight of PAA also was varied. Following polyplex formulation, heparin was added at a weight ratio of 5:1 heparin:siRNA and incubated for 30 min. The solutions were subjected to gel electrophoresis and the amount of free siRNA was quantified using ImageJ. Results are shown as the mean of data obtained from three independent experiments. 198
- Figure 5.8: Cellular uptake of mPEG-*b*-P(APNBMA)/240 kDa PAA siRNA polyplexes over a range of PAA/siRNA weight ratios. Cells were incubated in polyplex solutions formulated with Dy647-labeled siRNA, and cellular fluorescence was measured using flow cytometry. The mean fluorescence intensity (MFI) per μg of siRNA was computed and normalized to the MFI of cells that were treated with 0/100 polyplexes. Results are shown as the mean \pm standard deviation of data obtained from three independent experiments. 201
- Figure 5.9: Model predictions of silencing efficiency fold change of mPEG-*b*-P(APNBMA)/PAA ternary siRNA polyplexes. The relative amounts of heparin-induced siRNA release (Figure 5.7) were inputted into the RNAi model to predict the fold change in GAPDH protein silencing efficiency (on a per μg of siRNA basis) of each formulation relative to polyplexes without PAA (fold change = 1)..... 203

Figure 5.10: Heparin-induced siRNA release from polyplexes incorporating QDs. Varying amounts of QDs were added during mPEG-*b*-P(APNBMA)/240 kDa PAA/QD siRNA polyplex formation. Following complex formulation, heparin was added at a heparin:siRNA weigh ratio of 5:1 and incubated for 30 min. (A) Cartoon schematic of polyplex formation. (B) The solutions were subjected to gel electrophoresis. (C) The amount of free siRNA from the agarose gels was quantified using ImageJ. Results are shown as the mean \pm standard deviation of data obtained from three independent experiments. 205

Figure 5.11: Model predictions of protein silencing efficiencies of mPEG-*b*-P(APNBMA)/240 kDa PAA/QD siRNA polyplexes following irradiation with 365 nm light. Predictions from the kinetic model were computed on the basis of siRNA release data in Figure 5.10 and are shown as diamonds [0/100 PAA/siRNA (w/w) in green and 30/70 PAA/siRNA (w/w) in pink]. The predicted values (diamonds) were compared to experimental data (bars) [0/100 polyplexes in orange and 30/70 polyplexes in blue]. Experimental results are shown as the mean \pm standard deviation of data obtained from three independent experiments. The red dashed line represents the maximum level of GAPDH protein silencing achievable with a single dose of siRNA.⁴⁶ . 206

Figure 5.12: Light-induced polyplex disassembly of mPEG-*b*-P(APNBMA) polyplexes. The complexes were formulated with various combinations of 2 nM QDs, 30 wt% PAA, and fluorophore-labeled siRNA. Following irradiation with 365 nm light for varying lengths of time, the fluorescence intensity was measured. (A) The FRET efficiency was computed for each complex composition as follows: no modifications (green), QDs (blue), PAA (purple), and QDs and PAA (red). Results are shown as the mean \pm standard deviation of data obtained from three independent experiments for each time point. (B) The FRET ratio following 10 min of irradiation. The results are reported as the average fluorescence of three independent samples for each irradiation time. *Note: all of the groups (at 10 min) are statistically different from each other ($p < 0.05$).* 207

- Figure 5.13: FRET-based detection of polyplex disassembly inside cells. (A) Representative flow cytometry histograms showing the fluorescence intensity distributions of cells treated with light for various lengths of time. (B) The median FRET fluorescence intensity of cells treated with light for various lengths of time, normalized to cells that were not treated with 365 nm light (0 min). Results are reported as the mean \pm standard deviation of data obtained from three independent experiments. 209
- Figure 5.14: Representative visualization of an isolated QD-containing polyplex using cryo-TEM. A solution of mPEG-*b*-P(APNBMA)/PAA (30 wt% 240 kDa)/QD (1 nM) siRNA polyplexes was formulated and prepared for cryo-TEM analyses. The white circular line indicates the approximate edge of the polyplex to guide the eye. The dark 5-10 nm spheres are QDs, which appear confined within the polyplex. The scale bar represents 100 nm..... 211
- Figure 5.15: Representative cryogenic transmission electron microscopy (cryo-TEM) micrographs of mPEG-*b*-P(APNBMA)/PAA (30 wt% 240 kDa)/QD (1 nM) siRNA polyplexes. (A) A reproduction of the micrograph displayed in Figure 5.14, except the white dashed circular line was removed for visual clarity. (B) Representative micrograph of another polyplex. (C) A micrograph that shows two polyplexes that were intentionally burned to create holes in the polymer/siRNA complexes. All scale bars represent 100 nm. *Note: The few QDs that were not clustered within the polyplex likely were displaced during cryo-TEM sample preparation.* 211
- Figure 5.16: Light-induced siRNA release and mPEG-*b*-P(APNBMA) cleavage of UCNP-containing polyplexes. (A) Polyplexes were formulated with a UCNP/siRNA (w/w) ratio of 3 and incubated in solutions containing no SDS or SDS with an S/P ratio of 2.5 for 30 min. The polyplexes were then irradiated with either no light, 365 nm light for 5 min, 980 nm light for 5 min, or 980 nm light for 15 min. The solutions were analyzed *via* gel electrophoresis. (B) The solutions obtained from (A) also were measured using UV-Vis spectroscopy. (C) The peak absorbance of mPEG-*b*-P(APNBMA) at 316 nm was tracked to determine if polymer cleavage occurred. 214

Figure 6.1: Photo-controlled IL1 β protein silencing with mPEG- <i>b</i> -P(APNBMA) polyplexes, Lipofectamine RNAiMAX lipoplexes, and hybrid nanocomplexes. AoAFs were treated with siRNA using the various carriers, irradiated with 365 nm light for either 0 min (black bars) or 10 min (gold bars), and lysed for western blot analysis at 48 h post-transfection. Data represent the IL1 β protein expression levels relative to the levels of the loading control glyceraldehyde 3-phosphate dehydrogenase (GAPDH), normalized to the protein levels in controls with no siRNA treatment. Results are shown as the mean \pm standard deviation of data obtained from three independent experiments.	233
Figure 6.2: Schematic depicting the formulation of the hybrid nanocomplexes. First, nucleic acids (siRNA) were encapsulated in lipoplexes using cationic lipid (Lipofectamine RNAiMAX). Second, anionic polymer (PAA) was added to reverse the lipoplexes surface charge. Third, a mixture of photo-responsive cationic polymers (mPEG- <i>b</i> -P(APNBMA) _n with 50% n = 7.9 and 50% n = 23.6, on a molar basis of cationic amine groups) was incorporated into the formulation to form the hybrid nanocomplexes.	235
Figure 6.3: Aortic adventitial fibroblast (AoAF) cell viabilities following treatment with either polyplexes, lipoplexes, or hybrid nanocomplexes with without 365 nm light irradiation. 48 h following siRNA and light treatment, an Alamar Blue (AB) assay was used to measure cell viability relative to cells that were untreated. Results are reported as the mean \pm standard deviation of data obtained from three independent experiments.	237
Figure 6.4: Light-triggered siRNA release from hybrid nanocomplexes. The nanocarriers were formulated, incubated in sodium dodecyl sulfate (SDS) solutions at an S/P ratio (S: sulfates on SDS, P: phosphates on siRNA) of 4 to simulate lipid-rich intracellular environments, and irradiated with 365 nm light for various lengths of time. (A) The solutions were analyzed by gel electrophoresis analyses, and (B) the amount of free siRNA was quantified on the basis of relative band intensities via ImageJ software. Results are reported as the mean \pm standard deviation of data obtained from three independent experiments.	238

Figure 6.5: Dynamics of IL1 β and CDH11 protein silencing following a single dose (A) or double dose (B) of siRNA. Kinetic modeling was used to predict the temporal IL1 β (dashed red line) and CDH11 (dashed blue line) protein expression following doses of siRNA. Initial protein concentrations were normalized to 100, and the model predictions were verified experimentally using western blotting. Data points represent the normalized IL1 β (red diamonds) or CDH11 (blue squares) protein expression levels relative to the loading control. Experimental results are shown as the mean \pm standard deviation of data obtained from three independent samples. (A) AoAFs were transfected with the hybrid nanocomplexes at $t = 0$ h, irradiated with 365 nm light to release the siRNA 3.5 h post-transfection, and lysed at the times indicated by the data points. (B) AoAFs were transfected with the hybrid nanocomplexes at $t = 0$ h and $t = 72$ h, irradiated with 365 nm light 3.5 h after each transfection, and lysed at the times indicated by the data points. 240

Figure 6.6: Attenuation of myofibroblast differentiation (α SMA protein expression) following siRNA dosing. AoAFs underwent transfection with different siRNA formulations and were treated with either 0 or 10 ng mL⁻¹ TGF- β 1 to induce differentiation. (A) Representative ICC micrographs of AoAFs 4 days post-transfection following a single dose of siRNA. AoAFs were stained for F-actin (magenta), α SMA (green), and nuclear DNA (blue). Scale bars = 50 μ m. *Note: A representative zoomed-in micrograph of F-actin staining that shows stress fibers is displayed in Figure D.2.* (B) Quantification of relative α SMA protein expression from single dose ICC micrographs in (A). (C) Quantification of relative α SMA protein expression from double dose ICC micrographs [not shown], characterized on day 8. The average total fluorescence intensity of α SMA relative to F-actin of at least 100 cells per sample was measured using ImageJ for both the single and double dose regimens. All results are shown as the mean \pm standard deviation of data obtained from three independent experiments. An asterisk indicates a statistically significant difference in α SMA protein expression in comparison to the no siRNA and 10 ng mL⁻¹ TGF- β 1 treatment control ($p < 0.05$). 246

Figure 6.7: Attenuation of myofibroblast differentiation (α SMA mRNA expression) following the two different siRNA dosing schedules. AoAFs underwent transfection at either $t = 0$ h (A) or $t = 0$ h and $t = 72$ h (B) with various siRNA formulations and were treated with either 0 or 10 ng mL^{-1} TGF- β 1 to induce differentiation. (A) qPCR analyses of α SMA mRNA expression levels 3 days post-transfection in the single dose regimen. (B) qPCR analyses of α SMA mRNA expression levels 7 days after the first transfection [4 days after the second transfection] in the double dose regimen. qPCR values were normalized to the levels in the no siRNA and no TGF- β 1 treatment control for each dosing schedule. All results are shown as the mean \pm standard deviation of data obtained from three independent samples. A single asterisk indicates a statistically significant difference in α SMA mRNA expression in comparison to the no siRNA and 10 ng mL^{-1} TGF- β 1 treatment control, and a double asterisk indicates a statistically significant difference in α SMA mRNA expression in comparison to the IL1 β siRNA treatment formulation ($p < 0.05$). 249

Figure 6.8: Proliferation of AoAFs following the single or double dose siRNA regimen. AoAFs were treated with different siRNA formulations and irradiated with 365 nm light for 10 min after each transfection. The change in the number of cells was measured using the AlamarBlue assay 4 days or 7 days after the first transfection for the single dose (orange bars) and double dose (purple bars) experiments, respectively. Data represent the normalized extents of cellular proliferation relative to cells that were not treated with siRNA, with 100 indicating no change relative to untreated cells. A value of 0 indicates no change in the absolute number of cells from the time of transfection. Results are shown as the mean \pm standard deviation of data obtained from three independent experiments. An asterisk indicates a statistically significant difference in proliferation in comparison to the no siRNA treatment controls ($p < 0.05$). 251

Figure 6.9: Effect of cell density on myofibroblast differentiation following CDH11 knockdown. AoAFs were plated at 10,000 cells cm^{-2} (low density) or 30,000 cells cm^{-2} (high density), transfected with CDH11 siRNA, and treated with 10 ng mL^{-1} TGF- β 1 to induce differentiation. ICC analyses were conducted to measure (A) CDH11 or (B) α SMA protein expression. (A) Representative ICC micrographs of AoAFs 2 days post-transfection. AoAFs were stained for F-actin (magenta), CDH11 (yellow), and nuclear DNA (blue). Scale bars = 50 μm . (B) Quantification of α SMA protein expression from ICC analyses. The average total fluorescence intensity of α SMA relative to F-actin of at least 100 cells per sample was measured using ImageJ. Results are shown as the mean \pm standard deviation of data obtained from three independent samples. An asterisk indicates a statistically significant difference in α SMA protein expression in comparison to the no siRNA treatment control at the appropriate cell density ($p < 0.05$). 254

Figure 6.10: Gene silencing in rabbit aortic fibroblasts using different siRNAs. The siRNAs were encapsulated in Lipofectamine RNAiMAX lipoplexes separately or pooled in equal weight ratios (1/3 each) and delivered to rabbit aortic fibroblasts. qPCR analyses of IL1 β mRNA expression levels 24 h post-transfection were conducted, and the qPCR values were normalized to the levels in the no treatment control. All results are shown as the mean \pm standard deviation of data obtained from three independent samples. An asterisk indicates a statistically significant difference in IL1 β mRNA expression in comparison to the pooled siRNA treatment ($p < 0.05$). 255

Figure 6.11: Gene silencing efficiency of hybrid nanocomplexes in rabbit aortic fibroblasts. Pooled siRNA was delivered using the hybrid nanocomplexes (same composition as used in human AoAFs), and the cells were protected from or irradiated with 365 nm light for 10 min. qPCR analyses of IL1 β mRNA expression levels 24 h post-transfection were conducted, and the qPCR values were normalized to the levels in the no treatment control. All results are shown as the mean \pm standard deviation of data obtained from three independent samples. A single asterisk indicates a statistically significant difference in IL1 β mRNA expression in comparison to the no treatment control, and a double asterisk indicates a statistically significant difference in IL1 β mRNA expression in comparison to cells treated with IL1 β -targeting siRNA but not light ($p < 0.05$). 257

- Figure 7.1: Representative view of the surgical field following skeletonization of the left common carotid artery in a rabbit (R = rostral, C = caudal). This figure was adapted with permission from Robinson, K. G.; Scott, R. A.; Heseck, A. M.; Woodford, E. J.; Amir, W.; Planchon, T. A.; Kiick, K. L.; Akins, R. E., Reduced arterial elasticity due to surgical skeletonization is ameliorated by abluminal PEG hydrogel. *Bioeng. Transl. Med.* 2017, Accepted Article.² Copyright 2017..... 273
- Figure 7.2: Antenna dyes (green) absorb NIR irradiation (red wavy arrows) and transfer it *via* FRET (brown arrows) to the UCNP core (yellow sphere). Upconversion is defined by a process in which the absorption of two or more low-energy (NIR) photons leads to the emission of a single photon with higher energy in the visible or UV regions (rainbow wavy arrow). This figure was adapted with permission from Zou, W. Q.; Visser, C.; Maduro, J. A.; Pshenichnikov, M. S.; Hummelen, J. C., Broadband dye-sensitized upconversion of near-infrared light. *Nat. Photon.* 2012, 6 (8), 560-564.⁶ Copyright 2012, Rights Managed by Nature Publishing Group. 275
- Figure 7.3: The generic form of the mPEG-*b*-P(APNBMA) polymers. Various alterations to the molecular structure of the APNBMA monomer unit could be made to tune the photo-responsive nature of the polymer. First, the α -group on the benzylic carbon, which is depicted as R_1 , can be modified. A methyl group is commonly substituted in this position to increase the quantum yield ($R_1 = \text{Me}$). Second, a hydrogen on the aromatic ring (R_2 position) can be substituted with a methoxy ($R_2 = \text{OMe}$) to provide a bathochromic shift in the excitation spectrum..... 277
- Figure 7.4: The absorbance spectrum of mPEG-*b*-P(APNBMA). The maximum excitation wavelength is ~ 316 nm, and the absorbance drops off rapidly at longer wavelengths (approaching no absorbance ≥ 400 nm).278
- Figure A.1: Compensation matrices used to correct for signal spillover in Figure 3.10. The APC and PE channels primarily detected signals from individual fluorophores (control samples) and the PE-Texas Red channel primarily detected the signal attributed to FRET..... 298
- Figure C.1: Emission spectra of lanthanide atom doped NaYF₄ upconverting nanoparticles (UCNPs) as a function of irradiation intensity. The UCNPs were excited with 980 nm light, and the resulting emission was characterized. These measurements were performed by Eric Chen from the Doty lab at the University of Delaware..... 301

Figure C.2: Polyplex formation and siRNA release as a function of the UCNP loading ratio. (A) Acid-functionalized UCNPs were added to the polyplex formulations at various loading ratios (UCNP/siRNA [w/w]), and heparin was added (heparin/siRNA [w/w] of 5) to induce siRNA release. Then, the solutions were subjected to gel electrophoresis. (B) The free siRNA bands in the gel in (A) were quantified using ImageJ analyses.	302
Figure C.3: Average polyplex size as a function of UCNP loading ratio. Polyplexes were formulated with various loading ratios of UCNP/siRNA (w/w) and analyzed using dynamic light scattering (DLS).....	303
Figure D.1: Cell doubling time of AoAFs, as evaluated by the AlamarBlue assay. Results are reported as the mean \pm standard deviation of data obtained from three independent samples.....	304
Figure D.2: Representative micrograph showing F-actin stress fibers at a higher magnification. The scale bar represents 25 μ m.....	307
Figure D.3: Changes in alpha smooth muscle actin (α SMA) mRNA expression (marker of myofibroblast differentiation) over the course of one week without transforming growth factor beta 1 (TGF- β 1) treatment. Quantitative PCR (qPCR) analyses compared the α SMA mRNA expression levels on day 7 relative to day 0. ² Results are shown as the mean \pm standard deviation of data obtained from three independent samples. The samples were not significantly different from each other at a significance level of 0.05.....	308

ABSTRACT

Nucleic acid delivery has garnered significant interest as a biomedical research tool and therapeutic approach for the treatment of devastating diseases, as evidenced by the thousands of clinical trials that have been conducted over the past few decades. Small interfering ribonucleic acids (siRNA)s are particularly promising due to their ability to mediate transient post-transcriptional sequence-specific gene knockdown of aberrantly expressed proteins. Although cationic polymers have proven to be effective siRNA delivery vehicles, several problems related to a lack of spatiotemporal control over nucleic acid binding *vs.* release have hindered their clinical impact. To address these challenges, a nanocarrier system comprised of a photo-responsive block copolymer was developed that encapsulated and protected siRNA, stimulated cellular uptake, and induced light-triggered gene silencing. The work in this dissertation builds on this system to facilitate the translation of the approach into animal models and provide insights into siRNA release. Specifically, the dissertation is broken down into four primary objectives: 1) to develop a mechanistic understanding of nanocarrier disassembly and design methods for regulating the amount, location, and timing of siRNA activity; 2) to improve nanocarrier efficiencies through the formulation of mixed polymer complexes and predict dose responses using simple kinetic modeling; 3) to elucidate the effects of incorporating anionic excipients into nanocarriers and impart diagnostic characteristics into the formulations; and 4) to enable on/off control over gene silencing in human primary cells and mitigate maladaptive cellular responses that lead to high rates of cardiovascular graft failures. Overall, the work

presented in this dissertation improved the efficiency and capabilities of photo-responsive siRNA delivery vehicles, provided a new combination of methods for probing the structure-function relationships of siRNA-polymer assemblies, established a simple kinetic model that accurately predicted siRNA dose responses, demonstrated the potential of lipid-polymer hybrid nanocomplexes in primary cells, and contributed new insights into the fundamental mechanisms that govern nucleic acid binding *vs.* release. These advances, along with the suggestions for future work, may help facilitate the translation of nucleic acid therapies into the clinic.

Chapter 1

INTRODUCTION AND MOTIVATIONS

1.1 Nucleic Acid Delivery

Nucleic acid delivery is a powerful biomedical research tool and therapeutic approach aimed at regulating gene expression through the introduction of plasmid deoxyribonucleic acid (DNA), messenger ribonucleic acid (mRNA), antisense oligonucleotides, small interfering ribonucleic acid (siRNA), and other nucleic acids.¹ Specifically, gaining control over protein/transcript expression has provided scientists with the abilities to study gene functions, identify gene products, establish disease models, and manipulate cellular responses.² Perhaps the most potentially transformative applications of nucleic acid delivery include disease treatment and regenerative medicine, as evidenced by a number of product approvals within the last few years.³ For example, Glybera, a gene therapy for lipoprotein lipase deficiency, was approved in Europe in 2012.⁴ Several antisense products also have been approved in the United States for the treatment of devastating indications such as cytomegalovirus retinitis, homozygous familial hypercholesterolemia, and Duchenne muscular dystrophy.⁵ Moreover, thousands of gene therapy clinical trials have been initiated in the last few decades, with many of these trials advancing to late stages of development.⁶

1.1.1 siRNA enables gene silencing

Therapeutic approaches that exploit RNA interference (RNAi) offer a particularly attractive strategy for regulating gene expression to treat a wide range of acquired and hereditary diseases.⁷ siRNA molecules can engage this natural pathway by interacting with cellular machinery to mediate post-transcriptional sequence-specific gene silencing of aberrantly expressed proteins.⁸ siRNA is a class of double-stranded RNA that is usually 20-24 base pairs in length with two overhanging nucleotides and phosphorylated 5' ends and hydroxylated 3' ends on each strand.⁹ As shown in Figure 1.1, in the cytoplasm, a siRNA duplex binds to the RNA-induced silencing complex (RISC) and becomes unwound. While the passenger (sense) strand is ejected and degraded, the guide (antisense) strand remains engaged with the RISC and acts as a template for the RISC to recognize complementary mRNA transcripts.¹⁰ Argonaute2 (AGO2), one of the key proteins in the human RISC, cleaves the complementary mRNA, which subsequently is degraded by the cell.¹¹ The guide strand-RISC can then seek out other mRNA strands and induce transcript cleavage, effectively propagating gene silencing by halting translation of the targeted protein.¹²

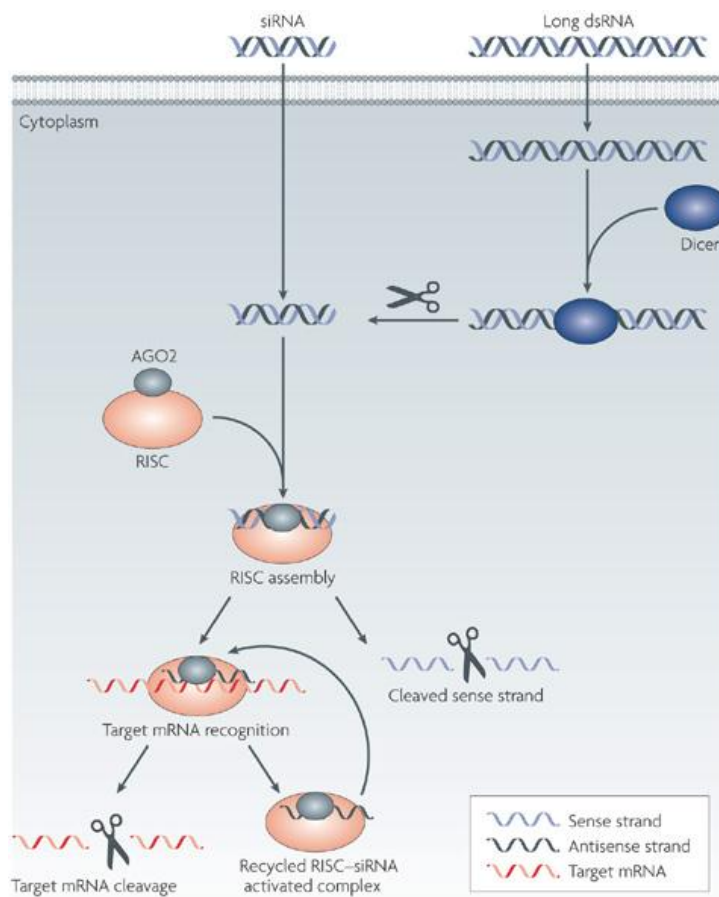


Figure 1.1: Schematic of the RNAi mechanism. This figure was adapted with permission from K.A. Whitehead, R. Langer, D.G. Anderson, Knocking down barriers: advances in siRNA delivery, *Nat. Rev. Drug Discov.* 8(2) (2009) 129-138.¹³ Copyright 2009, Rights Managed by Nature Publishing Group.

The development of reliable siRNA design algorithms has enabled the production of synthetic siRNA duplexes that have the capacity to target virtually any gene of interest with minimal off-target effects.¹⁴ siRNA has enormous inherent advantages in practical/therapeutic application through its clinically demonstrated safety profile, capacity to harness the endogenous gene regulatory machinery using a simple one-component construct, high potency and sequence-specificity, and

modularity.^{15, 16} Additionally, chemical modification strategies for the RNA backbone have conferred enhanced resistance to enzymatic hydrolysis and nuclease degradation, reduced immune responses through Toll-like receptor pathways, and improved thermodynamic stability for *in vivo* applications.¹³ These characteristics have already advanced siRNA therapeutics into late-stage human clinical trials for the treatment of debilitating conditions as varied as metastatic melanoma, diabetic macular edema, Ebola, and hepatitis C,^{15, 17} indicating the enormous promise of siRNA platforms for a range of applications in human health.

1.2 Delivery Vehicles

Despite these advances, naked siRNA is still susceptible to enzymatic degradation and has limited capacity for cellular uptake because of its relatively large size and negative charge, thus necessitating a carrier strategy that employs siRNA effectively in the modulation of gene expression.^{13, 18} The vast majority of gene delivery vehicles tested in the clinic to date involved modified viruses, which have naturally evolved over billions of years to efficiently mediate gene transfer.^{19, 20} Unfortunately, viral vectors suffer from several drawbacks, including fundamental safety concerns regarding immunogenicity, mutagenicity, and tumorigenicity, low loading capacities, storage difficulties, and nanocarrier formulation challenges.^{21, 22} Nonviral delivery vehicles, including polymer-, lipid-, and inorganic nanoparticle-based carriers, avoid many of the obstacles faced by viral vectors and represent promising alternatives.^{21, 23}

1.2.1 Polyplexes

In particular, cationic polymers have garnered significant interest in recent years.¹ These materials offer numerous appealing properties including excellent control over chain length, synthetic versatility, low dispersities, and biocompatibility.^{24, 25} Cationic polymers can electrostatically bind negatively charged siRNA and self-assemble into nanoscale complexes (polyplexes) that are capable of efficient gene transfer. In fact, in 2010, the first in-human phase I clinical trial of patients with cancerous solid tumors that used a targeted nanoparticle delivery system for systemic administration of siRNA was completed, and these nanocarriers were formulated with polymeric materials.^{15, 26} Although these trials provided some encouraging outcomes, the studies uncovered numerous challenges that must be overcome before such therapies are made commercially available.²⁷

1.3 Controlling Binding vs. Release

Many of the shortcomings of nonviral siRNA nanocarriers are related to a lack of control over siRNA binding vs. release.^{1, 28} Effective polyplex systems must satisfy seemingly contradictory demands at various points along the delivery pathway (Figure 2).^{29, 30} In particular, several reports have emphasized the importance of maintaining nanocarrier stability and siRNA binding/integrity in the presence of anionic proteoglycans and nucleases in the extracellular environment.³¹⁻³³ For example, Zuckerman *et al.* found that cationic cyclodextrin-containing polymer (CDP)-based siRNA nanoparticles were rapidly disassembled at the glomerular basement membrane (GBM) of the kidney due to interactions with heparan sulfate, a negatively charged proteoglycan that is abundant throughout the body.³⁴ A complementary study by Abdelhady and coworkers employed atomic force microscopy in liquid to demonstrate

that unprotected DNA, which is more degradation-resistant than siRNA, is broken down within minutes in the presence of nucleases.³³ Although the addition of cationic generation 4 polyamidoamine dendrimers slowed the degradation process, the nucleic acid cargo was still insufficiently packaged in the polyplexes to maintain complete integrity. These reports highlight the need to find cationic polymers that can stably bind siRNA and protect the cargo prior to cellular uptake.

At the same time, multiple studies have demonstrated that inefficient intracellular siRNA release is a major bottleneck restricting delivery in the cytoplasm, thereby hampering siRNA interactions with RISC.³⁵⁻³⁸ For example, Shim *et al.* showed that polyplexes comprised of unmodified linear polyethylenimine (L-PEI) mediated only ~5% gene silencing in NIH/3T3 cells due to inefficient siRNA unpackaging, as evidenced by the highly colocalization of the polymer and siRNA in the cytoplasmic and nuclear compartments.³⁵ In a related report, Han and coworkers demonstrated that galactose-modified trimethyl chitosan-cysteine (GTC) polyplexes carrying VEGF-targeting siRNA did not effectively reduce tumor growth compared to other types of polyplexes.³⁸ The authors partially attributed this behavior to a lack of siRNA release from the GTC-siRNA complexes. Taken together, the competing requirements of binding *vs.* release necessitate a compromise between stability and unpackaging in most polyplexes, especially in systems with limited means to manipulate electrostatic interactions.^{39, 40}

A number of strategies have been explored to provide better control over siRNA activity. These approaches include the development of stimuli-responsive materials, the formulation of mixed block copolymer nanocarriers, and the incorporation of anionic excipients. The sections below detail previous work in each of these strategies

and lay out the advantages and drawbacks of each. Ultimately, a combination of these strategies may provide the best control over siRNA binding *vs.* release.

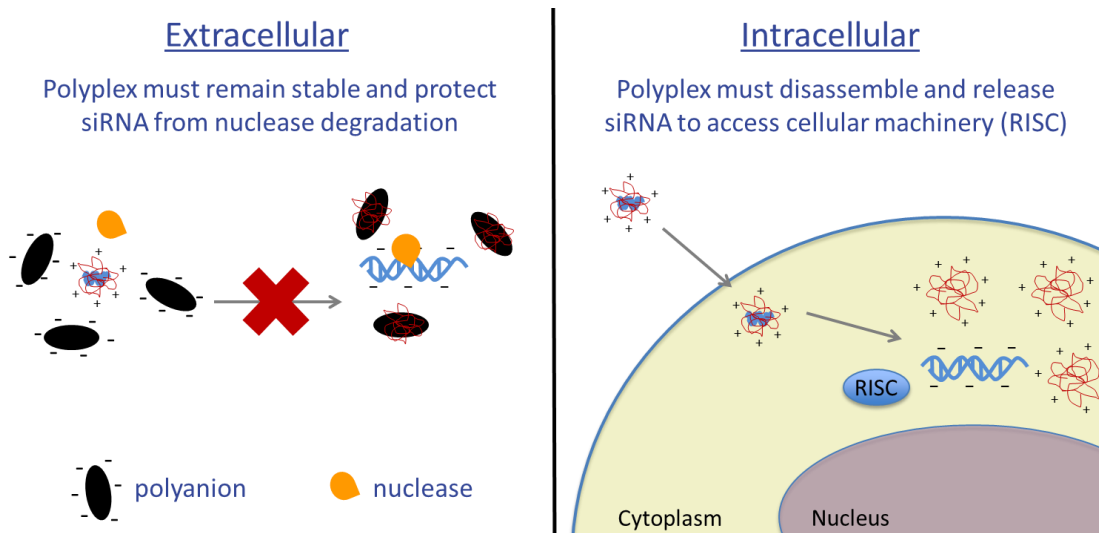


Figure 1.2: siRNA polyplexes must satisfy seemingly contradictory demands of remaining stable extracellularly but disassembling intracellularly. The competing requirements of siRNA binding *vs.* release are some of the most significant challenges hindering the translation of siRNA nanocarrier systems.

1.3.1 Stimuli-responsive materials

One of the most promising strategies for enhancing regulation over siRNA binding *vs.* release is the use of stimuli-responsive materials.^{41,42} A wide variety of biomaterials have been engineered with changeable nucleic acid binding affinity in response to biological or external stimuli (Figure 1.3).^{25,43} Specifically, these characteristics have been incorporated into polymers through the addition of different functional moieties that are sensitive to a diverse set of triggers.^{44,45} When a given stimulus is introduced, the polymers' binding capacity for siRNA can be altered to

enhance release through changes in molecular forces and/or nanostructure.⁴⁶⁻⁴⁸

Although the task of precisely controlling nucleic acid activity remains challenging, significant advances in the development of stimuli-responsive materials have shown tremendous promise.⁴⁹ These strategies are discussed in more detail in the following sections.

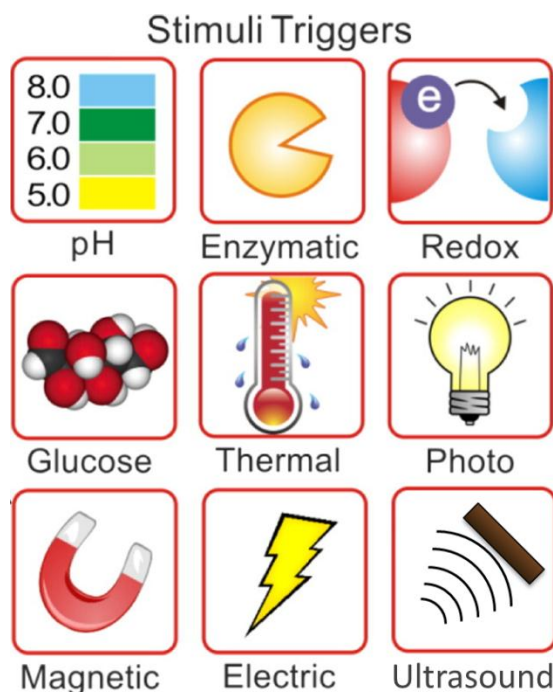


Figure 1.3: Different stimuli that have been used in biomaterials to gain better control over nucleic acid binding vs. release. This figure was adapted with permission from Y. Lu, W.J. Sun, Z. Gu, Stimuli-responsive nanomaterials for therapeutic protein delivery, *J. Control. Release* 194 (2014) 1-19.50 Copyright 2014 Elsevier B.V. All rights reserved.

1.3.1.1 Biological stimuli-responsive nanocarriers

The biological and/or cellular environment provides a diverse range of signals that can be used to alter nanocarrier structure and induce nucleic acid release.⁴¹ Some

of these triggers include local changes in pH,⁵¹⁻⁵⁴ redox potential,⁵⁵⁻⁵⁷ enzyme/substrate concentration,^{58, 59} oxygen content,⁶⁰ and temperature.^{61, 62} Perhaps the most common of these strategies is pH-sensitive nanocarriers that rely on the acidification of the endosomes as the cargo is trafficked intracellularly to lysosomes. For example, Shim *et al.* synthesized acid-degradable ketalized linear polyethylenimine (KL-PEI) to overcome the challenges of intracellular siRNA release (example discussed above).³⁵ The authors found that the pH-responsive polymers degraded during endosomal trafficking and resulted in polyplex disassembly and increased siRNA release into the cytoplasm. This relatively simple modification allowed gene silencing to reach ~50% efficiency, which was an order of magnitude higher than the unmodified L-PEI polyplexes. As an example of a redox potential-sensitive system, Nuhn and coworkers developed nanogels with disulfide cross-linkers for redox-triggered release of siRNA and nanoparticle degradation in the reductive conditions of the cytoplasm.⁵⁵ These nanocarriers were stable in buffered solutions but released all of the siRNA when incubated in 20 mM dithiothreitol (DTT), a reducing agent used to simulate the redox potential in the cytoplasm.

These encouraging reports support the concept that biological stimuli-responsive materials are able to take advantage of natural differences in conditions within cells to improve gene silencing efficiencies.⁶³ However, these strategies provide inadequate control over the extent of nucleic acid activity, particularly in space and time.⁶⁴ Additionally, the heterogeneous nature of living organisms and cells makes it difficult to develop a biologically-sensitive material that can be applied universally. These challenges are compounded by the fact that it is extremely difficult to find a stimulus threshold that is wide enough to allow for minor fluctuations in the

environment without prematurely inducing siRNA release, but also narrow enough that the nanocarriers can be rapidly triggered to release the payload before being exocytosed or degraded in lysosomes.^{65, 66}

1.3.1.2 Externally-triggered nanocarriers

As an alternative to relying on the natural biological environment, externally applied stimuli can promote siRNA delivery with user-defined control. Some of these stimuli include magnetic fields,^{67, 68} ultrasound,⁶⁹⁻⁷¹ and light.⁷²⁻⁷⁴ These triggers are able to direct nucleic acid release from polyplexes in targeted tissues on-demand, allowing for at least some degree of spatiotemporal control.⁷⁵ In addition to controlling gene activity in space and time, these approaches also may allow for the amount of siRNA release to be easily tuned on the basis of the strength and/or duration of the applied stimulus.⁷⁶ For example, Burke *et al.* enhanced the transfection efficiency of poly(ethylene glycol) (PEG)/PEI nanocomplex gene carriers that were delivered with ultrasound-sensitive microbubbles in mice by tailoring the stimulus parameters.⁷⁷ The authors found that the application of ultrasound facilitated PEG/PEI nanocomplex delivery from the bloodstream into the targeted skeletal muscle cells and subsequently increased nucleic acid release into the nucleus. Thus, approaches that exploit externally applied stimuli may not only be able to improve nucleic acid delivery efficiencies, but also provide user-defined targeting to specific cell/tissue populations.⁷⁸

One of the most promising external stimuli is light. Photo-sensitive materials offer unique advantages such as rapid response to the stimulus,⁷⁹ exquisite spatial resolution with minimal diffusive effects,⁸⁰ and tunability of light wavelength and intensity.^{81, 82} These characteristics have enabled the development of systems capable

of precisely timed light-triggered release of active nucleic acids.⁸³⁻⁸⁶ The spatiotemporal specificity in such systems is particularly beneficial for regenerative medicine and other biomedical fields.⁸⁷⁻⁸⁹ However, most of these systems rely on photocaging the nucleic acid or conjugating the nucleic acid to inorganic nanoparticles. For example, Nguyen *et al.* controlled siRNA activity inside cells by protecting the siRNA with a photocaging group and irradiating with various doses of light to knockdown genes in an effort to change cellular phenotypes.⁹⁰ Although such strategies have successfully increased control over siRNA activity, many of these systems require tedious and expensive nucleic acid modifications and/or use cytotoxic materials.

An alternative approach is the incorporation of photo-sensitive groups into polymers.^{91,92} Light-active functional moieties are able to undergo photochemical cleavage reactions or isomeric rearrangements depending on the specific functional group used.⁹³ The most commonly used functional group is *ortho*-nitrobenzyl (*o*-NB), which absorbs ultraviolet (UV) and near-infrared light and cleaves to form carboxylic acid and nitrosobenzaldehyde groups.^{94,95} In particular, the production of the carboxylic acid introduces a negatively charged carboxylate ion in aqueous conditions above pH ~3.⁹⁴ Also, the photochemical cleavage rate and absorbance spectrum of *o*-NB can be altered by substituting various molecular groups onto the aromatic ring.^{96,97} These strategies have allowed for more efficient photocleavage reactions and two-photon excitation due to red-shifted absorption, making these materials more useful for biomedical applications.^{98,99} Nevertheless, even the unmodified *o*-NB moiety has been successfully used to induce cleavage in materials used for gene delivery. Han *et al.* induced nucleic acid release by complexing DNA with cationic groups that were

linked to gold nanoparticles using an *o*-NB group, which cleaved upon UV light irradiation.⁸⁶ The relatively small cationic leaving group was no longer able to electrostatically condense the DNA, resulting in intracellular DNA release and controlled transfection. In addition to *o*-NB, other photoactive functional groups, such as derivatives of azobenzene, diazonaphthoquinone, and pyrenylmethyl esters, can be used depending on the targeted application.^{100, 101}

1.3.2 Mixed block copolymer formulations

Regardless of the stimuli-responsive nature of a delivery vehicle, the strengths of the nucleic acid interactions need to be optimized to enable a balance between siRNA binding *vs.* release. One of the most common strategies to address this challenge is to tune the nucleic acid binding capacity by systematically varying the molecular weight and/or charge density of the cationic component.^{102, 103} Generally, increasing the number of cationic groups increases the polymer binding efficiency and cellular uptake of the polyplexes; however, increased positive charge also hinders siRNA release in the cytoplasm and results in greater cytotoxicity of the nanocarriers.¹⁰⁴ Most studies must compromise and use polymers with intermediate binding forces that balance these factors to improve nucleic acid delivery.⁴⁰ Furthermore, such systematic approaches often require the synthesis of small libraries of polymers, a process that can be both tedious and costly.^{105, 106} An alternative and more flexible strategy for improving the control of siRNA release is the use of mixed polyplexes assembled from polymers with different compositions.^{18, 107} Modulations to the net cationic charge can be achieved simply by changing the molar ratios of as few as two polymers, allowing for rapid determination of structure-function relationships.¹⁰⁸⁻¹¹⁰

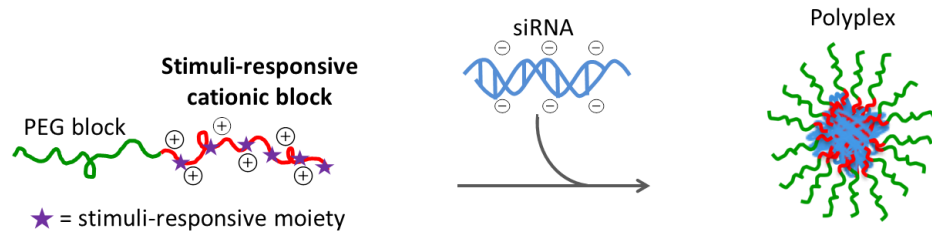
The mixed polymer approach is particularly appealing when working with cationic block copolymers (BCP)s, which offer the ability to potentially decouple functions.¹¹¹ BCPs are comprised of two or more chemically-distinct polymer “blocks” that are covalently bound to form one continuous chain.¹¹² The linking of polymer chains that are chemically different enables the combination of unique properties within a macromolecule and allows for self-assembly behavior on the nanoscale that is not possible with a homopolymer.¹¹³ In addition to these benefits, BCPs offer numerous appealing properties including excellent control over block lengths, unsurpassed tailorability, controlled and predictable self-assembly in solution, and access to a bottom-up approach for generating nanocarriers for nucleic acid delivery.^{113, 114} More details regarding this strategy are discussed in Chapter 4.

1.3.3 Incorporation of anionic excipients

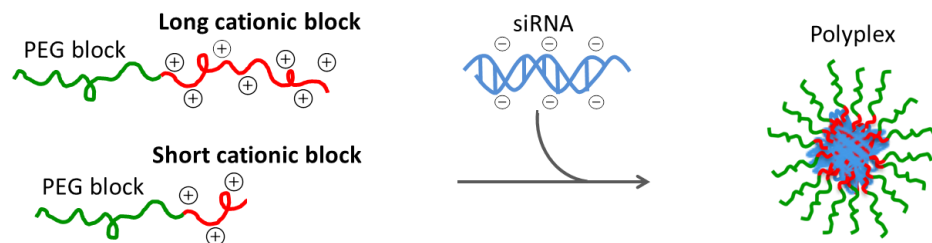
Despite the use of stimuli-responsive materials and/or mixed block copolymer formulations, a significant amount of the delivered nucleic acids remains stably encapsulated in the nanocarriers and is not able to engage the cellular machinery (e.g., RISC).^{37, 115} An approach for overcoming this limitation is the incorporation of additional components to modulate the release of siRNA.¹¹⁶ These components often are polymers, peptides, proteins, or glycosaminoglycans with high negative charge densities¹¹⁷⁻¹¹⁹ that can alter nucleic acid binding properties, while also providing enhanced ability to release the payload from the polyplexes.^{120, 121} Specifically, anionic excipients that have a strong binding affinity for the cationic polymers may provide additional stability to the electrostatically assembled polyplexes while simultaneously enabling improved release of siRNA.¹¹⁶ For example, Han *et al.* reported that the incorporation of anionic γ -poly(glutamic acid) (γ -PGA) or sodium

tripolyphosphate (TPP) into galactose-modified trimethyl chitosan-cysteine polyplexes tuned the electrostatic interactions and increased siRNA release, resulting in significantly enhanced gene silencing.³⁸ Other anionic excipients also have shown tremendous promise in modulating nucleic acid binding *vs.* release, and further details are discussed in Chapter 5. Ultimately, a combination of stimuli-responsive materials, mixed BCP formulations, and incorporation of anionic excipients may be needed to enhance gene silencing and obtain precise control over nucleic acid activity (Figure 1.4).

Stimuli-responsive polymers



Mixing BCPs



Anionic excipients

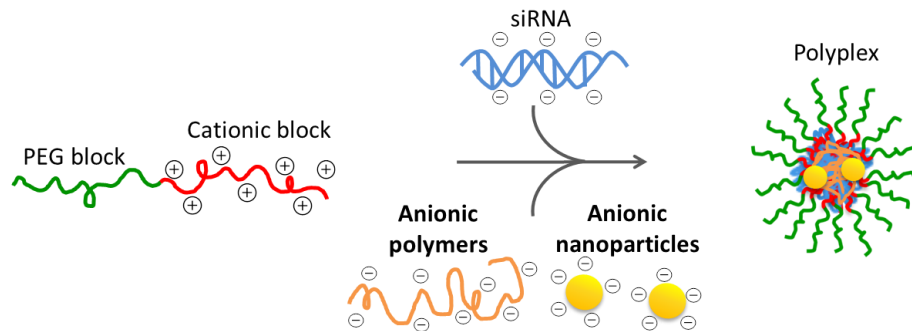


Figure 1.4: Overview of three of the main strategies (stimuli-responsive materials, mixed BCP formulations, and incorporation of anionic excipients) used to enhance control over siRNA binding vs. release. Ultimately, a combination of these three distinct strategies may provide the best opportunity to improve gene silencing efficiencies and gain precise control over nucleic acid activity.

1.4 Spatiotemporal Control over Gene Expression

Ideal nanocarriers would not only satisfy the requirements of balancing siRNA binding *vs.* release, but also provide spatiotemporal control over RISC assembly and subsequent gene knockdown. This is important because improved methods to enable spatiotemporal control over gene expression are necessary to overcome fundamental challenges that hinder biomedical research and therapeutics.^{82, 122} For example, high-resolution spatiotemporal manipulation of gene activity is needed to probe the complex network of cell-to-cell interactions governing differentiation during embryonic development.² Spatial regulation of gene expression also would facilitate the generation of cell microarrays for the high-throughput identification of functional gene products, which is critical for continued advancements in drug discovery.¹²³ Moreover, new approaches to precisely modulate gene activity with minimal off-target effects are crucial for the generation of intricate tissue scaffolds, which require exquisite control over cellular growth and signaling for use in clinical applications.⁸⁷

Over the past two decades, inducible promoter systems have been the predominant strategy for manipulating gene expression *via* chemically-regulated initiation of transcriptional activation.¹²⁴ However, the spatial control offered by these promoter approaches is limited due to the diffusive nature of the extracellular inducers. Recently, state-of-the-art optogenetic regulation systems were developed as an alternative means to provide improved spatiotemporal resolution through light-induced transcriptional control.¹²⁵⁻¹³⁰ The ability to limit off-target effects and achieve rapid activation and deactivation kinetics make optogenetic systems invaluable tools in the field of tissue engineering.⁸² Unfortunately, these systems have numerous drawbacks that may prevent them from realizing their full potential in clinical settings. First, most optogenetic tools lack the capacity to regulate endogenous genes.¹³¹

Second, the introduction of non-human components may interfere with native cellular pathways and stimulate immune responses.¹³¹ Third, difficulties may arise if the multiple components in photo-sensitive protein-based assemblies must be delivered, a situation that is difficult to resolve with high efficiency and often requires the use of viral expression vectors that introduce safety concerns such as immunogenicity and mutation/oncogene activation.¹³²

An alternative approach for spatiotemporal gene regulation is the controlled delivery of nucleic acids. A number of stimuli-sensitive constructs, including responsive siRNA nanocarriers and photocaging tools, have been designed to trigger activation of siRNA and impart spatial control over gene silencing.⁴¹ For example, a variety of strategies have been reported that limit the delivery of nucleic acids to specific spatial regions, including nanoparticles that are sensitive to stimuli such as redox potential¹³³ and magnetic fields,¹³⁴ or reverse-transfections employing transgenes or siRNAs patterned onto substrates.^{123, 135, 136} All of these approaches improve spatial control over nucleic acid delivery, but they typically require specialized and/or tedious protocols for spatial patterning that may be difficult to implement on larger scales or in tissue engineering/regenerative medicine applications. Furthermore, many of these approaches lack precise and dynamic control over the interactions between the carrier molecules and the nucleic acid cargoes, leading to limited modulation of the extent of gene activity. These shortcomings underscore the need for novel strategies capable of precisely controlling siRNA binding *vs.* release intracellularly in a spatiotemporal fashion.

1.4.1 Applications in regenerative medicine: coronary artery bypass grafting

A specific application that would greatly benefit from improved spatiotemporal control over gene expression is related to cardiovascular disease, which is the leading cause of death worldwide.¹³⁷ Vascular reconstructive surgeries, including the placement of bypass grafts, have become routine procedures for treating these ailments.¹³⁸ Unfortunately, even standard treatments, such as autologous vein grafts from the leg fail ~50% of the time within a few years due to inappropriate vessel remodeling.¹³⁹ These graft failures are primarily driven by maladaptive cellular responses elicited by tissue injury and hemodynamic stress.¹⁴⁰ Anastomoses, the sites of surgical vessel connection, are at particular risk due to suture line scarring, stricture, and higher incidences of stenosis and fibrosis (Figure 1.5).¹⁴¹ Unfortunately, although drug eluting stents and externally-applied films have shown promise in preventing complications, these interventions provide inadequate spatial and temporal control to modulate cell behaviors appropriately in all regions of the graft conduit.^{142, 143} New methods are needed that can locally target the key cell types involved in failure. Such approaches could enable improved healing responses by tuning the application and release of regulatory therapies according to the localized environment within the site of injury.¹⁴⁴

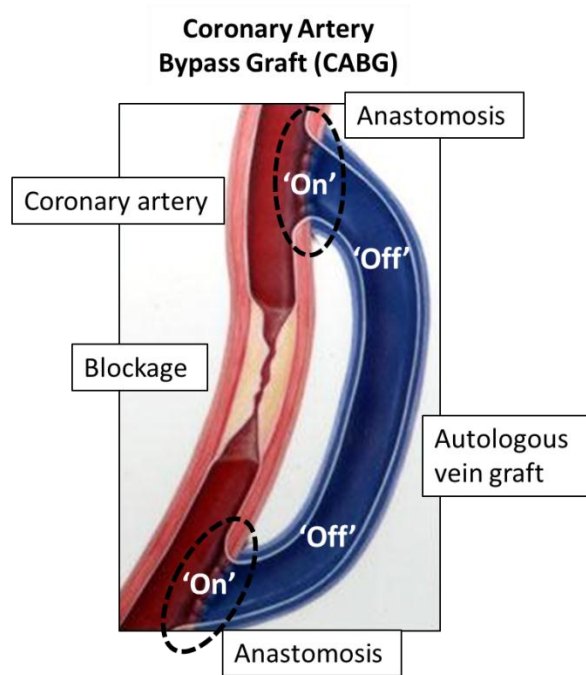


Figure 1.5: Depiction of a coronary artery bypass graft. The autologous vein graft is placed to bypass the blockage and is sutured to the coronary artery at anastomoses. Current therapeutic approaches lack the spatial control needed to reduce maladaptive responses in the anastomoses ('on') while avoiding off-target effects in the rest of the graft conduit ('off'). The cartoon of the graft was adapted from: <http://www.mobilevascular.com/bypass-surgery.html>. (March 17, 2017).

1.5 Gene Silencing Dynamics and Dosing Regimens

Although the biomaterial strategies outlined above (e.g., section 1.3.1.2) have enhanced spatiotemporal control over siRNA delivery, a limited understanding of the dynamic silencing response persists.¹⁴⁵ Successful application of RNAi depends on numerous biological parameters, such as cell doubling time, as well as mRNA and protein half-lives.^{146, 147} In particular, diseases characterized by rapid cell division, such as cancer, are difficult to treat with siRNAs because dilution effects exclude the possibility of sustained protein knockdown with a single dose.¹⁴⁷ Thus, multiple doses

must be administered to maintain robust gene silencing over a prolonged period of time.

The majority of RNAi protocols and dosing schedules reported in the literature are chosen on the basis of precedence, or through trial and error, rather than being optimized for the system of interest. Consequently, multiple experiments must be conducted to screen for conditions that achieve the desired level and/or duration of knockdown; this tedious approach often fails to identify improved dosing regimens.¹⁴⁸ For example, due to cost and time limitations of experimentally testing siRNA dosing schedules, Bartlett *et al.* were unable to find a dosing frequency that significantly improved tumor growth inhibition in a syngeneic mouse cancer model.¹⁴⁹ However, the authors used kinetic modeling to provide critical insights into the underlying causes for these shortcomings, which guided the design of dosing regimens that were later employed in clinical trials.²⁷ These studies demonstrate the importance of developing methods capable of predicting effective dosing protocols, particularly in translational medicine.

Kinetic modeling can provide insights into the kinetics of the RNAi process and enable the rapid identification of optimum dosing schedules tailored to a given system. To date, a few such models have been published.^{145-147, 149-152} These models have been valuable tools, and in many cases, have provided a framework to predict changes in gene expression and identify rate-limiting steps. For example, Chen *et al.* employed kinetic models to determine that the rate of nanocarrier unpackaging correlated strongly with modulations in gene expression using polyplexes made with PEI, chitosan, and polyphosphoramidate.³⁰ The work inspired additional efforts to enhance

nucleic acid delivery through responsive biomaterials design,¹⁵³ and it demonstrated the utility of models for improving nanocarrier efficacy.

However, modeling approaches have most often been applied to commercial gene delivery systems (e.g. Lipofectamine, Oligofectamine, PEI),^{30, 147, 150} which are incapable of precisely controlled and tunable nucleic acid activity. These material limitations have precluded widespread use of the kinetic models in biomedical fields that require precise temporal control and/or gradients in gene expression. Furthermore, many of these models require knowledge of numerous kinetic parameters that complicate their implementation. An alternative approach is to simplify the model to include only the most important rate-limiting steps and allow for RNAi effects to be averaged across an entire cell population. The development of delivery vehicles capable of externally-triggered siRNA release would provide greater versatility in the timing and magnitude of gene silencing, thereby facilitating the use of streamlined models to predict dosing schedules in regenerative medicine.

1.6 Novel Photo-Responsive Block Copolymer

To address the challenges discussed above, our group synthesized novel and tailorable cationic photo-responsive diblock copolymers, mPEG-*b*-poly(5-(3-(amino)propoxy)-2-nitrobenzyl methacrylate) [mPEG-*b*-P(APNBMA)_n]. The polymers are comprised of cationic and nonfouling blocks, the structure of which enables stable nucleic acid binding and encapsulation within nanoscale electrostatic complexes surrounded by a “stealth” PEG coating.¹⁵⁴ Photocleavable *o*-NB moieties link pendant ammonium cations to the polymer backbone and enable light-induced hydrolysis and charge reversal in the polymer chain for rapid release of complexed nucleic acids. Furthermore, the polymers have tunable molecular weights and low

dispersities. The synthesis and characterization of the polymers were conducted by Prof. Matthew Green and Dr. Tiffany Suekama, and the specific procedures and characterization results are outlined in great detail in a previous publication by the groups.¹⁵⁵ Initial testing of siRNA polyplex formulations was conducted by Dr. Abbygail Foster (in collaboration with Chad Greco for the heparin stability, serum/nuclease stability, cell viability, and gene silencing experiments), and the resulting data was published in a previous article by the group.¹⁵⁶ The subsequent sections provide an overview of the critical points related to: 1) the synthesis and characterization of the polymers; and 2) the properties of the siRNA polyplexes.

1.6.1 Polymer synthesis and characterization

The text, tables, and figures in section 1.6.1 are adapted and reprinted with permission from Green, M. D.; Foster, A. A.; Greco, C. T.; Roy, R.; Lehr, R. M.; Epps, T. H., III; Sullivan, M. O., Catch and release: photocleavable cationic diblock copolymers as a potential platform for nucleic acid delivery. *Polym. Chem.* 2014, 5 (19), 5535-5541.¹⁵⁵ Copyright 2014, Published by The Royal Society of Chemistry.

A PEG macroinitiator was used to provide access to controlled radical polymerization (CRP) techniques, i.e., atom-transfer radical polymerization (ATRP). CRP enables tunable molecular weights, compositions, dispersities, and end-group functionalities. A vital building block in the scheme was the monomer, 5-(3-((*tert*-butoxycarbonyl)amino)propoxy)-2-nitrobenzyl methacrylate (Boc-APNBMA), which contained a methacrylate and protected amine functionality to facilitate ATRP. Photo-responsive character was introduced through the incorporation of an *o*-NB ester moiety. Cleavage of the Boc-protecting group following ATRP revealed the final cationic and photo-responsive block copolymer. The monomer and the subsequent

protected and ionic block copolymers were prepared as depicted in Figure 1.6. The placement of the photoactive *o*-NB ester between the polymer backbone and the ammonium cation is key to the block copolymer design as applied to nucleic acid delivery. This location leads to charge reversal and facilitates the binding and release mechanism desired for efficiently delivering nucleic acids. Thus, the design combines the highlighted criteria, including: biocompatible PEG components, polymers with tailorable composition and molecular weights, cationic moieties that support tight polyplex formation, and photo-responsive groups for controlled spatiotemporal release of the nucleic acid. The unique combination of characteristics dramatically enhances the potential of these photo-responsive block copolymers for nucleic acid delivery.

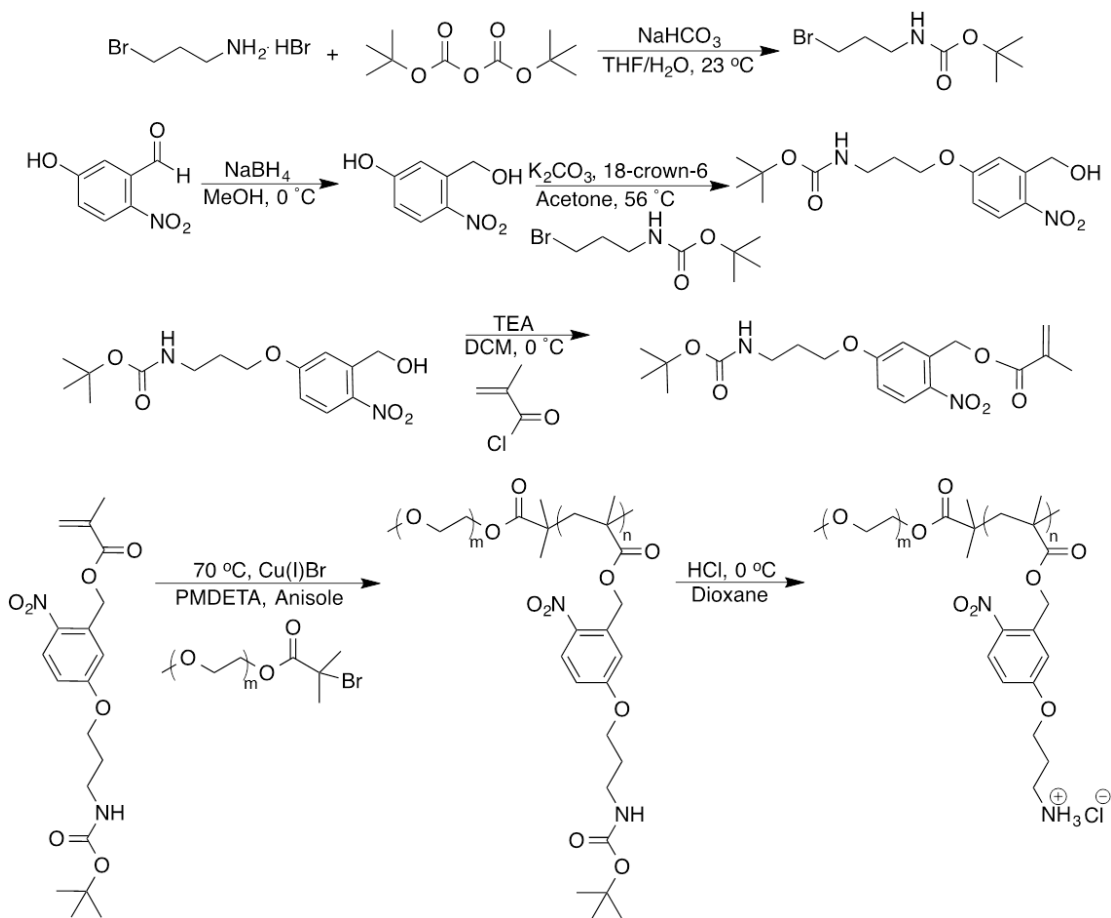


Figure 1.6: Overview of the synthetic scheme of mPEG-*b*-P(APNBMA)_n.

Developing structure-property relationships is critical to the design and optimization of polymeric nanocarriers, necessitating the synthesis of polymers with well-defined characteristics. Thus, ATRP of Boc-APNBMA from a mPEG-Br macroinitiator ($5,300 \text{ g mol}^{-1}$, $D = 1.05$) was used to generate well-defined mPEG-*b*-P(Boc-APNBMA) block copolymers. Boc-APNBMA content and overall copolymer molecular weight were tuned by manipulating the monomer to macroinitiator ratio. The size exclusion chromatography (SEC) traces in Figure 1.7 demonstrate the shift in elution volume upon a change in the monomer to macroinitiator ratio. Narrow

molecular weight distributions ($\mathcal{D} \leq 1.16$) for mPEG-*b*-P(Boc-APNBMA)_n supported the controlled nature of the polymerization during Boc-APNBMA chain extension.

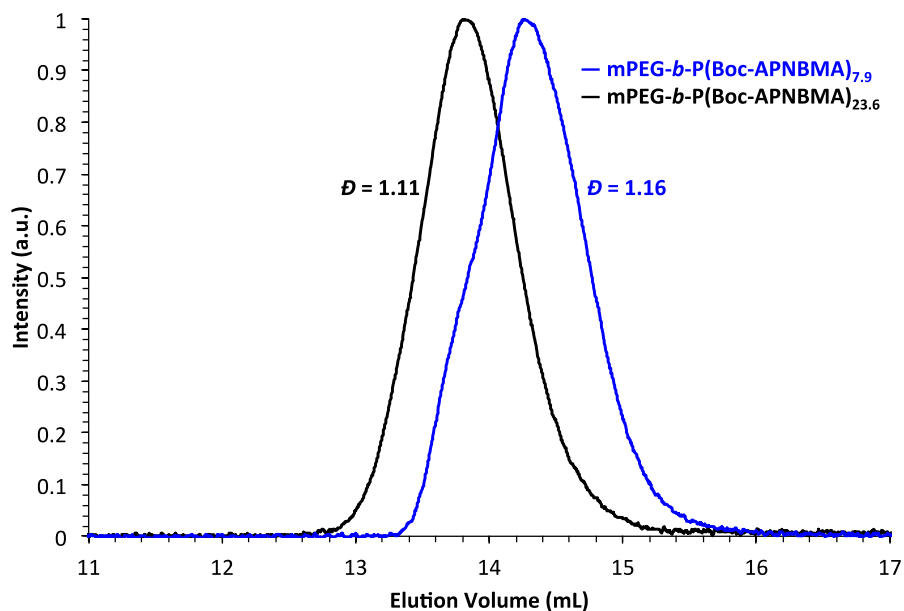


Figure 1.7: Size exclusion chromatograms of mPEG-*b*-P(Boc-APNBMA)_n.

Analysis of ¹H NMR spectroscopy data confirmed the chemical structures of the monomer, protected diblock copolymer, and cationic diblock copolymer (Figure 1.8). After ATRP, the appearance of mPEG-associated resonances at ~3.6 ppm, the elimination of resonances from the methacrylate C=C bond between 5.7-6.3 ppm, and the broadened resonances that correlated to the repeat unit functional groups supported the successful synthesis of mPEG-*b*-P(Boc-APNBMA)_n. The disappearance of the resonances at 1.4 ppm following acid treatment indicated complete conversion of mPEG-*b*-P(Boc-APNBMA)_n to mPEG-*b*-P(APNBMA)_n. Comparing the integrations of the terminal methoxy (3.4 ppm), PEG methylene (3.6 ppm), and Boc methylene

(1.4 ppm) resonances enabled the calculation of the number-average molecular weights (M_n)s for mPEG-*b*-P(Boc-APNBMA) $_n$, which were 8,400 g mol $^{-1}$ and 14,600 g mol $^{-1}$ for the two polymers (shortest and longest) depicted in Figure 1.7. Using a range of monomer to initiator ratios yielded a series of BCPs, and the three polymers (shortest, intermediate, longest) discussed herein illustrate the ability to tune and control molecular weight and dispersity. Table 1.1 summarizes the molecular weights obtained from ^1H NMR spectroscopy and the dispersities obtained from SEC for the three protected polymers and their deprotected counterparts.

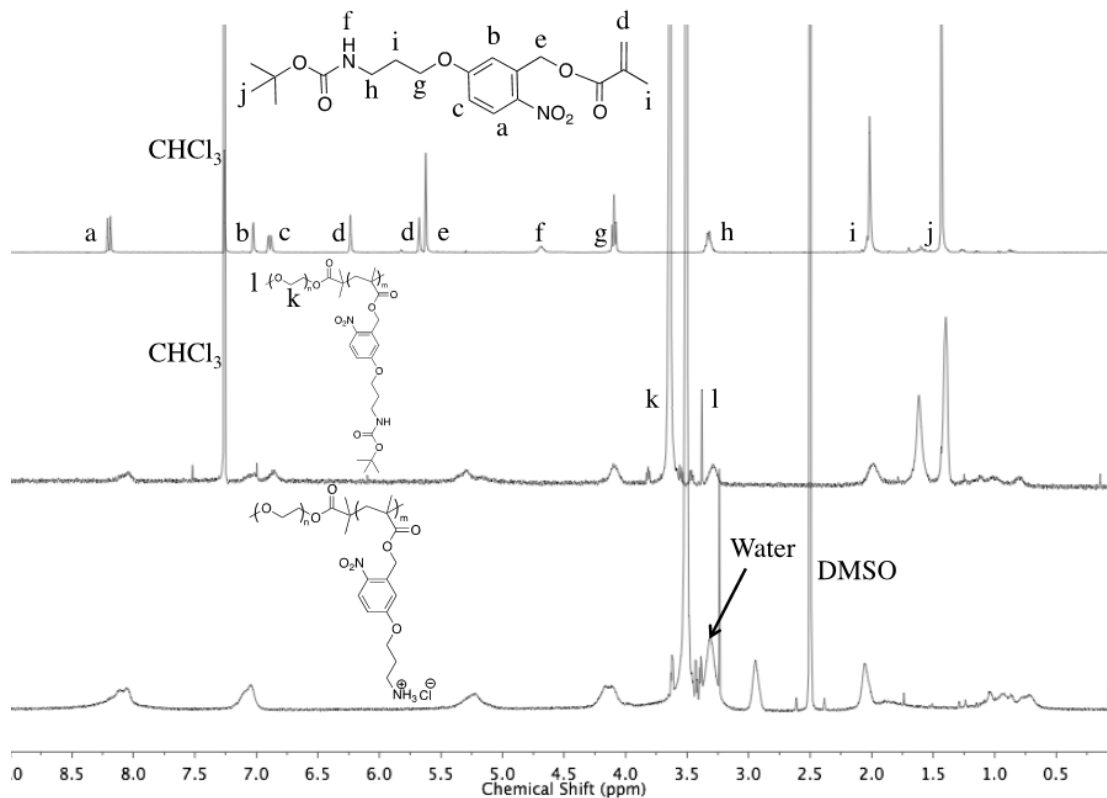


Figure 1.8: ^1H NMR spectroscopy of Boc-APNBMA monomer (top) in CDCl_3 , mPEG-*b*-P(Boc-APNBMA) $_n$ (middle) in CDCl_3 , and mPEG-*b*-P(APNBMA) $_n$ (bottom) in $\text{DMSO-}d_6$.

Table 1.1: Characterization of mPEG-*b*-P(Boc-APNBMA)_n using ¹H NMR spectroscopy and SEC.

Polymer	M_n^a (g mol ⁻¹)	\bar{D}^b
mPEG-Br	5,300	1.05
mPEG- <i>b</i> -P(Boc-APNBMA) _{7.9}	8,400	1.16
mPEG- <i>b</i> -P(APNBMA) _{7.9}	7,900	-
mPEG- <i>b</i> -P(Boc-APNBMA) _{16.6}	11,800	1.11
mPEG- <i>b</i> -P(APNBMA) _{16.6}	10,800	-
mPEG- <i>b</i> -P(Boc-APNBMA) _{23.6}	14,600	1.11
mPEG- <i>b</i> -P(APNBMA) _{23.6}	13,100	-

^a Determined using ¹H NMR spectroscopy, and subsequently used to calculate the degree of polymerization for each polymer (n = 7.9 [shortest], 16.6 [intermediate], and 23.6 [longest]). ^b Determined using SEC.

1.6.2 Properties of siRNA/mPEG-*b*-P(APNBMA) polyplexes

The text and figures in section 1.6.2 are adapted and reprinted with permission from Foster, A. A.; Greco, C. T.; Green, M. D.; Epps, T. H., III; Sullivan, M. O., Light-mediated activation of siRNA release in diblock copolymer assemblies for controlled gene silencing. *Adv. Healthc. Mater.* 2015, 4 (5), 760-770.¹⁵⁶ Copyright 2015 WILEY-VCH Verlag GmbH & Co. KGaA, Weinheim.

Following the synthesis of the mPEG-*b*-P(APNBMA)_{7.9} and mPEG-*b*-P(APNBMA)_{23.6} polymers, the abilities of these two polymers (shortest and longest) to bind siRNA and form effective polyplexes was explored. In particular, this section details: siRNA binding, polyplex stability, light-induced siRNA release, cellular uptake, cell viability, and gene silencing.

1.6.2.1 siRNA binding and polyplex formation

Efficient siRNA binding typically requires higher N/P (N: cationic amine groups on polymers, P: anionic phosphate groups on nucleic acids) ratios and/or higher molecular weight polycations as compared with DNA condensation.²⁹ Hence, the siRNA binding capacity of mPEG-*b*-P(APNBMA)_n block copolymers was tested as a function of P(APNBMA)_n block length. mPEG-*b*-P(APNBMA)_n ($M_n = 7,900 \text{ g mol}^{-1}$, $n = 7.9$ or $M_n = 13,100 \text{ g mol}^{-1}$, $n = 23.6$) was added to siRNA at various charge ratios (Figure 1.9) and the resulting solutions were analyzed *via* gel electrophoresis. Both mPEG-*b*-P(APNBMA)_{7.9} and mPEG-*b*-P(APNBMA)_{23.6} provided sufficiently strong interactions to complex siRNA at low N/P ratios (Figure 1.9C and 1.9D); however, the longer polymer encapsulated siRNA more efficiently. Upon addition of mPEG-*b*-P(APNBMA)_{23.6} at an N/P ratio of 0.5, there was an initial ~83% reduction in ethidium bromide fluorescence. Further addition of the polymer ($N/P \geq 1$) fully inhibited migration and low levels of fluorescence became visible in the wells. The fluorescence in the wells decreased with continued polymer addition, and disappeared completely above an N/P ratio of 4, suggesting that mPEG-*b*-P(APNBMA)_{23.6} effectively complexed siRNA. Given the high siRNA binding affinity of mPEG-*b*-P(APNBMA)_{23.6}, it is possible that the cationic and hydrophobic components in the APNBMA block may cooperatively condense and stabilize the siRNA/mPEG-*b*-P(APNBMA)_{23.6} structures.

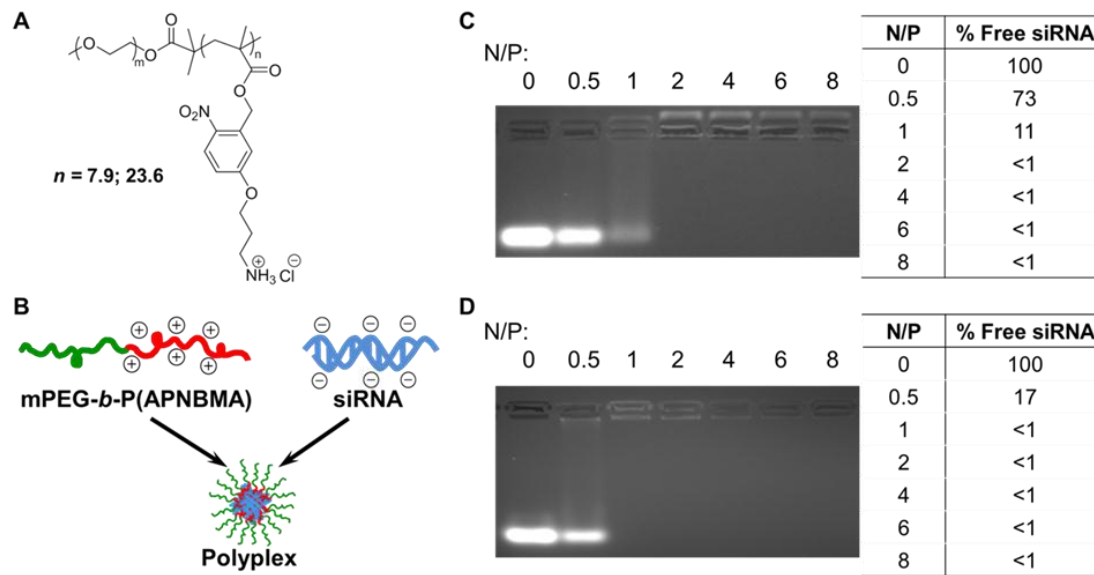


Figure 1.9: Characterization of siRNA/mPEG-*b*-P(APNBMA)_{*n*} polyplexes. Representative siRNA mobility assay in 4 wt% agarose gels stained with ethidium bromide. Polyplexes were prepared with (A) mPEG-*b*-P(APNBMA)_{7.9} and (B) mPEG-*b*-P(APNBMA)_{23.6}. Lane 1 of both gels is siRNA alone (N/P = 0) while the remaining lanes show siRNA complexed with polymer at varied N/P ratios. Tabulated values indicate percentages of free siRNA based on ImageJ analysis of the free siRNA band.

1.6.2.2 Physical characterization and stability of polyplexes

Based on the increased binding efficiency of the 23.6 repeat unit copolymer, this polymer was used for subsequent investigations. The hydrodynamic diameters (D_H) of siRNA/mPEG-*b*-P(APNBMA)_{23.6} polyplexes were measured using dynamic light scattering (DLS) (Figure 1.10A) to determine whether these structures would be suitable for cellular uptake, as well as to determine whether D_H decreased as polymer binding affinity (and N/P ratio) increased. Polyplexes were formed at varied charge ratios ranging from N/P ratios of 2 to 8 based on the electrophoretic complexation data. The values of polyplex D_H for all polyplex formulations were below 150 nm,

significantly lower than the size limit that has been suggested for endocytic uptake (< 200 nm).¹⁵⁷ Furthermore, the sizes of the siRNA/mPEG-*b*-P(APNBMA)_{23.6} polyplexes were relatively constant as a function of N/P. These findings indicated a high binding affinity between siRNA and the longer polycation, consistent with electrophoresis data. Furthermore, the efficient siRNA complexation combined with the small D_H at $N/P \geq 4$ revealed an enhanced siRNA binding capacity compared to other PEG-polycation block copolymers used for siRNA delivery.^{158, 159} All siRNA/mPEG-*b*-P(APNBMA) polyplexes were formulated at an N/P ratio of 4 for all subsequent studies because this was the lowest amount of polymer that was needed to completely exclude ethidium bromide in Figure 1.9D and these polyplexes were appropriately sized (Figure 1.10).

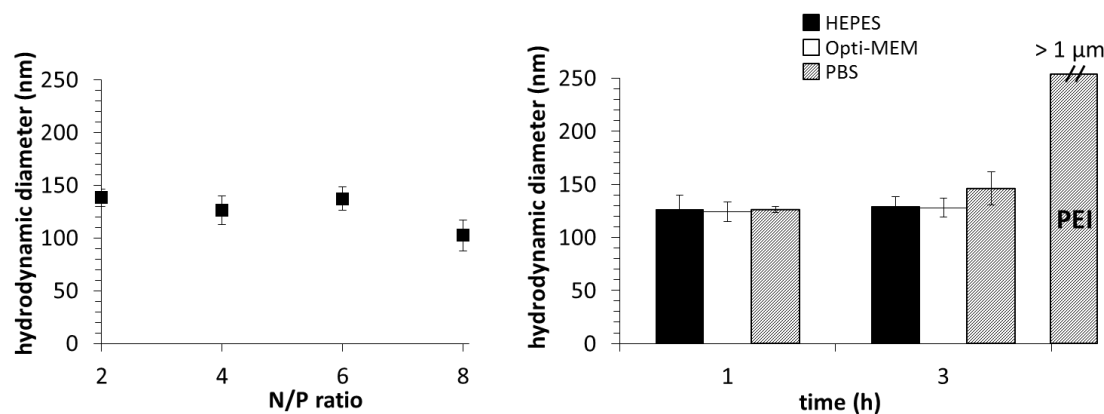


Figure 1.10: Polyplex characterization using DLS. (A) D_H of polyplexes determined at various N/P ratios. (B) Representative D_H of polyplexes prepared at N/P ratio of 4 following a 1 h or a 3 h incubation in 20 mM HEPES (pH = 6; black), Opti-MEM (gray), or PBS containing 150 mM NaCl (diagonal lines). siRNA/PEI polyplexes also were incubated in PBS for 1 h for comparison.

Stealth coatings such as PEG are well known to promote colloidal stability and resist non-specific protein adsorption and opsonization in a number of gene delivery structures.¹⁶⁰⁻¹⁶³ Thus, the nonfouling characteristics of the incorporated PEG block were tested in the presence of physiological salt solutions and serum. Polyplexes were incubated in PBS (150 mM NaCl) or Opti-MEM (transfection medium containing protein supplements). Subsequently, the average D_H values of the polyplexes were measured by DLS to determine whether the polyplexes exhibited salt- or serum-induced changes in size as compared with polyplexes that were incubated in formulation buffer (20 mM HEPES, pH = 6) (Figure 1.10B). The polyplex sizes remained constant at ~120 nm following 1 h and 3 h incubations in Opti-MEM at 23 °C. Incubation in PBS over a 3 h period resulted in a slight increase in polyplex size from ~130 nm at 1 h to ~145 nm following a 3 h incubation. All polyplexes retained small sizes that were below the ~200 nm threshold for endocytic uptake.¹⁶⁴ Moreover, the stability of the siRNA/mPEG-*b*-P(APNBMA) polyplexes in PBS was much greater than that of siRNA/PEI polyplexes, which aggregated to sizes greater than 1 μm following a 1 h incubation in PBS. Based on the relative stability of the polyplex structures and the minimal increase in D_H , these studies suggested that the PEG block formed a protective corona following polyplex formation to resist both salt-induced aggregation and protein adsorption.

Polyanionic glycosaminoglycans such as heparin are major components of the extracellular matrix and have been shown to displace nucleic acids from their cationic carriers in numerous studies.^{165, 166} Thus, to evaluate the stability of mPEG-*b*-P(APNBMA)_{23.6} polyplexes against competing polyanions, the susceptibility of these polyplexes to heparin displacement as compared with siRNA/PEI polyplexes was

tested. siRNA/PEI polyplexes were prepared at N/P ratio of 6 to ensure effective binding of siRNA, and the mPEG-*b*-P(APNBMA)_{23.6} and PEI polyplexes were incubated with increasing heparin concentrations. Polyplex dissociation and siRNA release were monitored by electrophoresis (Figure 1.11). Gel mobility assays indicated greatly enhanced heparin stability for mPEG-*b*-P(APNBMA)_{23.6} structures, which continued to associate with siRNA and exclude ethidium bromide fluorescence in the wells of the gel for heparin/siRNA (w/w) ratios ≤ 1.5 (Figure 1.11A). An increase in the heparin/siRNA ratio to 2 resulted in polyplex loosening and demonstrated low levels of fluorescence in the well of the gel. Further increases of the heparin/siRNA ratio to 5 resulted in ~10% siRNA dissociation from the mPEG-*b*-P(APNBMA)_{23.6} structures (Figure 1.11C). In contrast, PEI preparations indicated siRNA displacement for heparin/siRNA (w/w) ratio ≥ 1.5 (Figure 1.11B) and ~50% siRNA dissociated for heparin/siRNA (w/w) ratio of 5. It is possible that hydrophobic groups in the cationic block may provide additional binding interactions to stabilize the siRNA polyplexes and provide increased stability against polyanion-mediated dissociation.

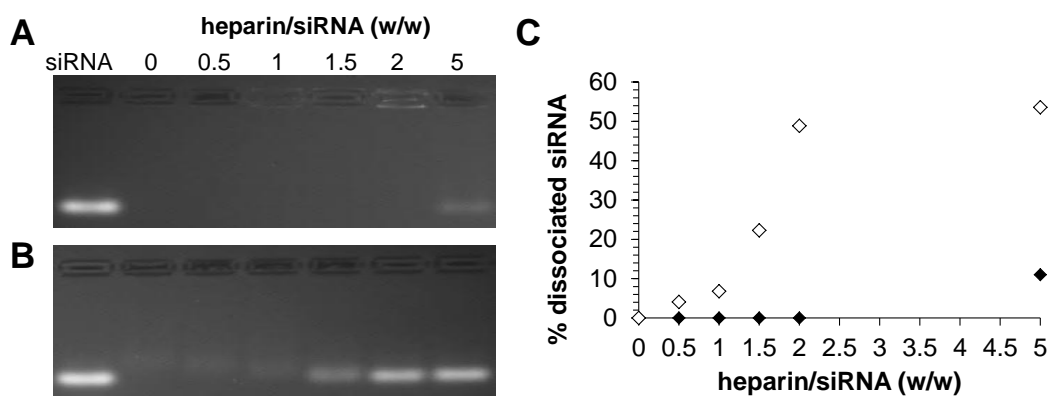


Figure 1.11: Heparin displacement of (A) siRNA/mPEG-*b*-P(APNBMA)_{23.6} polyplexes (N/P ratio of 4), and (B) siRNA/PEI polyplexes (N/P ratio of 6) incubated in the presence of increasing amounts of heparin. (C) Quantification of free siRNA in siRNA/mPEG-*b*-P(APNBMA)_{23.6} polyplexes (black) and siRNA/PEI polyplexes (white) based on gel image analysis using ImageJ.

The interactions between serum proteins and polyplexes also can lead to polyplex disassembly and subsequent degradation of siRNA by serum nucleases.¹⁶⁷ Hence, electrophoresis and serum/nuclease stability assays were performed to assess the structure of the serum-exposed mPEG-*b*-P(APNBMA)_{23.6} polyplexes (Figure 1.12A). Gel mobility shift assays on free siRNA treated with whole mouse serum produced a modest broadening of the siRNA band due to degradation (Figure 1.12A, Lane 2) compared to untreated siRNA (Lane 1). In contrast, no free siRNA band was visible for all serum-treated polyplex samples (Lanes 3-7). The increased background fluorescence in serum treated samples was attributed to interactions between ethidium bromide and serum components, as similar fluorescence occurred in the serum control (Lane 8). These data indicated that the siRNA was not displaced from the polyplex following incubation in serum.

siRNA/mPEG-*b*-P(APNBMA)_{23.6} polyplexes were exposed to RNase A to investigate the susceptibility of encapsulated siRNA to nuclease-mediated degradation (Figure 1.12B). The treatment of free siRNA with RNase A resulted in increased electrophoretic mobility of the siRNA, broadening of the siRNA band, and ~65% reduction in ethidium bromide fluorescence intensity (Lane 2). In contrast, siRNA released from RNase A-treated mPEG-*b*-P(APNBMA)_{23.6} polyplexes (Lane 5) indicated an ~14% reduction in ethidium bromide fluorescence intensity compared to siRNA released from polyplexes without nuclease treatment (Lane 4). These combined serum and nuclease stability results indicated that the binding affinity of the mPEG-*b*-P(APNBMA)_{23.6} for siRNA was sufficiently strong to prevent serum-mediated polyplex disassembly and provide enhanced resistance to nuclease degradation.

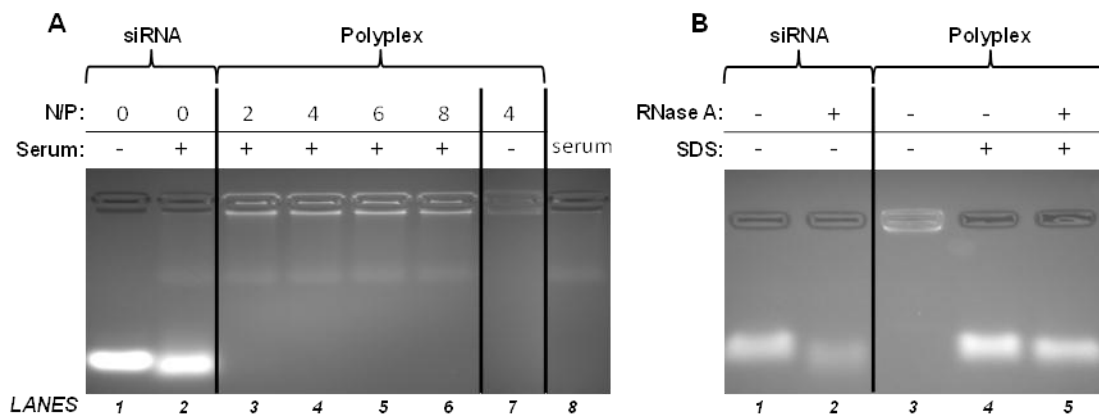


Figure 1.12: Gel mobility shift and nuclease stability analyses of siRNA polyplexes. (A) Stability of free siRNA and siRNA/mPEG-*b*-P(APNBMA)_{23.6} polyplexes against serum-mediated disassembly. Free siRNA and siRNA/mPEG-*b*-P(APNBMA)_{23.6} polyplexes prepared at N/P ratios of 2, 4, 6, and 8 were analyzed in the presence (+) or absence (-) of serum. (B) Stability of free siRNA and siRNA polyplexes (N/P ratio of 4) against RNase A-mediated degradation. Free siRNA and siRNA/mPEG-*b*-P(APNBMA)_{23.6} polyplexes were treated with RNase A (+) or RNase A-free (-) buffers, the nuclease reactions were terminated, and the polyplexes were either disassembled in SDS (+) or left intact (-).

1.6.2.3 UV-induced unpackaging

Given the efficient packaging and enhanced salt and serum stability of siRNA/mPEG-*b*-P(APNBMA)_{23.6} polyplexes, UV irradiation studies were performed to assess the efficacy of light-triggered siRNA release. Free mPEG-*b*-P(APNBMA)_{23.6} block copolymer as well as siRNA/mPEG-*b*-P(APNBMA)_{23.6} polyplexes were irradiated with 365 nm light, and UV/Vis spectroscopy was used to monitor changes in the characteristic absorbance of the *o*-NB ester at 316 nm to determine the extent of photocleavage (Figure 1.13).

The free polymer absorbance spectra displayed dramatic decreases in absorbance at 316 nm for UV exposure times up to 10 min, and smaller changes at

longer UV exposure times (Figure 1.13A). Irradiation of siRNA/mPEG-*b*-P(APNBMA)_{23.6} polyplexes yielded similar results under the same conditions, with a large decrease in absorbance after 10 min of irradiation (Figure 1.13B). This behavior was consistent with the typical cleavage behavior of *o*-NB-containing polymers, which disassemble in response to irradiation with UV light to form a carboxylic acid and nitrosobenzaldehyde.⁹⁵ The decrease in absorbance as a function of irradiation time followed an exponential decay for both the polymer and siRNA polyplex preparations. In particular, both the free polymer and polyplex spectra suggested complete cleavage of the *o*-NB group, based on the change in absorbance at 316 nm.

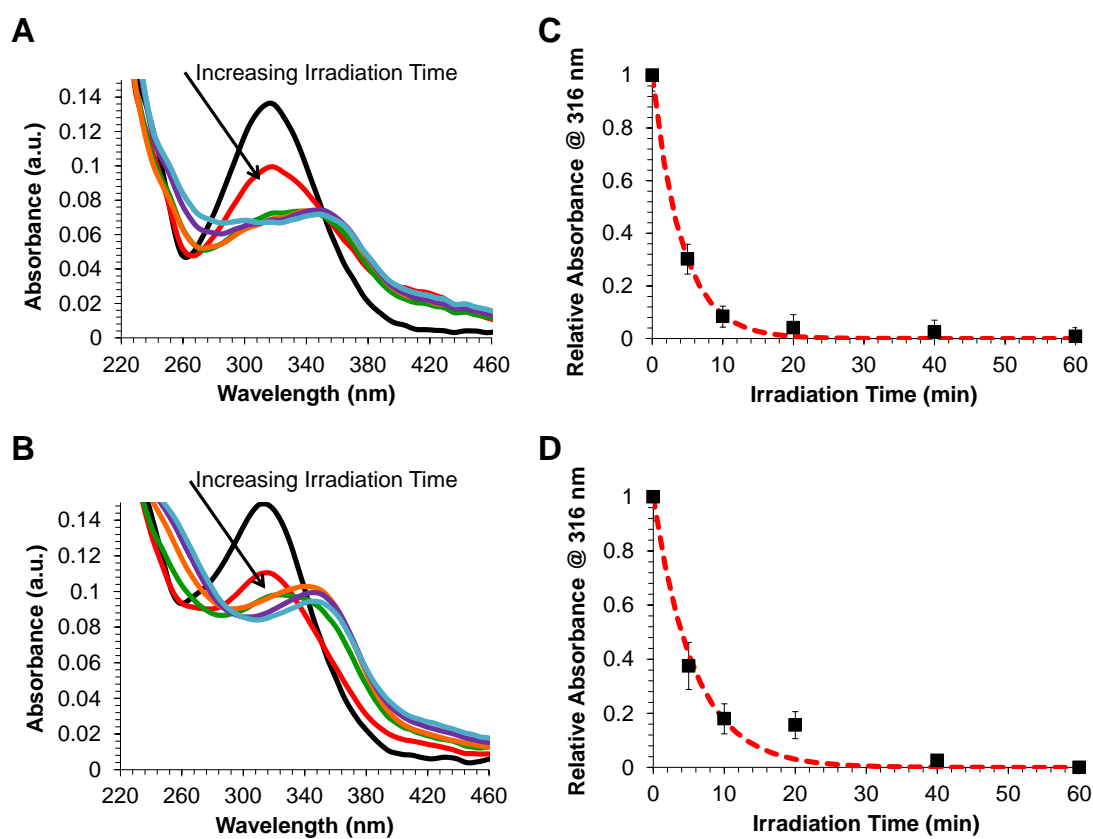


Figure 1.13: UV absorbance spectral changes of (A) mPEG-*b*-P(APNBMA)_{23.6} and (B) siRNA/mPEG-*b*-P(APNBMA)_{23.6} polyplexes following exposure to UV irradiation (365 nm, 200 W/m²) for 0 (black), 5 (red), 10 (orange), 20 (green), 40 (blue), or 60 (purple) min. Normalized absorbance (filled squares) at 316 nm for (C) mPEG-*b*-P(APNBMA)_{23.6} and (D) siRNA/mPEG-*b*-P(APNBMA)_{23.6} polyplexes as a function of UV irradiation time. The log of the normalized intensity, for which the red dashed line indicates an exponential decay fit to the normalized intensity. Error bars represent the standard deviation determined from the mean of three independent absorbance measurements.

The irradiated polyplexes were collected and analyzed *via* electrophoresis to determine the extent of light-induced siRNA release (Figure 1.14A). When the polyplexes were irradiated for short periods of time (≤ 10 min irradiation), siRNA migration was limited, but after ≥ 20 min of exposure, significant amounts of free

siRNA migrated down the gel. After 60 min of irradiation, additional siRNA migrated on the gel, yet release remained incomplete. Specifically, quantification of the free siRNA band intensities revealed that ~15% of the siRNA was released after a 20 min irradiation, and the levels of released siRNA increased up to ~24% as irradiation times increased (Figure 1.14B).

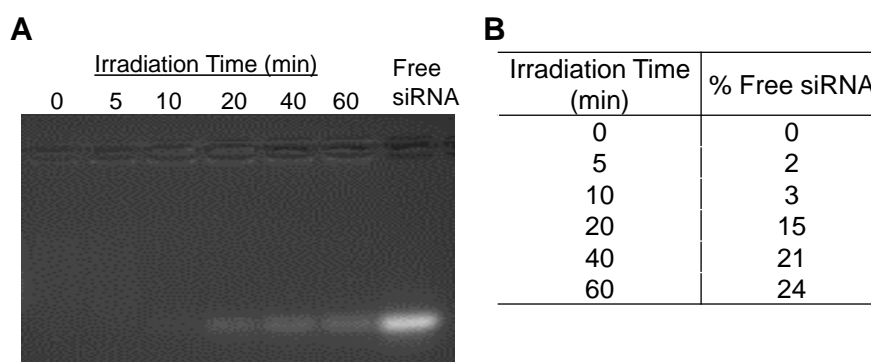


Figure 1.14: (A) Electrophoretic gel migration patterns of siRNA/mPEG-*b*-P(APNBMA)_{23.6} polyplexes after exposure to UV irradiation (365 nm, 200 W/m²) for varying periods of time. Free siRNA is shown for comparison. (B) Quantification of ethidium bromide fluorescence in the siRNA band using ImageJ analysis software.

These studies highlight a novel release property that has not been previously demonstrated in other light-sensitive nucleic acid binding polymers.¹⁶⁸ Specifically, this system provides robust polyplex stability against polyanion- or serum-mediated disassembly, along with light-mediated release of a significant fraction of siRNA following light exposure. Light-induced structural changes remove the hydrophobic and cationic moieties responsible for siRNA binding and elicit a charge reversal along the mPEG-*b*-P(APNBMA)_{23.6} polymer backbone, which may account for the

enhanced dissociation of these siRNA. Meanwhile, it is possible that the apparent lack of complete release following irradiation was an artifact in quantification caused by the continued association of cleaved polymer fragments with the siRNA. The continued association of these fragments could reduce ethidium bromide binding, especially given that these fragments contained phenyl rings that might prohibit the intercalation of the ethidium bromide molecules.

1.6.2.4 Cellular uptake

Given that mPEG-b-P(APNBMA)_{23,6} formed compact, salt- and serum-stable polyplexes that released siRNA upon light exposure, the polymer's ability to mediate cellular uptake in NIH/3T3 cells was investigated. Polyplexes were formulated with siRNA that was labeled with YOYO-1 iodide, visualized using fluorescence microscopy, and quantified *via* flow cytometry. Fluorescence microscopy showed rapid uptake of the labeled polyplexes, as indicated by the appearance of large quantities of intracellular YOYO-1-labeled structures after 1 h (Figure 1.15A). The punctate appearance in many of these structures suggested that the polyplexes were entrapped within endomembrane vesicular compartments within the cells, consistent with previous studies investigating the trafficking of siRNA polyplexes³⁵ and other nanostructures. After 3 h, there was a clear increase in intracellular YOYO-1, as well as a loss of the punctate structures and a shift to a uniformly diffuse intracellular distribution (Figure 1.15B). The diffuse staining pattern may be due to YOYO-1 dye leakage or cytoplasmic localization of the polyplexes as a result of endosomal escape.¹⁶⁹

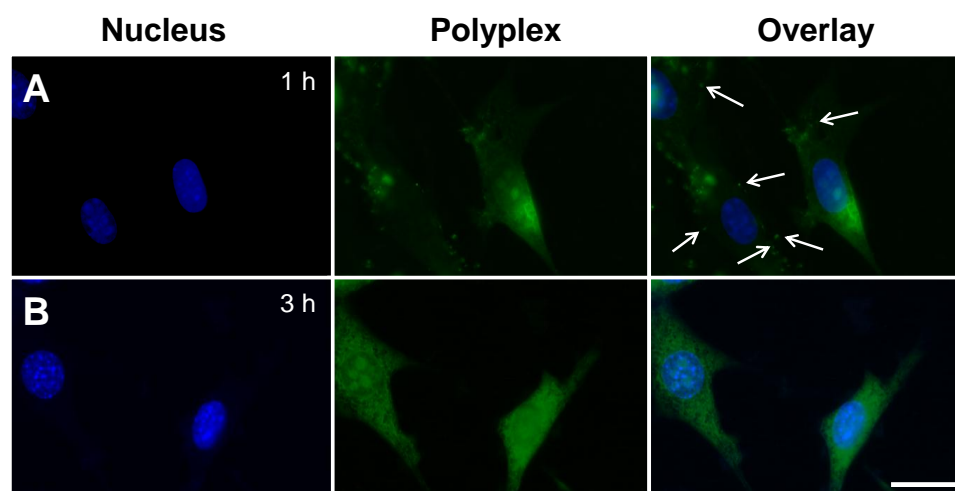


Figure 1.15: Representative fluorescence microscopy images showing the internalization of siRNA polyplexes in NIH/3T3 cells. siRNA was labeled with YOYO-1 iodide (green); the nucleus was stained with Hoechst (blue). Cells transfected with siRNA/mPEG-*b*-P(APNBMA)_{23.6} polyplexes for (A) 1 h, and (B) 3 h. Arrows indicate punctate polyplex structures, and the scale bar represents 25 μ m and applies to all images.

Flow cytometry was used to quantify the efficiency of cellular uptake and the amount of intracellular YOYO-1 iodide-labeled siRNA polyplexes (Figure 1.16). Following 1 h of polyplex exposure, the amount of siRNA that had been internalized from mPEG-*b*-P(APNBMA)_{23.6} polyplexes was comparable to the amount that had been internalized from Lipofectamine lipoplexes. Notably, the average intracellular concentration of siRNA increased up to 3 h post-transfection for the mPEG-*b*-P(APNBMA)_{23.6} polyplexes but remained constant for siRNA/Lipofectamine assemblies (Figure 1.16). Several studies have indicated that enhanced cellular uptake of gene delivery polyplexes could be due to excess polycations that remain free in solution after polyplex formation.^{69, 170, 171} Also, it is possible that the enhanced cytoplasmic distribution of siRNA/mPEG-*b*-P(APNBMA)_{23.6} polyplexes is due to

several features of free mPEG-*b*-P(APNBMA)_{23.6}, including the primary amines and hydrophobic phenyl rings in the cationic block, which may cooperatively interact with the endosomal membrane to facilitate cytoplasmic release.¹⁷²

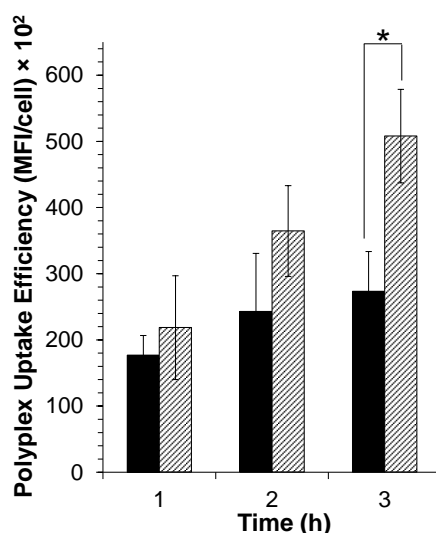


Figure 1.16: Cellular uptake of fluorescently-labeled siRNA complexes quantified using flow cytometry. Lipofectamine RNAiMax assemblies (black); mPEG-*b*-P(APNBMA)_{23.6} polyplexes (light gray). The mean fluorescence intensity (MFI, arbitrary units) of the cells that had internalized lipoplexes or polyplexes was quantified. Each data point represents the mean \pm standard deviation for a total of three separately prepared samples. An asterisk indicates a statistically significant difference at a given time point between the mPEG-*b*-P(APNBMA)_{23.6} polyplexes and the Lipofectamine lipoplexes ($p < 0.001$).

1.6.2.5 NIH/3T3 cell viability

Numerous studies have indicated significant cellular toxicity when using cationic polymers due to non-specific interactions with the cell surface and subsequent membrane disruption.^{173, 174} Thus, the cytotoxicity in cell populations transfected by siRNA polyplexes was tested using the AlamarBlue (AB) cell survival assay. AB-

based quantification revealed greater than 90% cell survival in all samples, and no additive/synergistic effects were found in cells that were treated with UV light in combination with siRNA/mPEG-*b*-P(APNBMA)_{23,6} polyplexes vs. UV light alone (Figure 1.17).

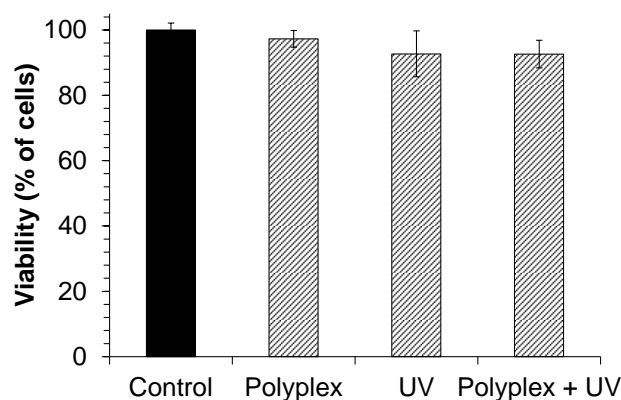


Figure 1.17: Cell viabilities 48 h after polyplex treatment, UV exposure, or the combination of polyplexes and UV exposure as measured by the AB assay. Percent viabilities are relative to untreated cells. Each data point represents the mean \pm standard deviation for a total of at least three separately prepared and analyzed samples. The untreated control sample is shown in black.

1.6.2.6 Gene silencing capacity of photo-responsive polyplexes

Based on the finding of triggered siRNA release in the characterization of polyplexes in cell-free studies, the on/off binding and silencing capacity of siRNA/mPEG-*b*-P(APNBMA)_{23,6} polyplexes was investigated in NIH/3T3 cells using glyceraldehyde 3-phosphate dehydrogenase (GAPDH) as a model gene target (Figure 1.18). Cells were transfected for 3 h and then irradiated for 20 min, as the fluorescence microscopy analyses had indicated the robust cytoplasmic distribution of

the polyplexes within the 3 h time frame (Figure 1.15). Cells transfected with GAPDH-targeting siRNA/mPEG-*b*-P(APNBMA)_{23.6} polyplexes exhibited a significantly higher level of GAPDH silencing following UV irradiation than cells treated with Lipofectamine assemblies, and moreover, these irradiated cells also exhibited enhanced silencing as compared to siRNA/mPEG-*b*-P(APNBMA)_{23.6} treated cells in the absence of UV irradiation. Specifically, quantification of the integrated optical density of GAPDH bands obtained through Western blot analysis indicated a ~70% reduction in GAPDH levels for cells transfected with siRNA/mPEG-*b*-P(APNBMA)_{23.6} polyplexes and UV light, but no reduction in GAPDH levels in cells transfected with the siRNA/mPEG-*b*-P(APNBMA)_{23.6} polyplexes in the absence of UV light, and only a ~30% reduction in GAPDH levels in cells transfected with Lipofectamine. The silencing behavior was specific to GAPDH, as delivery of non-targeting siRNA only minimally affected GAPDH levels.

These results highlight the unique capability of siRNA/mPEG-*b*-P(APNBMA)_{23.6} polyplexes to maintain stable association within cells in the absence of light. Additionally, ~70% reduction in GAPDH levels indicated an enhanced gene silencing capacity compared to other stimuli-responsive siRNA carriers, which reported ~50% protein silencing in response to changes in pH.¹⁷⁵ Based on the combined siRNA release and gene silencing studies, it is worth noting that complete siRNA release from the irradiated polyplexes does not appear to be necessary for gene silencing, as only 15% free siRNA (based on siRNA release in gel electrophoresis following 20 min of UV-irradiation) was required to obtain this silencing effect. These studies highlight the potential of mPEG-*b*-P(APNBMA)_n polymers to direct

siRNA delivery and further reveal an enhanced silencing capacity of mPEG-*b*-P(APNBMA)_{23.6} compared to a number of light-responsive siRNA nanocarriers.^{72, 83}

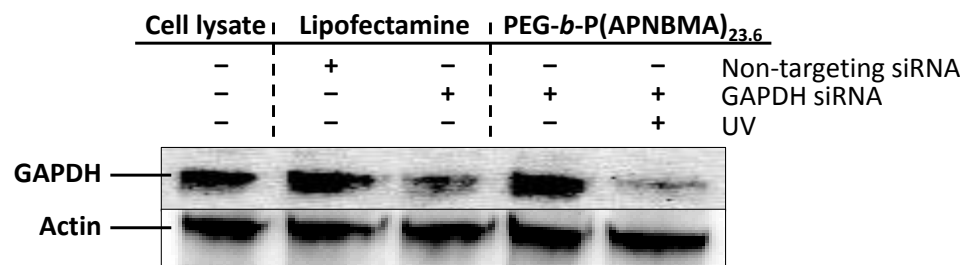


Figure 1.18: Western blot analysis of NIH/3T3 cell extracts collected 48 h post-transfection. Cells were treated with GAPDH targeted siRNA/mPEG-*b*-P(APNBMA)_{23.6} polyplexes with (+) or without (-) UV exposure (20 min), or with Lipofectamine lipoplexes containing either non-targeting or GAPDH targeting siRNAs.

1.6.3 Summary of the synthesis and preliminary characterization of the photo-responsive BCP

Our group synthesized a novel photo-responsive, methacrylate-based monomer and used ATRP to generate a pair of BCPs with tunable block lengths and narrow molecular weight distributions. The longer polymer was used for localized cytoplasmic delivery and light-activated release of siRNA. mPEG-*b*-P(APNBMA) provided strong siRNA binding to form salt-stable copolymer-based polyplexes that resisted aggregation following incubation in PBS, as compared to siRNA/PEI polyplexes that aggregated to sizes >1 μ m in diameter. The siRNA/mPEG-*b*-P(APNBMA) polyplexes also were stable in serum solutions and protected the siRNA from degradation. Moreover, delivery of siRNA/mPEG-*b*-P(APNBMA) polyplexes to NIH/3T3 cells facilitated nearly twice the amount of cellular uptake as Lipofectamine lipoplexes. UV irradiation of siRNA/mPEG-*b*-P(APNBMA) polyplexes cleaved the

o-NB and facilitated charge reversal on the polymer backbone and siRNA release. Furthermore, gene silencing experiments revealed the exquisite specificity and utility of this delivery approach. Specifically, by stimulating the photo-responsive polyplexes with UV light, a ~70% reduction in protein levels was achieved, as compared to no changes in protein levels for samples treated with siRNA/mPEG-*b*-P(APNBMA) polyplexes without irradiation, and only 30% reduction in Lipofectamine-treated cells. These results suggest that the capacity for efficient cytoplasmic release and distribution, as well as the user-controlled release mechanism allowing for on/ off control of siRNA binding and activity, will introduce significant versatility into the delivery platform relevant to a range of biological applications in developmental biology, regenerative medicine, and drug screening.

1.7 Dissertation Overview

The work described in this dissertation was aimed at understanding how to better control siRNA binding *vs.* release using a novel photo-responsive polymeric delivery system. The numerous challenges detailed in the above sections were addressed to enable on/off spatiotemporal control over siRNA release and allow for efficient gene silencing. These advances were made possible by the implementation of a variety of strategies for improving control over siRNA activity (such as the formation of mixed polymer nanocarriers and the incorporation of anionic excipients) and by the elucidation of the mechanisms that underlie the gene silencing process (which allowed for the creation of a simple kinetic model to predict the dynamics of protein knockdown). The lessons learned from each of these projects were combined to facilitate the development of a hybrid lipid-polymer formulation that was capable of efficiently transfecting human primary cells for biomedical applications related to

coronary artery bypass grafts. Thus, the primary goals of this dissertation were related to developing an understanding of structure-function relationships of siRNA nanocarriers that could be exploited to formulate delivery vehicles with improved efficiencies, tunable and predictable levels of siRNA release, integrated diagnostic capabilities, and the ability to transfect a variety of cell types for use in biomedical applications. A breakdown of the main themes in each data chapter (Chapters 3-6) is displayed in Figure 1.19.

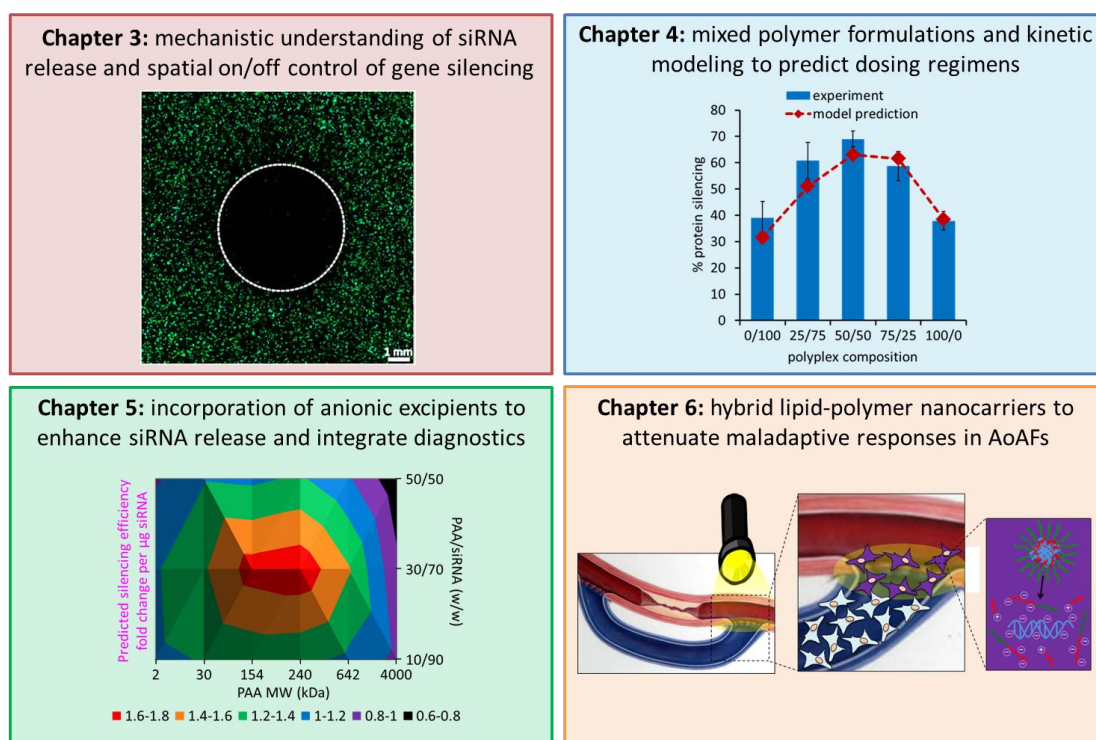


Figure 1.19: Overview of the topics of each data chapter.

Chapter 2 provides an introduction to the theoretical concepts and practical considerations of the most important experimental techniques utilized in this

dissertation. Chapter 3 explores the mechanisms governing siRNA release and the ability to spatiotemporally control gene silencing. These insights allowed for tunable mRNA and protein knockdown that could be predicted on the basis of simple kinetic modeling and siRNA release assays. Chapter 4 describes how mixed polymer nanocarriers were formulated with BCPs of different cationic block lengths to determine how polyplex structure and efficacy depended on the composition. Kinetic modeling also aided in predicting dosing regimens that could knockdown protein levels by a factor of two beyond the maximum levels that could be achieved with a single dose. Chapter 5 details the effects of incorporating anionic excipients, including polymers and QDs, into polyplexes. Ideal loading fractions and polymer molecular weights were identified that yielded excipient-containing polyplexes capable of mediating gene silencing twice as efficiently as unmodified polyplexes and that contained diagnostic properties as well. Chapter 6 describes how all of these advances were combined to enable on/off control over protein knockdown in human primary AoAFs. In particular, hybrid lipid-polymer nanocarriers that contained polymers of different block lengths and anionic excipients were formulated, and the kinetic modeling framework was employed to determine a dosing regimen for sustaining gene silencing over one week. These nanocarriers and predictive capabilities were exploited to attenuate fibrotic responses in AoAFs. Chapter 7 outlines how all of these insights provide an opportunity for translating these technologies into animal models (*in vivo*). Furthermore, suggestions for future work focus on strategies for implementing these formulations in rabbit models, ideas for changing the molecular architecture of the polymer, approaches for understanding and

enhancing endosomal escape, and expanding the use of the polyplexes to other systems/platforms.

REFERENCES

1. Burke, P. A.; Pun, S. H.; Reineke, T. M., Advancing polymeric delivery systems amidst a nucleic acid therapy renaissance. *ACS Macro Lett.* **2013**, 2 (10), 928-934.
2. Cambridge, S. B.; Geissler, D.; Calegari, F.; Anastassiadis, K.; Hasan, M. T.; Stewart, A. F.; Huttner, W. B.; Hagen, V.; Bonhoeffer, T., Doxycycline-dependent photoactivated gene expression in eukaryotic systems. *Nat. Methods* 2009, 6 (7), 527-531.
3. Sridharan, K.; Gogtay, N. J., Therapeutic nucleic acids: current clinical status. *Br. J. Clin. Pharmacol.* 2016, 82 (3), 659-672.
4. Yla-Herttuala, S., Endgame: Glybera finally recommended for approval as the first gene therapy drug in the European Union. *Mol. Ther.* 2012, 20 (10), 1831-1832.
5. Watts, J. K.; Corey, D. R., Silencing disease genes in the laboratory and the clinic. *J. Pathol.* 2012, 226 (2), 365-379.
6. Ginn, S. L.; Alexander, I. E.; Edelstein, M. L.; Abedi, M. R.; Wixon, J., Gene therapy clinical trials worldwide to 2012 an update. *J. Gene Med.* 2013, 15 (2), 65-77.
7. Agrawal, N.; Dasaradhi, P. V. N.; Mohammed, A.; Malhotra, P.; Bhatnagar, R. K.; Mukherjee, S. K., RNA interference: Biology, mechanism, and applications. *Microbiol. Mol. Biol. Rev.* 2003, 67 (4), 657-685.
8. Fire, A.; Xu, S. Q.; Montgomery, M. K.; Kostas, S. A.; Driver, S. E.; Mello, C. C., Potent and specific genetic interference by double-stranded RNA in *Caenorhabditis elegans*. *Nature* 1998, 391 (6669), 806-811.
9. Elbashir, S. M.; Harborth, J.; Lendeckel, W.; Yalcin, A.; Weber, K.; Tuschl, T., Duplexes of 21-nucleotide RNAs mediate RNA interference in cultured mammalian cells. *Nature* 2001, 411 (6836), 494-498.

10. Iwasaki, S.; Sasaki, H. M.; Sakaguchi, Y.; Suzuki, T.; Tadakuma, H.; Tomari, Y., Defining fundamental steps in the assembly of the *Drosophila* RNAi enzyme complex. *Nature* 2015, 521 (7553), 533-536.
11. Engels, J. W., Gene silencing by chemically modified siRNAs. *N. Biotechnol.* 2013, 30 (3), 302-307.
12. Hannon, G. J.; Rossi, J. J., Unlocking the potential of the human genome with RNA interference. *Nature* 2004, 431 (7006), 371-378.
13. Whitehead, K. A.; Langer, R.; Anderson, D. G., Knocking down barriers: advances in siRNA delivery. *Nat. Rev. Drug Discov.* 2009, 8 (2), 129-138.
14. de Fougerolles, A.; Vornlocher, H.-P.; Maraganore, J.; Lieberman, J., Interfering with disease: a progress report on siRNA-based therapeutics. *Nat. Rev. Drug Discov.* 2007, 6 (6), 443-453.
15. Davis, M. E.; Zuckerman, J. E.; Choi, C. H. J.; Seligson, D.; Tolcher, A.; Alabi, C. A.; Yen, Y.; Heidel, J. D.; Ribas, A., Evidence of RNAi in humans from systemically administered siRNA via targeted nanoparticles. *Nature* 2010, 464 (7291), 1067-1070.
16. Wittrup, A.; Lieberman, J., Knocking down disease: a progress report on siRNA therapeutics. *Nat. Rev. Genet.* 2015, 16 (9), 543-552.
17. Bouchie, A., Companies in footrace to deliver RNAi. *Nat. Biotechnol.* 2012, 30 (12), 1154-1157.
18. Miteva, M.; Kirkbride, K. C.; Kilchrist, K. V.; Werfel, T. A.; Li, H.; Nelson, C. E.; Gupta, M. K.; Giorgio, T. D.; Duvall, C. L., Tuning PEGylation of mixed micelles to overcome intracellular and systemic siRNA delivery barriers. *Biomaterials* 2015, 38, 97-107.
19. Zhang, Y.; Satterlee, A.; Huang, L., In vivo gene delivery by nonviral vectors: Overcoming hurdles? *Mol. Ther.* 2012, 20 (7), 1298-1304.
20. Barton, G. M.; Medzhitov, R., Retroviral delivery of small interfering RNA into primary cells. *Proc. Natl. Acad. Sci. U.S.A.* 2002, 99 (23), 14943-14945.
21. Jones, C. H.; Chen, C. K.; Ravikrishnan, A.; Rane, S.; Pfeifer, B. A., Overcoming nonviral gene delivery barriers: Perspective and future. *Mol. Pharm.* 2013, 10 (11), 4082-4098.

22. Vannucci, L.; Lai, M.; Chiuppesi, F.; Ceccherini-Nelli, L.; Pistello, M., Viral vectors: a look back and ahead on gene transfer technology. *New Microbiol.* 2013, 36 (1), 1-22.
23. Gooding, M.; Browne, L. P.; Quinteiro, F. M.; Selwood, D. L., siRNA delivery: From lipids to cell-penetrating peptides and their mimics. *Chem. Biol. Drug. Des.* 2012, 80 (6), 787-809.
24. Williford, J.-M.; Wu, J.; Ren, Y.; Archang, M. M.; Leong, K. W.; Mao, H.-Q., Recent advances in nanoparticle-mediated siRNA delivery. *Annu. Rev. Biomed. Eng.* 2014, 16, 347-370.
25. Kelley, E. G.; Albert, J. N. L.; Sullivan, M. O.; Epps, T. H., III, Stimuli-responsive copolymer solution and surface assemblies for biomedical applications. *Chem. Soc. Rev.* 2013, 42 (17), 7057-7071.
26. Davis, M. E., The first targeted delivery of siRNA in humans via a self-assembling, cyclodextrin polymer-based nanoparticle: from concept to clinic. *Mol. Pharm.* 2009, 6 (3), 659-668.
27. Zuckerman, J. E.; Davis, M. E., Clinical experiences with systemically administered siRNA-based therapeutics in cancer. *Nat. Rev. Drug Discov.* 2015, 14 (12), 843-856.
28. Ruvinov, E.; Kryukov, O.; Forti, E.; Korin, E.; Goldstein, M.; Cohen, S., Calcium-siRNA nanocomplexes: What reversibility is all about. *J. Control. Release* 2015, 203, 150-160.
29. Gary, D. J.; Puri, N.; Won, Y.-Y., Polymer-based siRNA delivery: Perspectives on the fundamental and phenomenological distinctions from polymer-based DNA delivery. *J. Control. Release* 2007, 121 (1-2), 64-73.
30. Chen, H. H.; Ho, Y.-P.; Jiang, X.; Mao, H.-Q.; Wang, T.-H.; Leong, K. W., Quantitative comparison of intracellular unpacking kinetics of polyplexes by a model constructed from quantum dot-FRET. *Mol. Ther.* 2008, 16 (2), 324-332.
31. Zuckerman, J. E.; Choi, C. H. J.; Han, H.; Davis, M. E., Polycation-siRNA nanoparticles can disassemble at the kidney glomerular basement membrane. *Proceedings of the National Academy of Sciences of the United States of America* 2012, 109 (8), 3137-3142.

32. Buyens, K.; Meyer, M.; Wagner, E.; Demeester, J.; De Smedt, S. C.; Sanders, N. N., Monitoring the disassembly of siRNA polyplexes in serum is crucial for predicting their biological efficacy. *J. Control. Release* 2010, 141 (1), 38-41.
33. Abdelhady, H. G.; Allen, S.; Davies, M. C.; Roberts, C. J.; Tendler, S. J. B.; Williams, P. M., Direct real-time molecular scale visualisation of the degradation of condensed DNA complexes exposed to DNase I. *Nucleic Acids Res.* 2003, 31 (14), 4001-4005.
34. Zuckerman, J. E.; Choi, C. H. J.; Han, H.; Davis, M. E., Polycation-siRNA nanoparticles can disassemble at the kidney glomerular basement membrane. *Proc. Natl. Acad. Sci. U.S.A.* 2012, 109 (8), 3137-3142.
35. Shim, M. S.; Kwon, Y. J., Acid-responsive linear polyethylenimine for efficient, specific, and biocompatible siRNA delivery. *Bioconjugate Chem.* 2009, 20 (3), 488-499.
36. Kim, H. J.; Miyata, K.; Nomoto, T.; Zheng, M.; Kim, A.; Liu, X.; Cabral, H.; Christie, R. J.; Nishiyama, N.; Kataoka, K., siRNA delivery from triblock copolymer micelles with spatially-ordered compartments of PEG shell, siRNA-loaded intermediate layer, and hydrophobic core. *Biomaterials* 2014, 35 (15), 4548-4556.
37. Gilleron, J.; Querbes, W.; Zeigerer, A.; Borodovsky, A.; Marsico, G.; Schubert, U.; Manygoats, K.; Seifert, S.; Andree, C.; Stoeter, M.; Epstein-Barash, H.; Zhang, L.; Koteliansky, V.; Fitzgerald, K.; Fava, E.; Bickle, M.; Kalaidzidis, Y.; Akinc, A.; Maier, M.; Zerial, M., Image-based analysis of lipid nanoparticle-mediated siRNA delivery, intracellular trafficking and endosomal escape. *Nat. Biotechnol.* 2013, 31 (7), 638-646.
38. Han, L.; Tang, C.; Yin, C., Effect of binding affinity for siRNA on the in vivo antitumor efficacy of polyplexes. *Biomaterials* 2013, 34 (21), 5317-5327.
39. Malmo, J.; Sorgard, H.; Varum, K. M.; Strand, S. P., siRNA delivery with chitosan nanoparticles: Molecular properties favoring efficient gene silencing. *J. Control. Release* 2012, 158 (2), 261-268.
40. Johnson, R. N.; Chu, D. S. H.; Shi, J.; Schellinger, J. G.; Carlson, P. M.; Pun, S. H., HPMA-oligolysine copolymers for gene delivery: Optimization of peptide length and polymer molecular weight. *J. Control. Release* 2011, 155 (2), 303-311.

41. Mura, S.; Nicolas, J.; Couvreur, P., Stimuli-responsive nanocarriers for drug delivery. *Nat. Mater.* 2013, 12 (11), 991-1003.
42. Du, F.-S.; Wang, Y.; Zhang, R.; Li, Z.-C., Intelligent nucleic acid delivery systems based on stimuli-responsive polymers. *Soft Matter* 2010, 6 (5), 835-848.
43. Wang, M. M.; Cheng, Y. Y., Temperature-responsive gene silencing by a smart polymer. *Bioconjugate Chem.* 2016, 27 (3), 495-499.
44. Shim, M. S.; Kwon, Y. J., Stimuli-responsive polymers and nanomaterials for gene delivery and imaging applications. *Adv. Drug Delivery Rev.* 2012, 64 (11), 1046-1058.
45. Won, Y.-W.; Yoon, S.-M.; Lee, K.-M.; Kim, Y.-H., Poly(oligo-D-arginine) with internal disulfide linkages as a cytoplasm-sensitive carrier for siRNA delivery. *Mol. Ther.* 2011, 19 (2), 372-380.
46. Li, J.; Yu, X.; Wang, Y.; Yuan, Y.; Xiao, H.; Cheng, D.; Shuai, X., A reduction and pH dual-sensitive polymeric vector for long-circulating and tumor-targeted siRNA delivery. *Adv. Mater.* 2014, 26 (48), 8217-8224.
47. Du, Z.; Xiang, S.; Zang, Y.; Zhou, Y.; Wang, C.; Tang, H.; Jin, T.; Zhang, X., Polyspermine imine, a pH responsive polycationic siRNA carrier degradable to endogenous metabolites. *Mol. Pharm.* 2014, 11 (10), 3300-3306.
48. Kozielski, K. L.; Tzeng, S. Y.; De Mendoza, B. A. H.; Green, J. J., Bio-reducible cationic polymer-based nanoparticles for efficient and environmentally triggered cytoplasmic siRNA delivery to primary human brain cancer cells. *ACS Nano* 2014, 8 (4), 3232-3241.
49. Kong, M.; Park, H.; Cheng, X. J.; Chen, X. G., Spatial-temporal event adaptive characteristics of nanocarrier drug delivery in cancer therapy. *J. Control. Release* 2013, 172 (1), 281-291.
50. Lu, Y.; Sun, W. J.; Gu, Z., Stimuli-responsive nanomaterials for therapeutic protein delivery. *J. Control. Release* 2014, 194, 1-19.
51. Liu, Z. H.; Zhang, N., pH-sensitive polymeric micelles for programmable drug and gene delivery. *Curr. Pharm. Des.* 2012, 18 (23), 3442-3451.

52. Chen, H. P.; Liu, X. P.; Dou, Y.; He, B. F.; Liu, L.; Wei, Z. H.; Li, J.; Wang, C. Z.; Mao, C. D.; Zhang, J. X.; Wang, G. S., A pH-responsive cyclodextrin-based hybrid nanosystem as a nonviral vector for gene delivery. *Biomaterials* 2013, 34 (16), 4159-4172.
53. Gaspar, V. M.; Marques, J. G.; Sousa, F.; Louro, R. O.; Queiroz, J. A.; Correia, I. J., Biofunctionalized nanoparticles with pH-responsive and cell penetrating blocks for gene delivery. *Nanotechnology* 2013, 24 (27), 275101.
54. Lin, Y. L.; Jiang, G. H.; Birrell, L. K.; El-Sayed, M. E. H., Degradable, pH-sensitive, membrane-destabilizing, comb-like polymers for intracellular delivery of nucleic acids. *Biomaterials* 2010, 31 (27), 7150-7166.
55. Nuhn, L.; Braun, L.; Overhoff, I.; Kelsch, A.; Schaeffel, D.; Koynov, K.; Zentel, R., Degradable cationic nanohydrogel particles for stimuli-responsive release of siRNA. *Macromol. Rapid Commun.* 2014, 35 (24), 2057-2064.
56. Tschiche, A.; Thota, B. N. S.; Neumann, F.; Schafer, A.; Ma, N.; Haag, R., Crosslinked redox-responsive micelles based on lipoic acid-derived amphiphiles for enhanced siRNA delivery. *Macromol. Biosci.* 2016, 16 (6), 811-823.
57. Dong, R. J.; Su, Y.; Yu, S. R.; Zhou, Y. F.; Lu, Y. F.; Zhu, X. Y., A redox-responsive cationic supramolecular polymer constructed from small molecules as a promising gene vector. *Chem. Commun.* 2013, 49 (84), 9845-9847.
58. Chu, D. S. H.; Johnson, R. N.; Pun, S. H., Cathepsin B-sensitive polymers for compartment-specific degradation and nucleic acid release. *J. Control. Release* 2012, 157 (3), 445-454.
59. Zhang, X. X.; Prata, C. A. H.; McIntosh, T. J.; Barthelemy, P.; Grinstaff, M. W., The effect of charge-reversal amphiphile spacer composition on DNA and siRNA delivery. *Bioconjugate Chem.* 2010, 21 (5), 988-993.
60. Perche, F.; Biswas, S.; Patel, N. R.; Torchilin, V. P., Hypoxia-responsive copolymer for siRNA delivery. *RNA Imaging: Methods and Protocols* 2016, 1372, 139-162.

61. Feng, G. J.; Chen, H. Y.; Li, J. J.; Huang, Q.; Gupte, M. J.; Liu, H.; Song, Y. M.; Ge, Z. S., Gene therapy for nucleus pulposus regeneration by heme oxygenase-1 plasmid DNA carried by mixed polyplex micelles with thermo-responsive heterogeneous coronas. *Biomaterials* 2015, 52, 1-13.
62. Yang, Z.; Cheng, Q.; Jiang, Q.; Deng, L. D.; Liang, Z. C.; Dong, A. J., Thermo-sensitive nanoparticles for triggered release of siRNA. *J. Biomater. Sci. Polym. Ed.* 2015, 26 (4), 264-276.
63. Shim, M. S.; Chang, S.-S.; Kwon, Y. J., Stimuli-responsive siRNA carriers for efficient gene silencing in tumors via systemic delivery. *Biomater. Sci.* 2014, 2 (1), 35-40.
64. Greco, C. T.; Epps, T. H., III; Sullivan, M. O., Mechanistic design of polymer nanocarriers to spatiotemporally control gene silencing. *ACS Biomater. Sci. Eng.* 2016, 2 (9), 1582-1594.
65. Eloy, J. O.; Petrilli, R.; Lopez, R. F. V.; Lee, R. J., Stimuli-responsive nanoparticles for siRNA delivery. *Curr. Pharm. Des.* 2015, 21 (29), 4131-4144.
66. Munsell, E. V.; Ross, N. L.; Sullivan, M. O., Journey to the center of the cell: current nanocarrier design strategies targeting biopharmaceuticals to the cytoplasm and nucleus. *Curr. Pharm. Des.* 2016, 22 (9), 1227-1244.
67. Kami, D.; Takeda, S.; Itakura, Y.; Gojo, S.; Watanabe, M.; Toyoda, M., Application of magnetic nanoparticles to gene delivery. *Int. J. Mol. Sci.* 2011, 12 (6), 3705-3722.
68. Borase, T.; Fox, E. K.; El Haddassi, F.; Cryan, S. A.; Brougham, D. F.; Heise, A., Glyco-copolyptide grafted magnetic nanoparticles: the interplay between particle dispersion and RNA loading. *Polym. Chem.* 2016, 7 (19), 3221-3224.
69. Chertok, B.; Langer, R.; Anderson, D. G., Spatial control of gene expression by nanocarriers using heparin masking and ultrasound-targeted microbubble destruction. *ACS Nano* 2016, 10 (8), 7267-7278.
70. Wu, B. L.; Qiao, Q.; Han, X.; Jing, H.; Zhang, H.; Liang, H. J.; Cheng, W., Targeted nanobubbles in low-frequency ultrasound-mediated gene transfection and growth inhibition of hepatocellular carcinoma cells. *Tumor Biology* 2016, 37 (9), 12113-12121.

71. Rapoport, N. Y.; Christensen, D. A.; Fain, H. D.; Barrows, L.; Gao, Z., Ultrasound-triggered drug targeting of tumors in vitro and in vivo. *Ultrasonics* 2004, 42 (1-9), 943-950.
72. Li, H.-J.; Wang, H.-X.; Sun, C.-Y.; Du, J.-Z.; Wang, J., Shell-detachable nanoparticles based on a light-responsive amphiphile for enhanced siRNA delivery. *R. Soc. Chem. Adv.* 2014, 4 (4), 1961-1964.
73. Liu, G.; Liu, W.; Dong, C. M., UV- and NIR-responsive polymeric nanomedicines for on-demand drug delivery. *Polym. Chem.* 2013, 4 (12), 3431-3443.
74. Liu, Y. C.; Le Ny, A. L. M.; Schmidt, J.; Talmon, Y.; Chmelka, B. F.; Lee, C. T., Photo-assisted gene delivery using light-responsive cationic vesicles. *Langmuir* 2009, 25 (10), 5713-5724.
75. Jayakumar, M. K. G.; Idris, N. M.; Zhang, Y., Remote activation of biomolecules in deep tissues using near-infrared-to-UV upconversion nanotransducers. *Proc. Natl. Acad. Sci. U.S.A.* 2012, 109 (22), 8483-8488.
76. Joglekar, M.; Trewyn, B. G., Polymer-based stimuli-responsive nanosystems for biomedical applications. *Biotechnol. J.* 2013, 8 (8), 931-945.
77. Burke, C. W.; Suk, J. S.; Kim, A. J.; Hsiang, Y. H. J.; Klibanov, A. L.; Hanes, J.; Price, R. J., Markedly enhanced skeletal muscle transfection achieved by the ultrasound-targeted delivery of non-viral gene nanocarriers with microbubbles. *J. Control. Release* 2012, 162 (2), 414-421.
78. Jiang, J. Q.; Tong, X.; Morris, D.; Zhao, Y., Toward photocontrolled release using light-dissociable block copolymer micelles. *Macromolecules* 2006, 39 (13), 4633-4640.
79. Sur, S.; Matson, J. B.; Webber, M. J.; Newcomb, C. J.; Stupp, S. I., Photodynamic control of bioactivity in a nanofiber matrix. *ACS Nano* 2012, 6 (12), 10776-10785.
80. Jayakumar, M. K. G.; Bansal, A.; Huang, K.; Yao, R. S.; Li, B. N.; Zhang, Y., Near-infrared-light-based nanopatform boosts endosomal escape and controls gene knockdown in vivo. *ACS Nano* 2014, 8 (5), 4848-4858.
81. Lee, H.; Kim, Y.; Schweickert, P. G.; Konieczny, S. F.; Won, Y.-Y., A photo-degradable gene delivery system for enhanced nuclear gene transcription. *Biomaterials* 2014, 35 (3), 1040-1049.

82. Motta-Mena, L. B.; Reade, A.; Mallory, M. J.; Glantz, S.; Weiner, O. D.; Lynch, K. W.; Gardner, K. H., An optogenetic gene expression system with rapid activation and deactivation kinetics. *Nat. Chem. Biol.* 2014, 10 (3), 196-202.
83. Huschka, R.; Barhoumi, A.; Liu, Q.; Roth, J. A.; Ji, L.; Halas, N. J., Gene silencing by gold nanoshell-mediated delivery and laser-triggered release of antisense oligonucleotide and siRNA. *ACS Nano* 2012, 6 (9), 7681-7691.
84. Huang, X.; Hu, Q.; Braun, G. B.; Pallaoro, A.; Morales, D. P.; Zasadzinski, J.; Clegg, D. O.; Reich, N. O., Light-activated RNA interference in human embryonic stem cells. *Biomaterials* 2015, 63 (0), 70-79.
85. Shah, S.; Rangarajan, S.; Friedman, S. H., Light activated RNA interference. *Angew. Chem. Int. Ed.* 2005, 44 (9), 1328-1332.
86. Han, G.; You, C. C.; Kim, B. J.; Turingan, R. S.; Forbes, N. S.; Martin, C. T.; Rotello, V. M., Light-regulated release of DNA and its delivery to nuclei by means of photolabile gold nanoparticles. *Angew. Chem. Int. Ed.* 2006, 45 (19), 3165-3169.
87. Saltzman, W. M.; Olbricht, W. L., Building drug delivery into tissue engineering. *Nat. Rev. Drug Discov.* 2002, 1 (3), 177-186.
88. Handwerker, R. G.; Diamond, S. L., Biotinylated photocleavable polyethylenimine: Capture and triggered release of nucleic acids from solid supports. *Bioconjugate Chem.* 2007, 18 (3), 717-723.
89. Kloxin, A. M.; Kasko, A. M.; Salinas, C. N.; Anseth, K. S., Photodegradable hydrogels for dynamic tuning of physical and chemical properties. *Science* 2009, 324 (5923), 59-63.
90. Nguyen, Q. N.; Chavli, R. V.; Marques, J. T.; Conrad, P. G.; Wang, D.; He, W. H.; Belisle, B. E.; Zhang, A. G.; Pastor, L. M.; Witney, F. R.; Morris, M.; Heitz, F.; Divita, G.; Williams, B. R. G.; McMaster, G. K., Light controllable siRNAs regulate gene suppression and phenotypes in cells. *Biochim. Biophys. Acta-Biomembranes* 2006, 1758 (3), 394-403.
91. Kim, M. S.; Diamond, S. L., Photocleavage of o-nitrobenzyl ether derivatives for rapid biomedical release applications. *Bioorg. Med. Chem. Lett.* 2006, 16 (15), 4007-4010.

92. Zhao, Y., Light-Responsive Block Copolymer Micelles. *Macromolecules* 2012, 45 (9), 3647-3657.
93. Klan, P.; Solomek, T.; Bochet, C. G.; Blanc, A.; Givens, R.; Rubina, M.; Popik, V.; Kostikov, A.; Wirz, J., Photoremovable protecting groups in chemistry and biology: reaction mechanisms and efficacy. *Chem. Rev.* 2013, 113 (1), 119-191.
94. Zhao, H.; Sterner, E. S.; Coughlin, E. B.; Theato, P., o-Nitrobenzyl alcohol derivatives: opportunities in polymer and materials science. *Macromolecules* 2012, 45 (4), 1723-1736.
95. Il'ichev, Y. V.; Schworer, M. A.; Wirz, J., Photochemical reaction mechanisms of 2-nitrobenzyl compounds: Methyl ethers and caged ATP. *J. Am. Chem. Soc.* 2004, 126 (14), 4581-4595.
96. Holmes, C. P., Model studies for new o-nitrobenzyl photolabile linkers: Substituent effects on the rates of photochemical cleavage. *J. Org. Chem.* 1997, 62 (8), 2370-2380.
97. Reichmanis, E.; Smith, B. C.; Gooden, R., Ortho-nitrobenzyl photochemistry - solution vs solid-state behavior. *J. Polym. Sci. A Polym. Chem.* 1985, 23 (1), 1-8.
98. Aujard, I.; Benbrahim, C.; Gouget, M.; Ruel, O.; Baudin, J. B.; Neveu, P.; Jullien, L., o-Nitrobenzyl photolabile protecting groups with red-shifted absorption: Syntheses and uncaging cross-sections for one- and two-photon excitation. *Chem. Eur. J.* 2006, 12 (26), 6865-6879.
99. Cameron, J. F.; Frechet, J. M. J., Photogeneration of organic-bases from ortho-nitrobenzyl-derived carbamates. *J. Am. Chem. Soc.* 1991, 113 (11), 4303-4313.
100. Fomina, N.; Sankaranarayanan, J.; Almutairi, A., Photochemical mechanisms of light-triggered release from nanocarriers. *Adv. Drug Deliv. Rev.* 2012, 64 (11), 1005-1020.
101. Zhao, Y., Photocontrollable block copolymer micelles: what can we control? *J. Mater. Chem.* 2009, 19 (28), 4887-4895.
102. deRonde, B. M.; Torres, J. A.; Minter, L. M.; Tew, G. N., Development of guanidinium-rich protein mimics for efficient siRNA delivery into human T cells. *Biomacromolecules* 2015, 16 (10), 3172-3179.

103. Liu, X.; Howard, K. A.; Dong, M. D.; Andersen, M. O.; Rahbek, U. L.; Johnsen, M. G.; Hansen, O. C.; Besenbacher, F.; Kjems, J., The influence of polymeric properties on chitosan/siRNA nanoparticle formulation and gene silencing. *Biomaterials* 2007, 28 (6), 1280-1288.
104. Kunath, K.; von Harpe, A.; Fischer, D.; Peterson, H.; Bickel, U.; Voigt, K.; Kissel, T., Low-molecular-weight polyethylenimine as a non-viral vector for DNA delivery: comparison of physicochemical properties, transfection efficiency and in vivo distribution with high-molecular-weight polyethylenimine. *J. Control. Release* 2003, 89 (1), 113-125.
105. Nelson, C. E.; Kintzing, J. R.; Hanna, A.; Shannon, J. M.; Gupta, M. K.; Duvall, C. L., Balancing cationic and hydrophobic content of PEGylated siRNA polyplexes enhances endosome escape, stability, blood circulation time, and bioactivity in vivo. *ACS Nano* 2013, 7 (10), 8870-8880.
106. Strand, S. P.; Lelu, S.; Reitan, N. K.; Davies, C. d. L.; Artursson, P.; Varum, K. M., Molecular design of chitosan gene delivery systems with an optimized balance between polyplex stability and polyplex unpacking. *Biomaterials* 2010, 31 (5), 975-987.
107. Pujol, M. O.; Coleman, D. J. L.; Allen, C. D.; Heidenreich, O.; Fulton, D. A., Determination of key structure-activity relationships in siRNA delivery with a mixed micelle system. *J. Control. Release* 2013, 172 (3), 939-945.
108. Wang, H.-X.; Xiong, M.-H.; Wang, Y.-C.; Zhu, J.; Wang, J., N-acetylgalactosamine functionalized mixed micellar nanoparticles for targeted delivery of siRNA to liver. *J. Control. Release* 2013, 166 (2), 106-114.
109. Wei, Z.; Hao, J.; Yuan, S.; Li, Y.; Juan, W.; Sha, X.; Fang, X., Paclitaxel-loaded Pluronic P123/F127 mixed polymeric micelles: Formulation, optimization and in vitro characterization. *Int. J. Pharm.* 2009, 376 (1-2), 176-185.
110. Li, Y.; Li, J.; Chen, B.; Chen, Q.; Zhang, G.; Liu, S.; Ge, Z., Polyplex micelles with thermoresponsive heterogeneous coronas for prolonged blood retention and promoted gene transfection. *Biomacromolecules* 2014, 15 (8), 2914-2923.
111. Mai, Y. Y.; Eisenberg, A., Self-assembly of block copolymers. *Chem. Soc. Rev.* 2012, 41 (18), 5969-5985.

112. Bates, F. S.; Fredrickson, G. H., Block copolymer thermodynamics - theory and experiment. *Annu. Rev. Phys. Chem.* 1990, 41, 525-557.
113. Epps, T. H., III; O'Reilly, R. K., Block copolymers: controlling nanostructure to generate functional materials - synthesis, characterization, and engineering. *Chem. Sci.* 2016, 7 (3), 1674-1689.
114. Hayward, R. C.; Pochan, D. J., Tailored assemblies of block copolymers in solution: it is all about the process. *Macromolecules* 2010, 43 (8), 3577-3584.
115. Wittrup, A.; Ai, A.; Liu, X.; Hamar, P.; Trifonova, R.; Charisse, K.; Manoharan, M.; Kirchhausen, T.; Lieberman, J., Visualizing lipid-formulated siRNA release from endosomes and target gene knockdown. *Nat. Biotechnol.* 2015, 33 (8), 870-876.
116. Liao, Z.-X.; Ho, Y.-C.; Chen, H.-L.; Peng, S.-F.; Hsiao, C.-W.; Sung, H.-W., Enhancement of efficiencies of the cellular uptake and gene silencing of chitosan/siRNA complexes via the inclusion of a negatively charged poly(γ -glutamic acid). *Biomaterials* 2010, 31 (33), 8780-8788.
117. Kurosaki, T.; Kitahara, T.; Fumoto, S.; Nishida, K.; Nakamura, J.; Niidome, T.; Kodama, Y.; Nakagawa, H.; To, H.; Sasaki, H., Ternary complexes of pDNA, polyethylenimine, and γ -polyglutamic acid for gene delivery systems. *Biomaterials* 2009, 30 (14), 2846-2853.
118. Tseng, S. J.; Zeng, Y.-F.; Deng, Y.-F.; Yang, P.-C.; Liu, J.-R.; Kempson, I. M., Switchable delivery of small interfering RNA using a negatively charged pH-responsive polyethylenimine-based polyelectrolyte complex. *Chem. Commun.* 2013, 49 (26), 2670-2672.
119. Syga, M.-I.; Nicoli, E.; Kohler, E.; Shastri, V. P., Albumin incorporation in polyethylenimine-DNA polyplexes influences transfection efficiency. *Biomacromolecules* 2016, 17 (1), 200-207.
120. Duceppe, N.; Tabrizian, M., Factors influencing the transfection efficiency of ultra low molecular weight chitosan/hyaluronic acid nanoparticles. *Biomaterials* 2009, 30 (13), 2625-2631.
121. Liao, Z.-X.; Peng, S.-F.; Chiu, Y.-L.; Hsiao, C.-W.; Liu, H.-Y.; Lim, W.-H.; Lu, H.-M.; Sung, H.-W., Enhancement of efficiency of chitosan-based complexes for gene transfection with poly(γ -glutamic acid) by augmenting their cellular uptake and intracellular unpackage. *J. Control. Release* 2014, 193, 304-315.

122. Wang, X.; Chen, X.; Yang, Y., Spatiotemporal control of gene expression by a light-switchable transgene system. *Nat. Methods* 2012, 9 (3), 266-269.
123. Ziauddin, J.; Sabatini, D. M., Microarrays of cells expressing defined cDNAs. *Nature* 2001, 411 (6833), 107-110.
124. Weber, W.; Fussenegger, M., Emerging biomedical applications of synthetic biology. *Nat. Rev. Genet.* 2012, 13 (1), 21-35.
125. Shimizu-Sato, S.; Huq, E.; Tepperman, J. M.; Quail, P. H., A light-switchable gene promoter system. *Nat. Biotechnol.* 2002, 20 (10), 1041-1044.
126. Polstein, L. R.; Gersbach, C. A., Light-inducible spatiotemporal control of gene activation by customizable zinc finger transcription factors. *J. Am. Chem. Soc.* 2012, 134 (40), 16480-16483.
127. Ye, H.; Daoud-El Baba, M.; Peng, R.-W.; Fussenegger, M., A synthetic optogenetic transcription device enhances blood-glucose homeostasis in mice. *Science* 2011, 332 (6037), 1565-1568.
128. Sauers, D. J.; Temburni, M. K.; Biggins, J. B.; Ceo, L. M.; Galileo, D. S.; Koh, J. T., Light-activated gene expression directs segregation of co-cultured cells in vitro. *ACS Chem. Biol.* 2010, 5 (3), 313-320.
129. Konermann, S.; Brigham, M. D.; Trevino, A. E.; Hsu, P. D.; Heidenreich, M.; Cong, L.; Platt, R. J.; Scott, D. A.; Church, G. M.; Zhang, F., Optical control of mammalian endogenous transcription and epigenetic states. *Nature* 2013, 500 (7463), 472-476.
130. Nihongaki, Y.; Yamamoto, S.; Kawano, F.; Suzuki, H.; Sato, M., CRISPR-Cas9-based photoactivatable transcription system. *Chem. Biol.* 2015, 22 (2), 169-174.
131. Mueller, K.; Naumann, S.; Weber, W.; Zurbriggen, M. D., Optogenetics for gene expression in mammalian cells. *Biol. Chem.* 2015, 396 (2), 145-152.
132. Yin, H.; Kanasty, R. L.; Eltoukhy, A. A.; Vegas, A. J.; Dorkin, J. R.; Anderson, D. G., Non-viral vectors for gene-based therapy. *Nat. Rev. Genet.* 2014, 15 (8), 541-555.

133. Aytar, B. S.; Muller, J. P. E.; Kondo, Y.; Abbott, N. L.; Lynn, D. M., Spatial control of cell transfection using soluble or solid-phase redox agents and a redox-active ferrocenyl lipid. *ACS Appl. Mater. Interfaces* 2013, 5 (17), 8283-8288.
134. Isalan, M.; Santori, M. I.; Gonzalez, C.; Serrano, L., Localized transfection on arrays of magnetic beads coated with PCR products. *Nat. Methods* 2005, 2 (2), 113-118.
135. Shalek, A. K.; Robinson, J. T.; Karp, E. S.; Lee, J. S.; Ahn, D.-R.; Yoon, M.-H.; Sutton, A.; Jorgolli, M.; Gertner, R. S.; Gujral, T. S.; MacBeath, G.; Yang, E. G.; Park, H., Vertical silicon nanowires as a universal platform for delivering biomolecules into living cells. *Proc. Natl. Acad. Sci. U.S.A.* 2010, 107 (5), 1870-1875.
136. Houchin-Ray, T.; Whittlesey, K. J.; Shea, L. D., Spatially patterned gene delivery for localized neuron survival and neurite extension. *Mol. Ther.* 2007, 15 (4), 705-712.
137. Lloyd-Jones, D.; Adams, R. J.; Brown, T. M.; Carnethon, M.; Dai, S.; De Simone, G.; Ferguson, T. B.; Ford, E.; Furie, K.; Gillespie, C.; Go, A.; Greenlund, K.; Haase, N.; Hailpern, S.; Ho, P. M.; Howard, V.; Kissela, B.; Kittner, S.; Lackland, D.; Lisabeth, L.; Marelli, A.; McDermott, M. M.; Meigs, J.; Mozaffarian, D.; Mussolino, M.; Nichol, G.; Roger, V. L.; Rosamond, W.; Sacco, R.; Sorlie, P.; Stafford, R.; Thom, T.; Wasserthiel-Smoller, S.; Wong, N. D.; Wylie-Rosett, J., Heart disease and stroke statistics-2010 update a report from the American Heart Association. *Circulation* 2010, 121 (7), e46-e215.
138. Motwani, J. G.; Topol, E. J., Aortocoronary saphenous vein graft disease - Pathogenesis, predisposition, and prevention. *Circulation* 1998, 97 (9), 916-931.
139. Conte, M. S., Molecular engineering of vein bypass grafts. *J. Vasc. Surg.* 2007, 45, 74A-81A.
140. Strauss, B. H.; Rabinovitch, M., Adventitial fibroblasts - Defining a role in vessel wall remodeling. *Am. J. Respir. Cell Mol. Biol.* 2000, 22 (1), 1-3.
141. Fitzgibbon, G. M.; Kafka, H. P.; Leach, A. J.; Keon, W. J.; Hooper, G. D.; Burton, J. R., Coronary bypass graft fate and patient outcome: Angiographic follow-up of 5,065 grafts related to survival and reoperation in 1,388 patients during 25 years. *J. Am. Coll. Cardiol.* 1996, 28 (3), 616-626.

142. Sousa, J. E.; Costa, M. A.; Abizaid, A. C.; Rensing, B. J.; Abizaid, A. S.; Tanajura, L. F.; Kozuma, K.; Van Langenhove, G.; Sousa, A.; Falotico, R.; Jaeger, J.; Popma, J. J.; Serruys, P. W., Sustained suppression of neointimal proliferation by sirolimus-eluting stents - One-year angiographic and intravascular ultrasound follow-up. *Circulation* 2001, 104 (17), 2007-2011.
143. Kawatsu, S.; Oda, K.; Saiki, Y.; Tabata, Y.; Tabayashi, K., External application of rapamycin-eluting film at anastomotic sites inhibits neointimal hyperplasia in a canine model. *Ann. Thorac. Surg.* 2007, 84 (2), 560-567.
144. Weman, S. M.; Salminen, U. S.; Penttila, A.; Mannikko, A.; Karhunen, P. J., Post-mortem cast angiography in the diagnostics of graft complications in patients with fatal outcome following coronary artery bypass grafting (CABG). *Int. J. Legal Med.* 1999, 112 (2), 107-114.
145. Cuccato, G.; Polynikis, A.; Siciliano, V.; Graziano, M.; di Bernardo, M.; di Bernardo, D., Modeling RNA interference in mammalian cells. *BMC Systems Biology* 2011, 5:19.
146. Raab, R. M.; Stephanopoulos, G., Dynamics of gene silencing by RNA interference. *Biotechnology and Bioengineering* 2004, 88 (1), 121-132.
147. Bartlett, D. W.; Davis, M. E., Insights into the kinetics of siRNA-mediated gene silencing from live-cell and live-animal bioluminescent imaging. *Nucleic Acids Res.* 2006, 34 (1), 322-333.
148. Greco, C. T.; Muir, V. G.; Epps, T. H., III; Sullivan, M. O., Efficient tuning of siRNA dose response by combining mixed polymer nanocarriers with simple kinetic modeling. *Acta Biomater.* 2017, 50, 407-416.
149. Bartlett, D. W.; Davis, M. E., Impact of tumor-specific targeting and dosing schedule on tumor growth inhibition after intravenous administration of siRNA-containing nanoparticles. *Biotechnol. Bioeng.* 2008, 99 (4), 975-985.
150. Varga, C. M.; Hong, K.; Lauffenburger, D. A., Quantitative analysis of synthetic gene delivery vector design properties. *Mol. Ther.* 2001, 4 (5), 438-446.
151. Roth, C. M., Quantitative measurements and rational materials design for intracellular delivery of oligonucleotides. *Biotechnol. Prog.* 2008, 24 (1), 23-28.

152. Parra-Guillen, Z. P.; Gonzalez-Aseguinolaza, G.; Berraondo, P.; Troconiz, I. F., Gene therapy: A pharmacokinetic/pharmacodynamic modelling overview. *Pharm. Res.* 2010, 27 (8), 1487-1497.
153. Edinger, D.; Wagner, E., Bioresponsive polymers for the delivery of therapeutic nucleic acids. *Wiley Interdiscip. Rev. Nanomed. Nanobiotechnol.* 2011, 3 (1), 33-46.
154. Dimitriou, M. D.; Zhou, Z. L.; Yoo, H. S.; Killops, K. L.; Finlay, J. A.; Cone, G.; Sundaram, H. S.; Lynd, N. A.; Barteau, K. P.; Campos, L. M.; Fischer, D. A.; Callow, M. E.; Callow, J. A.; Ober, C. K.; Hawker, C. J.; Kramer, E. J., A general approach to controlling the surface composition of poly(ethylene oxide)-based block copolymers for antifouling coatings. *Langmuir* 2011, 27 (22), 13762-13772.
155. Green, M. D.; Foster, A. A.; Greco, C. T.; Roy, R.; Lehr, R. M.; Epps, T. H., III; Sullivan, M. O., Catch and release: photocleavable cationic diblock copolymers as a potential platform for nucleic acid delivery. *Polym. Chem.* 2014, 5 (19), 5535-5541.
156. Foster, A. A.; Greco, C. T.; Green, M. D.; Epps, T. H., III; Sullivan, M. O., Light-mediated activation of siRNA release in diblock copolymer assemblies for controlled gene silencing. *Adv. Healthc. Mater.* 2015, 4 (5), 760-770.
157. Elsabahy, M.; Wooley, K. L., Design of polymeric nanoparticles for biomedical delivery applications. *Chem. Soc. Rev.* 2012, 41 (7), 2545-61.
158. Sun, T. M.; Du, J. Z.; Yan, L. F.; Mao, H. Q.; Wang, J., Self-assembled biodegradable micellar nanoparticles of amphiphilic and cationic block copolymer for siRNA delivery. *Biomaterials* 2008, 29 (32), 4348-4355.
159. Li, J. G.; Cheng, D.; Yin, T. H.; Chen, W. C.; Lin, Y. J.; Chen, J. F.; Li, R. T.; Shuai, X. T., Copolymer of poly(ethylene glycol) and poly((L)-lysine) grafting polyethylenimine through a reducible disulfide linkage for siRNA delivery. *Nanoscale* 2014, 6 (3), 1732-1740.
160. Harris, J. M.; Chess, R. B., Effect of pegylation on pharmaceuticals. *Nat. Rev. Drug. Discov.* 2003, 2 (3), 214-221.
161. Owens, D. E., III; Peppas, N. A., Opsonization, biodistribution, and pharmacokinetics of polymeric nanoparticles. *Int. J. Pharm.* 2006, 307 (1), 93-102.

162. Ogris, M.; Brunner, S.; Schuller, S.; Kircheis, R.; Wagner, E., PEGylated DNA/transferrin-PEI complexes: reduced interaction with blood components, extended circulation in blood and potential for systemic gene delivery. *Gene Ther.* 1999, 6 (4), 595-605.
163. Peracchia, M. T.; Harnisch, S.; Pinto-Alphandary, H.; Gulik, A.; Dedieu, J. C.; Desmaele, D.; d'Angelo, J.; Muller, R. H.; Couvreur, P., Visualization of in vitro protein-rejecting properties of PEGylated stealth (R) polycyanoacrylate nanoparticles. *Biomaterials* 1999, 20 (14), 1269-1275.
164. Grayson, A. C. R.; Doody, A. M.; Putnam, D., Biophysical and structural characterization of polyethylenimine-mediated siRNA delivery in vitro. *Pharm. Res.* 2006, 23 (8), 1868-1876.
165. Ruponen, M.; Ronkko, S.; Honkakoski, P.; Pelkonen, J.; Tammi, M.; Urtti, A., Extracellular glycosaminoglycans modify cellular trafficking of lipoplexes and polyplexes. *J. Biol. Chem.* 2001, 276 (36), 33875-33880.
166. Mao, S.; Neu, M.; Germershaus, O.; Merkel, O.; Sitterberg, J.; Bakowsky, U.; Kissel, T., Influence of polyethylene glycol chain length on the physicochemical and biological properties of poly(ethylene imine)-graft-poly(ethylene glycol) block copolymer/siRNA polyplexes. *Bioconjugate Chem.* 2006, 17 (5), 1209-1218.
167. Mahmoudi, M.; Lynch, I.; Ejtehadi, M. R.; Monopoli, M. P.; Bombelli, F. B.; Laurent, S., Protein-nanoparticle interactions: opportunities and challenges. *Chem. Rev.* 2011, 111 (9), 5610-5637.
168. Feng, L. Z.; Yang, X. Z.; Shi, X. Z.; Tan, X. F.; Peng, R.; Wang, J.; Liu, Z., Polyethylene glycol and polyethylenimine dual-functionalized nano-graphene oxide for photothermally enhanced gene delivery. *Small* 2013, 9 (11), 1989-1997.
169. Kim, S. H.; Jeong, J. H.; Kim, T. I.; Kim, S. W.; Bull, D. A., VEGF siRNA delivery system using arginine-grafted bio-reducible poly(disulfide amine). *Mol. Pharm.* 2009, 6 (3), 718-726.
170. Kelkar, S. S.; Reineke, T. M., Theranostics: combining imaging and therapy. *Bioconjugate Chem.* 2011, 22 (10), 1879-1903.
171. Xu, T.; Liu, W.; Wang, S. H.; Shao, Z. Z., Elucidating the role of free polycationic chains in polycation gene carriers by free chains of polyethylenimine or N,N,N-trimethyl chitosan plus a certain polyplex. *Int. J. Nanomed.* 2014, 9, 3231-3245.

172. Palermo, E. F.; Lee, D. K.; Ramamoorthy, A.; Kuroda, K., Role of cationic group structure in membrane binding and disruption by amphiphilic copolymers. *J. Phys. Chem. B* 2011, 115 (2), 366-375.
173. Moghimi, S. M.; Symonds, P.; Murray, J. C.; Hunter, A. C.; Debska, G.; Szewczyk, A., A two-stage poly(ethylenimine)-mediated cytotoxicity: Implications for gene transfer/therapy. *Mol. Ther.* 2005, 11 (6), 990-995.
174. Xue, H. Y.; Liu, S. M.; Wong, H. L., Nanotoxicity: a key obstacle to clinical translation of siRNA-based nanomedicine. *Nanomedicine* 2014, 9 (2), 295-312.
175. Hong, B. J.; Chipre, A. J.; Nguyen, S. T., Acid-degradable polymer-caged lipoplex (PCL) platform for siRNA delivery: facile cellular triggered release of siRNA. *J. Am. Chem. Soc.* 2013, 135 (47), 17655-17658.

Chapter 2

CHARACTERIZATION TECHNIQUES

This chapter describes the characterization techniques used to study the assembly/disassembly of polyplexes as well as determine how these formulations affected cellular responses. The complementary use of these techniques allowed for the elucidation of key structure-function relationships and informed the development of novel nanocarriers with enhanced properties and new functionalities. The concepts underlying the techniques are described in this chapter, and the results are presented and discussed in the following chapters.

2.1 Gel Electrophoresis

Gel electrophoresis is a common technique used to separate and analyze a mixed population of macromolecules such as nucleic acids or proteins.¹ An electric field is applied to separate the macromolecule mixtures in a gel matrix, allowing for the quantification of each species. In this dissertation, gel electrophoresis was employed to study the formation of polyplexes (details regarding the formulation of polyplexes can be found in the Materials and Methods sections of Chapters 3-6 [e.g. see section 3.2.2]) and the release of encapsulated siRNA from nanocarriers.

Matrices are formed through the gelation of polymers, resulting in porous networks of polymeric chains with sieving properties.² The gel matrices can be produced from a variety of materials; however, agarose often is used for studying nucleic acids because it is easy to cast and the resulting pore sizes are suitable for

separating nucleic acids with a wide range of molecular weights. The concentration of agarose can be increased to reduce the pore size, according to a correlation reported by Griess *et al.*³:

$$P_E = 118 \text{ nm} \times A^{-0.74} \quad (2.1)$$

in which P_E is the average effective pore size (nm) and A is the agarose percentage (wt%). Making a gel with smaller pore sizes is advantageous for separating short nucleic acids (e.g. siRNA).⁴ Additionally, other experimental conditions, such as applied voltage, run time, gel box length, and electrophoresis buffer, can be varied to enhance the degree of separation. In a uniform agarose gel, increasing the run time while decreasing the applied voltage gradient (voltage/length) can help improve the separation of species that have small differences in molecular weight.

The macromolecular samples can be loaded into pre-cast wells of a gel. When an electric current is applied across the gel, and the negatively charged nucleic acids move towards the positively charged anode. Components that are neutral or larger than the pores remain in the wells, and cationic components migrate in the opposite direction of the nucleic acids. The rate of migration through the gel depends on the macromolecular size, charge, and conformation.⁵ Molecular species that are small, highly anionic, and compact (e.g. spherical, not elongated) move through the gel at the fastest rate. For the case of siRNAs, all completely liberated molecules migrate down the gel at essentially the same rate (resulting in well-defined bands) because they do not significantly differ in size, charge, and conformation. However, siRNAs that are bound to other molecular species (e.g. cationic polymer chains) are hindered and migrate at a slower rate.

Following the separation of the species, the nucleic acids can be visualized using a staining agent (Figure 2.1). Ethidium bromide is an intercalating agent commonly used to detect nucleic acids. Upon excitation with UV light, ethidium bromide fluoresces when bound to nucleic acids in a concentration dependent manner.¹ The fluorescence intensity of each band can then be quantified to estimate the relative number of each species.

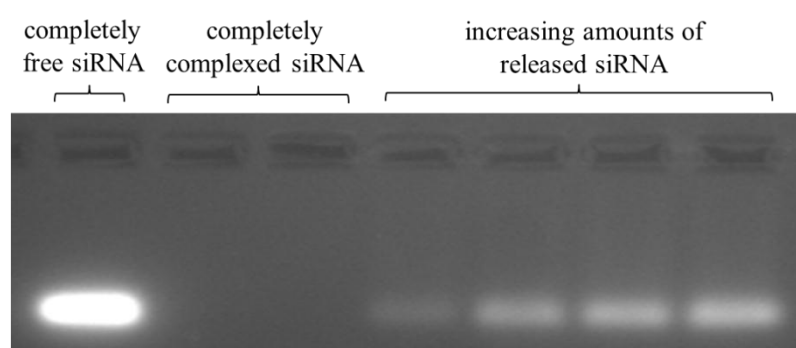


Figure 2.1: Representative micrograph of an agarose gel loaded with siRNA samples and pre-stained with ethidium bromide.

2.2 Dynamic Light Scattering (DLS)

Generally, light scattering techniques probe changes in the direction of a light wave due to variations in the surrounding medium properties. Dynamic light scattering, in particular, is used to gain insight into the diffusive characteristics of particles in solution on the basis of changes in the refractive index.⁶ As the particles move through the solution, the instantaneous scattered light intensity changes over time. These fluctuations in scattered intensity are related through the intensity autocorrelation function, $K(\tau)$, over the collection interval, T :⁷

$$K(\tau) = \frac{1}{T} \int_0^T I(t)I(t + \tau)dt \quad (2.2)$$

Or the dimensionless form, $g(\tau)$:

$$g(\tau) = \frac{\langle I(t)I(t+\tau) \rangle}{\langle I(t) \rangle^2} \quad (2.3)$$

Furthermore, the intensity autocorrelation function is mathematically related to the electric field correlation function, $g_1(\tau)$, by the Bloch–Siegert theorem⁸:

$$g(\tau) = 1 + |g_1(\tau)|^2 \quad (2.4)$$

For particles undergoing Brownian motion, $g_1(\tau)$ can be simplified to give:

$$g(\tau) = 1 + e^{-2Dq^2\tau} \quad (2.5)$$

in which q^2 is the scattering wavevector modulus and D is the diffusivity. The scattering vector modulus depends on the distance traveled by the particles in the given time delay, τ . Importantly, the diffusivity can be related to particle size. If the particles are assumed to be spherical and monodisperse, the Stokes-Einstein equation can be used to calculate the average particle radius⁹:

$$D = \frac{kT}{6\pi\eta R} \quad (2.6)$$

in which k is the Boltzmann constant, T is the temperature, η is the solvent viscosity, and R is the particle's hydrodynamic radius. Smaller particles diffuse more rapidly in solution, and the corresponding correlation functions decay at a faster rate. When plotted as a function of the delay time, these correlation functions are shifted to lower times compared to the functions for larger particles (Figure 2.2). Theoretically, an infinitely large particle would have a perfect correlation over the short delay times typically probed during DLS (on the order of up to several hundred microseconds).

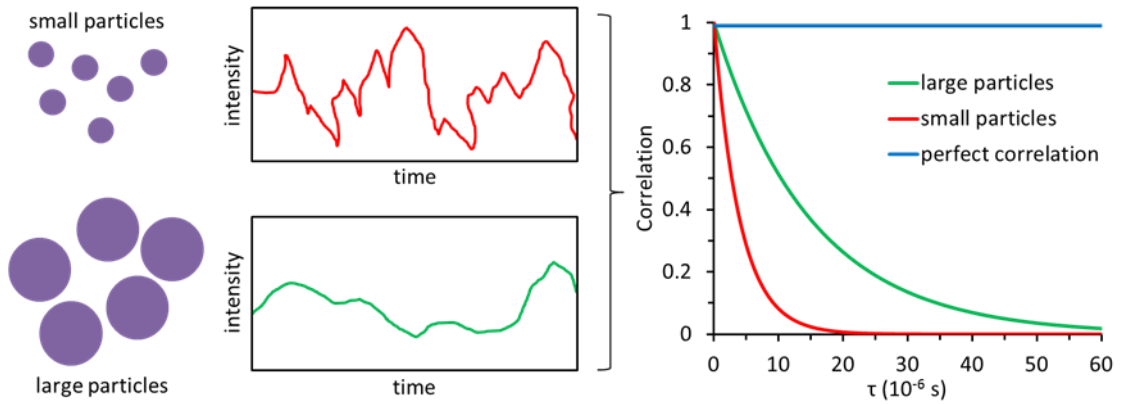


Figure 2.2: Comparison of diffusive properties and correlation functions of small and large particles. The smaller particles diffuse more quickly, resulting in more rapid fluctuations in light intensity and shorter correlation times.

The validity of the two assumptions of spherical and monodisperse particles is an important consideration when analyzing DLS data. Polyplex systems documented in the literature tend to be random aggregates of polymer/siRNA that are approximately spherical with fairly high dispersities.¹⁰ Thus, the shape assumption usually is an accurate approximation; however, the assumption of a monodisperse population is not valid in most cases. A number of models that account for particle polydispersity have been developed. For example, the cumulant expansion is one the simplest and most widely used models, and it assumes that the particles are monomodal and are described by a Gaussian-like distribution¹¹:

$$g_1(\tau) = e^{-\Gamma\tau} \left(1 + \frac{\mu_2}{2!} \tau^2 + \dots \right) \quad (2.7)$$

in which Γ is the average decay constant. Γ can be related to the particle diffusivity, and ultimately to the average hydrodynamic particle radius *via* the Stokes-Einstein equation, through the following relationship:

$$\Gamma = Dq^2 \quad (2.8)$$

The second term of the cumulant expansion model is usually limited to only the second order expansion because this approximation is sufficient for accurately capturing the decay of the correlation function in most cases. Thus, DLS can accurately characterize nanoparticle populations that are approximately spherical and monomodal, as was the case for the formulations studied in this dissertation.

2.3 Fluorescence Correlation Spectroscopy (FCS)

FCS is a powerful technique that can be used to determine the diffusive properties and concentrations of fluorescent molecules in both extra- and intra-cellular environments. Similar to DLS, FCS is an analysis of fluctuations in light intensity that allows for the generation of correlation functions.¹² Two of the unique advantages of FCS include single molecule detection in serum/live cells and the ability to resolve extremely dilute molecular species (as low as picomolar concentrations).¹³ However, a drawback of the technique is that a fluorescent tag must be incorporated into the macromolecule of interest, potentially altering the native behavior of the system.

FCS is commonly employed on confocal microscopes due to the instruments' precisely defined optics, which are enabled by confocal pinholes that exclude all light coming from outside the region of interest.¹⁴ The high spatial resolution of a confocal microscope is required to detect extremely small numbers of molecules. Specifically, a laser beam can be focused on a confocal volume of ~1 fL that contains only 1-100 fluorescently tagged particles (Figure 2.3).¹⁵ As the macromolecules diffuse due to Brownian motion, they randomly enter the confocal volume and fluoresce. The number of particles must be sufficiently low so that each diffusing molecule contributes significantly to the fluctuation in the signal; however, the concentration

cannot be too sparse or else it will take an unreasonable amount of time to measure enough particles in each sample to obtain robust statistics.

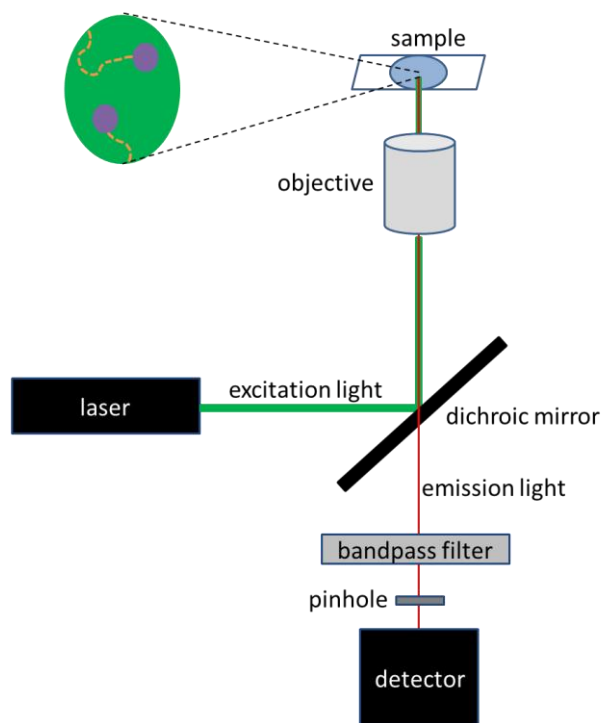


Figure 2.3: Schematic of a typical FCS experimental setup. The excitation light (green) is directed to the sample and excites the fluorophores in the confocal volume. The resulting emission signal (red) is transmitted through a dichroic mirror. Before reaching the detector, the light is passed through a bandpass filter and pinhole that exclude all light that is outside the designated wavelength range or is not from the confocal volume, respectively.

The freely moving particles diffuse in and out of the confocal volume, and the fluctuations in fluorescence intensity provide information about the concentration and diffusion properties of those particles. An autocorrelation function is generated on the basis of these fluctuations, and diffusive properties can be extracted in a very similar

manner as DLS. A single-component model of normally diffusing particles is the simplest model to describe polyplexes in FCS analyses. The autocorrelation function can be fit as a Gaussian distribution as¹⁶:

$$G(t) = 1 + \frac{1}{N} \left(1 + \frac{4Dt}{w_o^2}\right)^{-1} \left(1 + \frac{4Dt}{z_o^2}\right)^{-\frac{1}{2}} \quad (2.9)$$

in which w_o and z_o are the sample width and length, respectively, D is the diffusion coefficient, and N is the number of particles in the confocal volume. $G(0)$, or the correlation at $t = 0$ s, is related to the average number of particles in the confocal volume, as follows:

$$G(0) = \frac{1}{\langle N \rangle} \quad (2.10)$$

If the confocal volume is known, the average concentration can be calculated. Moreover, the diffusion coefficient can be computed and related to the average particle radius using the Stokes-Einstein equation (Equation 2.6), assuming that the particles are spherical and monodisperse.

Other models, such as the two-component and anomalous diffusion models, also can be used to describe complicated systems with multiple populations. Although models with more parameters will produce better fits when the additional terms are allowed to be free, the fitting often produces results that were not physically possible. To overcome this challenge, key parameters must be constrained (fixed) to match the realistic characteristics of the systems; however, this approach can bias the results, as more assumptions must be made. Alternatively, FCS can be adopted to easily estimate the distributions of particles in different populations through analysis of the baseline of the fluorescence intensities (count rates).¹⁷ A particularly useful application of this

method is the quantification of free siRNA, for which the count rates of each solution represent the baseline fluorescence intensities:

$$\% \text{ free siRNA} = \frac{\text{count rate}_{\text{polyplex}} - \text{count rate}_{\text{blank}}}{\text{count rate}_{\text{free siRNA}} - \text{count rate}_{\text{blank}}} \times 100 \quad (2.11)$$

In this work, the 5' end of siRNA molecules was labeled with a Dy547 fluorophore to enable tracking of siRNAs that were free in solution or complexed in polyplexes. The siRNAs were studied in buffered solutions, serum, and live cells, demonstrating the ability of FCS to analyze particle diffusion *in situ*. These analyses gave insights into the sizes and stabilities of polyplexes, the number of siRNA molecules released from polyplexes, and the intracellular fate of siRNAs/polyplexes.

2.4 Flow Cytometry

Flow cytometry is a laser-based technique used for the high-throughput quantitative analysis of particles and cells. This method allows for the simultaneous characterization of physical and chemical properties of the specimen. Specifically, information regarding particle size and morphological complexity can be obtained from the forward and side scattered light, respectively, and chemical details (e.g. fluorescence) can be determined using numerous wavelength-specific detectors.¹⁸ Flow cytometers are capable of measuring thousands of particles per second, and the data can be read in real time.¹⁹

To conduct a flow cytometry experiment, cells should be prepared in an ice-cold buffered solution at a concentration of approximately 10^6 cells mL^{-1} . Immediately before analysis, the cells can be gently vortexed or shaken to break up any aggregates that formed in solution. Once the cells are drawn into the flow cytometer, they enter a liquid stream of sheath fluid that aligns the cells into a single-

file line. The flow passes through the light beams, and the scattered and fluorescent light is captured by multiple detectors. The intensity of each fluorescent channel is recorded, amplified, and sent to a computer for further analysis. Specialized software, such as FlowJo, is needed to process the data.

The value of every detected particle/cell is usually displayed on a two-dimensional dot plot of forward *vs.* side scattered intensity with a logarithmic scale. The data must be separated into subregions so that the subsequent analyses focus on the desired cell population. For example, the live cell population should be separated from the dead cell and cellular debris populations (Figure 2.4). This process is referred to as “gating” and is essential for obtaining accurate data.²⁰ After the live cell population has been properly gated, the fluorescence intensity distribution of each sample can be plotted as a histogram for visualization. Additionally, the fluorescence characteristics of the population can be quantified in terms of a wide variety of metrics, including the mean and median fluorescence intensities per cell.

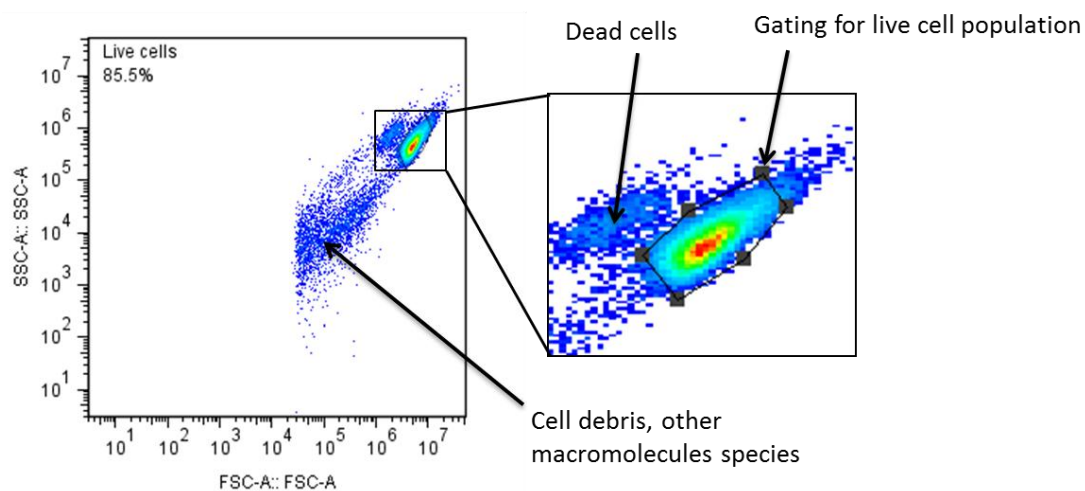


Figure 2.4: Representative two-dimensional dot plot of forward vs. side scattered intensity. 85.5% of the detected particles were designated to be considered live cells (within the 6-sided polygon gate). The gate was applied to this population due to the specimen's large size (indicated by high forward scattering) and fairly complex morphology (indicated by medium-high side scattering). The remaining 14.5% of particles were determined to be either dead cells (slightly smaller size and more complex morphology) or cell debris/other macromolecular species (much smaller size and less complex morphology).

In this dissertation, flow cytometry was employed to measure the fluorescence distributions of cell populations to study cellular uptake and polyplex stability. siRNA molecules were labelled with the desired fluorophores and delivered to cells for both types of experiments. For uptake experiments, the goal was to determine how much siRNA entered the cells. Thus, the level of cellular uptake was estimated by measuring the change in fluorescence intensity of each cell relative to the autofluorescence signal.

To probe intracellular polyplex stability, polyplexes were formed with siRNAs that were labeled with two different fluorophores capable of undergoing FRET.

Polyplex stability was monitored by analyzing the ratio of the two fluorophore emission intensities. Multiple detection channels were needed; however, signal spillover in the acceptor channel from the donor fluorophore added complexity to the analysis. To address this challenge, a compensation matrix was generated. The values of the matrix depend on the amount of signal bleedthrough from each fluorophore into a different channel, which can be determined using control samples (e.g. polyplexes with only a single fluorophore).²¹ If performed correctly, the resulting fluorescence intensity distributions of the control samples should have the same median fluorescence intensity as untransfected cells (due to autofluorescence). Most flow cytometry software packages have algorithms that can automatically determine the compensation matrix values if given the appropriate controls; however, the values may need to be manually tuned to achieve the best results. The matrix is applied to the raw data to correct for the signal spillover, allowing for accurate estimates of FRET efficiencies. For example, a representative compensation matrix for the FRET experiments in section 3.3.5 is shown in Figure 2.5.

	APC	PE	PE-Texas Red
APC	100.0%	0.1%	2.5%
PE	0.0%	100.0%	33.8%
PE-Texas Red	0.0%	24.4%	100.0%

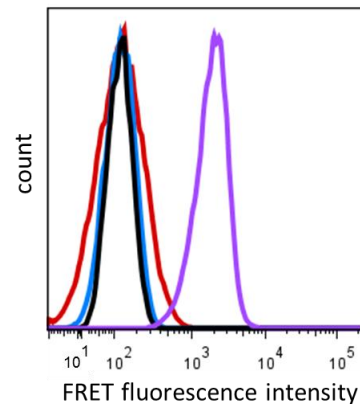


Figure 2.5: Representative compensation matrix and compensated histogram distributions of FRET intensities. The APC and PE channels primarily detected signals from individual fluorophores (control samples) and the PE-Texas Red channel primarily detected the signal attributed to FRET. After compensation, the distributions of the control samples (blue is donor fluorophore and red is acceptor fluorophore) had the same median fluorescence intensity as the distribution of untransfected cells (black). The compensation procedure allowed the true FRET signal (purple) to be isolated while taking signal spillover into account.

2.5 Western Blotting

The western blot is a common technique used to detect specific proteins and their relative abundance from an extract containing many different species. The method relies on antibodies to uniquely bind the proteins of interest in a concentration dependent manner. Western blotting is considered to be semi-quantitative in nature because it allows for the estimation of relative protein concentrations in a sample.²²

To determine the expression level of a specific protein in a sample of cells, the total protein content must be extracted. The cells should be lysed with an ice-cold detergent-containing buffer with protease inhibitors to reduce enzyme-mediated protein degradation. Afterwards, the proteins must be denatured to enable the separation of proteins by molecular weight in a gel. All secondary and tertiary

structures can be removed through the heating of samples to 100 °C for at least 5 min and the addition of strong reducing agents such as mercaptoethanol. Sodium dodecyl sulfate (SDS) also is added to coat the proteins in a negative charge to allow the samples to be subjected to SDS polyacrylamide gel electrophoresis (SDS-PAGE). Analogous to agarose gel electrophoresis, the lower molecular weight species migrate further down the polyacrylamide gel when a current is applied.

The separated protein species are in the gel, making them inaccessible to antibodies. Therefore, the protein must be transferred to a thin-layered membrane, often made of either nitrocellulose or polyvinylidene difluoride (PVDF).²³ While both membrane materials bind proteins (but do not preferentially bind certain types of proteins), PVDF membranes are sturdier and can withstand multiple probing and stripping cycles. An electroblotting process utilizes a current to transfer the negatively charged protein to the membrane while maintaining the same protein orientation as in the gel. The proteins remain bound to the membrane due to hydrophobic and electrostatic interactions.

The membrane materials were chosen for their ability to non-specifically bind proteins to facilitate protein transfer. However, antibodies also are proteins that will adsorb to the membrane. Thus, the empty sites on the membrane must be covered with other protein to block this non-specific antibody binding. Two of the most common blocking agents are 3-5 wt% non-fat milk and bovine serum albumin (BSA) solutions in Tris-buffered saline with 0.1 vol% Tween 20 (TBST). The choice of blocking agent depends on the particular antibodies used. The membrane should be incubated in the blocking solution for at least one hour, and this blocking step reduces

the final background intensity to make it easier to differentiate the targeted protein species.

To detect the protein of interest, a two-step process of antibody incubations is performed. This two-step process is generally preferred because it enables signal amplification and flexibility in antibody choice.²⁴ First, a primary antibody that specifically binds to the targeted protein is added and incubated overnight at 4 °C to ensure complete binding. The next day, the membrane is washed numerous times to remove any excess primary antibody. Next, a secondary antibody is added for approximately 1 h, usually at room temperature. The secondary antibody binds to any antibody generated by a specific animal. For example, if the primary antibody was produced in a rabbit, the secondary antibody should be anti-rabbit. The secondary antibody is linked to a reporter molecule such as horseradish peroxidase (HRP). Following more wash steps, the membrane is exposed to a solution containing a chemiluminescent agent that can be cleaved by HRP. The luminescence can be detected using an imager, and the signal intensity is proportional to the amount of bound secondary antibody (Figure 2.6). The resulting micrograph can be quantified using image analysis software (e.g., ImageJ) to determine the band intensity of each sample.

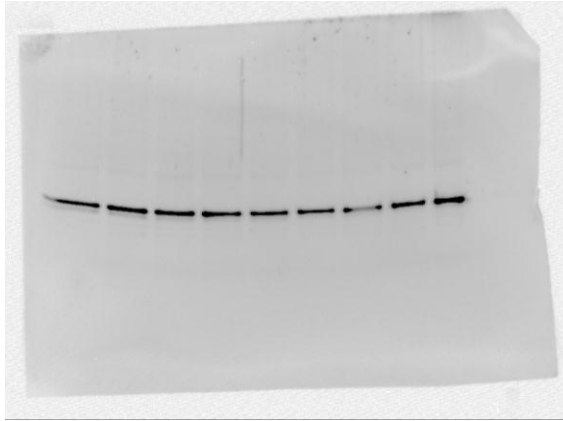


Figure 2.6: Representative image of a western blot membrane following the addition of a chemiluminescent substrate. Nine different protein samples were analyzed, and the resulting bands can be quantified to determine the protein content in each sample.

A “housekeeping” protein also must be probed to account for loading differences that may impact the accuracy of the quantification analysis. To minimize signal bleedthrough from other proteins, the membrane should be stripped of all antibodies using a stripping solution (see section 4.2.5 for more details). Next, the membranes can be blocked, incubated in a different primary antibody overnight, reprobed with a secondary antibody, imaged, and quantified. The band intensities of the housekeeping gene are usually assumed to be representative of the total protein content loaded in each well. These intensity values are used to normalize the intensity values measured for the protein of interest.

2.6 Immunocytochemistry (ICC)

Similar to western blotting, ICC provides quantitative information regarding protein expression in cell samples. Additionally, ICC allows for the direct visualization of the proteins’ cellular location(s), which is necessary for detailed

trafficking or protein expression studies. This advantage is enabled through the application of antibodies *in situ*, as opposed to lysing the cells and measuring the total protein content of a population during western blotting.²⁵ Another consequence of this analytical difference is that ICC is only capable of quantifying relatively small numbers of cells (on the order of hundreds) at once, whereas western blotting measures the average expression of potentially millions of cells per experiment.

The cells must be stabilized before preparing the specimens for antibody probing. In particular, chemical fixatives should be added to stabilize cell morphology, inactivate proteolytic enzymes, protect samples against contamination and decomposition, and strengthen samples to withstand further processing.²⁶ The most commonly used chemical fixative is formaldehyde, which crosslinks cellular proteins and nucleic acids by reacting with primary amines to form partially-reversible methylene bridges. After fixation, the cells can be stored at 4 °C in PBS for at least a few days.

Even after the cells have been fixed, the intact membranes would block antibodies from penetrating into the cells and binding to the targeted proteins.²⁷ To overcome this problem, the membrane should be permeabilized with a detergent. One of the most common permeabilizing agents is TritonX-100, which effectively pokes large holes in cellular membranes to allow for the detection of intracellular proteins. Following permeabilization, the cells should be blocked to reduce non-specific antibody binding. The addition of a 5 vol% bovine serum albumin solution is a common blocking step that effectively reduces off-target fluorescence.

Following the same logic pertaining to western blotting, two-step antibody staining protocols are usually used in ICC experiments. The cells should be incubated

overnight at 4 °C in a solution of primary antibody targeting the protein of interest, washed to remove excess antibody, and stained with a second antibody solution. The secondary antibodies often are conjugated to fluorophores that can be directly visualized using fluorescence microscopy. Other staining agents, including Hoechst (nuclear DNA) and Phalloidin (F-actin) stains, also can be added to aid in visualizing the details of each cell (Figure 2.7).

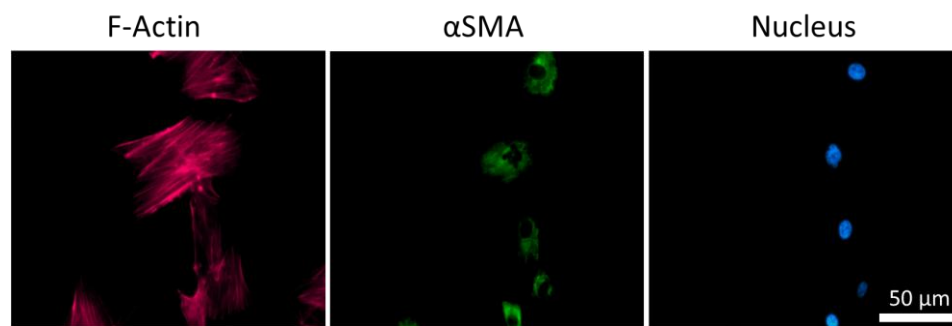


Figure 2.7: Representative ICC micrographs. F-Actin was stained with Phalloidin-660 (magenta), α SMA was stained with rabbit α SMA-targeting primary antibodies and secondary goat anti-rabbit AF488-labelled secondary antibodies (green), and nuclear DNA was stained with Hoechst 33258 (blue).

The specimens can be imaged using fluorescence microscopes. It is important to maintain the same exposure, intensity, and gain settings across all samples to ensure that the fluorescence intensities remain consistent. Moreover, control samples without any staining agents are needed to determine the levels of autofluorescence. The resulting micrographs can be analyzed using software such as ImageJ.²⁸ Specifically, the fluorescence intensities can be quantified to gain insights into the expression levels of the corresponding protein targets.

2.7 Reverse Transcription Quantitative Polymerase Chain Reaction (RT-qPCR)

RT-qPCR is a sensitive technique used to analyze gene expression at the transcript level. The method is comprised of two main phases – reverse transcription (RT) and quantitative polymerase chain reaction (qPCR).²⁹ The first step reverse transcribes the mRNA transcripts into complementary DNA (cDNA) amplicons. The second step follows standard PCR protocols, except that it is conducted in a quantitative manner and enables the monitoring of DNA concentrations in real time. Some of the advantages of RT-qPCR include speed, sensitivity, precision, and repeatability.²⁹ At the same time, the high sensitivity of the technique makes it quite expensive because the reaction reagents must have precisely defined compositions and be of the highest quality (usually needs to be purchased from specialized vendors).

RT-qPCR is one of the most common methods used to probe changes in the mRNA expression levels of cells. Before analyses can be performed, the mRNA needs to be extracted from the cells. Cells should be lysed using a detergent mixture that stabilizes the degradation-susceptible transcripts (e.g., TRIzol). Standard purification protocols from the lysis buffer's manufacturers should be followed to isolate the mRNA and remove all genomic DNA. The effectiveness of this purification step is critical, as the PCR reaction is extremely sensitive to impurities. Next, the concentration of the isolated mRNA solutions can be measured using a spectrophotometer such as a NanoDrop 2000. The purified mRNA samples can be stored at -20 °C for a few days prior to analysis.

Before RT-qPCR can be performed, forward and reverse primers must be designed and ordered from specialized vendors. These primers anneal to the cDNA templates and allow for the amplification of the targeted strands.³⁰ Specifically, the

primers bind to the beginning and end of the DNA section that is going to be amplified, and DNA polymerases synthesize the complementary strand in between these two primers. Primers can be designed using online software and genome databases available from the National Center for Biotechnology Information. The most important criteria for selecting good primer pairs are: the primers should avoid cross homology and be specific to only the desired product (ideally, all other possible products contain at least two base pair mismatches), the primers should have melting temperature of 57-63 °C, the guanine-cytosine (GC) content of each primer should be 50-60%, the primers should be 18-22 base pairs long, the amplicon size should be approximately 75-200 base pairs long, the amplicon should not contain any secondary structure, and the amplicon should span exon-exon junctions.³⁰ Usually, it is best to design multiple primer pairs and test each set to determine which pair is the most specific and reliable.

The fastest and most direct method for performing RT-qPCR is to combine both phases (RT and qPCR) into a single step. Using this strategy, the reagents needed for RT and qPCR are loaded into the same tube, and the two phases are carried out in succession. Master mixes that contain all of the shared reagents often are formulated to improve reproducibility. In this dissertation, the iTaq Universal SYBR Green One-Step Kit from Bio-Rad was used. The kit's master mix includes DNA polymerases, deoxyribose nucleoside triphosphates (dNTPs), Mg²⁺, SYBR Green dyes, and a blend of stabilizers and enhancers. The master mix is combined with the isolated mRNA templates, reverse transcriptases, forward and reverse primers, and water. The reagents should be mixed in the proportions suggested by Bio-Rad. For the most accurate results, the samples should be mixed in replicates of at least three.

Before running RT-qPCR, the thermal cycler must be programmed to follow the desired heating and detection schedule.³¹ These schedules differ slightly based on the kit but generally follow the same steps. In the case of the iTaq Universal SYBR Green One-Step Kit, the cycler is held at 50 °C for 10 min to allow the RT reaction to take place, which reverse transcribes mRNA into DNA in a proportional manner. The qPCR phase takes place in two steps that are repeated 30-45 times. First, the tubes are heated to 95 °C for 10 s to denature the double-stranded DNA strands and to initially activate the DNA polymerases. Second, the tubes are cooled to 60 °C for 30 s to allow for the annealing of the primers and the extension of the amplicon by the DNA polymerases. As the PCR progresses, the number of DNA strands doubles after each cycle.³¹ Thus, the number of DNA strands grows exponentially, making it easy to quantify and enabling the detection of extremely small starting concentrations of the targeted sequence.

Fluorescent dyes (e.g., SYBR Green) fluoresce when intercalated with double-stranded DNA. When the DNA reaches the log linear phase of amplification during the PCR process, the fluorescence intensity becomes detectable beyond the background signal. The cycle number at which this occurs is called the quantification cycle (C_q). Smaller C_q values indicate that there were fewer transcripts initially present. The $\Delta\Delta CT$ method was used for fold change analysis of all qPCR data presented in this dissertation, and the details are explained below.³² Furthermore, an example calculation is displayed in Table A.1 in Appendix A.

To account for loading differences, a housekeeping gene also is quantified. The difference in C_q values between the targeted gene and the housekeeping gene for each sample can be related to the difference of an untreated control sample³²:

$$d = (C_{q,target} - C_{q,housekeep})_{test} - (C_{q,target} - C_{q,housekeep})_{untreated} \quad (2.12)$$

If the specimens were loaded correctly, the C_q values of the housekeeping gene should be the same for every sample. Furthermore, the housekeeping genes usually have higher natural expression levels than the targeted gene, meaning that they have lower C_q values than the targeted genes. Next, the normalized mRNA expression level (m) of a test sample relative to the untreated control can be expressed as a percentage by:

$$m = 100 \times 2^{-d} \quad (2.13)$$

Additionally, multiple controls are needed to confirm the validity of the experiment. No template controls (NTC)s verify that there was no significant contamination or primer-dimer formation in each sample. No reverse transcriptase controls (NRT)s determine whether significant amount of unpurified genomic DNA was present in each sample. If the C_q values of these controls are much greater than the corresponding test sample (by at least seven cycles), these contamination possibilities can be ruled out as insignificant contributors to the fluorescence signal. A typical plot of the amplification curves for the test and control samples is shown in Figure 2.8.

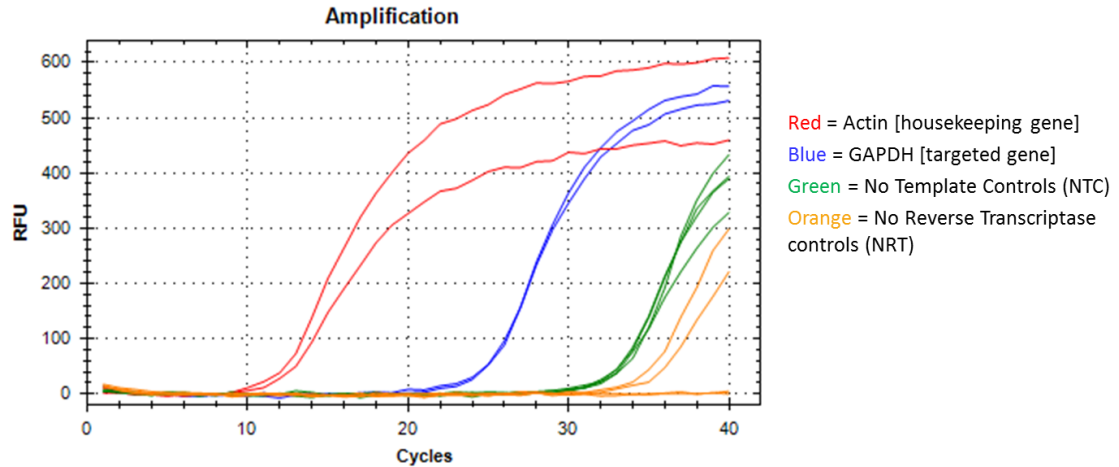


Figure 2.8: Representative amplification curves for test and control samples. The housekeeping gene test samples had C_q values of ~ 11 , and the targeted gene test samples had C_q values of ~ 24 . All NTC and NRT control samples had C_q values that were much greater than the corresponding test samples, indicating that contamination was not a significant factor in this experiment.

Furthermore, a melt curve analysis should be conducted after the PCR cycles have finished to confirm that the amplified products have a melting temperature that is close to the expected temperature, which can be estimated using online predictive software.³¹ This analysis is accomplished by gradually heating the final products from 65 °C to 95 °C by ramping up the temperature by 0.5 °C every 2 s. The heating will cause the double-stranded products to denature, resulting in the loss of a fluorescence signal from the intercalated SYBR Green dyes. The slope of the change in fluorescence intensity over temperature, or the derivative of the melt curve, can be plotted. The melting temperature of each product can be determined by analyzing the peak of each curve, and each product should have a single peak that is consistent across all samples of the particular gene.

REFERENCES

1. Lee, P. Y.; Costumbrado, J.; Hsu, C. Y.; Kim, Y. H., Agarose gel electrophoresis for the separation of DNA fragments. *J. Vis. Exp.* **2012**, (62), e3923.
2. Viovy, J. L., Electrophoresis of DNA and other polyelectrolytes: Physical mechanisms. *Rev. Mod. Phys.* **2000**, 72 (3), 813-872.
3. Griess, G. A.; Moreno, E. T.; Easom, R. A.; Serwer, P., The sieving of spheres during agarose-gel electrophoresis - quantitation and modeling. *Biopolymers* **1989**, 28 (8), 1475-1484.
4. Serwer, P., Agarose gels - properties and use for electrophoresis. *Electrophoresis* **1983**, 4 (6), 375-382.
5. Sharp, P. A.; Sugden, B.; Sambrook, J., Detection of 2 restriction endonuclease activities in haemophilus-parainfluenzae using analytical agarose-ethidium bromide electrophoresis. *Biochemistry* **1973**, 12 (16), 3055-3063.
6. Boyd, R. D.; Pichaimuthu, S. K.; Cuenat, A., New approach to inter-technique comparisons for nanoparticle size measurements; using atomic force microscopy, nanoparticle tracking analysis and dynamic light scattering. *Colloids Surf., A* **2011**, 387 (1-3), 35-42.
7. Borsali, R.; Pecora, R., *Soft-Matter Characterization*. Springer: New York, 2008.
8. Goldberg, W. I., Dynamic light scattering. *Am. J. Phys.* **1999**, 67 (12), 1152-1160.
9. Hiemenz, P. C.; Lodge, T. P., *Polymer Chemistry, Second Edition*. CRC Press: Boca Raton, 2007.
10. DeRouchey, J.; Schmidt, C.; Walker, G. F.; Koch, C.; Plank, C.; Wagner, E.; Radler, J. O., Monomolecular assembly of siRNA and poly(ethylene glycol)-peptide copolymers. *Biomacromolecules* **2008**, 9 (2), 724-732.

11. Frisken, B. J., Revisiting the method of cumulants for the analysis of dynamic light-scattering data. *Appl. Opt.* **2001**, *40* (24), 4087-4091.
12. Elson, E. L.; Magde, D., Fluorescence correlation spectroscopy .1. Conceptual basis and theory. *Biopolymers* **1974**, *13* (1), 1-27.
13. Remaut, K.; Lucas, B.; Raemdonck, K.; Braeckmans, K.; Demeester, J.; De Smedt, S. C., Can we better understand the intracellular behavior of DNA nanoparticles by fluorescence correlation spectroscopy? *J. Control. Release* **2007**, *121* (1-2), 49-63.
14. Parhamifar, L.; Wu, L. P.; Andersen, H.; Moghimi, S. M., Live-cell fluorescent microscopy platforms for real-time monitoring of polyplex-cell interaction: Basic guidelines. *Methods* **2014**, *68* (2), 300-307.
15. Troiber, C.; Kasper, J. C.; Milani, S.; Scheible, M.; Martin, I.; Schaubhut, F.; Kuechler, S.; Raedler, J.; Simmel, F. C.; Friess, W.; Wagner, E., Comparison of four different particle sizing methods for siRNA polyplex characterization. *Eur. J. Pharm. Biopharm.* **2013**, *84* (2), 255-264.
16. Rigler, R.; Mets, U.; Widengren, J.; Kask, P., Fluorescence correlation spectroscopy with high count rate and low-background - analysis of translational diffusion. *Eur. Biophys. J. Biophys.* **1993**, *22* (3), 169-175.
17. Buyens, K.; Meyer, M.; Wagner, E.; Demeester, J.; De Smedt, S. C.; Sanders, N. N., Monitoring the disassembly of siRNA polyplexes in serum is crucial for predicting their biological efficacy. *J. Control. Release* **2010**, *141* (1), 38-41.
18. Lee, H.; Kim, I. K.; Park, T. G., Intracellular trafficking and unpacking of siRNA/quantum dot-PEI complexes modified with and without cell penetrating peptide: confocal and flow cytometric FRET analysis. *Bioconjugate Chem.* **2010**, *21* (2), 289-295.
19. Menon, V.; Thomas, R.; Ghale, A. R.; Reinhard, C.; Pruszek, J., Flow cytometry protocols for surface and intracellular antigen analyses of neural cell types. *J. Vis. Exp.* **2014**, (94), e52241.
20. Lo, K.; Brinkman, R. R.; Gottardo, R., Automated gating of flow cytometry data via robust model-based clustering. *Cytometry Part A* **2008**, *73A* (4), 321-332.
21. Roederer, M., Spectral compensation for flow cytometry: Visualization artifacts, limitations, and caveats. *Cytometry* **2001**, *45* (3), 194-205.

22. Eaton, S. L.; Hurtado, M. L.; Oldknow, K. J.; Graham, L. C.; Marchant, T. W.; Gillingwater, T. H.; Farquharson, C.; Wishart, T. M., A guide to modern quantitative fluorescent western blotting with troubleshooting strategies. *J. Vis. Exp.* **2014**, (93), e52099.
23. Burnette, W. N., Western Blotting: Electrophoretic transfer of proteins from sodium dodecyl sulfate-polyacrylamide gels to unmodified nitrocellulose and radiographic detection with antibody and radioiodinated protein A. *Anal. Biochem.* **1981**, *112* (2), 195-203.
24. Eslami, A.; Lujan, J., Western blotting: sample preparation to detection. *J. Vis. Exp.* **2010**, *44*, e2359.
25. Mize, R. R.; Holdefer, R. N.; Nabors, L. B., Quantitative immunocytochemistry using an image analyzer. I. Hardware evaluation, image processing, and data analysis. *J. Neurosci. Methods* **1988**, *26* (1), 1-23.
26. Berod, A.; Hartman, B. K.; Pujol, J. F., Importance of fixation in immunohistochemistry: use of formaldehyde solutions at variable pH for the localization of tyrosine hydroxylase. *J. Histochem. Cytochem.* **1981**, *29* (7), 844-850.
27. Jamur, M. C.; Oliver, C., Permeabilization of cell membranes. *Immun. Methods and Protocols* **2010**, *588*, 63-66.
28. Jensen, E. C., Quantitative analysis of histological staining and fluorescence using ImageJ. *Anat. Rec.* **2013**, *296* (3), 378-381.
29. Derveaux, S.; Vandesompele, J.; Hellemans, J., How to do successful gene expression analysis using real-time PCR. *Methods* **2010**, *50* (4), 227-230.
30. Taylor, S.; Wakem, M.; Dijkman, G.; Alsarraj, M.; Nguyen, M., A practical approach to RT-qPCR-Publishing data that conform to the MIQE guidelines. *Methods* **2010**, *50* (4), S1-S5.
31. VanGuilder, H. D.; Vrana, K. E.; Freeman, W. M., Twenty-five years of quantitative PCR for gene expression analysis. *Biotechniques* **2008**, *44* (5), 619-626.
32. Schmittgen, T. D.; Livak, K. J., Analyzing real-time PCR data by the comparative C-T method. *Nat. Protoc.* **2008**, *3* (6), 1101-1108.

Chapter 3

siRNA RELEASE: MECHANISTIC UNDERSTANDING AND SPATIOTEMPORAL CONTROL

This chapter describes a procedure for spatiotemporally controlling protein knockdown, methods for understanding the mechanisms that govern polyplex stability and siRNA release, and the development of a simple kinetic model to predict gene silencing. The text, equations, tables, and figures in this chapter are adapted and reprinted with permission from Greco, C. T.; Epps, T. H., III; Sullivan, M. O., Mechanistic design of polymer nanocarriers to spatiotemporally control gene silencing. *ACS Biomater. Sci. Eng.* 2016, 2 (9), 1582-1594. Copyright 2016 American Chemical Society.

3.1 Introduction

Improved methods to enable spatiotemporal control over gene expression are necessary to overcome fundamental challenges that hinder biomedical research and therapeutics.^{1,2} More broadly, control over gene activity in space and time would address common problems in drug delivery including low efficacy and toxic side effects in off-target cells or organs.³ To meet these needs, polymer nanostructures have enormous potential to regulate gene expression by controlling cellular exposure to nucleic acids such as small interfering RNAs (siRNA)s. The ability to spatiotemporally control gene expression through siRNAs will overcome significant challenges associated with inducible promoter systems and optogenetic regulators of transcription, which represent the primary control approaches to date.⁴⁻⁸ These tools

have numerous drawbacks including off-target effects,² limited capacity to regulate endogenous genes,⁹ safety concerns such as immunogenicity and mutation/oncogene activation,¹⁰ and difficulties in delivering multi-component assemblies.¹¹ Meanwhile, siRNA has enormous inherent advantages in practical/therapeutic application through its clinically-demonstrated safety profile¹² and capacity to harness the endogenous gene regulatory machinery using a simple, one-component construct. Hence, materials able to control siRNA delivery/activation in space and time would unlock an easily translatable platform for a wide range of new embryonic development, drug discovery, and regenerative medicine technologies.

While multiple approaches to control siRNA transfer have been explored, methods to spatially constrain activation through regulation of siRNA binding *vs.* release mimic nature's strategies for gene regulation within chromatin and have particular appeal from an application standpoint. Such methods would avoid practical challenges in controlling extracellular nanocarrier diffusion that have reduced the precision of previous approaches to administer nucleic acid cargoes selectively, to certain cell subpopulations.^{13, 14} In particular, materials approaches employing responsive polymers would offer a unique opportunity to study and regulate the multivalent binding interactions that govern stability in polyplexes, which are a pivotal determinant of siRNA activity and efficacy in long-term applications.¹⁵⁻¹⁹ The insights gained from such studies would inform new polymer design frameworks with enhanced activity, while also improving the capacity to accurately predict gene silencing.

Herein, tailorable mPEG-*b*-poly(5-(3-(amino)propoxy)-2-nitrobenzyl methacrylate) [mPEG-*b*-P(APNBMA)] block copolymers (BCP)s²⁰ were used to

develop a mechanistic understanding of how nanocarrier stability defines intracellular siRNA activity. The polymer nanostructures were able to maintain siRNA dormancy, through stable binding and sequestration, prior to application of the photo-trigger.²¹ Additionally, precisely tuned siRNA release could be quantified, and therefore, used to predict gene silencing using simple kinetic modeling. The polymers are comprised of cationic and nonfouling blocks, the structure of which enables unusually stable nucleic acid binding, even in the presence of serum, and encapsulation within nanoscale electrostatic complexes (polyplexes) surrounded by a “stealth” coating. Furthermore, light-responsive materials offer numerous advantages such as highly localized application with minimal diffusive effects, rapid response times, tailorable dosage control, and ease of use.²²⁻²⁶ Thus, the specific photo-triggered unpackaging mechanism of this system makes it ideal for probing fundamental questions in material design leading to improved dynamic control over siRNA activity.

Notably, this photo-responsive polymer was used to demonstrate precise and highly efficient on/off spatial control of protein silencing, with single cell resolution in murine fibroblasts and terminally differentiated human primary fibroblasts. The polyplexes facilitated photo-controlled knockdown of both the exogenous green fluorescent protein (GFP) gene and the endogenous glyceraldehyde-3-phosphate dehydrogenase (GAPDH) gene, with mRNA silencing that was tunable over a range of 0% to 86%, demonstrating excellent potential versatility in controlling a range of gene targets. Moreover, maximal gene silencing was achieved using concentrations of siRNA five-fold lower than typical formulations due to the ability to rapidly release sufficient amounts of siRNA to saturate the cellular RNA-induced silencing complex (RISC) machinery. Specifically, the link between siRNA release and RISC saturation

was identified through the development of a simple reaction rate model incorporating polymer-siRNA release kinetics, which demonstrated that polymer-siRNA unbinding using the photo-responsive construct was not the rate limiting step in gene silencing. Moreover, advanced bioimaging techniques such as fluorescence correlation spectroscopy (FCS) and Förster resonance energy transfer (FRET) were used to monitor intracellular polyplex stability and correlate experimentally-measured siRNA release kinetics with model parameters. These methods further verified that variations in gene knockdown were related directly to light-induced changes in polyplex structure and the extent of siRNA release into the cytoplasm. Thus, this work highlights the ability to define gene silencing with high resolution and a wide dynamic range, and this approach is combined with tunable gene silencing predicted by kinetic modeling to address critical questions regarding polymer nanostructures and nucleic acid delivery.

3.2 Materials and Methods

3.2.1 Materials

The mPEG-*b*-P(APNBMA)_{23.6} polymer ($M_n = 13,100 \text{ g mol}^{-1}$) was synthesized *via* atom-transfer radical polymerization as described previously.²⁰ All siRNA molecules were obtained purified and pre-annealed from GE Healthcare Dharmacon, Inc. (Chicago, IL). ON-TARGETplus siRNAs (anti-GAPDH and non-targeted) were used as received. Custom-made siRNA (both Dy547- and Dy647-labeled) were designed to target GAPDH and were terminally modified with 5'-P and a single fluorophore (sense: 5' Dy547/Dy647-GUGUGAACACGAGAAUAUU 3'; antisense: 5'-P-UAUUUCUCGUGGUUCACACUU 3'). Primers were purchased from

Eurofins MWG Operon (Huntsville, AL) and had the following sequences: GAPDH forward 5' CGGGTTCCTATAAATACGGACTGC 3'; GAPDH reverse 5' CCCAATACGGCCAAATCCGT 3'; β -actin forward 5' CTGTCGAGTCGCGTCCA 3'; β -actin reverse 5' TCATCCATGGCGAACTGGTG 3'. The anti-GAPDH and the secondary HRP antibodies for western blotting were ordered from AbCam (Cambridge, MA). The anti-actin antibody was purchased from Santa Cruz Biotechnology (Dallas, TX). The iTaqTM Universal SYBR[®] Green One-Step Kit and optical flat 8-cap strips were purchased from Bio-Rad (Hercules, CA). A bicinchoninic acid (BCA) protein assay kit and bovine serum albumin (BSA) were obtained from Pierce (Rockford, IL). SuperSignalTM West Dura Chemiluminescent Substrate, Opti-MEM[®] media and TRIzol[®] Reagent were purchased from Thermo Fisher Scientific (Waltham, MA). Lipofectamine 2000, Lipofectamine RNAiMAX, and Silencer[®] GFP siRNA were obtained from Life Technologies (Grand Island, NY). Dulbecco's modification of Eagle's medium (DMEM) and PBS (150 mM NaCl) solutions were purchased from Corning Life Sciences – Mediatech Inc. (Manassas, VA). All other cell culture reagents were purchased from Thermo Fisher Scientific (Waltham, MA).

3.2.2 Preparation of siRNA/mPEG-*b*-P(APNBMA) nanocarrier

Polyplexes were formed using a self-assembly method *via* solution mixing followed by vortexing for 30 s. Solutions of siRNA were prepared at 32 $\mu\text{g ml}^{-1}$ in 20 nM 4-(2-hydroxyethyl)piperazine-1-ethanesulfonic acid (HEPES) buffer at pH 6.0 in plastic microcentrifuge tubes. Polymer solutions containing the appropriate amount of mPEG-*b*-P(APNBMA)_{23,6} also were made with equal volumes (same volumes as siRNA solutions). The polymer solutions were added to the siRNA solutions (pipetted

over 3 s while vortexing the entire solution) to form polyplexes at an N/P ratio (N: amine groups on mPEG-*b*-P(APNBMA), P: phosphate groups on siRNA) of 4. Following vortexing for 30 s, the formulations were incubated at room temperature, in the dark, for 20 min before analyses. *Note: While vortexing, ensure that the solution stably rotates around the microcentrifuge tube (does not randomly fly around the tube).*

3.2.3 Cell culture

Mouse embryonic fibroblasts (NIH/3T3) were obtained from the American Type Culture Collection (ATCC), Manassas, VA). The cells were cultured following ATCC protocols in DMEM supplemented with 10 vol% fetal bovine serum (FBS) and 1 vol% penicillin-streptomycin. Human aortic adventitial fibroblasts (AoAF) were obtained from Lonza (Walkersville, MD) and cultured following Lonza protocols in stromal cell basal medium supplemented with the SCGM SingleQuot Kit. Both cell types were cultured at 37 °C in a humidified atmosphere with 5 vol% CO₂.

3.2.4 *In vitro* cell transfection

NIH/3T3 cells were seeded in six-well plates at a density of 10,000 cells cm⁻² and allowed to adhere and recover for 24 h. Growth medium was removed, PBS was added during a wash step, and Opti-MEM® reduced serum media was added to the plates. Polyplex solutions were added to the wells at the desired final siRNA molar concentrations and incubated for 3 h before being replaced with fully supplemented growth medium. For transfections with 365 nm light treatment, the cells were incubated for 20 min prior to replacing the growth medium with Opti-MEM® without phenol red. Samples were placed on a 37 °C hot plate and irradiated for the specified

length of time by 365 nm light at an intensity of 200 W m^{-2} . Subsequently, fully supplemented growth medium was added to the well for the remainder of the culture period.

3.2.5 Spatiotemporal control over gene silencing

NIH/3T3 and AoAF cells were seeded in six-well plates and transfected with gWiz GFP plasmid DNA (pDNA) (Genlantis, San Diego, CA) using Lipofectamine 2000 according to the manufacturer's protocols and Silencer® GFP siRNA/mPEG-*b*-P(APNBMA) polyplexes simultaneously. Control samples not treated with GFP-targeted siRNA also were included. A photomask composed of aluminum foil and black paper was used to block half of the well from 365 nm light, and the cells were irradiated from underneath the plate for 20 min or 10 min, for NIH/3T3 or AoAF cells, respectively. The cells were imaged 48 h post-transfection on a Leica 6000 fluorescence microscope (Wetzlar, Germany).

3.2.6 GAPDH protein knockdown

Gene silencing was monitored at the protein expression level by western blot analyses. Transfections were carried out as described with anti-GAPDH siRNA while varying the irradiation time, and the cells were cultured for 48 h post-transfection. Protein was extracted by incubating the cells in a lysis solution composed of 0.5 vol% Triton X-100, 0.5% sodium deoxycholate, 150 mM NaCl, 5 mM Tris-HCl (pH 7.4), 5 mM EDTA, and 1x Halt Protease and Phosphatase Inhibitor cocktail. The total protein concentration of each sample was measured using a BCA Protein Assay Reagent Kit. Equal amounts of protein were subjected to 4% - 20% sodium dodecyl sulfate polyacrylamide gel electrophoresis (SDS-PAGE) for 35 min at 150 V.

Subsequently, the protein was transferred onto a poly(vinylidene fluoride) membrane for 70 min at 20 V. The membrane was blocked in 5 vol% BSA in Tris–HCl-buffered saline (50 mM Tris–HCl, pH 7.4, 150 mM NaCl) containing 0.1 vol% Tween 20 (TBST) at room temperature for 1 h. The membrane was incubated with an anti-GAPDH rabbit monoclonal IgG primary antibody ($0.5 \mu\text{g mL}^{-1}$ in TBST) and an anti-actin rabbit polyclonal IgG ($0.3 \mu\text{g mL}^{-1}$ in TBST) at 4 °C overnight. The next day, the membrane was incubated with a solution of goat anti-rabbit polyclonal IgG antibody conjugated to horseradish peroxidase (HRP) ($0.4 \mu\text{g mL}^{-1}$ in TBST) at room temperature for 1 h. Target proteins were visualized with the SuperSignal™ West Dura Chemiluminescent Substrate. The band intensity of each target protein was quantified using ImageJ software.²⁷

3.2.7 GAPDH mRNA knockdown

siRNA-mediated GAPDH knockdown was measured at the mRNA expression level using quantitative PCR (qPCR). Transfections were carried out as described while varying the irradiation time, and the cells were cultured for 24 h post-transfection. Total RNA was isolated by TRIzol® Reagent according to the manufacturer's protocols. The iTaq™ Universal SYBR® Green One-Step Kit and the specific GAPDH and β -actin primers were used to prepare samples in triplicate as described in the manufacturer's protocols. The cDNA synthesis and qPCR steps were conducted on a Bio-Rad CFX96™ using the following conditions: 10 min at 50 °C; 1 min at 95 °C; 40 cycles of 10 s at 95 °C and 30 s at 60 °C, and finally a 65 °C to 95 °C ramp at 0.5 °C increment steps every 5 s. The $\Delta\Delta\text{CT}$ method was used for fold change analysis,²⁸ and all test sample data were normalized to untreated cell data.

Details related to the $\Delta\Delta\text{CT}$ method are described in Chapter 2 (section 2.7), and an example calculation is shown in Table A.1 in Appendix A.

3.2.8 Characterizing siRNA release

Polyplex formation and the extent of siRNA release were investigated using gel electrophoresis and FCS. After polyplex formulation with Dy547-labeled siRNA, solutions containing sodium dodecyl sulfate (SDS) were added to the polyplexes at the appropriate S/P, and the resulting solutions were incubated at room temperature for 30 min. These samples were loaded into a chamber of two glass slides and a rubber gasket and subsequently exposed to 365 nm light at an intensity of 200 W m^{-2} for the specified duration of time. The polyplex solutions were incubated for 30 min before analysis. For gel electrophoresis, 6x loading dye (3:7 (v/v) glycerol:water) was added to a portion of the polyplex solutions. These samples were loaded into the wells of a 2 wt% agarose gel containing $0.5 \mu\text{g mL}^{-1}$ ethidium bromide. Gels were run at 100 V for 30 min before imaging on a Bio-Rad Gel Doc XR. The band intensity of each sample was quantified with the aid of ImageJ software. For FCS, polyplex solutions were placed on cover slips, which then were attached to a microscope glass slide by SecureSeals from Life Technologies (Grand Island, NY). FCS measurements were performed on an LSM 780 confocal microscope (Carl Zeiss, Oberkochen, Germany) using a 488 nm laser and a 40x (numerical aperture = 1.2) water immersion apochromat objective. Thirty measurements, each lasting 10 s, were taken for each sample. Data analysis was performed with ZEN 2010 software (Carl Zeiss). The structural and measurement parameters were determined using a solution of AlexaFluor555 dye with an assumed diffusion coefficient of $340 \mu\text{m}^2 \text{ s}^{-1}$. The percent of siRNA release was computed using the assay developed by Buyens *et al.*²⁹ Briefly,

the baseline count rate of every solution was measured (while keeping the siRNA concentration constant) using FCS. The amount of siRNA released was computed according to equation 2.11 (see Chapter 2).

3.2.9 FRET efficiencies in aqueous solutions

Polyplexes were formulated as described with equal molar ratios of Dy547- and Dy647-labeled siRNA. Following the described light treatment procedure detailed above, polyplex solutions were loaded into cuvettes. The fluorescence signal was measured by a Fluoromax-4 fluorescence spectrophotometer (Horiba, Kyoto, Japan) using an excitation wavelength of 488 nm and detecting the emission spectrum from 525-750 nm. The results are reported as the average fluorescence ratios of three independent samples for each irradiation time, and the emission spectra were normalized and overlaid for visual clarity. The raw values for the fluorescence ratios are reported in Table A.2 in Appendix A.

3.2.10 FRET: flow cytometry

Polyplex stability in cells was analyzed by measuring fluorescence using flow cytometry. Cells were seeded for transfection as described above. Polyplex solutions were formed with equal molar ratios of Dy547- and Dy647-labeled siRNA to measure FRET. Formulations containing unlabeled or single-labeled siRNA also were used as controls to account for signal bleed-through. After a 3 h incubation with 20 nM siRNA, the cells were washed with a PBS solution containing $10 \mu\text{g ml}^{-1}$ heparin to remove extracellular polyplexes.³⁰ The samples were irradiated with 365 nm light and subsequently allowed to recover in fully supplemented growth medium for 30 min. Next, the cells were collected for analysis following standard trypsin-mediated

protocols. After resuspension in PBS, the cells were passed through a 35 μm nylon mesh filter to remove aggregates and stored at 4 $^{\circ}\text{C}$ until analysis. Flow cytometry measurements were obtained on a BD FACSAriaII (BD Biosciences, San Jose, CA) approximately 5 h post-transfection, and at least 15,000 live cells were analyzed per sample. The phycoerythrin (PE)-Texas Red filter set (excitation: 488 nm, emission: 710 nm) was used to measure the FRET signal, and the PE filter set (excitation: 488 nm, emission: 575 nm) and allophycocyanin (APC) filter set (excitation: 633 nm, emission: 670 nm) were used to measure fluorescence signals from Dy547 and Dy647, respectively. Data analysis was performed using FlowJo software. To account for signal bleed-through in the PE-Texas Red fluorescence intensity, a compensation matrix was used such that the median fluorescence of the control samples was equal to the autofluorescence signal from transfected cells (see section 2.4 for more details and Figure A.1 in Appendix A for matrix values).

3.2.11 FRET: confocal microscopy

The stability and distribution of polyplexes in cells were visualized using confocal microscopy. Cells were plated on cover slips in six-well plates using the described transfection protocol. Polyplex solutions were formulated using equal molar ratios of Dy547- and Dy647-labeled siRNA. Following 365 nm light treatment, the cover slips were attached to a microscope glass slide containing live cell imaging media by SecureSeals and kept at 37 $^{\circ}\text{C}$ until analysis. Imaging was performed on the confocal microscope as described above with emission channels of 525-630 nm and 661-758 nm used for the Dy547 and Dy647 fluorescence signals, respectively. These channels were optimized to remove any detectable signal bleed-through using unlabeled and single-labeled siRNA control samples. The images were processed

using ZEN 2010 software and quantified using Volocity imaging software (PerkinElmer, Waltham, MA). The Manders' colocalization coefficient was computed to estimate the fraction of polyplexes undergoing FRET. A total of 30 cells per sample were chosen randomly for quantification purposes.

3.2.12 Intracellular FCS

Intracellular polyplex diffusion characteristics and siRNA release were analyzed using FCS. Cells were seeded on cover slips in six-well plates, and Dy547-labeled siRNA polyplexes were delivered following the described transfection protocol. After the samples were treated with 365 nm light, the coverslips were attached to glass slides in live cell imaging media using SecureSeals and incubated at 37 °C. FCS measurements were performed on the confocal microscope as described above. At least fifty measurements of 10 s each were taken for each sample. Autocorrelation and data analyses were performed with ZEN 2010 software. The structural and measurement parameters of the instrument were determined using a solution of AlexaFluor555 dye and assuming a diffusion coefficient of $340 \mu\text{m}^2 \text{s}^{-1}$ (for calibration).³¹

3.3 Results and Discussion

3.3.1 Spatiotemporal control over gene silencing

One of the most common shortcomings in siRNA delivery vehicles, particularly in applications requiring well-defined spatiotemporal modulation of gene expression, is the lack of control over siRNA binding and release leading to off-target effects and/or inefficient siRNA utilization.³² This issue was addressed through photo-responsive siRNA polyplexes (Figure 3.1A) that led to patterned silencing of a

gene that has a visible (fluorescent) signal. NIH/3T3 cells were induced to express GFP through plasmid transfection with Lipofectamine 2000, and anti-GFP siRNAs were delivered simultaneously to the cells using mPEG-*b*-P(APNBMA). Subsequently, a photomask was applied to limit the light exposure to only a portion of the cell population. As shown in Figure 3.1B, when an annular photomask was applied, NIH/3T3 cells that were irradiated with biocompatible dosages of light^{21, 33} displayed extremely low levels of GFP expression, which indicated that the polyplexes released sufficient amounts of siRNA to cleave nearly all of the GFP transcripts. Conversely, NIH/3T3 cells that were completely protected from irradiation exhibited robust GFP expression that was comparable to controls (no siRNA treatment, Figure 3.1C), suggesting that the GFP-targeted polyplexes remained completely dormant in the absence of light.

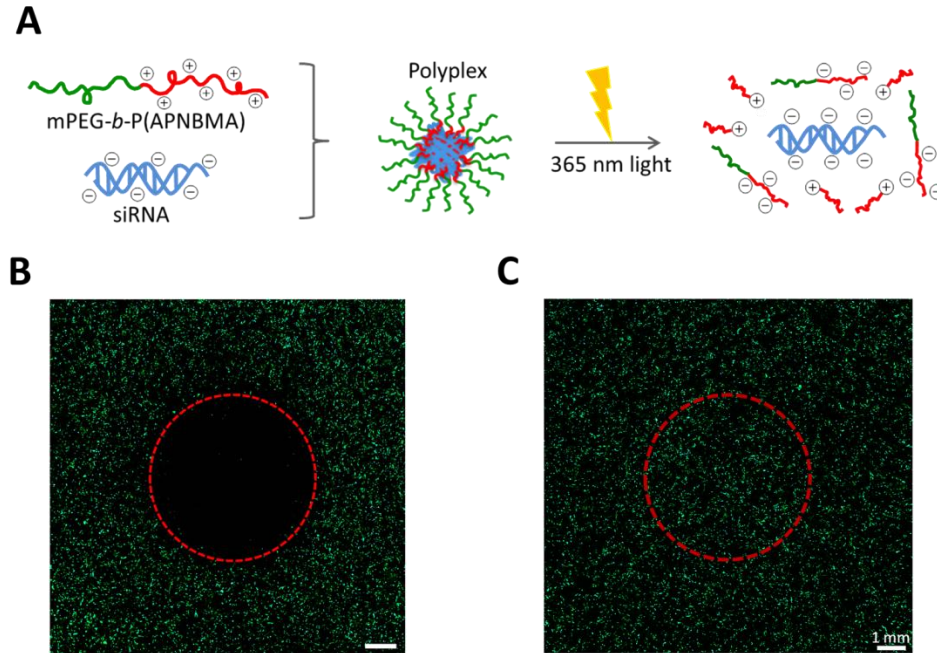


Figure 3.1: On/off spatiotemporal control over nanocarrier disassembly to modulate expression of an exogenous gene. (A) Schematic of polyplex self-assembly and light-induced polymer charge reversal to release the siRNA. (B and C) Wide-field view of circular patterning in GFP expression. Cells were transfected with (B) GFP pDNA/Lipofectamine 2000 lipoplexes and GFP-targeting siRNA/mPEG-*b*-P(APNBMA) polyplexes or (C) GFP pDNA/Lipofectamine 2000 lipoplexes and no siRNA. A circular photomask was applied prior to 20 min of 365 nm light irradiation. The dashed red line represents the edge of the photomask, and the scale bars represent 1 mm and apply to both images.

To examine the resolution and versatility of the technique, a line-pattern was generated, and GFP expression was monitored on a cellular length scale (Figure 3.2A). Similar to the results with the annular photomask, GFP expression in cells protected from the photo-stimulus was comparable to controls with no siRNA treatment (Figure 3.2B), and there was essentially no detectable GFP expression on the side of the plate treated with light. Furthermore, a well-defined boundary between GFP-expressing

and silenced cells was visible in the center of the plate with cell-level resolution, which is crucial for generating complex tissue constructs with controlled intracellular regenerative responses.²⁶ Notably, cells treated with non-targeted siRNA and 365 nm light for 20 min remained fluorescent, ruling out non-specific silencing or adverse effects from polyplex delivery and irradiation (Figure 3.2C).

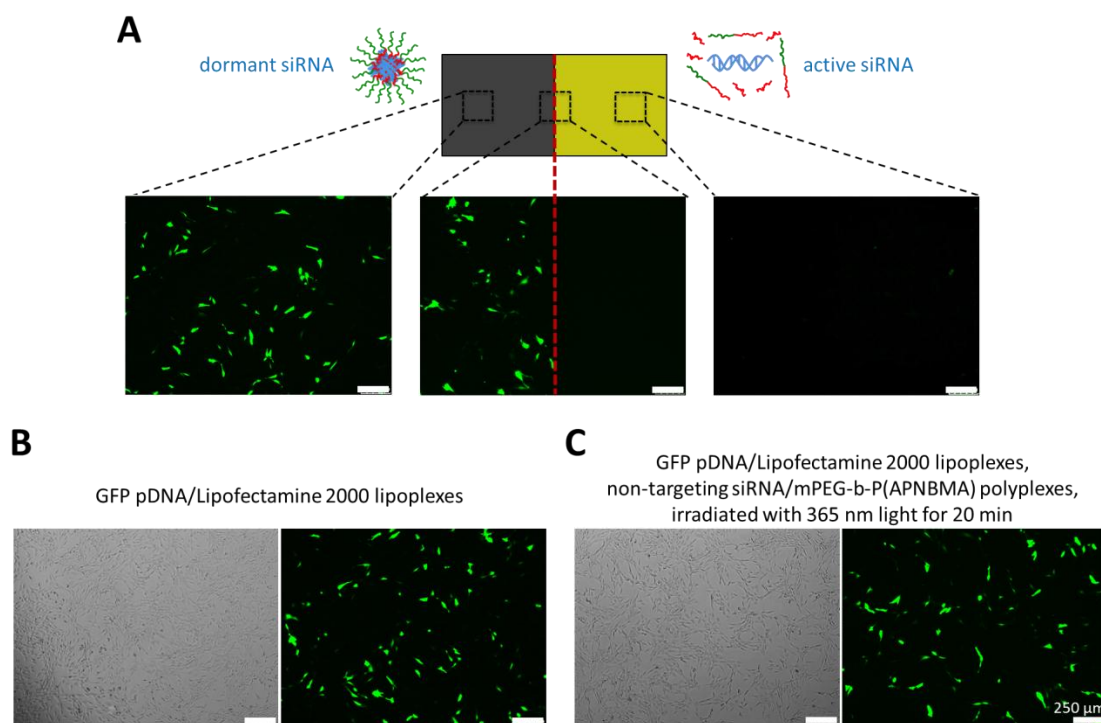


Figure 3.2: Zoomed-in view of line-patterning of GFP expression with cell-to-cell resolution. (A) NIH/3T3 cells were co-transfected with pDNA/Lipofectamine 2000 and GFP-targeting siRNA/mPEG-*b*-P(APNBMA), and half of the plate was covered with a photomask prior to 20 min of 365 nm light irradiation. (B and C) Phase contrast microscopy (left) and fluorescence microscopy (right) images of NIH/3T3 cells. (B) Cells were treated with GFP pDNA/Lipofectamine 2000 lipoplexes and no siRNA or (C) GFP pDNA/Lipofectamine 2000 and non-targeting siRNA/mPEG-*b*-P(APNBMA) and irradiated with 365 nm light for 20 min. The scale bars represent 250 μm and apply to all images.

While the ability to regulate gene expression in murine fibroblasts was promising, typical applications in regenerative medicine require human primary cells, which can be much more refractory to gene modulation approaches than most cell lines.³⁴ Accordingly, light-mediated control over GFP silencing was demonstrated in human aortic adventitial fibroblasts (AoAF)s, a mesenchymal cell type relevant to a range of tissue repair applications and often resistant to transfection.^{35, 36} Using analogous treatment approaches to those used in murine cells, the nearly complete knockdown of GFP expression upon application of the photo-stimulus in AoAFs (Figure 3.3) was demonstrated. The controlled gene silencing in these human primary fibroblasts demonstrates the versatility of the materials and methods for the regulation of siRNA exposure. Furthermore, it indicates that the technique can be applied directly to cell types relevant to tissue engineering and cell microarray applications without the typical cytotoxic responses seen with many commercial carriers.^{35, 37, 38}

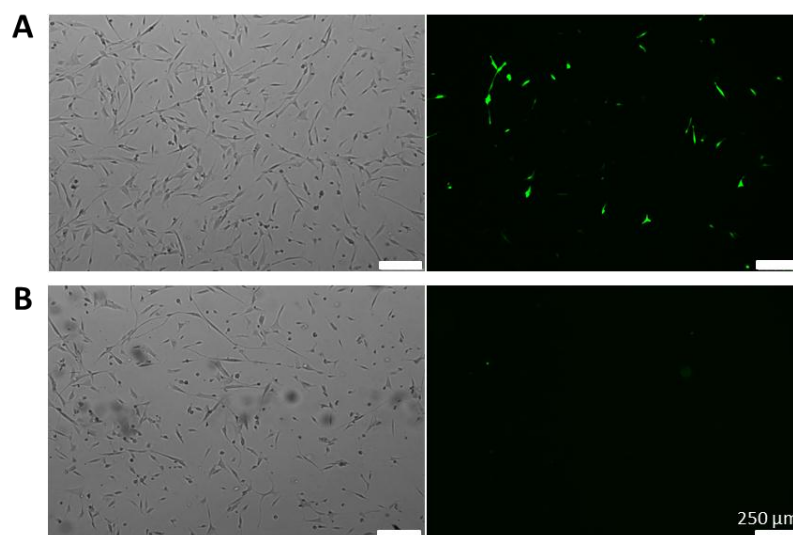


Figure 3.3: On/off spatiotemporal control over expression of an exogenous gene in human aortic adventitial fibroblast (AoAF) cells using mPEG-*b*-P(APNBMA) polyplexes. Phase contrast microscopy (left) and fluorescence microscopy (right) images were taken 24 h post-transfection. Cells were co-transfected with GFP DNA and GFP-targeting siRNA and either (A) covered with a photomask or (B) left unmasked. The covered and unmasked cells were exposed to 10 min of 365 nm light irradiation. The scale bars represent 250 μm and apply to all images.

3.3.2 Tuning gene silencing through light dosage and concentration effects

In addition to controlling gene expression in an on/off manner, nanocarriers also should be able to induce a wide range of gene silencing efficiencies to mimic native gene expression gradients. To demonstrate tunable gene silencing, the responses of transfected cells upon the application of various dosages of light were examined. Polyplexes were delivered to NIH/3T3 cells, and GFP and GAPDH were used as the model exogenous and endogenous gene targets, respectively. After a 3 h incubation with 20 nM siRNA polyplexes, the cells were exposed to 365 nm light for different times, and changes in GFP and GAPDH protein expression levels were

measured 48 h post-transfection. As shown in Figure 3.4A, no significant change in GFP expression was noted in the absence of light, which confirmed the stability and dormancy of the polyplexes reported previously.²¹ Increased light dosages resulted in significant decreases in the cellular fluorescent intensities with <1% of the original fluorescence signal detectable following 10 min of light treatment (Figure 3.4B). Tunable gene silencing also was examined for the model endogenous gene GAPDH due to its ubiquitous nature and housekeeping functions. As shown in Figure 3.4C, cells that were not exposed to the photo-stimulus did not exhibit protein knockdown. Moreover, polyplex dormancy was sustained over incubation times up to 96 h post-transfection (Figure 3.4D), demonstrating the low probability for off-target release. The enhanced stability of the nanocarriers could be due to the hydrophobic groups in the cationic block that provide additional binding interactions to stabilize the siRNA polyplexes. In fact, hydrophobic modification of cationic polymers is a common strategy in the literature for improving polyplex stability in polyanion-rich environments such as serum.^{20, 39} Upon application of light, polyplexes stimulated significant gene silencing, and the extent of knockdown, as determined by GAPDH protein expression levels, ranged from 0% to 70% depending upon the duration of irradiation. Control experiments ruled out any significant effects on cell viability²¹ and GAPDH gene expression mediated solely by light exposure (Figure 3.4E), demonstrating that gene silencing was target-specific and occurred through utilization of the RNAi machinery.

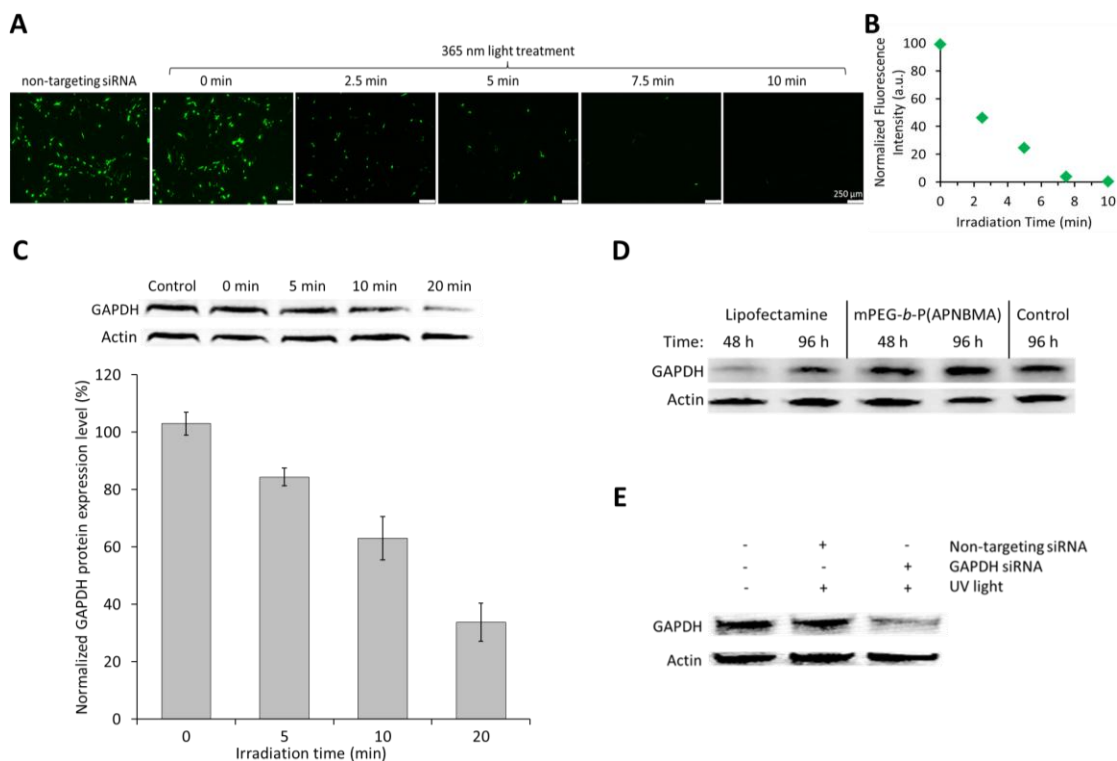


Figure 3.4: Tunable protein silencing of model exogenous and endogenous genes in NIH/3T3 cells. (A) A panel of representative microscopy images of GFP expression in cells following treatment with GFP-targeting siRNA/mPEG-*b*-P(APNBMA) polyplexes and exposure to 365 nm light for varying lengths of time. The scale bars represent 250 μ m and apply to all images. (B) The overall intensities of representative fluorescence microscopy images (panel A) were quantified using ImageJ software, and values were normalized to the intensity of cells that were not treated with GFP-targeted siRNA. (C) Representative western blot analyses and quantification of GAPDH protein expression levels as a function of irradiation time. Cells were treated with 20 nM siRNA polyplexes and subsequently exposed to 365 nm light for varying lengths of time. Data represent the GAPDH protein expression levels relative to the levels of the loading control β -actin, normalized to the native protein levels in controls with no siRNA treatment. Results are shown as the mean \pm standard deviation of data obtained from three independent experiments. (D) Western blot analysis of GAPDH protein knockdown using extended incubation periods (48 h or 96 h) prior to cell lysis. Cells were treated with GAPDH-targeting siRNA that was packaged with mPEG-*b*-P(APNBMA) or Lipofectamine RNAiMAX. (E) Western blot analysis of GAPDH protein knockdown following treatment with mPEG-*b*-P(APNBMA) polyplexes and irradiation for 20 min.

Delivery systems capable of maximizing silencing and inducing robust protein knockdown would be beneficial for many applications in the patterning of gene expression. To test if more than 70% GAPDH protein silencing was possible, siRNA concentrations were increased from 20 nM to 40 nM while keeping the irradiation time constant at 20 min. Cells treated with 40 nM siRNA polyplexes showed uptake of >50% more polyplexes than cells treated with 20 nM siRNA (Figure 3.5A and 3.5B), as indicated by flow cytometry analyses. Despite the enhanced cellular uptake, no further improvement in GAPDH protein knockdown was achieved (Figure 3.5C). Also, it is noteworthy that the polyplexes exhibited no silencing in the absence of light, even at the elevated concentrations, confirming that the polyplexes remained fully intact and dormant without a stimulus. Such control over siRNA activity using light demonstrates that these nanocarriers have the potential to reduce undesired side effects in off-target cells, which is a key challenge in the clinical implementation of nucleic acid therapies.³

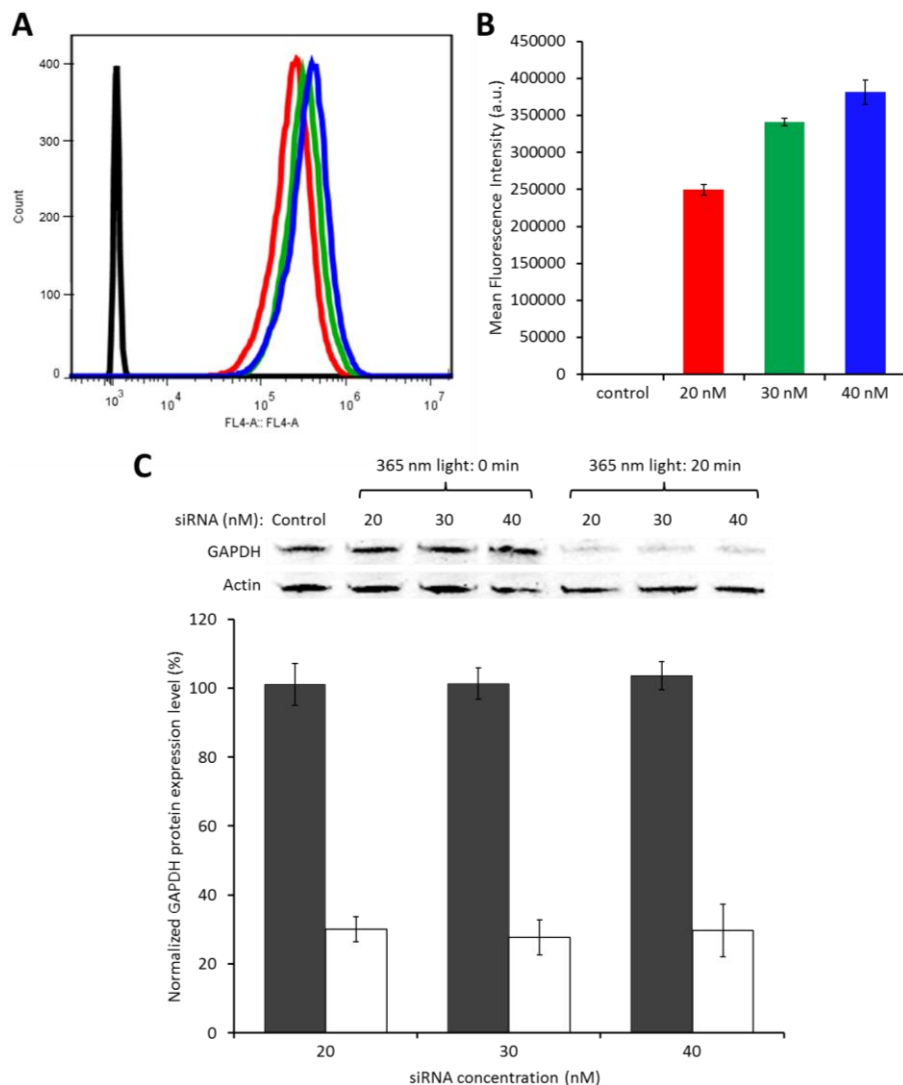


Figure 3.5: Cellular uptake and gene silencing efficiencies of mPEG-*b*-P(APNBMA) polyplexes over a range of siRNA concentrations. (A) Cells were incubated in polyplex solutions formulated with Dy647-labeled siRNA at concentrations of 0 nM (black), 20 nM (red), 30 nM (green), or 40 nM (blue) siRNA, and cellular fluorescence was measured using flow cytometry. (B) The mean fluorescence intensity per cell (from panel A) was computed. (C) Cells were treated with varying siRNA polyplex concentrations and subsequently exposed to 365 nm light for 0 min (dark gray bars) or 20 min (white bars). Data represent the GAPDH protein expression levels relative to the levels of the loading control β -actin, normalized to the native protein levels in controls with no siRNA treatment. Results are shown as the mean \pm standard deviation of data obtained from three independent experiments.

As detailed below, the lack of measurable enhancement in protein knockdown after the internalization of more siRNA (Figure 3.5C) is most likely due to the relatively long half-life of the GAPDH protein, reported to be >35 h in NRK-52E rat kidney epithelial cells.⁴⁰ Even if the RNAi pathway were 100% efficient and the released siRNA cleaved all available GAPDH mRNAs, pre-existing protein would not be completely degraded and cleared by cells at 48 h post-transfection; i.e. the time western blot analyses were started. Additionally, another study delivering siRNA targeting GAPDH found ~70% protein knockdown to be the maximum level achievable after 48 h in H1299 human lung carcinoma cells,⁴¹ which agrees with the maximum silencing achieved in this work. Furthermore, previous experiments have shown that RISC assembly is saturable by excessive free siRNA.⁴² The duration of this state is determined by the intracellular siRNA concentration, which directly depends on siRNA stability and dilution effects due to cell division and growth.⁴³ RNAi effects have been shown to last for only a few days before recovering to pre-treatment levels in rapidly-dividing cell lines, such as NIH/3T3 cells, with minimum protein levels often found approximately 48 h post-transfection.⁴⁴

A complementary and more direct method for monitoring siRNA-mediated gene silencing is to measure the mRNA expression levels through qPCR. As the intracellular half-life of GAPDH mRNA is ~8 h,⁴⁵ mRNA levels were measured to determine if changes in these levels would capture the true extent of silencing. After transfection, cells were lysed and prepared for qPCR quantification 24 h post-transfection to ensure that the mRNA levels were measured before they started to recover due to siRNA dilution after cell division. Similar to the protein analyses, no silencing was exhibited in cells without light treatment, but the degree of mRNA

knockdown increased with irradiation time (Figure 3.6A). Furthermore, the apparent extent of silencing after 20 min of irradiation increased such that only ~14% GAPDH mRNA remained at 24 h post-transfection. Because the cells were lysed ~3 mRNA half-lives after the introduction of siRNA, the maximum amount of silencing is expected to result in ~13% remaining mRNA, which is consistent with the data and supports the hypothesis that the RNAi pathway was utilized fully. Moreover, the level of mRNA knockdown after 20 min light irradiation did not change significantly while increasing the siRNA concentration, which is consistent with the protein expression data and further suggests that RISC assembly was saturated by excess siRNAs (Figure 3.6B).

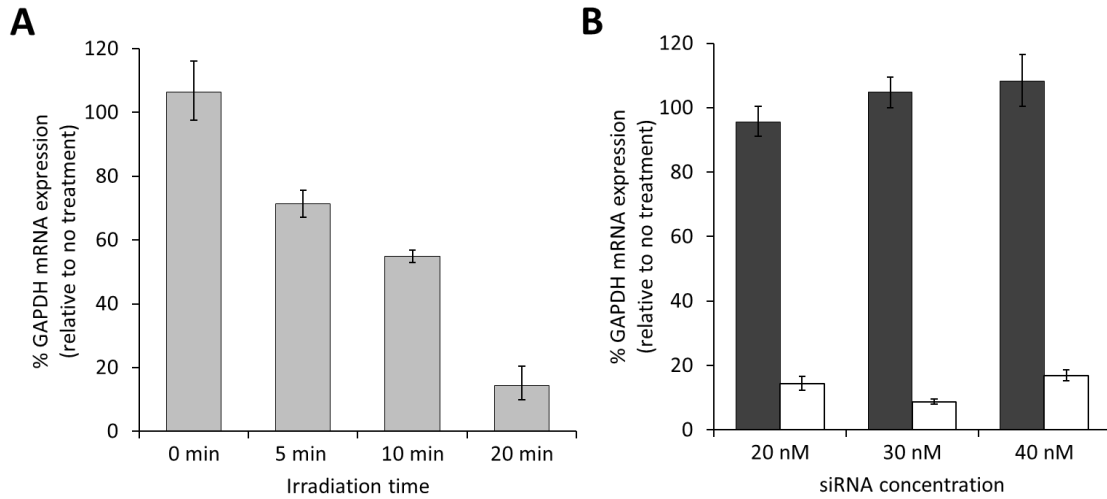


Figure 3.6: qPCR analyses of GAPDH mRNA silencing as a function of irradiation time and siRNA concentration. (A) Cells were treated with 20 nM siRNA polyplexes and then exposed to 365 nm light for varying lengths of time. (B) Cells were treated with varying siRNA polyplex concentrations and then exposed to 365 nm light for 0 min (dark gray bars) or 20 min (white bars). Data represent the GAPDH mRNA expression levels relative to β -actin mRNA levels, normalized to the native levels in controls with no treatment siRNA treatment. Results are reported as the mean \pm standard deviation of data obtained from three independent replicates.

3.3.3 Modeling the gene silencing process

To generate a more detailed profile of the dynamic nature of the RNAi reactions, a non-compartmentalized kinetic model of the system (Equations 3.1-3.3) was developed, consisting of terms accounting for synthesis (mRNA and protein), degradation (mRNA, protein, and siRNA), siRNA-catalyzed mRNA turnover, and siRNA dilution effects due to cell division. Specifically, a set of ordinary differential equations was used to model the changes in concentrations of mRNA, protein, and siRNA as a function of time. The terms k_{mRNA} , k_{siRNA} , and k_{prot} are the rate constants for the production of mRNA, siRNA, and protein, respectively. The terms $k_{\text{m,deg}}$,

$k_{s,deg}$, and $k_{p,deg}$ are the rate constants for the degradation of mRNA, siRNA, and protein, respectively. Degradation rate constants were computed on the basis of the component half-lives reported in literature,^{40, 44, 45} and production rate constants were fit to ensure that mRNA and protein steady-state values were reached in the absence of siRNA.

$$\frac{d[mRNA]}{dt} = k_{mRNA}[DNA] - k_{m,deg}[mRNA] - k_{siRNA}[siRNA] \quad (3.1)$$

$$\frac{d[protein]}{dt} = k_{prot}[mRNA] - k_{p,deg}[prot] \quad (3.2)$$

$$\frac{d[siRNA]}{dt} = -k_{s,deg}[siRNA] \quad (3.3)$$

The simplified system of equations considers only the most important, rate-determining processes and was designed to capture changes in protein and mRNA levels induced through RNAi effects averaged across the entire cell population. The model predictions confirmed that the relatively long half-lives, which govern the degradation of GAPDH protein and mRNA, were the limiting factors in achieving complete knockdown 48 h post-transfection (Figure 3.7A). Taken together, the experimental data and theoretical model both indicated that the amount of free siRNA released by a 20 min irradiation of 20 nM siRNA polyplexes was sufficient to maximize target-gene knockdown. Furthermore, the 20 nM siRNA concentration is significantly lower than the siRNA concentrations used by many other polyplex systems in literature, which often require at least 100 nM siRNA to mediate significant levels of gene silencing, depending on the specific target gene and cell type.⁴⁵⁻⁴⁷

The kinetic model also was used to study how gene silencing efficiencies could be tuned by varying the dosage of light. The amounts of siRNA released in response to light (which were obtained from quantitative analyses as described in the next

section) were input into the kinetic model and allowed us to accurately predict the experimentally measured protein silencing efficiency over the range of irradiation conditions (Figure 3.7B), further indicating that gene expression can be modulated through controlled siRNA release. Moreover, the agreement between the simplified model and experimental results validated the use of Equations 3.1-3.3 in the analyses, and it demonstrated that the model incorporates all of the critical rate-determining steps for this system. It is important to note that the development of this kinetic model was possible only because the nanocarriers are extremely stable intracellularly, yet can be triggered to alter the polymer binding affinity on-demand, in response to light.

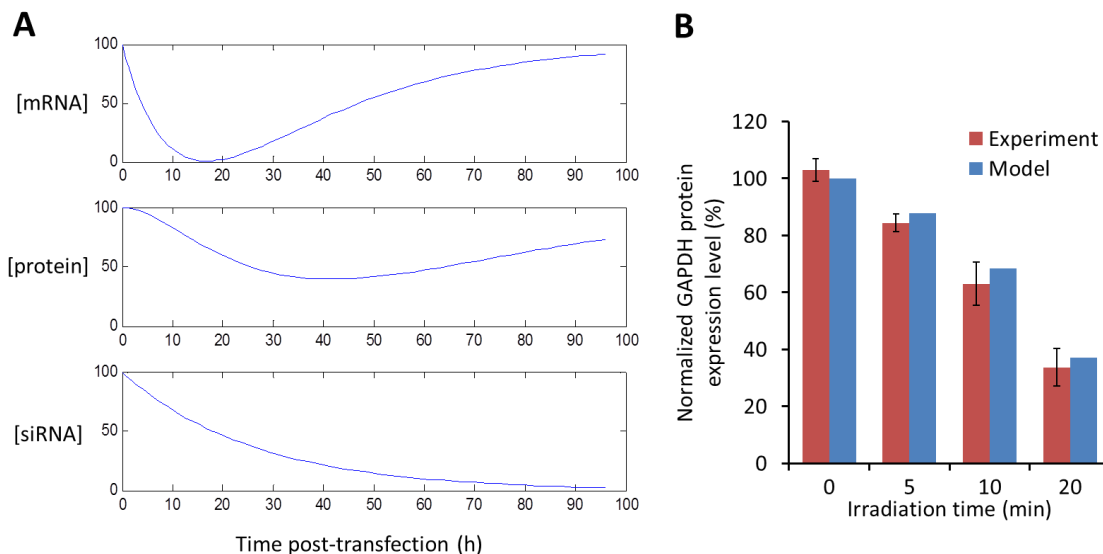


Figure 3.7: Mass action kinetic model that predicts GAPDH silencing following siRNA release from mPEG-*b*-P(APNBMA) polyplexes. (A) The set of equations (3.1-3.3) was solved using differential equation solver ode45 in MATLAB and plotted up to 96 h post-transfection. All concentrations were normalized to 100 at the time of transfection. The terms k_{mRNA} , k_{siRNA} , and k_{prot} are the rate constants for the production of mRNA, siRNA, and protein, respectively. The terms $k_{m,deg}$, $k_{s,deg}$, and $k_{p,deg}$ are the rate constants for the degradation of mRNA, siRNA, and protein, respectively. Degradation rate constants were computed on the basis of the component half-lives reported in literature,^{40, 44, 45} and production rate constants were fit to ensure mRNA and protein steady-state values were reached in the absence of siRNA. (B) Model predictions of protein silencing efficiencies of mPEG-*b*-P(APNBMA) polyplexes following irradiation with 365 nm light for varying lengths of time. Predictions from the kinetic model (blue bars) were computed on the basis of siRNA release data in Figure 3.8C (blue bars). These values were compared to experimental data (red bars) from Figure 3.4C.

3.3.4 Controlling siRNA release

The protein and mRNA silencing studies for siRNA/mPEG-*b*-P(APNBMA) polyplexes demonstrated that the extent of target-gene knockdown depends directly upon the amount of light irradiation. This finding suggests that the irradiation-

dependent charge reversal of the polymer backbone allows tunable gene silencing by altering the stability of the polyplexes and thereby liberating varying amounts of siRNA.

To assess the degree of siRNA released as a function of irradiation conditions, polyplexes were formulated in a buffered solution (containing SDS), exposed to light, and subjected to gel electrophoresis. SDS, an anionic surfactant, was added to the solutions prior to irradiation to better simulate intracellular environments containing lipid membranes. Following a 30 min pre-incubation time with SDS at an S/P ratio (S: sulfate groups on SDS, P: phosphate groups on siRNA) of 15, the polyplexes were irradiated, and release was probed using gel electrophoresis, as shown in Figure 3.8A. With no 365 nm light exposure, mPEG-*b*-P(APNBMA) completely retained all siRNA and excluded ethidium bromide as indicated by the lack of a free siRNA band and minimal fluorescence in the well. Increasing amounts of siRNA were liberated from the polyplexes following longer irradiation times. Approximately 16% of the siRNA was released after 20 min of illumination, based on quantification of the siRNA band through image analysis, with minimal additional improvement after 40 min. Additionally, smears appeared below the well in the irradiated samples, indicating the presence of partially liberated siRNAs still bound to cationic polymer groups and/or polymer fragments. It is unknown whether these siRNA structures are accessible enough in the intracellular environment to bind to RISC. Moreover, complete siRNA liberation was only achieved at extremely high concentrations of SDS (S/P of 200). This indicated that the nanocarriers were remarkably stable in the simulated intracellular environment, and demonstrated that the polyplexes remained dormant unless exposed to the photo-stimulus.

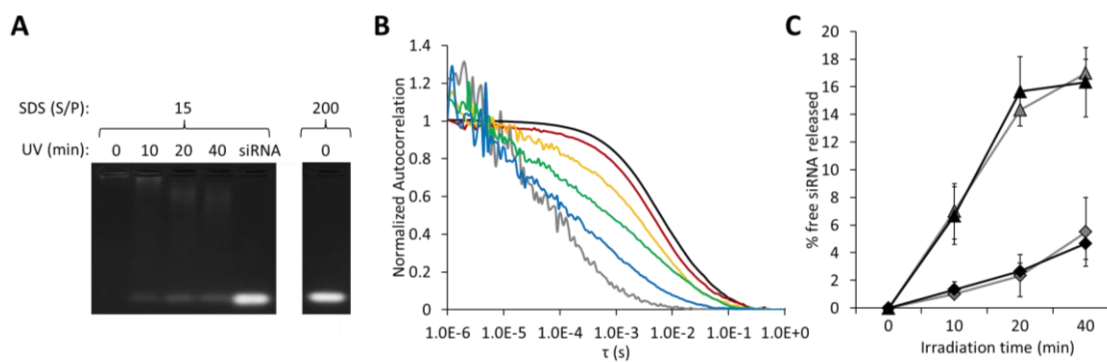


Figure 3.8: Representative gel mobility shift and fluorescence correlation spectroscopy (FCS) analyses of light-induced siRNA release. (A) Gel electrophoresis data from polyplex solutions with varying SDS and light dosages. (B) Normalized autocorrelation functions of polyplex solutions with varying light dosages as follows: 0 min (black), 10 min (red), 20 min (yellow), and 40 min (green) all at SDS S/P of 15; 0 min at SDS S/P of 200 (blue); free siRNA (gray). (C) Quantification of siRNA released on the basis of gel mobility studies (black) and FCS (gray). Polyplexes were pre-incubated in solutions containing no SDS (S/P of 0; diamonds) or SDS at S/P of 15 (triangles). Results are shown as the mean \pm standard deviation of data obtained from three independent samples.

To provide a more detailed characterization of the released siRNA structures, FCS was performed to analyze fluctuations in fluorescence intensities in the solution and estimate the component diffusion patterns following irradiation.⁴⁸ As shown in Figure 3.8B, these experiments indicated that free siRNA exhibited short lag times (τ), indicative of a fast diffusing species with a diffusion coefficient of $140 \mu\text{m}^2 \text{s}^{-1}$. Using the Stokes-Einstein equation (Equation 2.6), a hydrodynamic diameter of $\sim 3 \text{ nm}$ was estimated, which is consistent with the approximate size of an siRNA molecule.⁴⁹ When the siRNAs were packaged into polyplexes, much longer lag times were measured. These polyplexes had average diameters of $\sim 140 \text{ nm}$, which was consistent with dynamic light scattering data reported previously.²¹ The polyplexes each incorporated ~ 250 siRNAs, based on the number of fluorescent particles computed

from the value of the autocorrelation function at $\tau = 0$ s (Table 3.1). As the polyplexes were exposed to 365 nm light for longer periods of time, the autocorrelation function began to exhibit behavior indicative of increasing amounts of released siRNA, as demonstrated by shifts towards shorter lag times. An assay developed by Buyens *et al.* was adapted to quantify the fraction of free siRNA and monitor polyplex disassembly,²⁹ in which changes in the baseline fluorescence intensity were used to calculate the percent of free siRNA. In these studies, no free siRNA was detectable after complexation with mPEG-*b*-P(APNBMA), either before or after incubation in SDS (S/P of 15). As the irradiation time increased, more siRNA was liberated from the polyplexes (Figure 3.8C). Furthermore, analysis of the slower diffusing populations indicated that the polyplexes swelled in size following irradiation (up to ~150 nm after 40 min). Estimates of the percent of free siRNA obtained using FCS were in excellent agreement with the gel electrophoresis results. It is interesting to note that only 6% of the siRNA was liberated following 10 min of irradiation with SDS. Previous work indicated that 81% of the cationic groups were cleaved after 10 min of irradiation,²¹ suggesting that a majority of the polymer must undergo charge-reversal before significant amounts of siRNA are released. Thus, light-mediated charge reversal of the polymer backbone enabled on-demand and precisely tuned siRNA liberation from the nanocarriers. Moreover, these quantitative siRNA release results were used directly in the development of the simple model that accurately captures gene silencing trends as indicated by Figure 3.7B.

Table 3.1: Representative estimation of the number of siRNAs per mPEG-*b*-P(APNBMA) polyplex. The number of fluorescent particles (raw data) was computed by the ZEN 2010 software on the basis of the value of the autocorrelation function at $\tau = 0$ s. The dilution factor was estimated on the basis of the concentrations of siRNAs that were added during sample preparation. The relative number of particles was calculated by multiplying the number of particles (raw data) by the dilution factor. The normalized number of particles was computed by dividing the relative number of particles by 2.7 (relative number of polyplexes).

sample	raw data: number of particles	dilution factor	relative number of particles	normalized number of particles
free siRNA	12.3	54	660	247
polyplex	2.7	1	2.7	1

3.3.5 Monitoring polyplex structural changes

Polyplex structure and morphology may play an important role in siRNA packaging efficiency and the nanocarrier's propensity to fully release siRNA. FRET is a powerful and especially sensitive technique for detecting nanoscale changes in the distance between molecules. Polyplex formation, stability, and loosening can be monitored through the covalent labeling of siRNA molecules with one of two different fluorophores that have overlapping excitation and emission spectra.⁵⁰ Due to their high charge density, siRNAs repel each other when free in solution and typically are not in close enough proximity to transfer energy. However, when forced into mPEG-*b*-P(APNBMA) polyplexes, the donor and acceptor fluorophores attached to the locally aggregated siRNAs underwent energy transfer if they were within a Förster radius of one another.

In this study, Dy547 and Dy647 were chosen to be the donor and acceptor fluorophores, respectively. When the siRNAs were simply mixed in solution in equimolar ratios, no energy transfer was detectable. However, a strong fluorescence emission from Dy647 was visible when the siRNAs were complexed with mPEG-*b*-

P(APNBMA) (Figure 3.9A). Furthermore, the acceptor signal decreased, and the donor signal increased, as the polyplexes were exposed to light for longer times. The ratio of the donor and acceptor emission peak intensities was computed to quantify the FRET efficiency (Figure 3.9B). In the absence of the photo-stimulus, the peak intensity of the acceptor fluorophore was greater than that of the donor fluorophore, indicating efficient energy transfer due to the proximity of the fluorophores (~5 nm).⁵¹ However, the ratio of the two peaks decreased quickly as a function of irradiation time. Over 90% of the FRET signal was lost within 20 min of irradiation, indicating that the fluorophores had an average separation distance of at least 8 nm. This finding stands in contrast to the data in Figure 3.8C that showed only ~2% of the siRNA was released following 20 min of light exposure in the absence of SDS. Thus, FRET is an appropriate technique for detecting subtle changes in polyplex structure that lead to small fractions of cargo release. Clearly, the polyplexes were starting to loosen or change structure such that the siRNA molecules were spaced slightly further apart, but the change was insufficient to release high fractions of siRNA or cause detectable changes in overall polyplex diameter in buffered solutions. Thus, even though only small fractions of siRNA were released completely from the polyplexes, the results still indicate efficient gene silencing that likely was a result of the partial loosening of these structures.

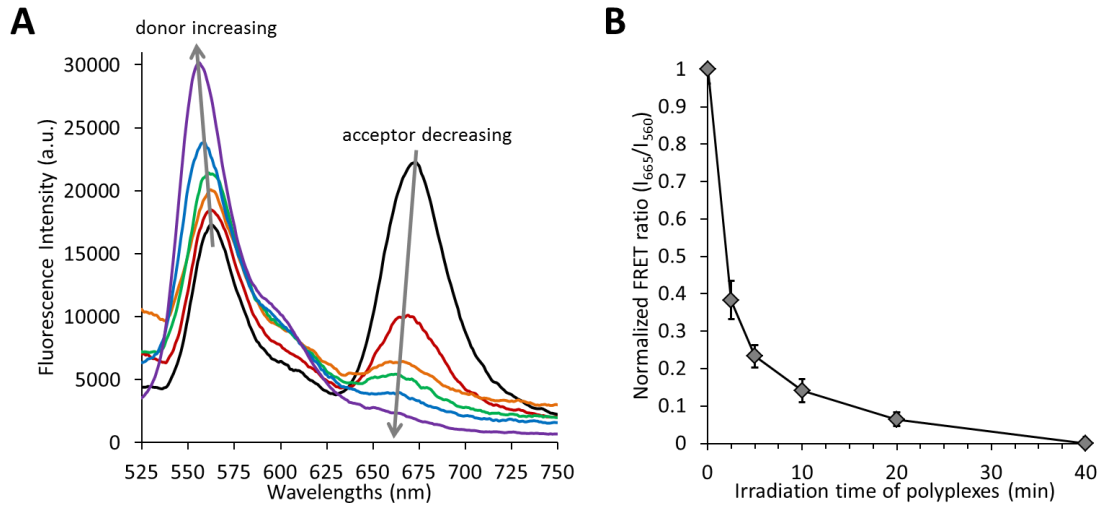


Figure 3.9: Fluorescence emission spectra of polyplexes undergoing FRET as a function of irradiation time. (A) Polyplexes were formed with equal molar ratios of donor and acceptor fluorophore-labeled siRNA molecules and exposed to varying dosages of 365 nm light as follows: 0 min (black), 2.5 min (red), 5 min (orange), 10 min (green), 20 min (blue), 40 min (purple). (B) Normalized ratio between the intensities of the acceptor and donor peaks (I_{665}/I_{560}) of three independent samples for each time point. The lines connecting data points are to guide the eye.

Polyplex stability strongly depends on the environment, particularly in protein-rich settings such as the inside of a cell. An additional benefit of employing FRET with the chosen fluorophores is that the fluorescence can be measured intracellularly due to the fluorophores' brightness and photostability. Thus, polyplexes were formed and delivered as described previously with equimolar concentrations of the donor and acceptor fluorophore-labeled siRNAs, and the intracellular FRET reaction subsequently was analyzed by flow cytometry at approximately 5 h post-transfection. The excitation laser was at 488 nm (direct excitation of donor), and the emission detector filter was at 710 nm (emission of acceptor) to detect the fluorescence signal attributed to polyplexes undergoing FRET. A compensation matrix was used to

account for the minimal fluorescence that was attributable to signal bleed-through (see section 2.4 for more details and Figure A.1 in Appendix A for matrix values). The traces in Figure 3.10 indicate that cells not exposed to light exhibited a strong FRET signal, indicating that the polyplexes remained remarkably stable over long time periods within the intracellular environment. However, when the light exposure time increased, the FRET signal decreased quickly, such that the FRET signal was barely detectable following 20 min of irradiation. Interestingly, the photo-induced, time-dependent loss of FRET measured in solution closely matched the decrease seen intracellularly, suggesting that the extent of polyplex loosening occurred on the same time-scale in both environments (Figure 3.11).

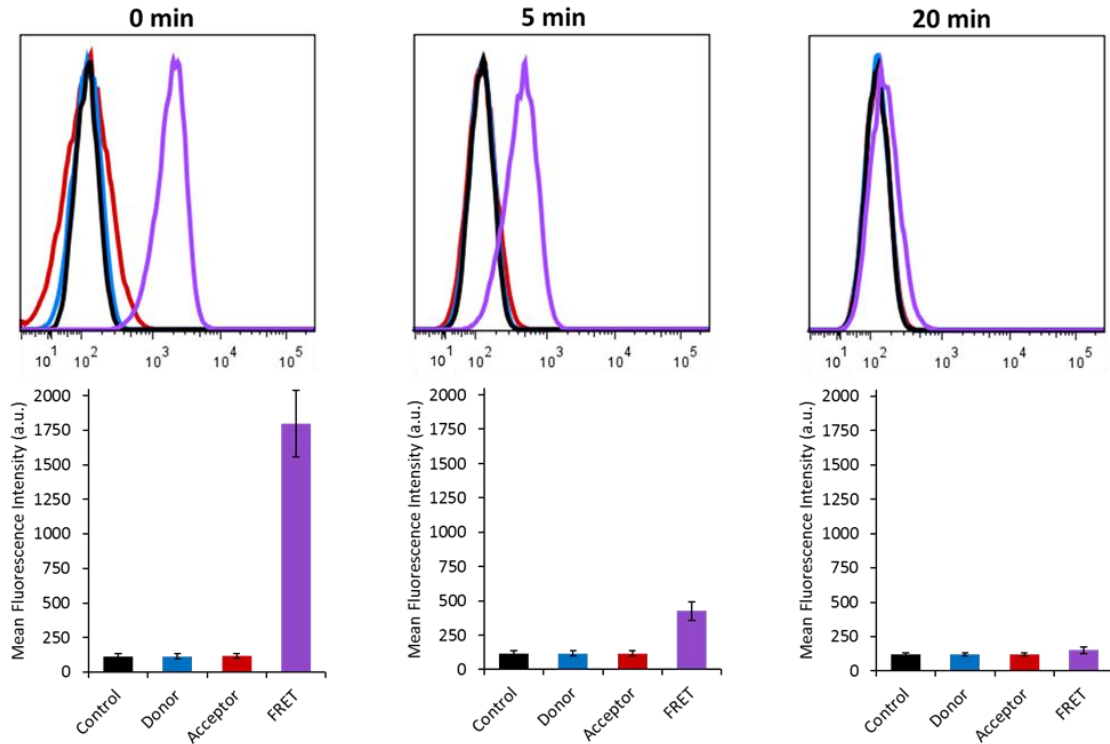


Figure 3.10: Representative flow cytometry data showing the intracellular FRET signal following 365 nm light irradiation of transfected NIH/3T3 cells. The fluorescence signals from cells treated with no siRNA (black), Dy547-siRNA (blue), Dy647-siRNA (red), or Dy547- and Dy647-siRNA (purple) over a series of varying irradiation times were quantified by the mean fluorescence intensity (MFI) per cell. Results are shown as the mean \pm standard deviation of data obtained from three independent experiments, and the compensation matrices are reported in Figure A.1 in Appendix A.

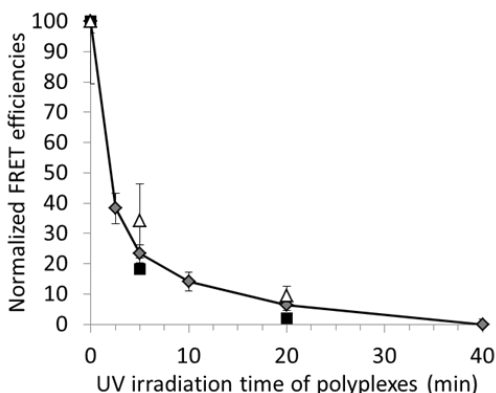


Figure 3.11: Normalized FRET efficiencies as a function of mPEG-*b*-P(APNBMA) polyplex exposure to 365 nm light irradiation. FRET efficiencies of polyplexes in solution were measured through fluorescence spectroscopy (gray diamonds), and cellular FRET efficiencies were measured *via* flow cytometry (black squares) or confocal microscopy (white triangles). In solution, normalized FRET efficiencies were computed from the ratio between the donor and acceptor peaks for polyplexes. In cells, the normalized FRET efficiencies were determined from the fluorescence intensities attributed to FRET after accounting for both autofluorescence and donor/acceptor bleed-through signals. Results are shown as the mean \pm standard deviation of data obtained from three independent experiments, and the raw values for FRET in solution as measured by fluorescence spectroscopy are recorded in Table A.2 in Appendix A.

Flow cytometry analysis was useful for finding the total FRET signal in a given cell containing potentially hundreds of polyplexes; however, information about the individual polyplexes was lost. Confocal microscopy allowed intracellular FRET to be studied in more detail to determine the uniformity of the polyplex unpackaging process. Polyplexes were formulated and delivered under the same conditions as in the flow cytometry experiments above, and subsequently, transfected cells were imaged. An excitation wavelength of 488 nm was used to selectively excite the donor fluorophore. Two distinct emission detection wavelength channels were chosen such that the acceptor fluorescence signal was visible only when FRET was occurring.

Regardless of irradiation time, all samples showed robust cellular uptake as indicated by the appearance of numerous punctate structures within each cell (Figure 3.12A). Each distinct punctate structure likely was comprised of a small collection of polyplexes that were trafficking through endomembrane vesicular compartments.^{21, 52} The appearance of the donor fluorescence signal continued to persist as the irradiation time increased, as expected. However, the number of punctate structures exhibiting acceptor fluorescence due to FRET decreased dramatically as the length of light exposure increased.

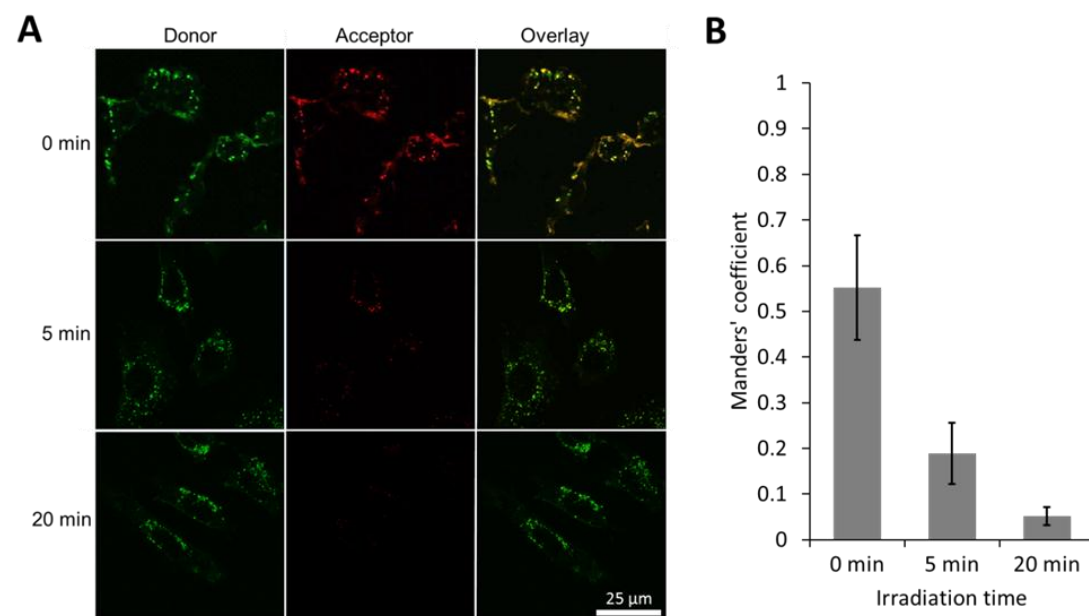


Figure 3.12: Confocal microscopy images and colocalization quantification of intracellular FRET as a function of irradiation time. (A) Selectively exciting the donor fluorophore produced fluorescence signals unique to the donor (green) and acceptor (red) fluorophores. The overlay of these two images is displayed as yellow. The scale bar represents 25 μm and applies to all images. (B) Quantification of micrographs using the Manders' correlation coefficient to compute the fraction of polyplexes undergoing FRET. Results are reported as the mean ± standard deviation of data obtained from 30 randomly chosen cells per sample.

The extent of colocalization was quantified using the Manders' correlation coefficient,⁵³ which is defined as the fraction of image pixels of the probe of interest that are colocalized with a secondary probe. For the present study, the Manders' coefficient represents the fraction of donor fluorophores that overlap with detectable acceptor fluorophores, which corresponds to the fraction of punctate structures, or groups of polyplexes, that have retained their structures well enough to facilitate FRET. In the absence of light, more than half of the internalized polyplexes remained stable and did not significantly start to disassemble, whereas application of light dramatically decreased detectable FRET signals such that >90% of polyplexes disassembled to the point that the siRNAs were no longer within the Förster radius (Figure 3.12B). These findings are remarkably consistent with the FRET data in the absence of cells, as well as with the flow cytometry data of the averaged intracellular responses (Figures 3.9 and 3.10, respectively), as summarized in Figure 3.11. These consistencies demonstrated the relative homogeneity of the polyplexes as well as the similar progression of the light-induced reaction when it occurred inside *vs.* outside of cells. Additionally, these findings reinforce the suggestion that light-induced changes in polymer structure, as opposed to the external solution conditions, are the key factor influencing polyplex disassembly kinetics.

3.3.6 Detection of intracellular siRNA release

FCS can be used to probe the diffusive behaviors of species in cells and provide information about the extent of free siRNA released in the cytoplasm. Polyplexes were formulated with labeled siRNAs, delivered to cells, and irradiated with light for varying lengths of time. As shown in Figure 3.13, the autocorrelation function of the diffusing siRNAs in cells that had not been exposed to 365 nm light

exhibited a primary population with long lag times, indicative of a slow diffusing species. As the irradiation time increased, the curve shifted towards faster lag times. The autocorrelation function for cells treated with 20 min of light had an inflection point, suggesting that at least two distinct populations with very different diffusive characteristics existed in the sample. These data were fit with a two-component model and the computed diffusion coefficients were $28 \mu\text{m}^2 \text{s}^{-1}$ and $0.0025 \mu\text{m}^2 \text{s}^{-1}$ for the fast and slow diffusing populations, respectively, in the cells treated with 20 min of light. The faster diffusing species, presumably intracellular free siRNA, was found to have a diffusion coefficient $\sim 20\%$ of that found for free siRNA in aqueous solution. This decrease in effective mobility is explained by the crowded cytoplasmic cell environment and is consistent with literature values found for similarly sized oligonucleotides within cells.^{54, 55} The slower moving species had a diffusion coefficient approximately three orders of magnitude slower than polyplexes in buffered solution. The dramatic decrease in polyplex mobility is due to the slow intracellular trafficking of endosomal cargo along microtubules and is consistent with values found for similarly sized polyplexes within cells.⁵⁶ Thus, the computed diffusion coefficients are able to describe a population of free siRNA localized in the cytoplasm as well as a population of intact polyplexes being trafficked in endosomes. Furthermore, the autocorrelation functions indicated that the fraction of free siRNA increased with irradiation time, as evidenced by the shift towards shorter lag times (Figure 3.13) in agreement with the gel electrophoresis and FCS data in Figure 3.8. These fundamental experiments probing photo-induced siRNA release and monitoring intracellular changes in polyplex structure were pivotal to the implementation of a kinetic model that accurately predicts gene silencing efficiencies (Figure 3.7).

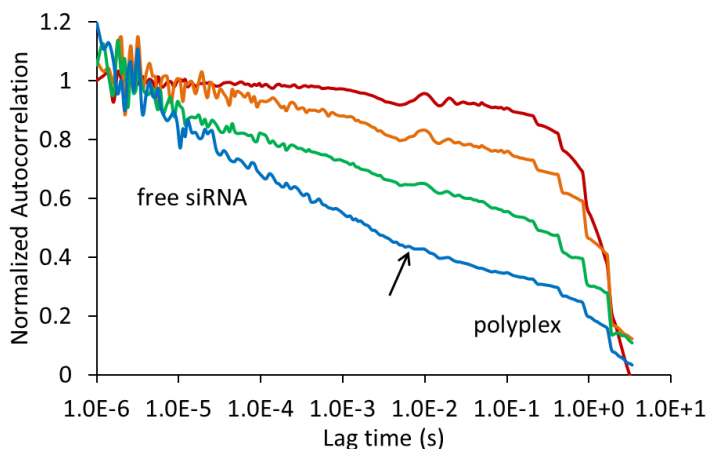


Figure 3.13: Normalized FCS autocorrelation functions showing the intracellular diffusion patterns of siRNA molecules following 365 nm light irradiation. Cells were treated with 365 nm light for 0 min (red), 5 min (orange), 10 min (green), or 20 min (blue) after the delivery of labeled polyplexes. The arrow indicates an inflection point in the 20 min irradiation autocorrelation function.

3.4 Conclusions

The unique properties of photo-responsive polymers were exploited to elucidate fundamental mechanisms governing siRNA release from polymer delivery vehicles. These pivotal studies informed both development of an accurate predictive framework and achieved maximal gene silencing. The polyplexes facilitated precise (cellular length scale) on/off spatiotemporal control over exogenous gene activity in human primary fibroblasts and murine fibroblasts. For the particular case of GAPDH, a model endogenous target, gene silencing was tunable up to a maximum of ~70% and ~86% at the protein and mRNA levels, respectively. Moreover, kinetic modeling demonstrated that these maximum gene knockdown efficiencies were commensurate with the maximum achievable gene silencing levels using a single dose of siRNA, which was a consequence of the characteristic gene degradation rates for the target

genes (mRNA and protein half-lives). Using FCS and FRET, the monitoring of subtle changes in polyplex structure intracellularly confirmed that the nanocarriers maintained dormancy in the absence of the photo-trigger. These mechanistic insights enabled both quantification of the amount of light-induced siRNA release and accurate prediction of gene silencing levels with the kinetic model. Thus, this chapter highlights the synergistic insights obtained by combining photo-responsive mPEG-*b*-P(APNBMA) polymers that enable on/off and spatially resolved control over siRNA activity, with the predictive capabilities of kinetic modeling. The procedures developed in the chapter allowed for the elucidation of the mechanisms that govern polyplex stability and siRNA release, and these findings were critical for achieving spatiotemporal control over gene expression and generating a simple kinetic model that can predict gene silencing.

REFERENCES

1. Wang, X.; Chen, X.; Yang, Y., Spatiotemporal control of gene expression by a light-switchable transgene system. *Nat. Methods* **2012**, *9* (3), 266-269.
2. Motta-Mena, L. B.; Reade, A.; Mallory, M. J.; Glantz, S.; Weiner, O. D.; Lynch, K. W.; Gardner, K. H., An optogenetic gene expression system with rapid activation and deactivation kinetics. *Nat. Chem. Biol.* **2014**, *10* (3), 196-202.
3. Gao, S.; Dagnaes-Hansen, F.; Nielsen, E. J. B.; Wengel, J.; Besenbacher, F.; Howard, K. A.; Kjems, J., The effect of chemical modification and nanoparticle formulation on stability and biodistribution of siRNA in mice. *Mol. Ther.* **2009**, *17* (7), 1225-1233.
4. Weber, W.; Fussenegger, M., Emerging biomedical applications of synthetic biology. *Nat. Rev. Genet.* **2012**, *13* (1), 21-35.
5. Shimizu-Sato, S.; Huq, E.; Tepperman, J. M.; Quail, P. H., A light-switchable gene promoter system. *Nat. Biotechnol.* **2002**, *20* (10), 1041-1044.
6. Ye, H.; Daoud-El Baba, M.; Peng, R.-W.; Fussenegger, M., A synthetic optogenetic transcription device enhances blood-glucose homeostasis in mice. *Science* **2011**, *332* (6037), 1565-1568.
7. Sauers, D. J.; Temburni, M. K.; Biggins, J. B.; Ceo, L. M.; Galileo, D. S.; Koh, J. T., Light-activated gene expression directs segregation of co-cultured cells in vitro. *ACS Chem. Biol.* **2010**, *5* (3), 313-320.
8. Konermann, S.; Brigham, M. D.; Trevino, A. E.; Hsu, P. D.; Heidenreich, M.; Cong, L.; Platt, R. J.; Scott, D. A.; Church, G. M.; Zhang, F., Optical control of mammalian endogenous transcription and epigenetic states. *Nature* **2013**, *500* (7463), 472-476.
9. Mueller, K.; Naumann, S.; Weber, W.; Zurbriggen, M. D., Optogenetics for gene expression in mammalian cells. *Biol. Chem.* **2015**, *396* (2), 145-152.

10. Yin, H.; Kanasty, R. L.; Eltoukhy, A. A.; Vegas, A. J.; Dorkin, J. R.; Anderson, D. G., Non-viral vectors for gene-based therapy. *Nat. Rev. Genet.* **2014**, *15* (8), 541-555.
11. Nihongaki, Y.; Yamamoto, S.; Kawano, F.; Suzuki, H.; Sato, M., CRISPR-Cas9-based photoactivatable transcription system. *Chem. Biol.* **2015**, *22* (2), 169-174.
12. Davis, M. E.; Zuckerman, J. E.; Choi, C. H. J.; Seligson, D.; Tolcher, A.; Alabi, C. A.; Yen, Y.; Heidel, J. D.; Ribas, A., Evidence of RNAi in humans from systemically administered siRNA via targeted nanoparticles. *Nature* **2010**, *464* (7291), 1067-1070.
13. Aytar, B. S.; Muller, J. P. E.; Kondo, Y.; Abbott, N. L.; Lynn, D. M., Spatial control of cell transfection using soluble or solid-phase redox agents and a redox-active ferrocenyl lipid. *ACS Appl. Mater. Interfaces* **2013**, *5* (17), 8283-8288.
14. Isalan, M.; Santori, M. I.; Gonzalez, C.; Serrano, L., Localized transfection on arrays of magnetic beads coated with PCR products. *Nat. Methods* **2005**, *2* (2), 113-118.
15. Burke, P. A.; Pun, S. H.; Reineke, T. M., Advancing polymeric delivery systems amidst a nucleic acid therapy renaissance. *ACS Macro Lett.* **2013**, *2* (10), 928-934.
16. Shim, M. S.; Kwon, Y. J., Acid-responsive linear polyethylenimine for efficient, specific, and biocompatible siRNA delivery. *Bioconjugate Chem.* **2009**, *20* (3), 488-499.
17. Ruvinov, E.; Kryukov, O.; Forti, E.; Korin, E.; Goldstein, M.; Cohen, S., Calcium-siRNA nanocomplexes: What reversibility is all about. *J. Control. Release* **2015**, *203*, 150-160.
18. Liu, X.; Howard, K. A.; Dong, M. D.; Andersen, M. O.; Rahbek, U. L.; Johnsen, M. G.; Hansen, O. C.; Besenbacher, F.; Kjems, J., The influence of polymeric properties on chitosan/siRNA nanoparticle formulation and gene silencing. *Biomaterials* **2007**, *28* (6), 1280-1288.
19. Johnson, R. N.; Chu, D. S. H.; Shi, J.; Schellinger, J. G.; Carlson, P. M.; Pun, S. H., HPMA-oligolysine copolymers for gene delivery: Optimization of peptide length and polymer molecular weight. *J. Control. Release* **2011**, *155* (2), 303-311.

20. Green, M. D.; Foster, A. A.; Greco, C. T.; Roy, R.; Lehr, R. M.; Epps, T. H., III; Sullivan, M. O., Catch and release: photocleavable cationic diblock copolymers as a potential platform for nucleic acid delivery. *Polym. Chem.* **2014**, *5* (19), 5535-5541.
21. Foster, A. A.; Greco, C. T.; Green, M. D.; Epps, T. H., III; Sullivan, M. O., Light-mediated activation of siRNA release in diblock copolymer assemblies for controlled gene silencing. *Adv. Healthc. Mater.* **2015**, *4* (5), 760-770.
22. Huschka, R.; Barhoumi, A.; Liu, Q.; Roth, J. A.; Ji, L.; Halas, N. J., Gene silencing by gold nanoshell-mediated delivery and laser-triggered release of antisense oligonucleotide and siRNA. *ACS Nano* **2012**, *6* (9), 7681-7691.
23. Lee, H.; Kim, Y.; Schweickert, P. G.; Konieczny, S. F.; Won, Y.-Y., A photo-degradable gene delivery system for enhanced nuclear gene transcription. *Biomaterials* **2014**, *35* (3), 1040-1049.
24. Braun, G. B.; Pallaoro, A.; Wu, G.; Missirlis, D.; Zasadzinski, J. A.; Tirrell, M.; Reich, N. O., Laser-activated gene silencing via gold nanoshell-siRNA conjugates. *ACS Nano* **2009**, *3* (7), 2007-2015.
25. Li, H.-J.; Wang, H.-X.; Sun, C.-Y.; Du, J.-Z.; Wang, J., Shell-detachable nanoparticles based on a light-responsive amphiphile for enhanced siRNA delivery. *R. Soc. Chem. Adv.* **2014**, *4* (4), 1961-1964.
26. Huang, X.; Hu, Q.; Braun, G. B.; Pallaoro, A.; Morales, D. P.; Zasadzinski, J.; Clegg, D. O.; Reich, N. O., Light-activated RNA interference in human embryonic stem cells. *Biomaterials* **2015**, *63* (0), 70-79.
27. Schneider, C. A.; Rasband, W. S.; Eliceiri, K. W., NIH Image to ImageJ: 25 years of image analysis. *Nat. Methods* **2012**, *9* (7), 671-675.
28. Schmittgen, T. D.; Livak, K. J., Analyzing real-time PCR data by the comparative C-T method. *Nat. Protoc.* **2008**, *3* (6), 1101-1108.
29. Buyens, K.; Meyer, M.; Wagner, E.; Demeester, J.; De Smedt, S. C.; Sanders, N. N., Monitoring the disassembly of siRNA polyplexes in serum is crucial for predicting their biological efficacy. *J. Control. Release* **2010**, *141* (1), 38-41.

30. Larsen, J. D.; Reilly, M. J.; Sullivan, M. O., Using the epigenetic code To promote the unpackaging and transcriptional activation of DNA polyplexes for gene delivery. *Mol. Pharm.* **2012**, *9* (5), 1041-1051.
31. Ross, N. L.; Munsell, E. V.; Sabanayagam, C.; Sullivan, M. O., Histone-targeted polyplexes avoid endosomal escape and enter the nucleus during postmitotic redistribution of ER membranes. *Mol. Ther. Nucleic Acids* **2015**, *4*, e226.
32. Kwon, Y. J., Before and after endosomal escape: roles of stimuli-converting siRNA/polymer interactions in determining gene silencing efficiency. *Acc. Chem. Res.* **2012**, *45* (7), 1077-1088.
33. Tibbitt, M. W.; Kloxin, A. M.; Dyamenahalli, K. U.; Anseth, K. S., Controlled two-photon photodegradation of PEG hydrogels to study and manipulate subcellular interactions on soft materials. *Soft Matter* **2010**, *6* (20), 5100-5108.
34. Green, J. J.; Chiu, E.; Leshchiner, E. S.; Shi, J.; Langer, R.; Anderson, D. G., Electrostatic ligand coatings of nanoparticles enable ligand-specific gene delivery to human primary cells. *Nano Letters* **2007**, *7* (4), 874-879.
35. Robinson, K. G.; Nie, T.; Baldwin, A. D.; Yang, E. C.; Kiick, K. L.; Akins, R. E., Jr., Differential effects of substrate modulus on human vascular endothelial, smooth muscle, and fibroblastic cells. *J Biomed. Mater. Res. A* **2012**, *100A* (5), 1356-1367.
36. Bengali, Z.; Pannier, A. K.; Segura, T.; Anderson, B. C.; Jang, J. H.; Mustoe, T. A.; Shea, L. D., Gene delivery through cell culture substrate adsorbed DNA complexes. *Biotechnology and Bioengineering* **2005**, *90* (3), 290-302.
37. Ziauddin, J.; Sabatini, D. M., Microarrays of cells expressing defined cDNAs. *Nature* **2001**, *411* (6833), 107-110.
38. Breunig, M.; Lungwitz, U.; Liebl, R.; Goepferich, A., Breaking up the correlation between efficacy and toxicity for nonviral gene delivery. *Proc. Natl. Acad. Sci. U.S.A.* **2007**, *104* (36), 14454-14459.
39. Kizzire, K.; Khargharia, S.; Rice, K. G., High-affinity PEGylated polyacridine peptide polyplexes mediate potent in vivo gene expression. *Gene Therapy* **2013**, *20* (4), 407-416.

40. Franch, H. A.; Sooparb, S.; Du, J., A mechanism regulating proteolysis of specific proteins during renal tubular cell growth. *J. Biol. Chem.* **2001**, *276* (22), 19126-19131.
41. Malmo, J.; Sorgard, H.; Varum, K. M.; Strand, S. P., siRNA delivery with chitosan nanoparticles: Molecular properties favoring efficient gene silencing. *J. Control. Release* **2012**, *158* (2), 261-268.
42. Hutvagner, G.; Simard, M. J.; Mello, C. C.; Zamore, P. D., Sequence-specific inhibition of small RNA function. *PLoS Biol.* **2004**, *2* (4), 465-475.
43. Akhtar, S.; Benter, I. F., Nonviral delivery of synthetic siRNAs in vivo. *J. Clin. Invest.* **2007**, *117* (12), 3623-3632.
44. Bartlett, D. W.; Davis, M. E., Insights into the kinetics of siRNA-mediated gene silencing from live-cell and live-animal bioluminescent imaging. *Nucleic Acids Res.* **2006**, *34* (1), 322-333.
45. Dani, C.; Piechaczyk, M.; Audigier, Y.; Elsabouty, S.; Cathala, G.; Marty, L.; Fort, P.; Blanchard, J. M.; Jeanteur, P., Characterization of the transcription products of glyceraldehyde 3-phosphate-dehydrogenase gene in HeLa cells. *Eur. J. Biochem.* **1984**, *145* (2), 299-304.
46. Grayson, A. C. R.; Doody, A. M.; Putnam, D., Biophysical and structural characterization of polyethylenimine-mediated siRNA delivery in vitro. *Pharm. Res.* **2006**, *23* (8), 1868-1876.
47. Qian, J.; Berkland, C., pH-sensitive triblock copolymers for efficient siRNA encapsulation and delivery. *Polym. Chem.* **2015**, *6* (18), 3472-3479.
48. Troiber, C.; Kasper, J. C.; Milani, S.; Scheible, M.; Martin, I.; Schaubhut, F.; Kuechler, S.; Raedler, J.; Simmel, F. C.; Friess, W.; Wagner, E., Comparison of four different particle sizing methods for siRNA polyplex characterization. *Eur. J. Pharm. Biopharm.* **2013**, *84* (2), 255-264.
49. DeRouchey, J.; Schmidt, C.; Walker, G. F.; Koch, C.; Plank, C.; Wagner, E.; Radler, J. O., Monomolecular assembly of siRNA and poly(ethylene glycol)-peptide copolymers. *Biomacromolecules* **2008**, *9* (2), 724-732.
50. Alabi, C. A.; Love, K. T.; Sahay, G.; Stutzman, T.; Young, W. T.; Langer, R.; Anderson, D. G., FRET-labeled siRNA probes for tracking assembly and disassembly of siRNA nanocomplexes. *ACS Nano* **2012**, *6* (7), 6133-6141.

51. Bowen, M. E.; Weninger, K.; Ernst, J.; Chu, S.; Brunger, A. T., Single-molecule studies of synaptotagmin and complexin binding to the SNARE complex. *Biophysical Journal* **2005**, *89* (1), 690-702.
52. Veldhoen, S.; Laufer, S. D.; Trampe, A.; Restle, T., Cellular delivery of small interfering RNA by a non-covalently attached cell-penetrating peptide: quantitative analysis of uptake and biological effect. *Nucleic Acids Res.* **2006**, *34* (22), 6561-6573.
53. Manders, E. M. M.; Verbeek, F. J.; Aten, J. A., Measurement of colocalization of objects in dual-color confocal images. *J. Microsc-Oxford* **1993**, *169*, 375-382.
54. Verkman, A. S., Solute and macromolecule diffusion in cellular aqueous compartments. *Trends Biochem. Sci.* **2002**, *27* (1), 27-33.
55. Lukacs, G. L.; Haggie, P.; Seksek, O.; Lechardeur, D.; Freedman, N.; Verkman, A. S., Size-dependent DNA mobility in cytoplasm and nucleus. *J. Biol. Chem.* **2000**, *275* (3), 1625-1629.
56. Kulkarni, R. P.; Wu, D. D.; Davis, M. E.; Fraser, S. E., Quantitating intracellular transport of polyplexes by spatio-temporal image correlation spectroscopy. *Proc. Natl. Acad. Sci. U.S.A.* **2005**, *102* (21), 7523-7528.

Chapter 4

MIXED POLYMER NANOCARRIERS AND KINETIC MODELING TO PREDICT DOSING

This chapter describes the formulation of mixed polymer nanocarriers to improve gene silencing efficiencies and the implementation of simple kinetic modeling to predict dose responses. This work was conducted in collaboration with Victoria G. Muir. The text and figures in this chapter are adapted and reprinted with permission from Greco, C. T.; Muir, V. G.; Epps, T. H., III; Sullivan, M. O., Efficient tuning of siRNA dose response by combining mixed polymer nanocarriers with simple kinetic modeling. *Acta Biomater.* 2017, 50, 407-416. Copyright 2017 Acta Materialia Inc. Published by Elsevier Ltd.

4.1 Introduction

To overcome the challenges related to controlling small interfering RNA (siRNA) binding *vs.* release, many approaches have employed cationic block copolymers (BCP)s that electrostatically bind siRNA and self-assemble into nanoscale complexes (polyplexes).^{1,2} The unique characteristics of BCPs have been harnessed to improve control over siRNA release using several different strategies. One of the most common strategies is to tune the nucleic acid binding capacity through systematically varying the molecular weight and/or charge density of the cationic block.^{3,4} Generally, increasing the number of cationic groups increases the polymer binding efficiency and cellular uptake of the polyplexes; however, increased positive charge also hinders siRNA release in the cytoplasm and results in greater cytotoxicity

of the nanocarriers.^{5,6} Most studies must compromise and use polymers with intermediate binding forces that balance the above factors to improve nucleic acid delivery.⁵ Furthermore, such systematic approaches often require the synthesis of small libraries of polymers, a process that can be both tedious and costly.⁷

An alternative and more flexible strategy for improving the control of siRNA release is the use of mixed polyplexes assembled from polymers with different block compositions.^{8,9} Modulations to the net cationic charge can be achieved simply by changing the molar ratios of as few as two polymers, allowing for rapid determination of structure-function relationships.¹⁰⁻¹² For example, Omedes Pujol *et al.* prepared polymeric nanoparticles with varying ratios of two amphiphilic diblock copolymers that differed in their hydrophilic blocks (cationic or neutral).¹³ Mixed micelles that contained greater amounts of the cationic polymer mediated higher levels of gene knockdown, but also were found to be cytotoxic, presumably due to insufficient shielding of the cationic charge in the corona.

Perhaps the most promising strategy to control siRNA release involves the use of responsive materials, whose binding affinity for siRNA can be altered by application of a stimulus.¹⁴⁻¹⁶ Photo-sensitive nanocarriers offer unique advantages such as rapid response, exquisite spatial control with minimal diffusive effects, and tunability of light wavelength and intensity,¹⁷⁻²¹ ideal for topical wound repair and other regenerative medicine applications.²² However, although photo-responsive biomaterials have enhanced spatiotemporal control over siRNA delivery, a limited understanding of the dynamic silencing response persists.²³ RNA interference (RNAi) depends on numerous biological parameters, such as cell doubling time, as well as mRNA and protein half-lives.^{24,25} Diseases characterized by rapid cell division, such

as cancer, are difficult to treat with siRNAs because dilution effects exclude the possibility of sustained protein knockdown with a single dose.²⁵ Thus, multiple doses must be administered to maintain robust gene silencing over a prolonged period of time.

The majority of RNAi protocols and dosing schedules reported in the literature are chosen on the basis of precedence, or through trial and error. Multiple experiments must be conducted to screen for conditions that achieve the desired level and/or duration of knockdown, yet this tedious approach often fails to identify improved dosing regimens.²⁶ Kinetic modeling can provide critical insights into the underlying causes for these shortcomings. For example, Bartlett *et al.* used modeling approaches to identify a dosing frequency to induce tumor inhibition in a syngeneic mouse cancer model,²⁶ and these approaches later guided the design of dosing regimens employed in clinical trials.²⁷ Several other such models also have been published.^{23-26, 28-31} However, modeling approaches typically require knowledge of numerous kinetic parameters, and modeling has most often been applied to commercial gene delivery systems (e.g. Lipofectamine, Oligofectamine, PEI),^{25, 28, 30} which are incapable of precisely controlled and tunable nucleic acid activity. The development of delivery vehicles capable of externally-triggered siRNA release would provide greater versatility in the timing and magnitude of gene silencing, thereby facilitating the use of streamlined models to predict dosing schedules in regenerative medicine.

In this chapter, mixtures of novel and tailorable mPEG-*b*-poly(5-(3-(amino)propoxy)-2-nitrobenzyl methacrylate) [mPEG-*b*-P(APNBMA)_n] BCPs were combined with simple kinetic modeling for improved control over gene silencing. The

polymers have tunable molecular weights, low dispersities, and photocleavable moieties that permit light-induced charge reversal to initiate nucleic acid release.³² A nonfouling PEG block was incorporated to provide stability in physiological environments and resistance to opsonization. These BCPs have proven biocompatibility and protect siRNA in salt, serum, and nuclease solutions, while simultaneously stimulating siRNA release and gene-specific knockdown upon application of a cytocompatible photo-stimulus.³³

These properties were exploited to predict and regulate siRNA dosing effects through the formulation of polyplexes containing varying ratios of two different photo-responsive mPEG-*b*-P(APNBMA)_n polymers with cationic block lengths of $n = 7.9$ and $n = 23.6$ average repeat units. By tuning polyplex composition and application of the photo-stimulus, the extent of gene silencing was easily controlled and maximized. Furthermore, temporal control over siRNA release, combined with the use of the kinetic model, facilitated the accurate prediction of dynamic changes in mRNA and protein concentrations in response to one dose or multiple doses of siRNA. Thus, accurate gene modulation was demonstrated through integration of model-based design and stimuli-responsive control over siRNA application regimens, highlighting a unique method for overcoming limitations prevalent in a variety of RNAi applications.

4.2 Materials and Methods

4.2.1 Materials

The mPEG-*b*-P(APNBMA)_n polymers ($M_n = 7,900 \text{ g mol}^{-1}$, $n = 7.9$; $M_n = 13,100 \text{ g mol}^{-1}$, $n = 23.6$) were synthesized *via* atom-transfer radical polymerization as

described elsewhere.³² All siRNA molecules were purchased from GE Healthcare Dharmacon, Inc. (Chicago, IL). ON-TARGETplus non-targeting siRNAs and glyceraldehyde 3-phosphate dehydrogenase (GAPDH) siRNAs were used as received. Custom-made siRNA (both Dy547- and Dy647-labeled) targeting GAPDH were designed and terminally altered with 5'-P and a fluorophore (sense: 5' Dy547/Dy647-GUGUGAACCACGAGAAAUAUU 3'; antisense: 5' 5'-P-UAUUUCUCGUGGUUCACACUU 3'). Dulbecco's modification of Eagle's medium (DMEM) and PBS (150 mM NaCl) were obtained from Corning Life Sciences – Mediatech Inc. (Manassas, VA). Opti-MEM® media, SuperSignal™ West Dura Chemiluminescent Substrate, and TRIzol® Reagent were purchased from Thermo Fisher Scientific (Waltham, MA). Bovine serum albumin (BSA) and a bicinchoninic acid (BCA) protein assay kit were purchased from Pierce (Rockford, IL). The anti-GAPDH and secondary HRP antibodies were purchased from AbCam (Cambridge, MA). The anti-actin antibody was obtained from Santa Cruz Biotechnology (Dallas, TX). Primers were obtained from Eurofins MWG Operon (Huntsville, AL) with the following sequences: GAPDH forward 5' CGGGTTCCTATAAATACGGACTGC 3'; GAPDH reverse 5' CCCAATACGGCCAAATCCGT 3'; β-actin forward 5' CTGTTCGAGTCGCGTCCA 3'; β-actin reverse 5' TCATCCATGGCGAACTGGTG 3'. The iTaq™ Universal SYBR® Green One-Step Kit and optical flat 8-cap strips were purchased from Bio-Rad (Hercules, CA). All other reagents were obtained from Thermo Fisher Scientific (Waltham, MA).

4.2.2 Formulation of siRNA nanocarriers

Polyplexes were formed using a self-assembly method *via* solution mixing followed by gentle vortexing. Solutions of siRNA were prepared at 32 μg mL⁻¹ in 20

nM 4-(2-hydroxyethyl)piperazine-1-ethanesulfonic acid (HEPES) buffer at pH 6.0. Polymer solutions were prepared in HEPES buffer by adding appropriate amounts of mPEG-*b*-P(APNBMA)_{7.9} and mPEG-*b*-P(APNBMA)_{23.6} to vary the fraction of each polymer in solution, on a molar basis of cationic amine groups. The polymer solutions were added to equal volumes of siRNA solutions to achieve the desired total N/P ratios (N: cationic amine groups on polymer, P: anionic phosphate groups on siRNA). Polyplexes were incubated at room temperature in a dark environment for 30 min prior to further analysis.

4.2.3 Ethidium bromide exclusion assay

Polyplexes were formulated as described and subjected to gel electrophoresis. Gels were prepared with 4 wt% agarose and stained with 0.5 $\mu\text{g mL}^{-1}$ ethidium bromide. For analysis, 12.5 μL of polyplex solution was added to 2.5 μL of loading dye (3:7 (v/v) glycerol/water) before being added to the wells of the gel. Gels were run at 100 V for 30 min and imaged using a Bio-Rad Gel Doc XR (Hercules, CA). ImageJ software (National Institutes of Health, Bethesda, MD) was used to quantify the amounts of free siRNA by analyzing band intensities.

4.2.4 Cell culture and transfection

NIH/3T3 cells were purchased from the American Type Culture Collection (ATCC, Manassas, VA). The cells were cultured following ATCC protocols in DMEM supplemented with 10 vol% fetal bovine serum and 1 vol% penicillin-streptomycin. The cells were maintained at 37 °C in a humidified environment with 5 vol% CO₂. For transfections, cells were seeded in 6 well plates at a density of 100,000 cells per well. The cells were allowed to adhere and recover for 24 h. In preparation

for transfection, DMEM was removed, PBS was added in a wash step, and Opti-MEM® reduced serum media was added. Polyplex solutions at an N/P ratio of 4 were added to a final siRNA concentration of 20 nM, and the cells were incubated for 3 h. Following transfection, all cells were washed with PBS and incubated in fully supplemented media for 30 min. For samples undergoing 365 nm light treatment, the media was removed and replaced with Opti-MEM® without phenol red. The cells were subsequently irradiated with 365 nm light at an intensity of 200 W m⁻² for 10 min while on a 37 °C hot plate. Subsequently, cells were incubated in fully supplemented DMEM for the remainder of the culture duration.

4.2.5 Protein knockdown analysis

Western blot analyses were used to measure GAPDH protein silencing. In the single dose experiments, cells were transfected as described. Then, 48 h after the start of transfection, protein was extracted from the cells by adding a lysis solution composed of 0.5 vol% Triton X-100, 0.5% sodium deoxycholate, 150 mM NaCl, 5 mM Tris-HCl (pH 7.4), 5 mM EDTA, and 1x Halt Protease and Phosphatase Inhibitor cocktail. For the repeated dosing experiments, a second transfection of polyplexes was performed 28 h after the first transfection. Protein was extracted *via* cell lysis 75 h after the start of the first transfection. The total protein concentration of each sample was measured using the BSA Protein Assay Kit. The protein solutions were subjected to 4% - 20% sodium dodecyl sulfate polyacrylamide gel electrophoresis (SDS-PAGE) for 35 min at 150 V. The separated proteins then were transferred onto a poly(vinylidene fluoride) membrane at 18 V for 75 min. The membrane was subsequently blocked in 5 vol % BSA in Tris-HCl-buffered saline (50 mM Tris-HCl, pH 7.4, 150 mM NaCl) containing 0.1 vol % Tween 20 (TBST) at room temperature

for 1 h. The membrane was incubated overnight with anti-GAPDH rabbit monoclonal IgG primary antibody in TBST at 4 °C. The next day, the membrane was incubated in a solution of secondary goat anti-rabbit polyclonal IgG antibody conjugated to horseradish peroxidase (HRP) for 1 h. The SuperSignal™ West Dura Chemiluminescent Substrate was used to enable detection of the GAPDH bands through chemiluminescent imaging in a FluorChem Q (ProteinSimple, San Jose, CA), and the band intensities were quantified using ImageJ. To image the actin bands, the membrane was stripped for 15 min with Restore™ PLUS Western Blot stripping buffer, blocked in BSA solution for 1 h, and subsequently incubated with anti-actin rabbit monoclonal IgG primary antibody overnight. The next day, after incubation in a solution of secondary goat anti-rabbit polyclonal IgG antibody conjugated to HRP, chemiluminescent imaging was used to detect the actin bands.

4.2.6 Cellular uptake

Cells were seeded in 12-well plates at a density of 40,000 cells per well and allowed to adhere and recover for 24 h. Polyplex solutions were formed with Dy647-labeled siRNA, and these solutions were delivered to cells following the transfection protocol described in section 4.2.4. After the 3 h transfection, cells were washed with PBS solution and prepared for flow cytometry analysis following standard trypsin-based protocols. The cells were resuspended in PBS and filtered through a 35 µm nylon mesh to remove cell aggregates. Flow cytometry measurements were collected on an Accuri C6 instrument (BD Biosciences, San Jose, CA). The analysis was conducted at approximately 4.5 h post transfection, and at least 10,000 live cells were analyzed per sample. FlowJo v7 software (FlowJo, LLC, Ashland, OR) was used to analyze the data and quantify the mean fluorescence intensity per cell.

4.2.7 Light-induced siRNA release

Polyplex solutions were formed as described above, at varying fractions of mPEG-*b*-P(APNBMA)_{7.9}. Polyplexes were subsequently incubated in sodium dodecyl sulfate (SDS) solutions at an S/P ratio of 2.5 (S: sulfate groups on SDS, P: phosphate groups on siRNA) at room temperature in a dark environment for 30 min. Then, 62.5 μL of polyplex solution was sealed within a chamber composed of two glass slides with a rubber gasket. The polyplex solutions were subjected to irradiation with 365 nm light at 200 W m^{-2} for 0, 5, 10, 20, or 40 min. A volume of 12.5 μL of sample was removed at each time point, and the amount of released siRNA was quantified *via* the gel electrophoresis techniques described in section 3.2.8.

4.2.8 Kinetic modeling

The dynamic silencing response was estimated with a kinetic model. A system of ordinary differential equations was used to model the changes in concentrations of siRNA, mRNA, and protein (see Equations 3.1-3.3 in Chapter 3 [section 3.3.3] for more details).³⁴ Degradation rate constants were computed on the basis of the component half-lives reported in literature,^{25, 35} and production rate constants were fit to ensure mRNA and protein steady-state values were reached in the absence of siRNA. The set of equations was solved using differential equation solver ode45 in MATLAB, and relative concentrations were normalized to 100.

4.2.9 Polyplex size determination

Average polyplex diameters were determined *via* fluorescence correlation spectroscopy (FCS) analysis. Polyplexes were formulated with Dy547-labeled siRNA and placed on cover slips, and the coverslips were attached to glass microscope slides made by SecureSeals from Life Technologies (Grand Island, NY). FCS measurements

were performed on an LSM 780 confocal microscope (Carl Zeiss, Oberkochen, Germany) using a 488 nm laser and a 40x (numerical aperture = 1.2) water immersion apochromat objective. Thirty measurements, each lasting 8 s, were taken for each sample. Data analysis was performed with ZEN 2010 software (Carl Zeiss). The structural and measurement parameters were determined using a solution of AlexaFluor555 dye with an assumed diffusion coefficient of $340 \mu\text{m}^2 \text{s}^{-1}$.³⁶ The raw values are recorded in Table B.1 in Appendix B.

4.2.10 Zeta potential analysis

Polyplex solutions were prepared as described and diluted with HEPES buffer to a volume of 1 mL. The solutions were transferred to a cuvette and analyzed using a ZetaPALS zeta potential analyzer from Brookhaven Instruments (Brookhaven, CT). The samples were measured at 25 °C, and the Smoluchowski model was used to analyze the data. Reported values were computed as the average of three independent experiments comprising 10 measurements each, and the raw values are recorded in Table B.2 in Appendix B.

4.2.11 mRNA knockdown analysis

GAPDH mRNA knockdown was measured using qPCR. Single and double transfections were carried out as described in section 4.2.4, and RNA was isolated by TRIzol® Reagent, according to the manufacturer's protocols, at 48 h (single dose) and 75 h (double dose) post-transfection. The iTaq™ Universal SYBR® Green One-Step Kit and the specific GAPDH and β -actin primers were used to prepare samples for qPCR in triplicate as described in the manufacturer's protocols. The cDNA synthesis and qPCR steps were conducted on a Bio-Rad CFX96™ using the following

conditions: 10 min at 50 °C; 1 min at 95 °C; 40 cycles of 10 s at 95 °C and 30 s at 60 °C; and finally, a 65 °C to 95 °C ramp at 0.5 °C every 5 s. The $\Delta\Delta\text{CT}$ method was used for fold change analysis,³⁷ and all test sample data were normalized to untreated cell data. Details related to the $\Delta\Delta\text{CT}$ method are described in Chapter 2 (section 2.7).

4.3 Results

4.3.1 siRNA binding efficiencies

Ethidium bromide exclusion assays were conducted to analyze the siRNA binding efficiencies of polyplexes formed from various ratios of mPEG-*b*-P(APNBMA)_{7,9}/mPEG-*b*-P(APNBMA)_{23,6} polymers, on a fixed molar basis of cationic amine groups. As shown in Figure 4.1A, formulations comprised of larger fractions of the longer polymer encapsulated siRNA more efficiently. These differences in binding affinity were apparent at N/P ratios ≤ 1 (Figure 4.1B). Furthermore, the ability of the nanocarriers to sequester complexed siRNA was enhanced greatly at an N/P ratio of 4, as indicated by the complete disappearance of fluorescence in the wells. Hence, all polyplexes were made at an N/P ratio of 4 in subsequent experiments to ensure complete encapsulation of siRNA and to minimize excessive positive charge.

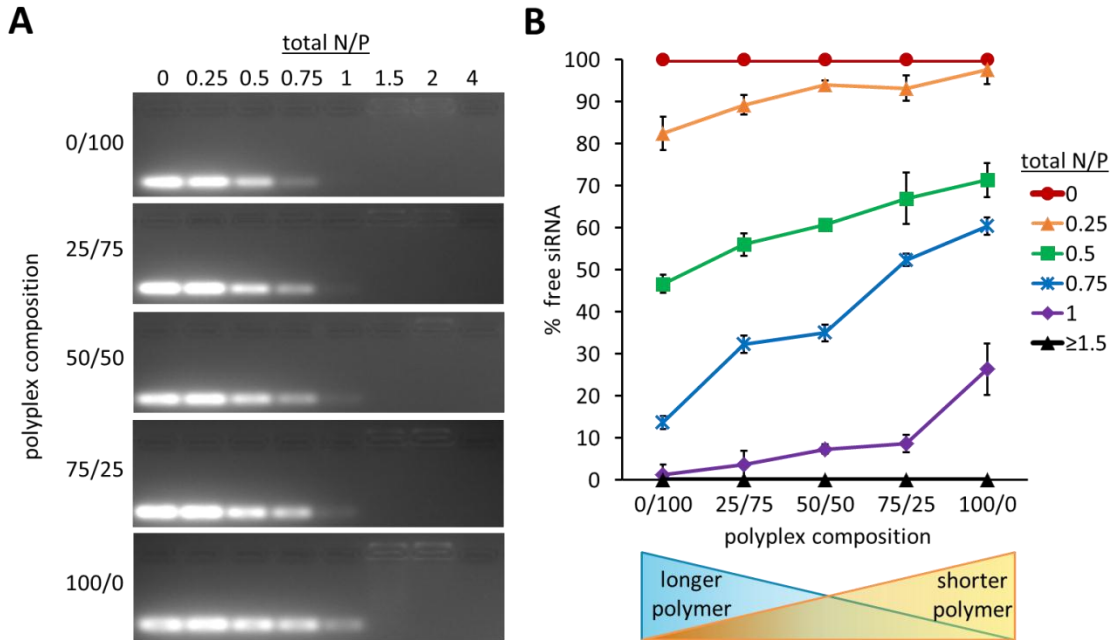


Figure 4.1: Ethidium bromide exclusion analyses of mPEG-*b*-P(APNBMA) polyplexes. The polyplex composition is defined as the ratio of mPEG-*b*-P(APNBMA)_{7.9}/mPEG-*b*-P(APNBMA)_{23.6} polymers, on a molar basis of cationic amine groups. (A) Representative gel electrophoresis images of polyplexes formed at varying total N/P ratios with different polymer compositions. (B) Quantification of the gel electrophoresis images in (A) calculated from ImageJ analysis of siRNA band intensities. Results are shown as the mean \pm standard deviation of data obtained from three independent experiments.

4.3.2 Tuning gene silencing

Given the differences in binding affinities in the different formulations, the gene silencing efficiency of each polyplex composition was examined. Mixed polyplexes containing siRNA targeting GAPDH, a model endogenous gene, were delivered to NIH/3T3 cells, and the cells were subsequently treated with 365 nm light. As shown in Figure 4.2, the 0/100 polyplexes [containing only mPEG-*b*-P(APNBMA)_{23.6}] exhibited ~40% protein knockdown, consistent with the literature.³⁴ Interestingly, the 100/0 formulation also was able to achieve a silencing efficiency of

~40%; however, all polyplexes comprised of a mixture of the two polymers exhibited enhanced knockdown levels, demonstrating that the degree of silencing was tunable on the basis of polyplex composition. In particular, the 50/50 formulation was able to mediate gene silencing most efficiently, with ~70% protein knockdown; this silencing effect is near the highest degree achievable with a single dose of siRNA given the half-lives of the targeted mRNA and protein.³⁴ This simple, yet powerful, strategy of mixing BCPs produced polyplexes with greater silencing efficiencies than nanocarriers comprised of a single polymer species, implying that the polymers were functioning in a synergistic manner.

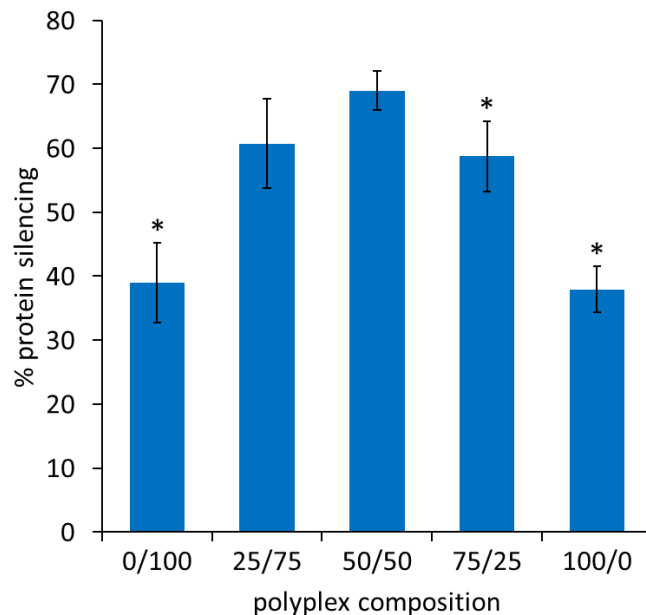


Figure 4.2: GAPDH protein silencing efficiencies of mPEG-*b*-P(APNBMA) polyplexes. The polyplex composition is defined as the ratio of mPEG-*b*-P(APNBMA)_{7,9}/mPEG-*b*-P(APNBMA)_{23,6} polymers, on a molar basis of cationic amine groups. Cells were treated with 20 nM siRNA polyplexes formed at an N/P ratio of 4, irradiated with 365 nm light for 10 min, and lysed for western blot analysis 48 h post-transfection. Polyplexes are formed from various ratios of mPEG-*b*-P(APNBMA)_{7,9}/mPEG-*b*-P(APNBMA)_{23,6} polymers on a fixed molar basis of cationic amine groups. Data represent the GAPDH protein expression levels relative to the levels of the loading control β -actin, normalized to the native protein levels in controls with no siRNA treatment. Results are shown as the mean \pm standard deviation of data obtained from three independent experiments. An asterisk indicates a statistically significant difference in silencing from the 50/50 composition ($p < 0.05$).

Many applications require carriers that are able not only to tune and maximize siRNA-mediated gene silencing, but also minimize off-target release and activity. As shown in Figure 4.3, cells transfected with any stably bound polyplex composition (e.g. an N/P ratio of 4) but not exposed to light treatment exhibited no gene knockdown. This result suggested that all of the polyplexes remained intact in the

cells unless triggered by the photo-stimulus, providing on/off control of siRNA activity.

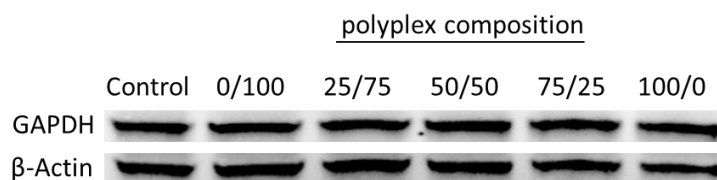


Figure 4.3: Western blot analysis of GAPDH protein levels following polyplex treatment without 365 nm light irradiation. Polyplexes were formed at a total N/P of 4, with different polymer compositions of mPEG-*b*-P(APNBMA)_{7.9}/mPEG-*b*-P(APNBMA)_{23.6}, on a molar basis of cationic amine groups. The cell extract was collected 48 h post-transfection. Relative band intensities were quantified on the basis of the change in GAPDH protein expression levels relative to the band intensity of the loading control, β -actin. These values were normalized to the native levels in controls with no treatment. No significant knockdown was exhibited in any samples in the absence of 365 nm irradiation.

4.3.3 Calculating siRNA availability to predicting gene silencing

To gain an understanding of why the mixed polyplexes were able to achieve enhanced gene silencing, the siRNA availability for each formulation was estimated. Within the context of *in vitro* experiments, the major barriers to activating the RNAi process are the cellular uptake of nanocarriers and the release of siRNA into the cytoplasm. Thus, quantitative estimates of how many siRNAs were able to overcome these two obstacles would enable the computation of siRNA availability. Kinetic modeling then could be employed to predict gene silencing efficiencies, given the relative number of siRNAs free to interact with the RISC for each formulation. Figure 4.4A depicts the critical biological barriers and provides an overview of the method for predicting the protein knockdown levels that were measured in Figure 4.2.

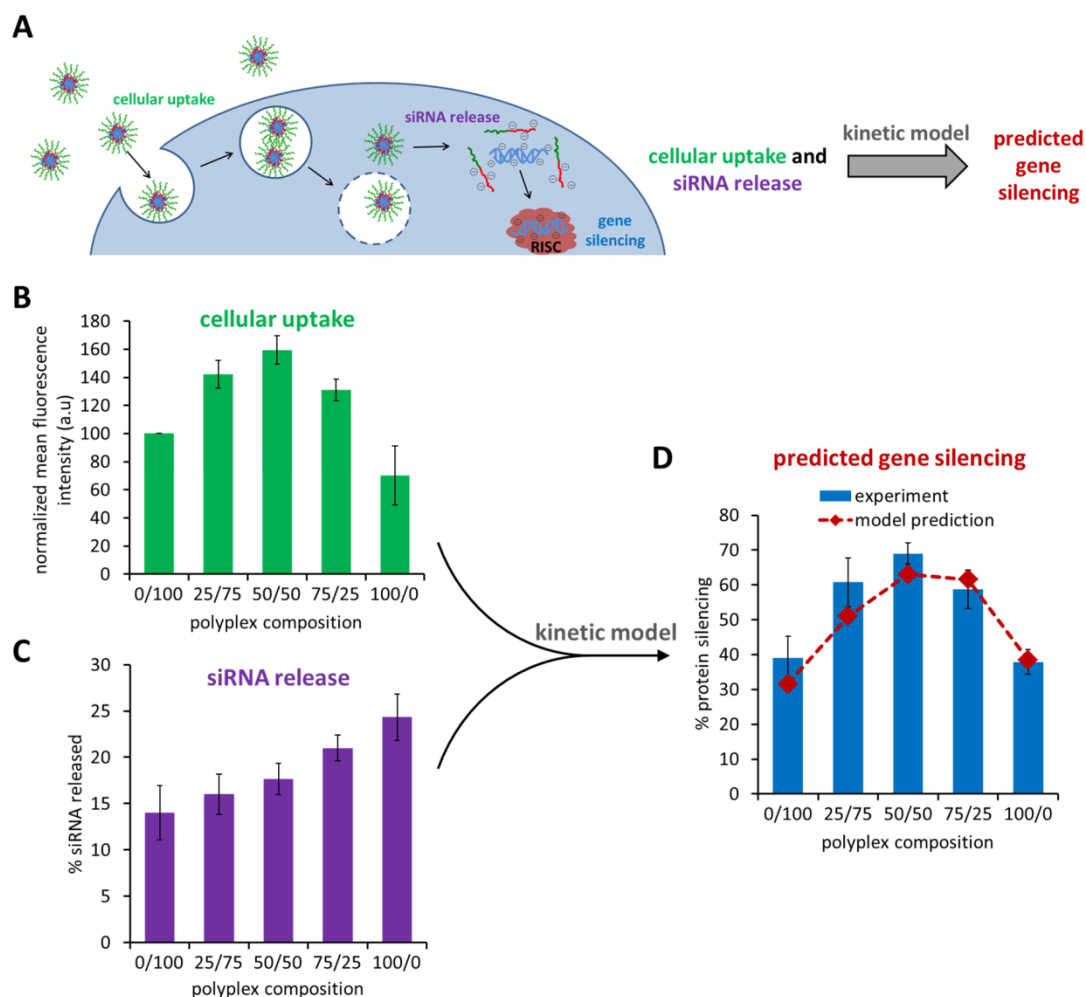


Figure 4.4: siRNA release and cellular uptake analyses to predict gene silencing using kinetic modeling. (A) Schematic of important biological barriers that determine the level of gene silencing, as estimated through the kinetic model. (B) Cellular uptake levels as a function of polyplex composition as measured by flow cytometry. The mean fluorescence intensity (MFI) per cell was normalized to the MFI for the 0/100 polyplexes. (C) Light-triggered release of siRNA from polyplexes following incubation in SDS solutions (S/P ratio of 2.5) and irradiation with 365 nm light for 10 min. The solutions were analyzed by gel electrophoresis analyses. (D) Kinetic modeling predictions of gene silencing on the basis of siRNA availability estimates from siRNA release and cellular uptake data. The predicted level of protein knockdown (red diamonds) was compared to the experimentally determined values from Figure 4.2 (blue bars). Results for all plots are shown as the mean \pm standard deviation of three independent samples.

4.3.3.1 Cellular uptake of polyplexes

The relative amount of siRNAs entering the cells through cellular internalization measurements was evaluated using fluorophore-labeled nucleic acids and detection through flow cytometry. As shown in Figure 4.4B, the level of cellular uptake varied as a function of the polymer composition of the nanocarriers. Cellular internalization efficiencies increased as the amount of mPEG-*b*-P(APNBMA)_{7,9} in the nanocarriers increased up to 50%; however, uptake efficiencies decreased beyond this critical threshold, and the 100/0 formulation was internalized least efficiently. The 50/50 polyplexes exhibited the highest level of cellular uptake with a normalized mean fluorescence intensity (MFI) of ~160%; i.e. 60% more uptake relative to 0/100 polyplexes. The significant differences in cellular uptake were found to be dependent on both nanocarrier size and surface charge (Figure 4.5), and could be enhanced through the simple mixing of the BCPs.

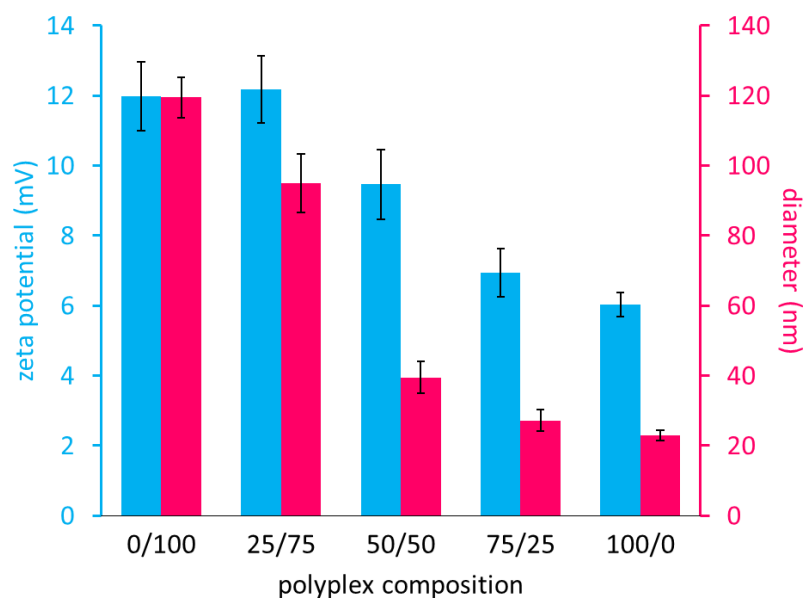


Figure 4.5: Average zeta potentials (light blue, associated with primary y-axis) and diameters (pink, associated with secondary y-axis) of polyplexes with varying compositions. Polyplexes were formed at a total N/P of 4, with different polymer compositions of mPEG-*b*-P(APNBMA)_{7,9}/mPEG-*b*-P(APNBMA)_{23,6}, on a molar basis of cationic amine groups. Results are shown as the mean \pm standard deviation of data obtained from three independent measurements.

4.3.3.2 Photo-triggered siRNA release

The ability of each nanocarrier to liberate siRNA upon application of the photo-stimulus was examined in SDS solutions that simulate lipid-rich intracellular environments.³⁴ As shown in Figure 4.4C, the amount of siRNA release was tunable on the basis of polyplex composition. Specifically, as the mPEG-*b*-P(APNBMA)_{7,9} content in the polyplexes increased, greater amounts of siRNA were liberated. Polyplexes containing a greater fraction of the longer polymer exhibited greater binding affinity for siRNA, which was consistent with the data in Figure 4.1.

4.3.3.3 Predicting gene silencing using kinetic modeling

Given that the levels of cellular uptake and light-induced polyplex disassembly were quantitatively determined as a function of nanocarrier composition, the relative amounts of total available siRNAs were computed for each formulation. These values were inputted into a kinetic model (Equations 3.1-3.3) as the amount of siRNA introduced following photo-triggered nanocarrier unpackaging. The model described the dynamic changes in siRNA, mRNA, and protein concentrations on the basis of component half-lives and cellular doubling times, as described in detail elsewhere.³⁴ Predictions of the changes in protein expression levels were subsequently computed and are displayed in Figure 4.4D as red diamonds. The model accurately captured the experimentally measured gene silencing data from Figure 4.2 (blue bars). Specifically, the model predicted that the 50/50 formulation would exhibit the greatest level of gene silencing. All mixed polyplexes also were calculated to be more efficient than either the 0/100 or 100/0 formulations. Thus, gene silencing efficiencies can be accurately predicted *a priori* through the use of the simple kinetic model on the basis of facile siRNA release and cellular uptake measurements.

4.3.4 Dynamic silencing response

The kinetic model also was employed to determine when the minimum protein level for a single dose of siRNA would be reached. The 50/50 formulation was used as the basis of the model because these polyplexes exhibited the maximum knockdown efficiency (Figure 4.2). As shown in Figure 4.6A, the mRNA and protein levels maintained their steady-state values before the introduction of siRNA, which was released only after light exposure at 3.5 h post-transfection. A rapid decrease in the mRNA levels was immediately apparent, followed by the slower decrease of the

protein levels. The amount of siRNA decreased with time, primarily due to dilution through cell division. Consequently, the mRNA expression levels reached a minimum level of <10% and started to recover, which caused the protein levels to plateau at ~36% (~64% silencing) before protein expression started to increase at 48 h post-transfection.

As depicted in Figure 4.6B, the kinetic model accurately captured the experimentally determined protein expression levels of the dynamic silencing response of the 50/50 polyplexes. Additionally, the model predicted GAPDH mRNA levels to be ~45%, which was in agreement with qPCR measurements, further validating the utility of the model. Thus, a streamlined and easily implemented kinetic modeling approach was able to accurately capture on/off silencing dynamics.

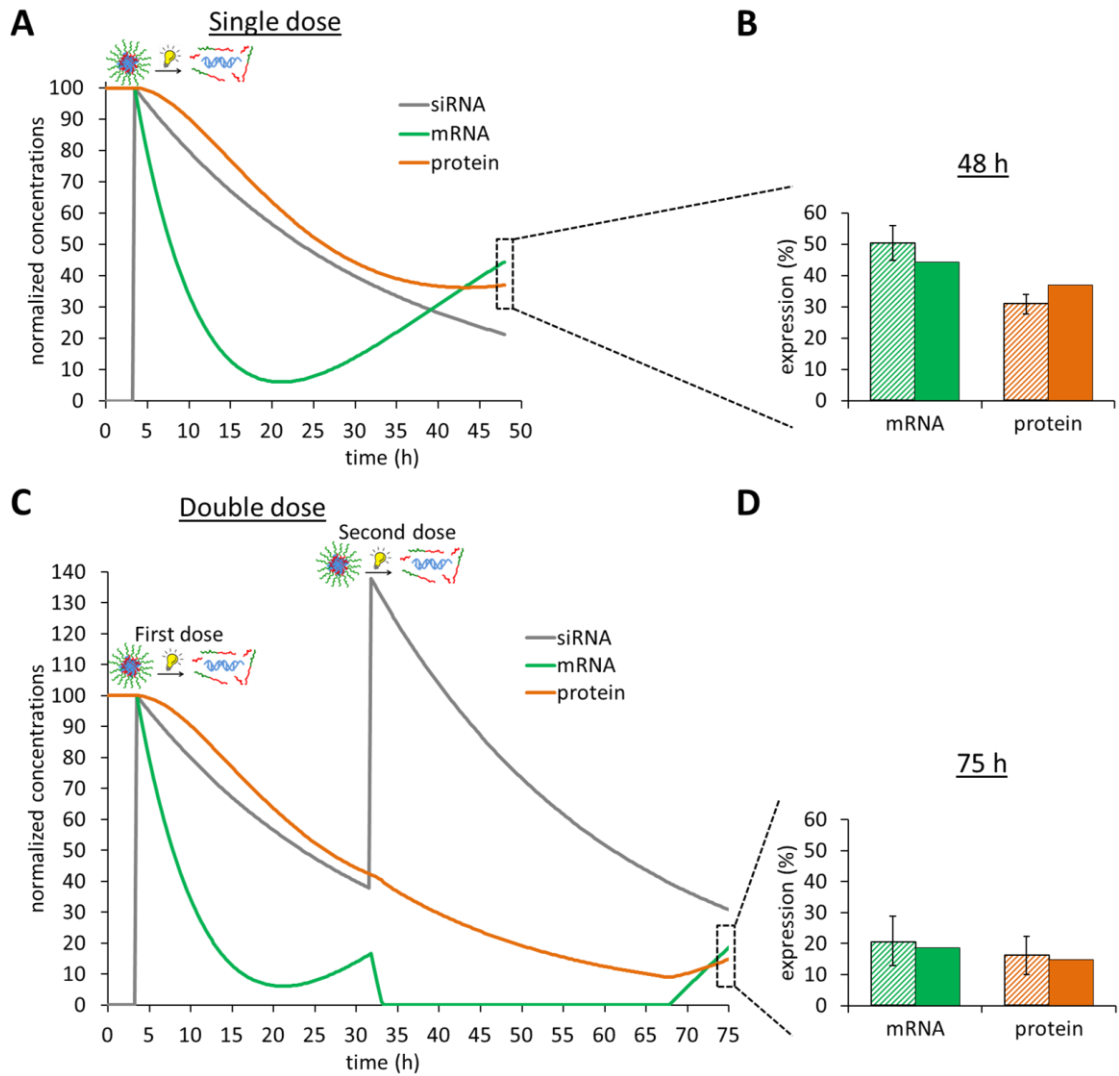


Figure 4.6: (A & C) Kinetic models predict the dynamic nature of the GAPDH silencing process with a single dose (A) and double dose (C) of siRNA. Initial protein and mRNA concentrations were normalized to 100. A dose of siRNA was introduced 3.5 h after each transfection, which corresponds to the time of 365 nm light treatment. (B & D) Cells were lysed at 48 h or 75 h following either a single dose (B) or double dose (D) of siRNA, respectively. GAPDH mRNA and protein expression levels were determined through qPCR and western blot experiments, respectively. Model predictions of mRNA (green) and protein (orange) expression levels at the end points of 48 h and 75 h are presented as solid bars; experimental values are presented as diagonal striped bars. Experimental values are shown as the mean \pm standard deviation of data obtained from three independent samples.

4.3.4.1 Dosing regimens and dynamic silencing response with multiple siRNA treatments

The model was used to predict the response to numerous dosing schedules to determine the optimal time to deliver the second dose of siRNA with the 50/50 polyplexes. Model results indicated that polyplexes delivered at 28 h post-transfection followed by 365 nm light irradiation 3.5 h later would result in significantly enhanced protein knockdown before those levels would start to recover at ~75 h post-transfection (Figure 4.6C). To test the validity of the mathematical model, mRNA and protein expression levels were measured at 75 h post-transfection as shown in Figure 4.6D. These experimentally determined values were in excellent agreement with the model results.

A noteworthy result of the above dosing studies was a reduction in GAPDH protein expression to ~15%, which is a factor of two below the minimum level achievable with a single dose (~30%). Therefore, repeated dosing was a successful method for further silencing GAPDH beyond the limits of a traditional single dose. Also, it is important to note that no gene knockdown was detected in cells that were not treated with light during the double dosing schedule, indicating that the polyplexes remained intact and the encapsulated siRNA remained dormant over several days (Figure 4.7). Taken together, the on/off release nature of the polyplexes, combined with the dosing schedule informed by kinetic modeling, enabled a two-fold decrease in the remaining GAPDH protein levels compared to the minimum single dose level.

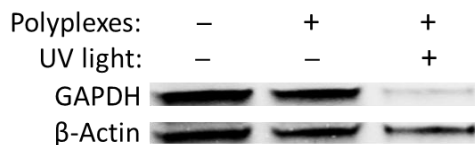


Figure 4.7: Representative western blot used to analyze GAPDH protein levels following a double dose delivery of polyplexes. Cells were transfected for 3 h with mPEG-*b*-P(APNBMA)_{7.9}/mPEG-*b*-P(APNBMA)_{23.6} polyplexes (50/50) containing GAPDH-targeting siRNA and irradiated 0.5 h later with 365 nm light for 10 min. A second transfection was performed 28 h after the first transfection, and the cell extract was collected 75 h after the first transfection (47 h after the second transfection). Relative band intensities were quantified on the basis of GAPDH protein expression levels and normalized to the band intensity of the loading control, β-actin. These values then were normalized to the native levels in controls with no treatment. No significant knockdown was noted without 365 nm light exposure. However, GAPDH protein levels were reduced to ~15% with 365 nm light treatment following the double dosing schedule, as compared to a minimum achievable reduction of ~30% after a single dose.

4.4 Discussion

Some of the most significant challenges that have hindered the clinical success of siRNA therapies are a lack of control over binding *vs.* release from the delivery vector and an insufficient understanding of the link between gene silencing dynamics and siRNA dosing. To address these challenges, mixed polymer formulations were designed that enhanced nucleic acid release in a controllable manner, which aided in the development of accurate predictive frameworks for dosing. One of the most common strategies for tuning nucleic acid binding affinity is through the variation of the molecular weight and/or charge density of the cationic polymer.^{3,4} Generally, BCPs with longer cationic blocks package siRNA more efficiently.⁵ To harness this molecular weight effect through a simpler and more scalable approach, nanocarriers

were formed with various ratios of the shorter and longer mPEG-*b*-P(APNBMA) polymers. As shown in Figure 4.1, the amount of free siRNA at a given N/P ratio decreased as the percentage of the longer polymer in the formulation increased. Despite the three-fold difference in number of cationic groups per polymer chain, formulations consisting of only the shorter polymer were able to produce compact nanocarriers at a relatively low N/P ratio of 4. Thus, all polyplexes were formulated at an N/P ratio of 4 to minimize the number of free mPEG-*b*-P(APNBMA) polymer chains in solution.

The gene silencing capacity of each formulation was analyzed to determine whether the differences in polymer binding strengths would affect the initiation of the RNAi process. Notably, without exposure to the photo-stimulus, all polyplexes remained inactive and did not mediate any detectable gene knockdown, including the 100/0 formulation comprised entirely of the weaker binding polymer (Figure 4.3). The complete dormancy was surprising, given that many other siRNA delivery systems undergo rapid polyanion- or serum-induced disassembly in the extracellular environment, leading to limited cellular uptake and gene silencing efficacy.^{38, 39} The result demonstrates the high stability of mPEG-*b*-P(APNBMA) polyplexes in polyanion-rich intracellular environments, likely due to cooperative electrostatic and hydrophobic interactions.³³ Robust stability is necessary to minimize undesired off-target effects in fields requiring precise spatiotemporal control over gene expression, such as regenerative medicine.²² Furthermore, the unique stability of the polyplexes ensures that siRNA is only released on-demand, ultimately enabling precisely controlled dosing regimens.

Upon treatment with 365 nm light, the nanocarriers induced silencing that was tunable on the basis of the polyplex composition due to the synergistic effects of simply mixing BCPs (Figure 4.2). In particular, the 50/50 polyplexes exhibited ~70% silencing, which is approximately the highest degree of knockdown achievable with a single dose of siRNA in rapidly dividing cells due to the relatively long half-life of the GAPDH protein.^{34,40} Specifically, studies have shown that even when sufficiently large amounts of siRNA are delivered to saturate the available RISC, the activated RISC complex is diluted too rapidly by cell division to degrade all of the target mRNA.⁴¹ Meanwhile, target proteins with a long half-life, such as GAPDH, do not fully degrade before mRNA levels begin to recover. Notably, the combined modeling and experimental results demonstrated the ability to achieve a level of silencing previously shown to correspond to RISC saturation³⁴ while using siRNA at a concentration of 20 nM; this concentration is significantly lower than concentrations used by many similar polyplex systems in literature (typically ≥ 100 nM).^{38,42} The efficacy of the mixed BCP polyplexes may be due to the combination of enhanced siRNA binding stability, resulting in minimal losses of siRNA to nucleases, and the ability to saturate RISC more efficiently *via* rapid siRNA release in the cytoplasm. Accordingly, the structure-function relationships underlying cellular processing and availability of siRNA were investigated.

The extent of cellular uptake is well-known to depend upon the size and zeta potential of the nanocarrier.⁴³⁻⁴⁵ Furthermore, the compositions of mixed polyplex and coacervate systems play major roles in determining nanocarrier structural characteristics.⁴⁶⁻⁴⁸ Recent reports have studied these effects with mixtures of BCPs comprised of different block constituents.^{8,13} In this work, the effects of mixing

chemically-identical BCPs of different molecular weights on nanocarrier structure were analyzed.

Analysis of polyplex size revealed that nanocarriers comprised of more mPEG-*b*-P(APNBMA)_{7.9} had smaller average diameters (Figure 4.5). This trend is explained by the lower charge density of the shorter polymers, which have only ~33% of the number of repeat units in the cationic block but are composed of the same PEG block, as the mPEG-*b*-P(APNBMA)_{23.6} polymers. Therefore, approximately three times as many mPEG-*b*-P(APNBMA)_{7.9} chains are needed to neutralize the anionic charges of the siRNA. This self-assembly process is influenced by the inherent molecular curvature of the BCPs to minimize energetically unfavorable conditions.⁴⁹ Thus, nanocarriers with smaller diameters are favored to accommodate the extra PEG chains in the corona and reduce steric effects. It also is important to note that a single population of polyplexes was detected for each formulation, suggesting that each polyplex was comprised of proportional amounts of each polymer. Although the effects of nanocarrier size on cellular internalization depend on the nanoparticle material and cell type, smaller particles are generally thought to be beneficial for more rapid endocytic uptake.^{43, 44, 50} Therefore, polyplexes with greater amounts of mPEG-*b*-P(APNBMA)_{7.9} would be expected to be internalized more efficiently.

The zeta potential of each formulation also was examined, and polyplexes comprised of higher fractions of mPEG-*b*-P(APNBMA)_{7.9} were found to have more neutral surface charges (Figure 4.5). This trend is the result of increased shielding of the positive polyplex core due to the inclusion of BCPs with higher mass fractions of PEG.^{8, 51} For example, despite their smaller sizes, the 0/100 polyplexes exhibited lower cellular uptake efficiencies because their low zeta potentials (~2 mV) hindered

electrostatically-driven transportation across the anionic cellular membrane.^{45, 52} The 50/50 polyplexes balanced the opposing requirements for efficient uptake with a relatively high zeta potential of ~10 mV and a relatively small diameter of ~40 nm. Thus, the nanocarrier surface charge and size were optimized *via* changes in polyplex composition to maximize cellular uptake, and ultimately overall gene silencing efficacy.

The use of mixtures of BCPs also affected the amount of siRNA release into the cytoplasm. Nanocarriers comprised of larger fractions of mPEG-*b*-P(APNBMA)_{7,9} disassembled to a greater extent upon application of the photo-stimulus (Figure 4.4C), which is consistent with reports in the literature that demonstrated polymers comprised of shorter cationic chains release nucleic acids more effectively.^{3, 6} Most notably, the 100/0 polyplexes released ~10% more siRNA than the 0/100 formulations. These quantitative analyses were critical in the computation of intracellular siRNA availability, which was used in combination with kinetic modeling to accurately capture the measured protein expression levels (Figure 4.4D). It is important to note that these predictions were made possible only because the nucleic acid delivery system is capable of precise and on-demand siRNA release.

The previous analyses explained why tuning the polyplex composition synergistically altered the gene silencing efficiencies of the formulations. However, developing a deeper understanding of the dynamic nature of the RNAi process in the system would help to identify rate-limiting steps and inform methods for further improving the level of protein knockdown with the existing formulations. The dynamic silencing process is governed by fundamental biological rates, such as cell doubling time and protein and mRNA half-lives. Therefore, these parameters directly

affect the maximum gene silencing efficiencies for each system with a single dose of siRNA. To demonstrate that the minimum protein levels were being measured 48 h post-transfection, kinetic modeling was employed. The characteristic rate parameters of NIH/3T3 cells and the GAPDH gene were used to generate predictions of mRNA and protein concentrations as a function of time. The model showed that 48 h post-transfection, a common time point in the literature for measuring protein knockdown, was indeed the optimal time when protein levels reached their minimum values and started to recover (Figure 4.6A). Furthermore, the modeling approaches showed that the silencing efficiency of this particular system was limited by two key factors. First, NIH/3T3 cells have rapid doubling times of ~24 h, which acts to dilute the intracellular siRNAs upon cell division. Second, because the GAPDH protein has a relatively long half-life, reported to be >35 h in NRK-52E rat kidney epithelial cells,⁵³ protein that was translated before the onset of transfection remains stable in the cell for long periods of time. Thus, within the rate-limiting constraints of the system, gene silencing was maximized through the combination of photo-responsive release and mixed polymer formulations.

The kinetic model was used to identify optimal times to measure changes in gene expression and also accurately capture the measured protein and mRNA levels (Figure 4.6B). Given that this approach considers only certain fundamental biological parameters, including cell doubling time and mRNA and protein half-lives, the predictions were remarkably accurate. Such simplicity is advantageous in modeling because it enables facile implementation compared to other relatively complicated models in the literature,⁵⁴ which makes it more likely to be widely adopted.

Additionally, it is noteworthy that the model was able to be streamlined only because these polyplexes exhibited precise control over the timing of siRNA release.

The photo-responsive nature of the mixed polyplex system enabled the 50/50 nanocarriers to mediate the maximum level of gene silencing achievable with a single dose of siRNA, as supported through the literature and kinetic modeling. Nonetheless, some biomedical applications require genes to be knocked down below a specific threshold in order to realize therapeutic efficacy.²⁶ Many siRNA-based applications would benefit from prolonged silencing greater than a few days. Multiple doses of siRNA must be administered to achieve these goals, particularly in rapidly dividing cell lines. However, dosing regimens often are not implemented due to concerns with cytotoxicity or a lack of predictive capabilities to determine an optimized dosing schedule.

After generating numerous dosing regimens using the mathematical model, 28 h after the first transfection was determined to be the optimal time to deliver the second dose. This dosing schedule allowed for the introduction of a second dose of siRNA as the mRNA levels started to recover due to dilution of the first dose following cell division (Figure 4.6C). The model also predicted that by 75 h post-transfection, mRNA levels would start to be restored, thus resulting in increased protein expression. These predictions were remarkably accurate, as confirmed by experimental measurements of mRNA and protein levels (Figure 4.6D). In particular, implementation of the dosing regimen resulted in a two-fold decrease in the concentration of remaining protein. These studies demonstrate the potential of delivering multiple doses of siRNA to achieve more robust gene knockdown, which was made possible through predictions from a mathematical model.

In addition to the implementation of kinetic modeling, the straightforward mixing of BCPs made it easy to maximize silencing and reduce synthesis workloads. To demonstrate these advantages, a third mPEG-*b*-P(APNBMA)_n BCP was synthesized with an intermediate cationic block length of $n = 16.6$. As shown in Figure 4.8, polyplexes made with this polymer were able to mediate >62% protein silencing, which is approximately the same level of knockdown exhibited by the 50/50 mixed formulation (Figure 4.2). Thus, the simple mixing of BCPs with short and long cationic blocks produced formulations at least as efficient as a polymer with optimized block lengths. Moreover, this strategy bypassed the tedious and time-consuming process of polymer synthesis required to generate a library of materials.

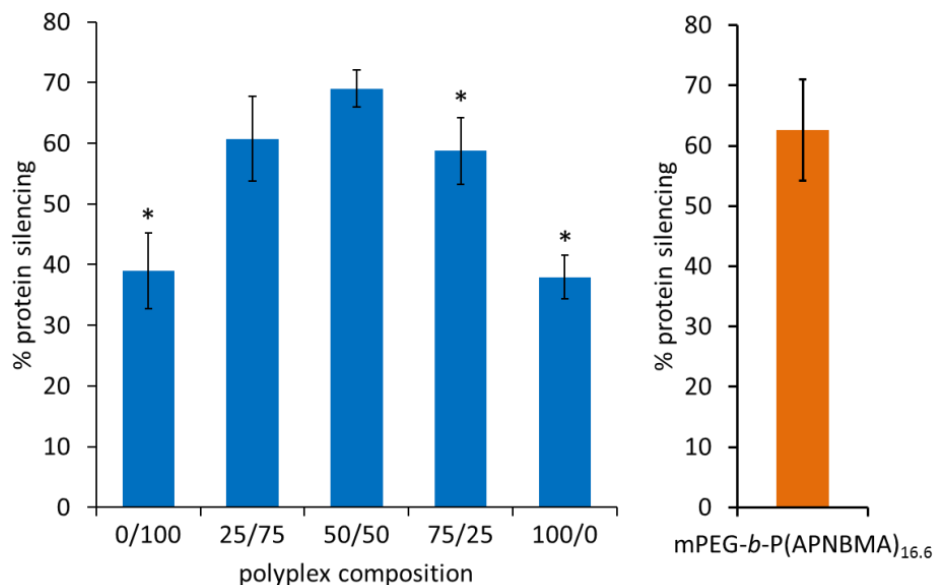


Figure 4.8: GAPDH protein silencing efficiencies of mPEG-*b*-P(APNBMA)/siRNA polyplexes. Polyplexes were formed at a total N/P of 4, with different polymer compositions of mPEG-*b*-P(APNBMA)_{7.9}/mPEG-*b*-P(APNBMA)_{23.6} (blue bars) or with mPEG-*b*-P(APNBMA)_{16.6} (orange bar). Cells were treated with 20 nM siRNA polyplexes, irradiated with 365 nm light for 10 min, and lysed for western blot analysis 48 h post-transfection. Data represent the GAPDH protein expression levels relative to the levels of the loading control β -actin, normalized to the native protein levels in controls with no siRNA treatment. Results are shown as the mean \pm standard deviation of data obtained from three independent experiments. An asterisk indicates a statistically significant difference in silencing from the 50/50 composition ($p < 0.05$).

4.5 Conclusions

The straightforward mixing of two photo-responsive BCPs resulted in the formulation of nanocarriers with enhanced silencing efficiencies as predicted by kinetic modeling. Upon delivery to cells, all polyplexes remained intact and did not induce protein knockdown prior to 365 nm irradiation; however, upon exposure to the photo-stimulus, the nanocarriers mediated temporally controlled gene silencing that was easily tunable on the basis of polyplex composition. Furthermore, the 50/50

formulation exhibited maximal knockdown of ~70% with a single dose of siRNA due to the saturation of cellular RNAi capacities. A simple kinetic model was employed to identify optimal double dosing schedules to further reduce GAPDH protein expression by a factor of two beyond the maximum level for a single dose. Moreover, the model confirmed that the gene silencing efficiencies were controlled by intracellular siRNA availability, as estimated through analysis of cellular uptake and light-induced siRNA release. Specifically, cellular uptake was enhanced by ~60% by optimizing nanocarrier size and zeta potential through the synergy of mixed BCPs. To my knowledge, this system is the first to mix photo-responsive, chemically-identical BCPs of different molecular weights to alter polyplex structures and improve efficacy. These findings and the kinetic modeling approach should be applicable to other stimuli-responsive polyplex systems with controlled siRNA release. Thus, this chapter uniquely combines advances in material design for improved spatiotemporal control over siRNA delivery with kinetic modeling capable of predicting gene silencing dynamics to inform optimal dosing schedules. These insights enabled enhanced gene silencing and facilitated the development of a dosing framework that can be exploited in other settings that require prolonged knockdown.

REFERENCES

1. Kelley, E. G.; Albert, J. N. L.; Sullivan, M. O.; Epps, T. H., III, Stimuli-responsive copolymer solution and surface assemblies for biomedical applications. *Chem. Soc. Rev.* **2013**, *42* (17), 7057-7071.
2. Williford, J.-M.; Wu, J.; Ren, Y.; Archang, M. M.; Leong, K. W.; Mao, H.-Q., Recent advances in nanoparticle-mediated siRNA delivery. *Annu. Rev. Biomed. Eng.* **2014**, *16*, 347-370.
3. Liu, X.; Howard, K. A.; dong, M. D.; Andersen, M. O.; Rahbek, U. L.; Johnsen, M. G.; Hansen, O. C.; Besenbacher, F.; Kjems, J., The influence of polymeric properties on chitosan/siRNA nanoparticle formulation and gene silencing. *Biomaterials* **2007**, *28* (6), 1280-1288.
4. deRonde, B. M.; Torres, J. A.; Minter, L. M.; Tew, G. N., Development of Guanidinium-Rich Protein Mimics for Efficient siRNA Delivery into Human T Cells. *Biomacromolecules* **2015**, *16* (10), 3172-3179.
5. Johnson, R. N.; Chu, D. S. H.; Shi, J.; Schellinger, J. G.; Carlson, P. M.; Pun, S. H., HPMA-oligolysine copolymers for gene delivery: Optimization of peptide length and polymer molecular weight. *J. Control. Release* **2011**, *155* (2), 303-311.
6. Kunath, K.; von Harpe, A.; Fischer, D.; Peterson, H.; Bickel, U.; Voigt, K.; Kissel, T., Low-molecular-weight polyethylenimine as a non-viral vector for DNA delivery: comparison of physicochemical properties, transfection efficiency and in vivo distribution with high-molecular-weight polyethylenimine. *J. Control. Release* **2003**, *89* (1), 113-125.
7. Strand, S. P.; Lelu, S.; Reitan, N. K.; Davies, C. d. L.; Artursson, P.; Varum, K. M., Molecular design of chitosan gene delivery systems with an optimized balance between polyplex stability and polyplex unpacking. *Biomaterials* **2010**, *31* (5), 975-987.

8. Miteva, M.; Kirkbride, K. C.; Kilchrist, K. V.; Werfel, T. A.; Li, H.; Nelson, C. E.; Gupta, M. K.; Giorgio, T. D.; Duvall, C. L., Tuning PEGylation of mixed micelles to overcome intracellular and systemic siRNA delivery barriers. *Biomaterials* **2015**, *38*, 97-107.
9. Nelson, C. E.; Kintzing, J. R.; Hanna, A.; Shannon, J. M.; Gupta, M. K.; Duvall, C. L., Balancing cationic and hydrophobic content of PEGylated siRNA polyplexes enhances endosome escape, stability, blood circulation time, and bioactivity in vivo. *ACS Nano* **2013**, *7* (10), 8870-8880.
10. Wang, H.-X.; Xiong, M.-H.; Wang, Y.-C.; Zhu, J.; Wang, J., N-acetylgalactosamine functionalized mixed micellar nanoparticles for targeted delivery of siRNA to liver. *J. Controlled Release* **2013**, *166* (2), 106-114.
11. Wei, Z.; Hao, J.; Yuan, S.; Li, Y.; Juan, W.; Sha, X.; Fang, X., Paclitaxel-loaded Pluronic P123/F127 mixed polymeric micelles: Formulation, optimization and in vitro characterization. *Int. J. Pharm.* **2009**, *376* (1-2), 176-185.
12. Li, Y.; Li, J.; Chen, B.; Chen, Q.; Zhang, G.; Liu, S.; Ge, Z., Polyplex micelles with thermoresponsive heterogeneous coronas for prolonged blood retention and promoted gene transfection. *Biomacromolecules* **2014**, *15* (8), 2914-2923.
13. Pujol, M. O.; Coleman, D. J. L.; Allen, C. D.; Heidenreich, O.; Fulton, D. A., Determination of key structure-activity relationships in siRNA delivery with a mixed micelle system. *J. Controlled Release* **2013**, *172* (3), 939-945.
14. Du, F.-S.; Wang, Y.; Zhang, R.; Li, Z.-C., Intelligent nucleic acid delivery systems based on stimuli-responsive polymers. *Soft Matter* **2010**, *6* (5), 835-848.
15. Won, Y.-W.; Yoon, S.-M.; Lee, K.-M.; Kim, Y.-H., Poly(oligo-D-arginine) with internal disulfide linkages as a cytoplasm-sensitive carrier for siRNA delivery. *Mol. Ther.* **2011**, *19* (2), 372-380.
16. Li, J.; Yu, X.; Wang, Y.; Yuan, Y.; Xiao, H.; Cheng, D.; Shuai, X., A reduction and pH dual-sensitive polymeric vector for long-circulating and tumor-targeted siRNA delivery. *Adv. Mater.* **2014**, *26* (48), 8217-8224.

17. Huang, X.; Hu, Q.; Braun, G. B.; Pallaoro, A.; Morales, D. P.; Zasadzinski, J.; Clegg, D. O.; Reich, N. O., Light-activated RNA interference in human embryonic stem cells. *Biomaterials* **2015**, *63* (0), 70-79.
18. Shah, S.; Rangarajan, S.; Friedman, S. H., Light activated RNA interference. *Angew. Chem. Int. Ed.* **2005**, *44* (9), 1328-1332.
19. Nguyen, Q. N.; Chavli, R. V.; Marques, J. T.; Conrad, P. G.; Wang, D.; He, W. H.; Belisle, B. E.; Zhang, A. G.; Pastor, L. M.; Witney, F. R.; Morris, M.; Heitz, F.; Divita, G.; Williams, B. R. G.; McMaster, G. K., Light controllable siRNAs regulate gene suppression and phenotypes in cells. *Biochim. Biophys. Acta-Biomembranes* **2006**, *1758* (3), 394-403.
20. Lee, H.; Kim, Y.; Schweickert, P. G.; Konieczny, S. F.; Won, Y.-Y., A photo-degradable gene delivery system for enhanced nuclear gene transcription. *Biomaterials* **2014**, *35* (3), 1040-1049.
21. Huschka, R.; Barhoumi, A.; Liu, Q.; Roth, J. A.; Ji, L.; Halas, N. J., Gene silencing by gold nanoshell-mediated delivery and laser-triggered release of antisense oligonucleotide and siRNA. *ACS Nano* **2012**, *6* (9), 7681-7691.
22. Saltzman, W. M.; Olbricht, W. L., Building drug delivery into tissue engineering. *Nat. Rev. Drug Discov.* **2002**, *1* (3), 177-186.
23. Cuccato, G.; Polynikis, A.; Siciliano, V.; Graziano, M.; di Bernardo, M.; di Bernardo, D., Modeling RNA interference in mammalian cells. *BMC Systems Biology* **2011**, *5*:19.
24. Raab, R. M.; Stephanopoulos, G., Dynamics of gene silencing by RNA interference. *Biotechnol. Bioeng.* **2004**, *88* (1), 121-132.
25. Bartlett, D. W.; Davis, M. E., Insights into the kinetics of siRNA-mediated gene silencing from live-cell and live-animal bioluminescent imaging. *Nucleic Acids Res.* **2006**, *34* (1), 322-333.
26. Bartlett, D. W.; Davis, M. E., Impact of tumor-specific targeting and dosing schedule on tumor growth inhibition after intravenous administration of siRNA-containing nanoparticles. *Biotechnol. Bioeng.* **2008**, *99* (4), 975-985.
27. Zuckerman, J. E.; Davis, M. E., Clinical experiences with systemically administered siRNA-based therapeutics in cancer. *Nat. Rev. Drug Discovery* **2015**, *14* (12), 843-856.

28. Varga, C. M.; Hong, K.; Lauffenburger, D. A., Quantitative analysis of synthetic gene delivery vector design properties. *Mol. Ther.* **2001**, *4* (5), 438-446.
29. Roth, C. M., Quantitative measurements and rational materials design for intracellular delivery of oligonucleotides. *Biotechnol. Prog.* **2008**, *24* (1), 23-28.
30. Chen, H. H.; Ho, Y.-P.; Jiang, X.; Mao, H.-Q.; Wang, T.-H.; Leong, K. W., Quantitative comparison of intracellular unpacking kinetics of polyplexes by a model constructed from quantum Dot-FRET. *Mol. Ther.* **2008**, *16* (2), 324-332.
31. Parra-Guillen, Z. P.; Gonzalez-Aseguinolaza, G.; Berraondo, P.; Troconiz, I. F., Gene therapy: A pharmacokinetic/pharmacodynamic modelling overview. *Pharm. Res.* **2010**, *27* (8), 1487-1497.
32. Green, M. D.; Foster, A. A.; Greco, C. T.; Roy, R.; Lehr, R. M.; Epps, T. H., III; Sullivan, M. O., Catch and release: photocleavable cationic diblock copolymers as a potential platform for nucleic acid delivery. *Polym. Chem.* **2014**, *5* (19), 5535-5541.
33. Foster, A. A.; Greco, C. T.; Green, M. D.; Epps, T. H., III; Sullivan, M. O., Light-mediated activation of siRNA release in diblock copolymer assemblies for controlled gene silencing. *Adv. Healthc. Mater.* **2015**, *4* (5), 760-770.
34. Greco, C. T.; Epps, T. H., III; Sullivan, M. O., Mechanistic design of polymer nanocarriers to spatiotemporally control gene silencing. *ACS Biomater. Sci. Eng.* **2016**, *2* (9), 1582-1594.
35. Dani, C.; Piechaczyk, M.; Audigier, Y.; Elsbouty, S.; Cathala, G.; Marty, L.; Fort, P.; Blanchard, J. M.; Jeanteur, P., Characterization of the transcription products of glyceraldehyde 3-phosphate-dehydrogenase gene in HeLa cells. *Eur. J. Biochem.* **1984**, *145* (2), 299-304.
36. Ross, N. L.; Munsell, E. V.; Sabanayagam, C.; Sullivan, M. O., Histone-targeted polyplexes avoid endosomal escape and enter the nucleus during postmitotic redistribution of ER membranes. *Mol. Ther. Nucleic Acids* **2015**, *4*, e226.
37. Schmittgen, T. D.; Livak, K. J., Analyzing real-time PCR data by the comparative C-T method. *Nat. Protoc.* **2008**, *3* (6), 1101-1108.

38. Buyens, K.; Meyer, M.; Wagner, E.; Demeester, J.; De Smedt, S. C.; Sanders, N. N., Monitoring the disassembly of siRNA polyplexes in serum is crucial for predicting their biological efficacy. *J. Control. Release* **2010**, *141* (1), 38-41.
39. Vader, P.; van der Aa, L. J.; Engbersen, J. F. J.; Storm, G.; Schiffelers, R. M., Physicochemical and biological evaluation of siRNA polyplexes based on PEGylated poly(amido amine)s. *Pharm. Res.* **2012**, *29* (2), 352-361.
40. Malmo, J.; Sorgard, H.; Varum, K. M.; Strand, S. P., siRNA delivery with chitosan nanoparticles: Molecular properties favoring efficient gene silencing. *J. Controlled Release* **2012**, *158* (2), 261-268.
41. Hutvagner, G.; Simard, M. J.; Mello, C. C.; Zamore, P. D., Sequence-specific inhibition of small RNA function. *PLoS Biol.* **2004**, *2* (4), 465-475.
42. Kim, H. J.; Miyata, K.; Nomoto, T.; Zheng, M.; Kim, A.; Liu, X.; Cabral, H.; Christie, R. J.; Nishiyama, N.; Kataoka, K., siRNA delivery from triblock copolymer micelles with spatially-ordered compartments of PEG shell, siRNA-loaded intermediate layer, and hydrophobic core. *Biomaterials* **2014**, *35* (15), 4548-4556.
43. Sahay, G.; Alakhova, D. Y.; Kabanov, A. V., Endocytosis of nanomedicines. *J. Controlled Release* **2010**, *145* (3), 182-195.
44. Hillaireau, H.; Couvreur, P., Nanocarriers' entry into the cell: relevance to drug delivery. *Cell. Mol. Life Sci.* **2009**, *66* (17), 2873-2896.
45. Gary, D. J.; Puri, N.; Won, Y.-Y., Polymer-based siRNA delivery: Perspectives on the fundamental and phenomenological distinctions from polymer-based DNA delivery. *J. Controlled Release* **2007**, *121* (1-2), 64-73.
46. Grabowska, A. M.; Kircheis, R.; Kumari, R.; Clarke, P.; McKenzie, A.; Hughes, J.; Mayne, C.; Desai, A.; Sasso, L.; Watson, S. A.; Alexander, C., Systemic in vivo delivery of siRNA to tumours using combination of polyethyleneimine and transferrin-polyethyleneimine conjugates. *Biomater. Sci.* **2015**, *3* (11), 1439-1448.
47. Wang, Y. L.; Kimura, K.; Dubin, P. L.; Jaeger, W., Polyelectrolyte-micelle coacervation: Effects of micelle surface charge density, polymer molecular weight, and polymer/surfactant ratio. *Macromolecules* **2000**, *33* (9), 3324-3331.

48. Bohidar, H.; Dubin, P. L.; Majhi, P. R.; Tribet, C.; Jaeger, W., Effects of protein-polyelectrolyte affinity and polyelectrolyte molecular weight on dynamic properties of bovine serum albumin-poly(diallyldimethylammonium chloride) coacervates. *Biomacromolecules* **2005**, *6* (3), 1573-1585.
49. Blanazs, A.; Armes, S. P.; Ryan, A. J., Self-assembled block copolymer aggregates: from micelles to vesicles and their biological applications. *Macromol. Rapid Commun.* **2009**, *30* (4-5), 267-277.
50. Chang, T.; Lord, M. S.; Bergmann, B.; Macmillan, A.; Stenzel, M. H., Size effects of self-assembled block copolymer spherical micelles and vesicles on cellular uptake in human colon carcinoma cells. *J. Mater. Chem. B* **2014**, *2* (19), 2883-2891.
51. Lin, W. J.; Hsu, W. Y., Pegylation effect of chitosan based polyplex on DNA transfection. *Carbohydr. Polym.* **2015**, *120*, 7-14.
52. Elsabahy, M.; Wooley, K. L., Design of polymeric nanoparticles for biomedical delivery applications. *Chem. Soc. Rev.* **2012**, *41* (7), 2545-2561.
53. Franch, H. A.; Sooparb, S.; Du, J., A mechanism regulating proteolysis of specific proteins during renal tubular cell growth. *J. Biol. Chem.* **2001**, *276* (22), 19126-19131.
54. Groenenboom, M. A. C.; Maree, A. F. M.; Hogeweg, P., The RNA silencing pathway: The bits and pieces that matter. *PLoS Comput. Biol.* **2005**, *1* (2), 155-165.

Chapter 5

INCORPORATION OF ANIONIC EXCIPIENTS FOR IMPROVED THERANOSTICS

This chapter describes the incorporation of anionic excipients into polyplexes to improve siRNA release and to impart diagnostic capabilities to the formulations. Specifically, poly(acrylic acid) polymers and quantum dots were used to enhance gene silencing efficiencies and allow for the dynamic self-reporting of polyplex disassembly. This work was conducted in collaboration with Jason C. Andrechak. The text, tables, and figures in this chapter are adapted and reprinted with permission from Greco, C. T.; Andrechak, J. C.; Epps, T. H., III; Sullivan, M. O., Anionic polymer and quantum dot excipients to facilitate siRNA release and self-reporting of disassembly in stimuli-responsive nanocarrier formulations. *Biomacromolecules* 2017, 18, 1814-1824. Copyright 2017 American Chemical Society.

5.1 Introduction

One of the primary advantages of small interfering RNA (siRNA) is its high potency, as only $\sim 10^3$ siRNAs per cell are needed to significantly suppress gene expression *in vitro* and *in vivo*.¹⁻³ However, most RNAi protocols require doses corresponding to $\sim 10^7$ - 10^9 siRNAs per cell,^{4,5} meaning that $< 0.01\%$ of the dosed siRNA molecules is available to engage the RNA-induced silencing complex (RISC), even in the most efficient delivery platforms. This inefficiency in siRNA usage is the cause of many practical issues that have hindered clinical translation, including dose-

limiting toxicities and prohibitively high costs associated with administering large excesses of expensive siRNAs.^{6,7}

One of the primary barriers to high delivery efficiencies is a lack of control over binding *vs.* release of siRNA nanopackages.^{8,9} These contradictory requirements necessitate a compromise between stability and release in most polymeric nanocomplexes (polyplexes),¹⁰ particularly in classical two-component (siRNA/cationic polymer) systems with limited means to manipulate electrostatic interactions. Compounding these issues is a lack of diagnostic tools available to mechanistically probe binding/release behavior *in vitro* and *in vivo*.

A promising strategy for addressing these challenges is the incorporation of additional components to modulate the release of siRNA and/or enable quantification of binding/release *in situ*.¹¹ These components often are polymers, peptides, proteins, or glycosaminoglycans with high negative charge densities¹²⁻¹⁴ that can alter nucleic acid binding properties, while also providing enhanced ability to release the payload from the polyplexes.^{15,16} Specifically, anionic excipients that have a strong binding affinity for the cationic polymers may provide additional stability to the electrostatically assembled polyplexes while simultaneously enabling improved release of siRNA.^{11,17} For example, Han *et al.* reported that the incorporation of γ -poly(glutamic acid) (γ -PGA) or sodium tripolyphosphate (TPP) into galactose-modified trimethyl chitosan-cysteine (GTC) polyplexes tuned the electrostatic interactions and increased siRNA release, resulting in enhanced gene silencing.¹⁷ In addition to enhancing siRNA release, numerous studies indicate that the addition of an anionic excipient can improve biocompatibility and affect cellular uptake.¹⁸ For example, the incorporation of γ -PGA into polyethylenimine (PEI)/nucleic acid

complexes increased cellular internalization and reduced toxicity.¹² Conversely, other reports demonstrated that anionic components reduce both passive uptake into cells and interactions with tissues throughout the body.^{19, 20} This stealthy behavior may be exploited *in vivo* to reduce non-specific cellular internalization and increase the delivery to the targeted tissue.^{19, 21}

The incorporation of anionic components also can provide integrated diagnostic/imaging capacities, which would be especially useful for locating and/or quantifying nanocarrier disassembly due to the innate capacity to dynamically report release events. Indeed, many promising theranostic strategies combine both therapeutic and diagnostic properties in a single formulation;²² however, these systems often require that the payload is labeled with the diagnostic agent²³ or conjugated to a nanoparticle.²⁴ Both labeling and conjugation approaches can attenuate nucleic acid binding and alter intracellular trafficking.²⁵ Thus, excipients that can simultaneously enhance efficacy and provide diagnostic capabilities would avoid competitive interactions that may hinder nucleic acid activity. Such integrated approaches would accelerate the testing of novel excipients to improve delivery efficiencies.

Although many excipient-containing formulations exhibit promising characteristics, several problems persist. One major challenge relates to finding a balance in binding affinity that allows for sufficient siRNA release without sacrificing extracellular stability.²⁶ For example, Huang *et al.* demonstrated that the addition of an anionic polymer, poly(glutamic acid)-*g*-poly(ethylene glycol) (PGA-*g*-mPEG), into poly(ϵ -caprolactone)-*g*-poly(N, N-dimethylaminoethyl methacrylate) (PCL-*g*-PDMAEMA)/siRNA polyplexes resulted in increased intracellular stability but reduced gene silencing efficiencies relative to unmodified polyplexes. This behavior

was attributed to loosened complexes that allowed siRNA to escape prior to cellular uptake,⁴ highlighting the challenging nature of producing stable multicomponent nanocarriers. Another key hurdle to the successful use of excipients in siRNA delivery is the lack of knowledge regarding optimal molecular weights, loading fractions, and charge densities of the anionic components.²⁷ Although these properties have been studied in coacervate systems and are critical determinants of nanocarrier efficacy,²⁸ few reports have provided quantitative understanding of how these parameters affect nucleic acid delivery systems and alter siRNA release and gene silencing.^{17, 27} For example, Schlegel *et al.* reported the use of PAA, among other anionic excipients, for enhanced delivery of siRNA liposomes but explored only a few molecular weights (4.5 or 1,100 kDa for PAA).²⁷ The inclusion of these PAA molecular weights only led to minor improvements in gene silencing, and the authors did not uncover direct structure-function relationships related to siRNA release.

In this chapter, poly(acrylic acid) (PAA) and quantum dots (QD)s were used as excipients in stimuli-responsive siRNA polyplexes. PAA was chosen because of its extensive use in a variety of FDA-approved products,²⁹ high anionic charge density (almost twice that of γ -PGA),²⁷ commercial availability, and low cost. Six different PAA molecular weights spanning three orders of magnitude were investigated to elucidate the effects of polymer chain length on polyplex stability and siRNA release. QDs coated with carboxylic acid groups were chosen due to their diagnostic capabilities (superior fluorescent properties and potential for bioimaging),³⁰ concentrated anionic charge density, and commercial availability.

PAA and/or QDs were incorporated into polyplex assemblies comprised of mPEG-*b*-poly(5-(3-(amino)propoxy)-2-nitrobenzyl methacrylate) [mPEG-*b*-

P(APNBMA)] block copolymers (BCP)s³¹ and siRNA (Figure 5.1). siRNA release/gene silencing was optimized by varying the weight ratio of siRNA and PAA (with the total weight of the anionic components held constant) and the molecular weight of PAA, and formulations comprised of 30/70 (w/w) PAA/siRNA with PAA molecular weights of 154 kDa and 240 kDa (an order of magnitude larger than siRNA) were the most efficient. The PAA-containing polyplexes were extremely stable for at least one week in storage and did not lose their efficacy when transfected in serum-supplemented media. Furthermore, the gene silencing efficiency of each formulation could be predicted *a priori* on the basis of heparin-induced siRNA release assays and RNAi modeling approaches. QDs also were incorporated into the polyplexes to produce multi-functional nanostructures with increased gene silencing efficiency and diagnostic capabilities. In particular, these nanocarriers self-reported polyplex disassembly with a Förster resonance energy transfer (FRET)-based detection system, and QD incorporation enhanced visualization *via* cryogenic transmission electron microscopy (cryo-TEM). Thus, the incorporation of anionic excipients is a promising method for improving delivery efficiencies, reducing costs, and mitigating toxicity-associated side effects associated with nucleic acid delivery.

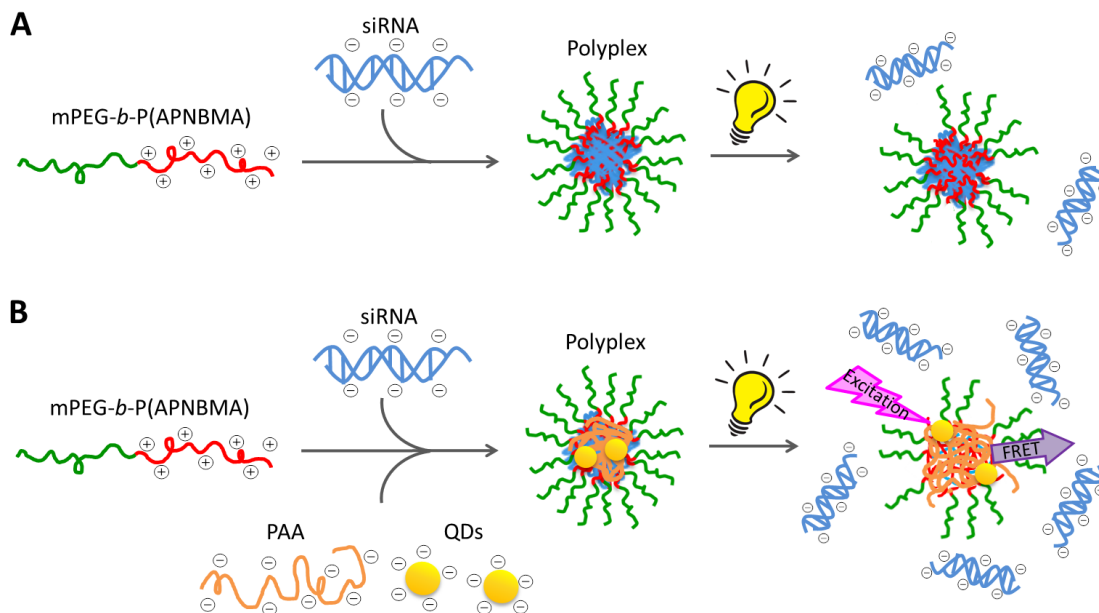


Figure 5.1: Cartoon schematic of mPEG-*b*-P(APNBMA) siRNA polyplexes (A) without PAA or QDs and (B) with PAA and QDs. Following polyplex formation, the formulations were treated with a photo-stimulus to trigger unpackaging of siRNA. The incorporation of the excipients resulted in enhanced and selective release of siRNA.

5.2 Materials and Methods

5.2.1 Materials

The mPEG-*b*-P(APNBMA)_{23,6} polymer ($M_n = 13.1$ kDa) was synthesized via atom-transfer radical polymerization as described previously.³¹ Non-targeted siRNA molecules (universal negative control) and branched PEI (25 kDa) were purchased from Sigma-Aldrich (St. Louis, MO). Anti-GAPDH siRNA was obtained from GE Healthcare Dharmacon, Inc. (Chicago, IL). PAA polymers of varying molecular weights were obtained from Polysciences, Inc. (Warrington, PA) ($M_w = 2$ kDa; 30 kDa; 4,000 kDa), Polymer Source (Dorval, Quebec, Canada) ($M_w = 154$ kDa; 642 kDa), and Acros Organics (Waltham, MA) ($M_w = 240$ kDa). Qdot® 605 ITK™

Carboxyl Quantum Dots and Opti-MEM® media were obtained from Life Technologies (Carlsbad, CA). Rabbit IgG polyclonal GAPDH antibody and secondary goat anti-rabbit IgG polyclonal horseradish peroxidase (HRP) antibody were purchased from AbCam (Cambridge, MA). The rabbit IgG polyclonal actin antibody was purchased from Santa Cruz Biotechnology (Dallas, TX). Dulbecco's Modified Eagle Medium (DMEM) and PBS (150 mM NaCl) solutions were purchased from Corning Life Sciences – Mediatech Inc. (Manassas, VA). TEM grids were obtained from Electron Microscopy Sciences (Hatfield, PA). Lanthanide atom doped NaYF₄ upconverting nanoparticles (UCNP)s capped with carboxylic acid were obtained from the Doty lab at the University of Delaware dispersed in 0.1 M mercaptopropionic acid (MPA) in water at a concentration of approximately 1 mg mL⁻¹. All other reagents were purchased from Thermo Fisher Scientific (Waltham, MA).

5.2.2 Preparation of nanocarriers

Polyplexes were formed by a self-assembly process through mixing of siRNA, PAA, QDs and mPEG-*b*-P(APNBMA) in 20 nM 4-(2-hydroxyethyl)piperazine-1-ethanesulfonic acid (HEPES) buffer at pH 6.0. A solution containing all anionic components (e.g., siRNA, PAA, QDs) and a solution containing the cationic mPEG-*b*-P(APNBMA) were prepared separately with equal volumes. The standard (unmodified) polyplex was comprised of 0.4 µg siRNA and mPEG-*b*-P(APNBMA) at an N/P (N: amine groups on mPEG-*b*-P(APNBMA); P: phosphate groups on siRNA) of 4 in a total volume of 25 µl. In PAA-modified polyplexes, the PAA/siRNA weight ratios were varied while holding the total weight of the anionic components constant. (*Note: the compositions of PAA-containing polyplexes are reported as PAA/siRNA (w/w) ratios.*) The cationic block copolymer solutions were added dropwise to the

anionic component solutions while mixing thoroughly *via* vortexing. The resulting solutions were incubated at room temperature for 30 min prior to further analysis.

5.2.3 Cell culture

Mouse embryonic fibroblasts (NIH/3T3) were obtained from the American Type Culture Collection (ATCC; Manassas, VA) and were cultured following ATCC protocols in a growth medium consisting of DMEM supplemented with 10 vol% fetal bovine serum (FBS) and 1 vol% penicillin-streptomycin (P/S). The cells were cultured in a humid environment maintained at 37 °C and 5 vol% CO₂.

5.2.4 *In vitro* cell transfection

NIH/3T3 cells were cultured in six-well plates at a density of 10,000 cells cm⁻² for 24 h. Before transfection, the supplemented growth medium was removed, and the cells were washed with PBS. Opti-MEM was added to the plates before the polyplex solutions were added dropwise to a final concentration of 20 nM in each well. Following a 3 h transfection period, the Opti-MEM was replaced with supplemented DMEM for a 30 min recovery period. The DMEM was replaced with phenol red-free Opti-MEM®, and the cells were irradiated with 365 nm light at an intensity of 200 W/m² for 10 min on a 37 °C hotplate. Supplemented DMEM was added to the wells after irradiation.

5.2.5 GAPDH protein knockdown

Cells were cultured for 48 h following transfection. The cells were lysed with a solution consisting of 0.5 vol% Triton X-100, 0.5% sodium deoxycholate, 150 mM NaCl, 5 mM Tris-HCl (pH 7.4), 5 mM EDTA, and 1x Halt Protease and Phosphatase Inhibitor cocktails. The total protein concentration for each sample was determined

with a BCA Protein Assay Reagent Kit, and the samples were subjected to 4% - 20% sodium dodecyl sulfate polyacrylamide gel electrophoresis for 35 min at 150 V. The protein was transferred to a poly(vinylidene fluoride) membrane at 18 V for 70 min, and the membrane was subsequently blocked in 5 vol% bovine serum albumin (BSA) in Tris-HCl-buffered saline (50 mM Tris-HCl, pH 7.4, 150 mM NaCl) containing 0.1 vol% Tween 20 (TBST) at room temperature for 1 h. The membrane was incubated in a solution of anti-GAPDH rabbit monoclonal IgG primary antibody ($0.5 \mu\text{g mL}^{-1}$ in TBST) at 4 °C overnight. Afterwards, the membrane was incubated with a solution of goat anti-rabbit polyclonal IgG antibody conjugated to HRP ($0.4 \mu\text{g mL}^{-1}$ in TBST) at room temperature for 1 h. Target proteins were visualized using SuperSignal™ West Dura Chemiluminescent Substrate with a FluorChem Q imager (ProteinSimple, San Jose, CA). Next, antibodies were stripped from the blot using Restore™ PLUS Western Blot stripping buffer for 15 min. The membrane was blocked in a 5% BSA solution for 1 h and then incubated in anti-actin rabbit polyclonal IgG ($0.3 \mu\text{g mL}^{-1}$ in TBST) overnight. The next day, after incubation with a solution of secondary goat anti-rabbit polyclonal IgG antibody conjugated to HRP, chemiluminescent imaging was used to detect the actin bands. The band intensity of each target protein was analyzed with ImageJ software.

5.2.6 Polyplex size determination using fluorescence correlation spectroscopy (FCS)

Polyplexes were formulated with Dy547-labeled siRNA and placed on cover slips, and the coverslips were attached to glass microscope slides using SecureSeals (Life Technologies, Grand Island, NY). FCS measurements were performed on an LSM 780 confocal microscope (Carl Zeiss, Oberkochen, Germany) using a 561 nm

laser and a 40x (numerical aperture = 1.2) water immersion apochromat objective. Thirty measurements, each lasting 8 s, were obtained for each sample. Data analysis was performed with ZEN 2010 software (Carl Zeiss), and the structural and measurement parameters were determined using a solution of AlexaFluor555 dye with an assumed diffusion coefficient of $340 \mu\text{m}^2 \text{s}^{-1}$.³²

5.2.7 Serum and storage stability assay

Polyplexes were formed either 30 min or 1 week prior to transfection. The GAPDH protein knockdown protocol described above was followed, except that transfections were carried out in DMEM containing 10 vol% FBS and 1 vol% P/S for serum stability experiments.

5.2.8 Heparin-induced siRNA release

Heparin was added to polyplex samples at a weight ratio of 5:1 (heparin:combined weight of siRNA and PAA). The solutions were gently vortexed and allowed to incubate in the dark at room temperature for 30 min. A 6x loading dye [3/7 (v/v) glycerol/water] was added to the polyplex solutions, and the solutions were subsequently loaded into a 2 wt% agarose gel containing $0.5 \mu\text{g mL}^{-1}$ ethidium bromide and run at 100 V for 30 min. The wells were imaged on a Bio-Rad Gel Doc XR, and the intensity of each free siRNA band was quantified using ImageJ software and compared to a control band of free siRNA.

5.2.9 RNAi modeling

A set of equations (Equations 3.1-3.3 in section 3.3.3) was solved using differential equation solver ode45 in MATLAB. The initial concentrations of siRNA were varied according to the heparin-induced siRNA release data.

5.2.10 FRET-based polyplex disassembly

Polyplexes were formulated as described with either 2 nM QD605 and 10 nM Dy647-labeled siRNA (for QD-containing polyplexes) or 10 nM Dy547- and 10 nM Dy647-labeled siRNA (for polyplexes not containing QDs). Following the light treatment procedure detailed above, polyplex solutions were loaded into cuvettes. The fluorescence emission (525-750 nm) was measured on a Fluoromax-4 fluorescence spectrophotometer (Horiba, Kyoto, Japan) using an excitation wavelength of 488 nm.

5.2.11 Flow cytometry to detect FRET-based polyplex disassembly

Polyplexes were formulated with mPEG-b-P(APNBMA)/PAA (30 wt% 240 kDa)/QD (2 nM)/Dy647 fluorophore-labeled siRNA polyplexes and transfected into NIH/3T3 cells. Following irradiation with 365 nm light for varying lengths of time, the fluorescence intensity was measured using flow cytometry on an Accuri C6 instrument (BD Biosciences, San Jose, CA) and analyzed using FlowJo v7 software (FlowJo, LLC, Ashland, OR). To account for signal bleed-through in the PE-Cy5.5 (FRET) fluorescence intensity, a compensation matrix was used such that the median fluorescence of the control samples (QD only and Dy647-siRNA only) was equal to the autofluorescence signal from untransfected cells.

5.2.12 Cryogenic transmission electron microscopy (cryo-TEM) imaging of nanocarriers

Polyplexes were formulated with 30/70 PAA/siRNA (240 kDa) and 1 nM QDs as described above. The formulations were air-dried until the solutions were ~10x concentrated. Cryo-TEM samples were prepared using a FEI Vitrobot. Before loading, carbon-coated copper TEM grids (C-flat™ holey carbon film with 200 mesh and Multihole patterning) were cleaned by plasma etching for 60 s. A 5µL drop of

polyplex solution was added to the grid, and the grid was blotted twice to remove the excess solution. The grids were plunged into cold liquid ethane to vitrify the sample and then transferred to liquid nitrogen. The grids were transferred to a Gatan cryotransfer holder and imaged with a FEI Talos TEM operating at 120 kV. The images were analyzed using DigitalMicrograph Version 3.9.4 and ImageJ Version 1.47. Cryo-TEM sample preparation and image acquisition was conducted by Dr. Tiffany Suekama.

5.3 Results and Discussion

5.3.1 Formulation of PAA-containing polyplexes

Ternary complexes were formulated with varying weight fractions of siRNA and PAA to determine how much of the cationic polymer was needed for complete encapsulation of siRNA in the presence of both siRNA and the PAA excipient. Ethidium bromide exclusion assays indicated that formulations made with larger fractions of PAA were not able to encapsulate siRNA as efficiently (Figure 5.2). Specifically, whereas siRNA in the 0/100 (PAA/siRNA) formulation was completely bound in polyplexes at an N/P ratio of 1, consistent with earlier studies,³³ free siRNA remained in the 30/70 and 50/50 formulations at an N/P ratio of 2 and was not completely encapsulated in these samples until an N/P of 4. Thus, all nanocarriers were formulated at an N/P ratio of 4 in subsequent studies to ensure complete encapsulation. The decrease in siRNA binding affinity upon PAA addition likely was a result of the higher anionic charge density of PAA,²⁷ resulting in lower effective charge ratios. In particular, the effective charge ratios of the 0/100, 10/90, 30/70, and 50/50 formulations are ~4.0, ~3.0, ~2.0, and ~1.4, respectively. The high anionic

charge of PAA is favorable for inducing greater amounts of siRNA release intracellularly because it leads to preferential retention of PAA relative to the siRNA.¹⁷

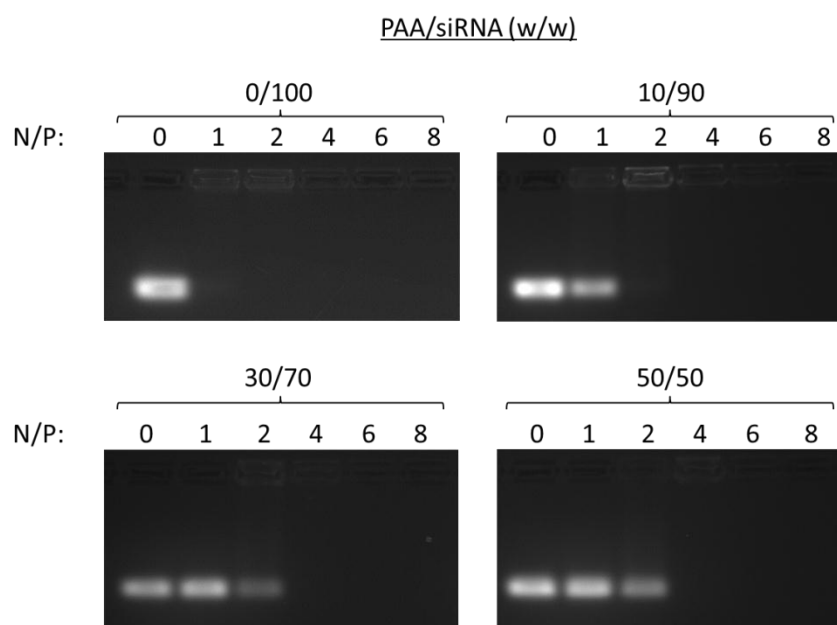


Figure 5.2: Representative ethidium bromide exclusion analyses of various formulations. Control polyplexes were formed at various N/P ratios with mPEG-*b*-P(APNBMA) and siRNA. Different formulations were made by substituting siRNA with 240 kDa PAA at various weight ratios while keeping the amount of mPEG-*b*-P(APNBMA) unchanged. Polyplex solutions were examined *via* gel electrophoresis.

5.3.2 Gene silencing of PAA-containing polyplexes

Given that PAA incorporation altered siRNA binding affinity, the effects of polyplex composition on gene silencing were investigated. To this end, the molecular weight of the PAA was varied over three orders of magnitude at various PAA loading fractions. Following transfection, cells were treated with a photo-stimulus, and the

protein silencing efficiency was measured. The fold change in silencing efficiency per weight of siRNA delivered was compared to control polyplexes formulated without PAA. As shown in Figure 5.3, all 10/90 formulations exhibited no significant differences in gene silencing in comparison to the control polyplexes. Polyplexes comprised of 50/50 PAA/siRNA also had protein knockdown levels comparable to 0/100 PAA polyplexes, although the efficacy of these formulations was more dependent on PAA molecular weight. Conversely, the 30/70 polyplexes comprised of 154 kDa and 240 kDa PAA demonstrated enhanced gene silencing that was nearly 100% more efficient than the polyplexes without PAA (2-fold difference). Within each loading fraction, the 4,000 kDa PAA formulations generated the least efficient silencing responses, and the intermediate PAA molecular weights provided the highest levels of knockdown. It is important to note that all formulations remained dormant and did not mediate protein silencing in the absence of 365 nm light (Figure 5.4). The on/off photo-controlled nature of the polyplexes is indicative of their intracellular stability and provides a distinct advantage over other polyplex systems for biomedical applications that require precise spatiotemporal control over gene expression.³⁴

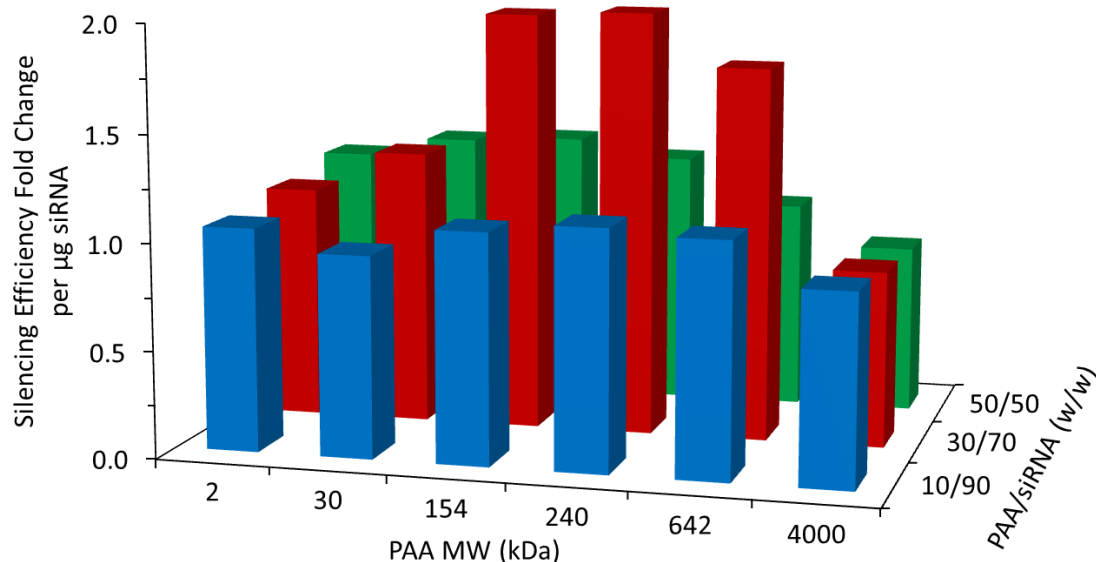


Figure 5.3: Silencing efficiency fold change of mPEG-*b*-P(APNBMA)/PAA ternary siRNA polyplexes. siRNA was substituted with PAA on a weight percent basis, and the molecular weight of PAA was varied. Cells were treated with 20 nM siRNA polyplexes, irradiated with 365 nm light for 10 min, and lysed for western blot analysis at 48 h post-transfection. Data represent the fold change in GAPDH protein silencing efficiency (on a per μg of siRNA basis) of each formulation relative to polyplexes without PAA (fold change = 1). Results are shown as the mean of data obtained from three independent experiments.

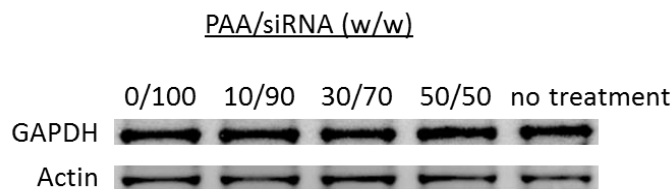


Figure 5.4: Representative western blot analysis of GAPDH protein levels following treatment with various mPEG-*b*-P(APNBMA)/240 kDa PAA siRNA formulations at an N/P ratio of 4 in the absence of light irradiation. The cell extract was collected 48 h post-transfection. Relative band intensities were quantified on the basis of the change in GAPDH protein expression levels relative to the band intensity of the loading control, β -actin. These values were normalized to the native levels in controls with no treatment.

5.3.3 Serum and storage stability

The most efficient formulation (30/70, 240 kDa) was analyzed further to elucidate the serum and storage stability of the polyplexes. First, polyplexes were exposed to either serum-free media or serum-supplemented media to determine if the polyplexes could resist serum-induced aggregation or degradation and maintain activity. FCS analyses suggested that there was no significant change in the average polyplex diameter following incubation in FBS for 3 h (Figure 5.5). As shown in Figure 5.6A, the mPEG-*b*-P(APNBMA)/PAA polyplexes mediated the same level of knockdown in serum-supplemented and serum-free media. However, polyplexes made with PEI, a cationic polymer commonly used in nucleic acid delivery, rapidly aggregated and were ineffective in silencing gene expression (Figure 5.6B). Furthermore, mPEG-*b*-P(APNBMA)/PAA polyplexes that were formulated and stored for one week prior to transfection exhibited similar gene silencing efficiencies as polyplexes used 30 min prior to transfections in serum-free media. mPEG-*b*-P(APNBMA)/PAA polyplexes that were stored for one week prior to transfection in serum-supplemented media mediated a higher gene silencing efficiency than PEI and mPEG-*b*-P(APNBMA) polyplexes without PAA in standard conditions (30 min storage, serum-free transfection media).

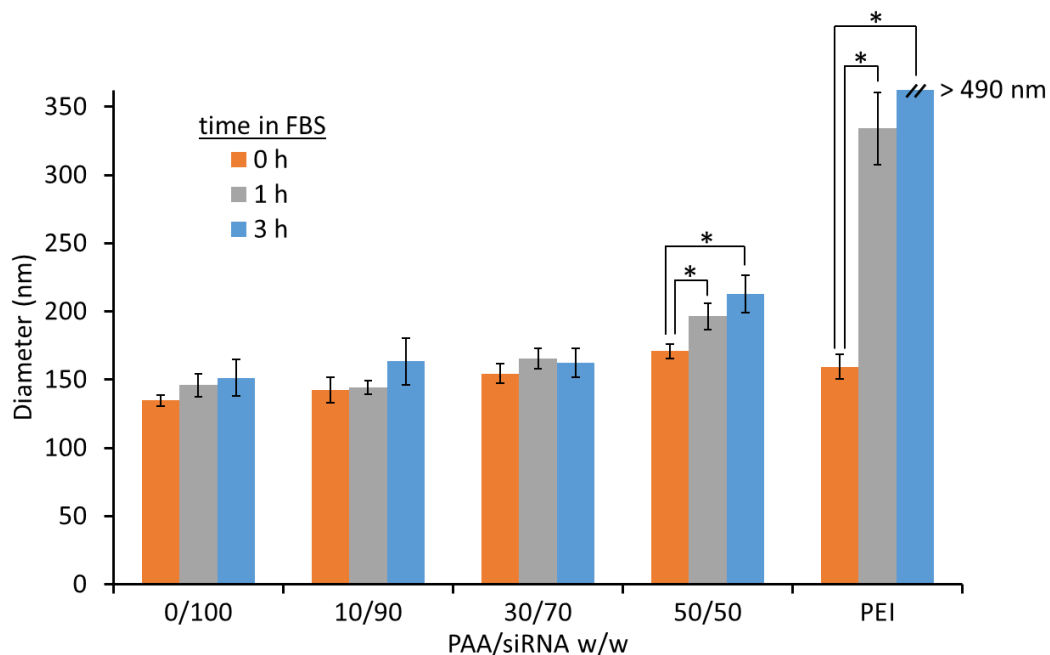


Figure 5.5: Serum stability of mPEG-*b*-P(APNBMA)/240 kDa PAA and PEI siRNA polyplexes, based upon analysis of polyplex size following exposure to 100% FBS for various lengths of time at 37 °C. The nanocarriers that were not exposed to FBS (0 h) were stored in the formulation buffer, HEPES buffer, at 37 °C prior to analysis. Average polyplex diameters were computed from FCS analyses. Results are shown as the mean \pm standard deviation of data obtained from three independent experiments. An asterisk indicates a statistically significant difference between polyplex sizes after exposure to FBS ($p < 0.05$).

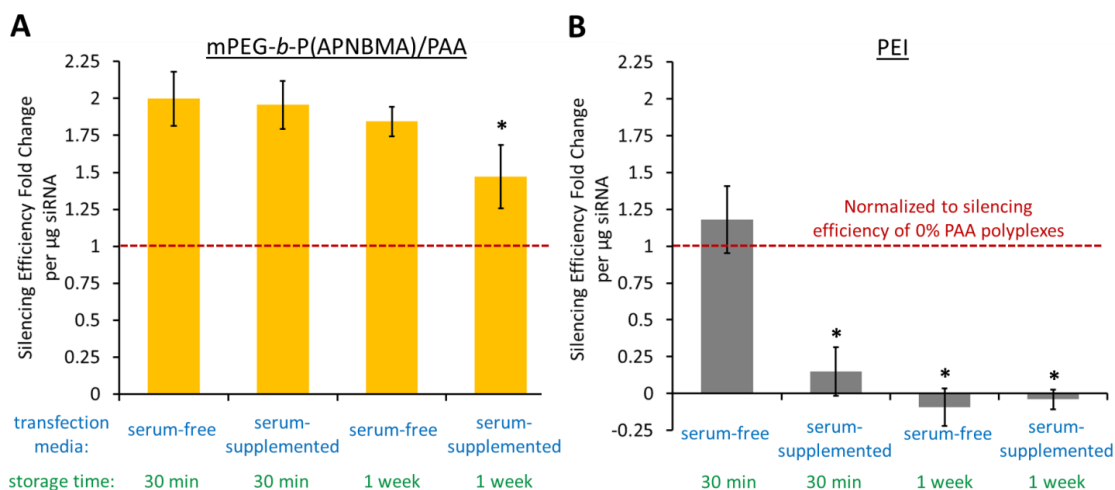


Figure 5.6: Polyplex stability in serum-containing media and following storage for one week. The silencing efficiencies of (A) mPEG-*b*-P(APNBMA)/PAA (30/70, 240 kDa) ternary siRNA polyplexes and (B) PEI/siRNA polyplexes were analyzed. Transfections were conducted in either OptiMEM (serum-free) or DMEM containing 10% FBS. Polyplexes were incubated for either 30 min or 1 week prior to transfection. Cells were treated with 20 nM siRNA polyplexes, irradiated with 365 nm light for 10 min, and lysed for western blot analysis at 48 h post-transfection. Data represent the fold change in GAPDH protein silencing efficiency (on a per μg of siRNA basis) of each sample relative to polyplexes without PAA (red dashed line). Results are shown as the mean \pm standard deviation of data obtained from three independent experiments. An asterisk indicates a statistically significant difference between a given sample and polyplexes incubated for 30 min prior to transfection in serum-free media ($p < 0.05$).

Polyplex stability in polyanion-rich environments, such as serum-containing culture media, is a particularly important problem that has limited translation of nucleic acid delivery vehicles.²⁶ Although many nanocarriers are able to resist aggregation and maintain their size in serum, protein-nanoparticle interactions remain a major challenge.³⁵ For example, Sizovs *et al.* formulated a number of nanocomplexes that exhibited promising serum stability properties, but most failed to

mediate gene knockdown in serum-supplemented media.³⁶ This phenomenon is representative of the widespread problem of biotransformation, a process by which proteins and other biomolecules adsorb to nanocarrier surfaces, forming a corona that critically alters the physico-chemical identity of the nanostructure *in vivo*.³⁷ These changes may inhibit cellular internalization, induce premature polyplex disassembly, or trigger activation of the immune system.^{36, 38} The fact that PAA-containing mPEG-*b*-P(APNBMA) polyplexes did not lose efficacy in serum-supplemented media suggests that these formulations are extremely stable and may be well suited for *in vivo* applications.

The ability of nanocarriers to remain stable over relatively long periods of time is another critical characteristic required for clinical use.³⁹ This feature is particularly important in settings that require numerous doses to be administered over multiple days, as a single batch of nanocarriers can be formulated and used for all doses. However, in the literature, the vast majority of polyplexes are formulated within a few hours of their desired use to minimize aggregation over time. Moreover, most polyplex systems capable of prolonged stability often require lyophilization or storage in non-ambient conditions, which hinders practical application.⁴⁰

The fact that the nanocarriers were able to mediate efficient gene silencing in serum-supplemented media following storage for one week is indicative of their robust stability in biological environments. In addition to the incorporation of an anti-fouling PEG block in mPEG-*b*-P(APNBMA), hydrophobic interactions between the aromatic rings in the cationic block and the siRNA backbone likely confer enhanced resistance to biotransformation.³³ Multiple reports also have demonstrated that formulating polyplexes with a combination of hydrophobic and electrostatic interactions improved

in vivo stability and gene silencing.^{41, 42} Nevertheless, subsequent studies were conducted in Opti-MEM to isolate the potential effects of heparin-induced siRNA release on gene silencing efficiencies.

5.3.4 Heparin-induced siRNA release and cellular uptake

The ability of anionic glycosaminoglycans, such as heparin, to mediate nucleic acid release from nanocarriers has been shown to be correlated with transfection efficiencies.⁴³ To this end, heparin stability assays were conducted to better understand why the various mPEG-*b*-P(APNBMA)/PAA polyplexes mediated different levels of gene silencing. Following addition of heparin at a 5:1 heparin:siRNA weight ratio, the percent of siRNA that was liberated from each formulation was measured by gel electrophoresis as shown in Figure 5.7. Generally, 10/90 and 50/50 polyplexes released smaller percentages of siRNA than 30/70 polyplexes. Formulations made with the highest molecular weight PAA (4,000 kDa) released the smallest fractions of siRNA, and formulations made with intermediate molecular weights (154 kDa and 240 kDa) disassembled to the greatest extent, particularly in the case of 30/70 polyplexes. Therefore, a range of PAA molecular weights and weight fractions was identified that exhibited the greatest amounts of siRNA release, consistent with gene silencing studies. Notably, although PAA was incorporated to increase gene silencing by reducing polymer-siRNA binding, mPEG-*b*-P(APNBMA)/PAA polyplexes remained sufficiently stable as to require high heparin:siRNA ratios to induce detectable siRNA release, in distinct contrast to PEI/siRNA polyplexes.³³

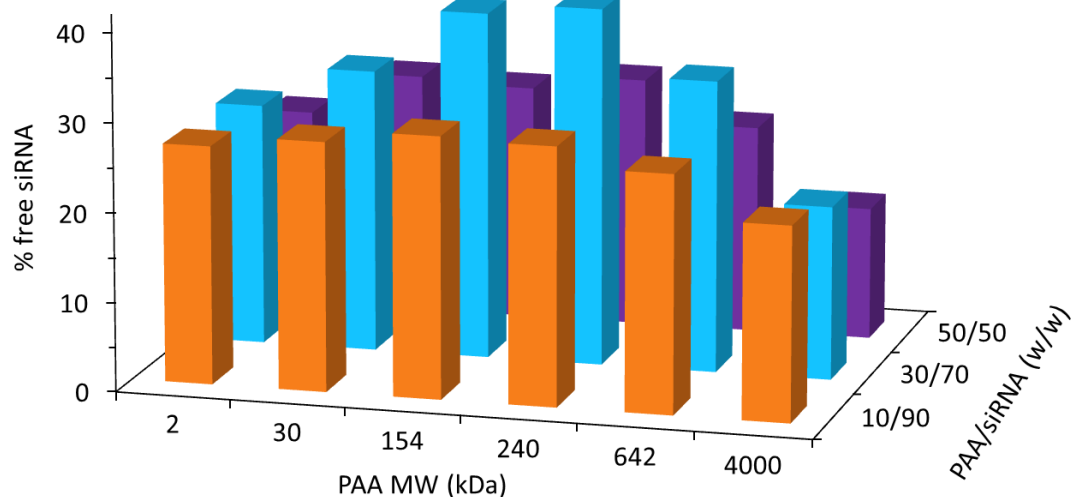


Figure 5.7: Heparin-induced siRNA release from mPEG-*b*-P(APNBMA)/PAA ternary siRNA polyplexes. siRNA was substituted with PAA on a weight percent basis, and the molecular weight of PAA also was varied. Following polyplex formulation, heparin was added at a weight ratio of 5:1 heparin:siRNA and incubated for 30 min. The solutions were subjected to gel electrophoresis and the amount of free siRNA was quantified using ImageJ. Results are shown as the mean of data obtained from three independent experiments.

The gene silencing trends reported in Figure 5.3 are remarkably similar to the siRNA release data shown in Figure 5.7, suggesting that the modulation of binding *vs.* release was a key factor dictating knockdown efficacy. In particular, formulations comprised of intermediate PAA weight fractions (30/70 PAA/siRNA) and intermediate PAA molecular weights (154-204 kDa) released the greatest amounts of siRNA and mediated the most efficient gene knockdown. These trends are influenced by a number of factors including excipient chain length, overall nanocarrier charge, and number of excipient molecules per nanocarrier. All 10/90 formulations exhibited silencing efficiencies similar to the control polyplexes without PAA, suggesting that a

10 wt% modification is not enough to significantly alter the physical properties of the nanocarriers. However, formulations that had 50 wt% of the siRNA replaced with PAA also did not mediate significantly improved gene silencing, which is a result of PAA having an anionic charge density approximately five times greater than siRNA. In particular, these nanocarriers had overall charge ratios that were close to neutral (effective charge ratio of ~ 1.4), which decreases the competitive binding interactions with intracellular polyanions that promote polyplex disassembly. The 30/70 formulations, on the other hand, possessed almost twice as many cationic charges as anionic charges (effective charge ratio of ~ 2.0) and strongly interacted with polyanions, such as heparin, to liberate siRNA.

For all weight fractions of PAA, but particularly in the case of 30/70 polyplexes, the optimal PAA molecular weights were approximately 10-20 times greater than the molecular weight of siRNA (~ 13 kDa). Many reports in the literature have demonstrated that the binding affinity of ionic polymers increases with molecular weight.^{10, 44} As the PAA molecular weight increases to molecular weights much greater than the molecular weight of siRNA, the electrostatic interactions are stronger and the PAA preferentially binds to the cationic polymer so that siRNA can be selectively released. At the same time, the longer PAA chains can form entanglements within the nanocarriers that stabilize the polyplexes and limit their disassembly.^{15, 45} Additionally, if the weight fraction of PAA is held constant, the number of individual polymers in each polyplex decreases as the molecular weight of PAA increases (Table 5.1). For example, the 30/70 4,000 kDa PAA nanocarriers would have ~ 0.3 PAA chains per polyplex, meaning that the majority of the nanocarriers are unmodified and contain no PAA. This analysis helps explain why this particular formulation exhibited

gene silencing efficiencies similar to the control polyplexes without PAA. Taken together, PAA polymers with intermediate molecular weights balance all of these effects (i.e., providing preferential binding, limiting the amount of chain entanglement, and distributing PAA chains in all polyplexes) more effectively than the high and low molecular weight polymers.

Table 5.1: Estimated number of PAA polymer chains per polyplex in various formulations.

		PAA MW (Da)					
		2k	30k	154k	240k	642k	4,000k
wt% PAA	10	110	12	2.4	1.5	0.6	0.1
	30	320	35	7.1	4.6	1.7	0.3
	50	530	59	12	7.7	2.9	0.5

Note: MW of siRNA is ~13 kDa

In addition to intracellular siRNA release, cellular uptake also may play a significant role in determining overall efficiency.¹⁶ Thus, cellular uptake analyses were conducted to investigate the effect of polyplex composition on nanocarrier internalization. The amount of siRNA uptake was proportional to the weight fraction of siRNA in the formulations (Figure 5.8), indicating that approximately the same number of polyplexes were being internalized regardless of the amount of PAA incorporation. Therefore, differences in cellular uptake likely do not significantly contribute to the differences in gene silencing efficiency.

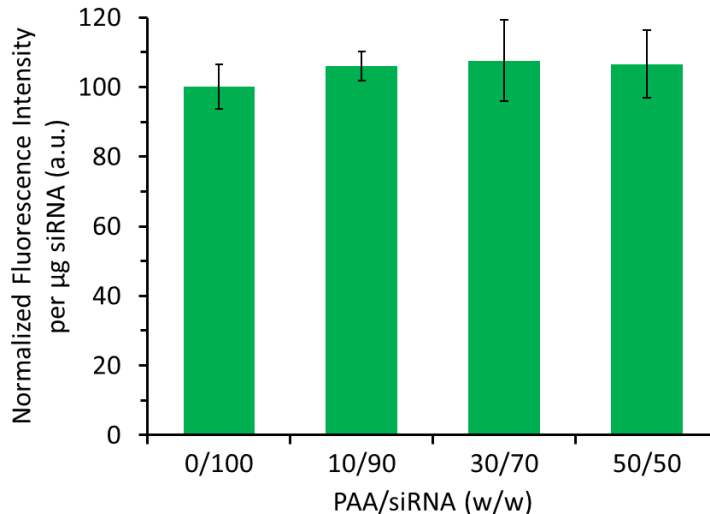


Figure 5.8: Cellular uptake of mPEG-*b*-P(APNBMA)/240 kDa PAA siRNA polyplexes over a range of PAA/siRNA weight ratios. Cells were incubated in polyplex solutions formulated with Dy647-labeled siRNA, and cellular fluorescence was measured using flow cytometry. The mean fluorescence intensity (MFI) per µg of siRNA was computed and normalized to the MFI of cells that were treated with 0/100 polyplexes. Results are shown as the mean ± standard deviation of data obtained from three independent experiments.

5.3.5 Predicting gene silencing *via* siRNA release assays

To verify that the gene silencing efficiency of each formulation was primarily controlled by the amount of siRNA the delivery vehicles could liberate, the siRNA release data from Figure 5.7 was inputted into a kinetic model of siRNA-mediated gene silencing established previously (see Chapter 3).⁴⁶ As shown in Figure 5.9, the model predicted gene silencing levels that were similar (< 15% for nearly all polyplex compositions) to those measured experimentally in Figure 5.3. The ability of this method to capture the complex process of gene silencing was particularly exciting given the simplicity of the heparin stability assays and kinetic modeling. The

accuracy of the predictions also suggested that siRNA release and protein/mRNA turnover, as opposed to other considerations (e.g. the effects that the polymer chains may have on RISC interactions with siRNA), were the rate-determining steps in this system. Furthermore, use of the kinetic model enabled generation of a “heat map” to identify the amount and molecular weight of excipient *a priori* for achieving a desired level of knockdown. These insights into PAA compositions are likely directly translatable to other anionic polymer excipients and stimuli-responsive polyplex systems. For example, a recent study screened numerous anionic excipients and found that the most effective formulation at inhibiting tumor growth in an *in vivo* mouse model contained an anionic polymer (γ -PGA) with a molecular weight within the ideal range determined herein.¹⁷ The authors partially attributed this enhancement to chain entanglement effects but did not vary the γ -PGA loading fraction to explore the effect of number of charged groups on polyplex efficacy. Thus, this streamlined approach to optimizing polyplex compositions may improve current systems and facilitate the introduction of other excipients more rapidly and efficiently.

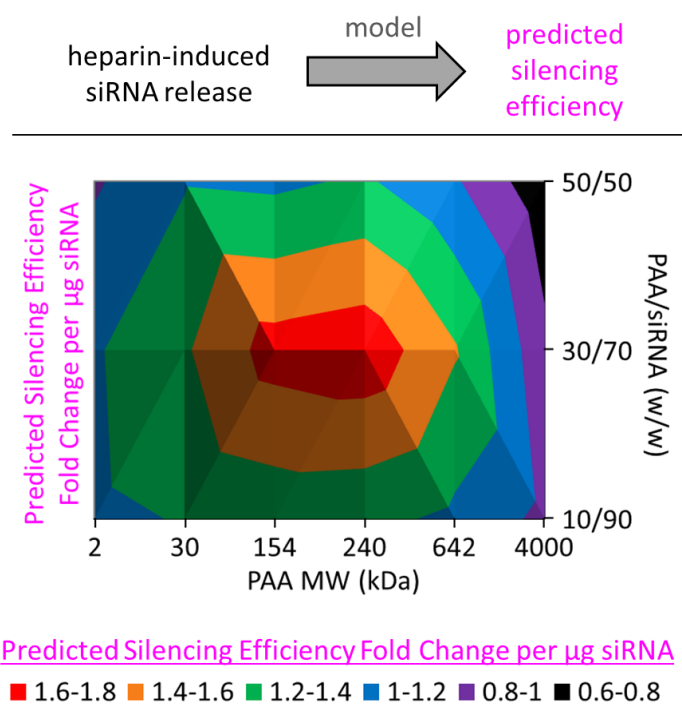


Figure 5.9: Model predictions of silencing efficiency fold change of mPEG-*b*-P(APNBMA)/PAA ternary siRNA polyplexes. The relative amounts of heparin-induced siRNA release (Figure 5.7) were inputted into the RNAi model to predict the fold change in GAPDH protein silencing efficiency (on a per μg of siRNA basis) of each formulation relative to polyplexes without PAA (fold change = 1).

5.3.6 Incorporation of quantum dots: selective siRNA release

In addition to PAA, other anionic components can be added to enhance the selective release of siRNA. Inclusion of QDs, which are ideally suited for fluorescence-based analyses and are amenable to bioimaging techniques,³⁰ may allow for the development of theranostic nanocarriers. Various concentrations of QDs were added to mPEG-*b*-P(APNBMA)/PAA polyplexes during formulation, as depicted in Figure 5.10A. Polyplexes incorporating PAA were comprised of 30/70 PAA/siRNA (240 kDa PAA), the most efficient formulation identified in Figure 5.3. Heparin-

induced siRNA release assays were conducted and visualized using gel electrophoresis. As shown in Figure 5.10B, increasing amounts of siRNA were released as the concentration of QDs increased. Moreover, selective release of siRNA was exhibited for QD concentrations of 0.5-2 nM and 0.5-1 nM for the 0/100 and 30/70 polyplexes, respectively, as indicated by the lack of free QDs migrating down the gel. The percent of siRNA released was quantified and is displayed in Figure 5.10C. The siRNA release efficiency was higher across all QD concentrations for the 30/70 polyplexes relative to the polyplexes without PAA. The siRNA release data was inputted into the RNAi model (see section 3.3.3) to predict protein knockdown levels, which were found to be in agreement with experimental data (Figure 5.11). Thus, inclusion of additional anionic components increased the selective release of siRNA and enhanced the gene silencing efficiency.

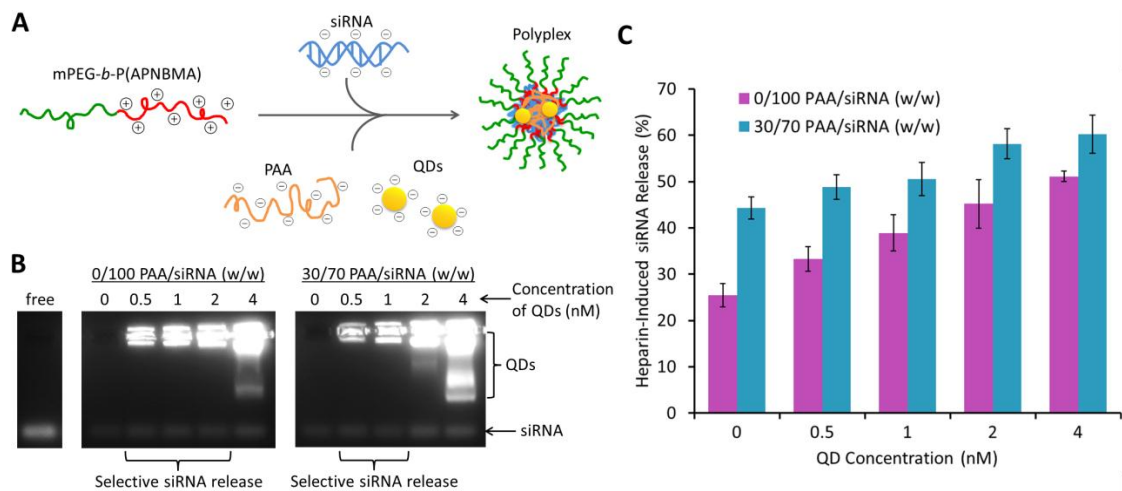


Figure 5.10: Heparin-induced siRNA release from polyplexes incorporating QDs. Varying amounts of QDs were added during mPEG-*b*-P(APNBMA)/240 kDa PAA/QD siRNA polyplex formation. Following complex formulation, heparin was added at a heparin:siRNA weigh ratio of 5:1 and incubated for 30 min. (A) Cartoon schematic of polyplex formation. (B) The solutions were subjected to gel electrophoresis. (C) The amount of free siRNA from the agarose gels was quantified using ImageJ. Results are shown as the mean \pm standard deviation of data obtained from three independent experiments.

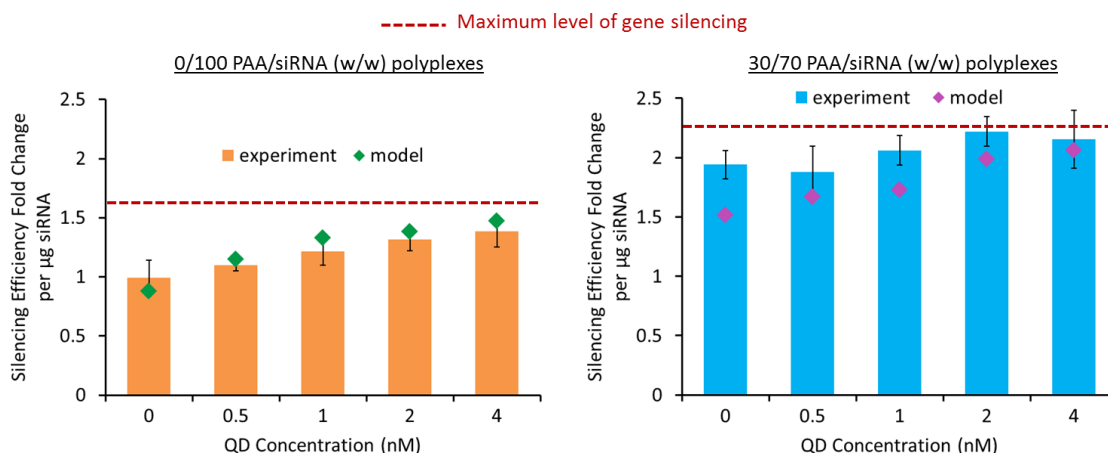


Figure 5.11: Model predictions of protein silencing efficiencies of mPEG-*b*-P(APNBMA)/240 kDa PAA/QD siRNA polyplexes following irradiation with 365 nm light. Predictions from the kinetic model were computed on the basis of siRNA release data in Figure 5.10 and are shown as diamonds [0/100 PAA/siRNA (w/w) in green and 30/70 PAA/siRNA (w/w) in pink]. The predicted values (diamonds) were compared to experimental data (bars) [0/100 polyplexes in orange and 30/70 polyplexes in blue]. Experimental results are shown as the mean \pm standard deviation of data obtained from three independent experiments. The red dashed line represents the maximum level of GAPDH protein silencing achievable with a single dose of siRNA.⁴⁶

5.3.7 QD-based FRET analyses of polyplex unpackaging

Monodisperse QDs have unique fluorescence properties, such as high photostability and narrow symmetric emission spectra, that make them ideal candidates for use in FRET-based analyses.³⁰ Polyplexes were formulated with various combinations of QDs, fluorescently labeled siRNA, and PAA before being irradiated with light for various lengths of time. The FRET ratio, defined as the ratio between the peak intensities of the donor (QD or Dy547-siRNA) and acceptor (Dy647-siRNA) fluorophores, was computed and is plotted in Figure 5.12A. Control polyplexes with no modifications lost the FRET signal the slowest, indicating that greater amounts of siRNA and QDs remained tightly packaged in the nanocarriers following irradiation.

All other formulations lost at least 90% of the FRET signal after 10 min of irradiation, indicating that the polyplexes loosened and that the average distance between siRNAs and QDs was at least 44% greater than the Förster radius (~9 nm).⁴⁷ Polyplexes modified with PAA disassembled more rapidly than polyplexes modified with QDs; however, polyplexes incorporating both QDs and PAA disassembled the fastest. These trends are particularly apparent following 10 min of irradiation, which is the duration of light treatment applied during transfections, as plotted in Figure 5.12B.

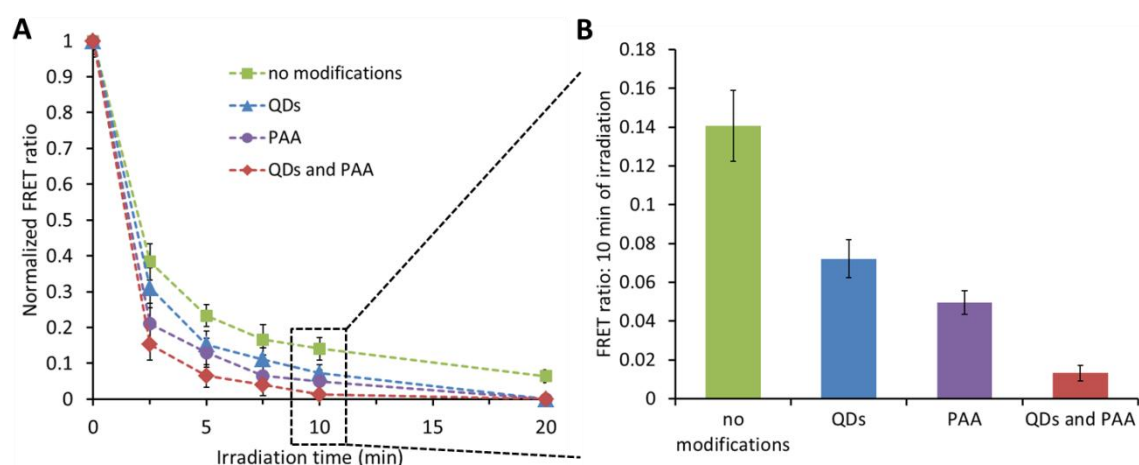


Figure 5.12: Light-induced polyplex disassembly of mPEG-*b*-P(APNBMA) polyplexes. The complexes were formulated with various combinations of 2 nM QDs, 30 wt% PAA, and fluorophore-labeled siRNA. Following irradiation with 365 nm light for varying lengths of time, the fluorescence intensity was measured. (A) The FRET efficiency was computed for each complex composition as follows: no modifications (green), QDs (blue), PAA (purple), and QDs and PAA (red). Results are shown as the mean \pm standard deviation of data obtained from three independent experiments for each time point. (B) The FRET ratio following 10 min of irradiation. The results are reported as the average fluorescence of three independent samples for each irradiation time. *Note: all of the groups (at 10 min) are statistically different from each other ($p < 0.05$).*

The fluorescence-based diagnostic capabilities of QDs also can easily be extended to live cells to enable analysis of polyplex disassembly. As shown in Figure 5.13, mPEG-*b*-P(APNBMA)/PAA (30 wt% 240 kDa)/QD (2 nM)/Dy647-siRNA polyplexes were formulated and transfected into NIH/3T3 cells. Following irradiation with 365 nm light for varying lengths of time, the FRET fluorescence intensity was measured using flow cytometry. Cells that were not irradiated with light exhibited strong fluorescence signals, and the fluorescence intensity decreased as the cells were irradiated with the photo-stimulus for longer times (Figure 5.13A). After 10 min of irradiation, ~95% of the FRET signal was lost (Figure 5.13B). The dynamics of polyplex loosening/disassembly in solution (Figure 5.12) were relatively consistent with those detected intracellularly (Figure 5.13), further indicating that siRNA release measurements in solution are a reasonable predictor of polyplex behavior inside cells.

Recently, the use of fluorescence-based imaging agents has become an essential tool in the fields of drug delivery and bioimaging.⁴⁸ The incorporation of QDs into the mPEG-*b*-P(APNBMA) complexes enabled the formation of nanocarriers that can self-report on their dynamic structural changes and disassembly in solution. Such information is critical for accessing the effectiveness of various excipients in nanocarriers, which can be used to predict gene silencing efficiencies using modeling methods discussed above. Given the excellent serum stability of the mPEG-*b*-P(APNBMA) complexes, the QD-containing nanocarriers may serve as effective *in vivo* fluorescence-based imaging probes.

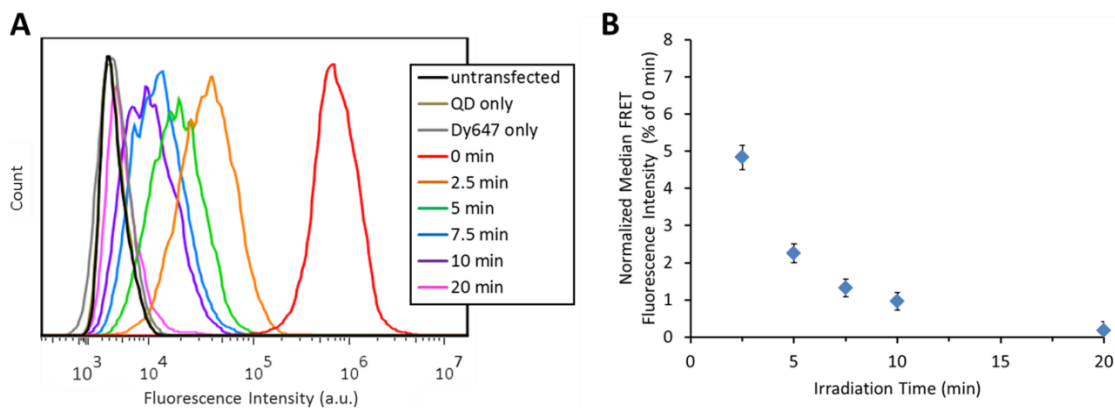


Figure 5.13: FRET-based detection of polyplex disassembly inside cells. (A) Representative flow cytometry histograms showing the fluorescence intensity distributions of cells treated with light for various lengths of time. (B) The median FRET fluorescence intensity of cells treated with light for various lengths of time, normalized to cells that were not treated with 365 nm light (0 min). Results are reported as the mean \pm standard deviation of data obtained from three independent experiments.

5.3.8 Cryo-TEM imaging of QD-containing polyplexes

In addition to their advantageous fluorescence properties, QDs also hold tremendous promise as diagnostic imaging agents for tracking delivery vehicles in live cells and *in vivo*.⁴⁹ The high electron density of QD cores provides better contrast relative to polymeric/nucleic acid systems, which often are barely visible due to their hydrated nature and low electron density.⁵⁰ Many types of electron microscopy are useful for studying nanoparticle distribution in tissue samples;^{1,51} however, cryo-TEM is uniquely suited for the analysis of nanocarriers in solution prior to delivery into biological samples. This powerful technique allows for the imaging of solution-assembled nanostructures in their native environment without the need for the samples to be stained or fixed.⁵¹ Specifically, cryo-TEM avoids many challenges associated with dry state TEM and atomic-force microscopy such as solvent evaporation, surface

interactions, chemical fixation, and staining, all of which may lead to structural changes and/or artifacts.⁵²

To access the bioimaging potential of the formulations, mPEG-*b*-P(APNBMA)/PAA/QD siRNA complexes were prepared and imaged using cryo-TEM (Figure 5.14). The QDs were clearly visible as dark spheres with diameters of 5-10 nm. Moreover, the QDs were clustered within polymer/siRNA complexes that appeared as a light shade relative to the QDs due to the low electron densities of mPEG-*b*-P(APNBMA) and siRNA (Figure 5.15A). The polyplexes had a consistent spherical-like morphology with average diameters of ~150 nm (Figure 5.15B), which is in agreement with the average sizes obtained using FCS (Figure 5.5). FCS analyses previously showed that ~250 siRNAs were incorporated into each polyplex.⁴⁶ Given that the siRNA was used at a 20x molar excess to the 1 nM QDs, ~13 QDs were expected to be included within each complex; the representative polyplexes imaged in Figure 5.14 and Figure 5.15 corroborated this estimate. Gel electrophoresis experiments verified that no QDs were free in solution (see also Figure 5.10 and the note in the caption of Figure 5.15). Without the high contrast provided by the QDs, the polymeric polyplexes would have been extremely difficult to distinguish (Figure 5.15C). Thus, the incorporation of QDs facilitated the bioimaging of polyplexes, which is an indispensable tool for tracking nanocarriers in diagnostic applications.

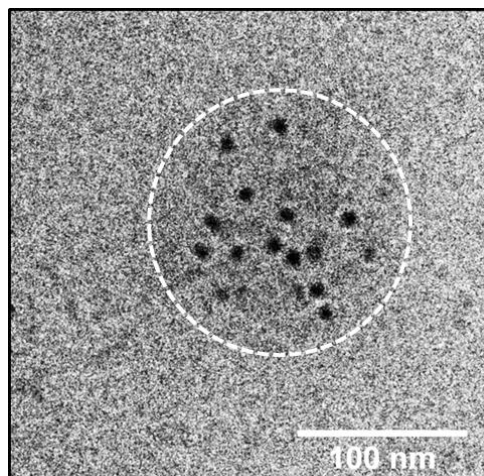


Figure 5.14: Representative visualization of an isolated QD-containing polyplex using cryo-TEM. A solution of mPEG-*b*-P(APNBMA)/PAA (30 wt% 240 kDa)/QD (1 nM) siRNA polyplexes was formulated and prepared for cryo-TEM analyses. The white circular line indicates the approximate edge of the polyplex to guide the eye. The dark 5-10 nm spheres are QDs, which appear confined within the polyplex. The scale bar represents 100 nm.

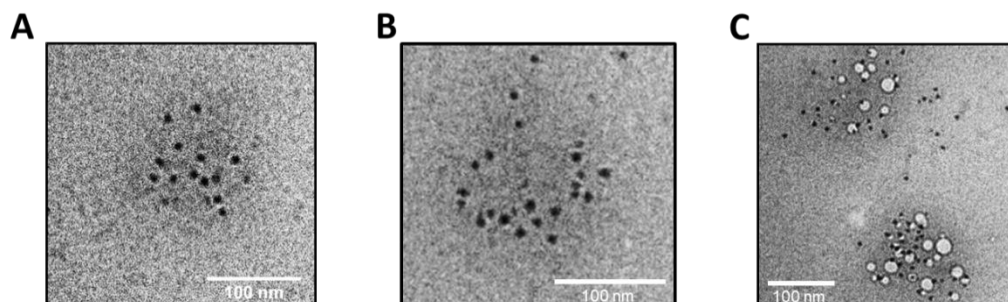


Figure 5.15: Representative cryogenic transmission electron microscopy (cryo-TEM) micrographs of mPEG-*b*-P(APNBMA)/PAA (30 wt% 240 kDa)/QD (1 nM) siRNA polyplexes. (A) A reproduction of the micrograph displayed in Figure 5.14, except the white dashed circular line was removed for visual clarity. (B) Representative micrograph of another polyplex. (C) A micrograph that shows two polyplexes that were intentionally burned to create holes in the polymer/siRNA complexes. All scale bars represent 100 nm. *Note: The few QDs that were not clustered within the polyplex likely were displaced during cryo-TEM sample preparation.*

5.3.9 Incorporation of UCNPs

Given the successful incorporation of anionic QDs into the polyplex for diagnostic purposes, the addition of anionic UCNPs to facilitate the use of near infrared (NIR) irradiation also was explored. This change in the polyplex composition is important because the application of 365 nm light in biomedical technologies has significant drawbacks related to penetration depth and cytotoxicity.⁵³ These issues can potentially be circumvented by exploiting UCNPs, which upconvert low energy light (NIR light, > 750 nm) to higher energy light (UV light, ~365 nm). UCNPs were synthesized by Dr. Christopher Milleville and characterized by Eric Chen from the Doty lab at the University of Delaware, and the emission spectra following excitation with 980 nm light are displayed in Figure C.1. Although the emission peak around 365 nm was very weak, it was still possible that this intensity would be sufficient to induce mPEG-*b*-P(APNBMA) cleavage and siRNA release.

To determine if the UCNPs could be encapsulated in polyplexes as QDs were, acid-functionalized UCNPs (negatively charged in water) were added to the polyplex formulations at various loading ratios, and the complexation with mPEG-*b*-P(APNBMA) was tested using gel electrophoresis (Figure C.2). As the UCNP/siRNA (w/w) loading ratio increased, the amount of heparin-induced siRNA release also increased, indicating that the UCNPs were influencing polyplex stability. DLS measurements also were conducted to confirm that the UCNPs were being incorporated into the polyplexes. These analyses found that the average hydrodynamic diameter increased significantly upon the addition of UCNPs, and that the sizes surpassed 200 nm at all UCNP/siRNA ratios ≥ 3 (Figure C.3). Only one population was detected using DLS, further suggesting that the UCNPs were

incorporated into the polyplexes. Moving forward, an UCNP/siRNA ratio of 3 was used to minimize the size of the complexes.

Next, the UCNP-containing polyplexes were irradiated with the highest possible intensity of 980 nm (NIR) light to determine if the UCNPs facilitated upconversion that was efficient enough to induce mPEG-*b*-P(APNBMA) charge reversal and siRNA release. As shown in Figure 5.16A, even polyplexes that were incubated in SDS solutions (S/P ratio of 2.5) and irradiated with 980 nm light for 15 min did not exhibit any siRNA release or polyplex loosening, whereas polyplexes irradiated with 365 nm light for 5 min released some siRNA and loosened (as indicated by the appearance of fluorescence in/near the wells). The lack of response from the NIR irradiation was likely due to insufficient mPEG-*b*-P(APNBMA) charge reversal. UV-Vis analyses were conducted to confirm this hypothesis (Figure 5.16B), and the polymer absorbance at 316 nm did not decrease following NIR irradiation for 5 or 15 min (Figure 5.16C), indicating that polymer cleavage did not occur. These results suggested that the upconversion process of these particular UCNPs (Figure C.1) was not nearly efficient enough to induce significant levels of mPEG-*b*-P(APNBMA) cleavage at the maximum irradiation intensity. This limitation is common, as most UCNPs suffer from very weak and narrowband NIR absorption.⁵⁴

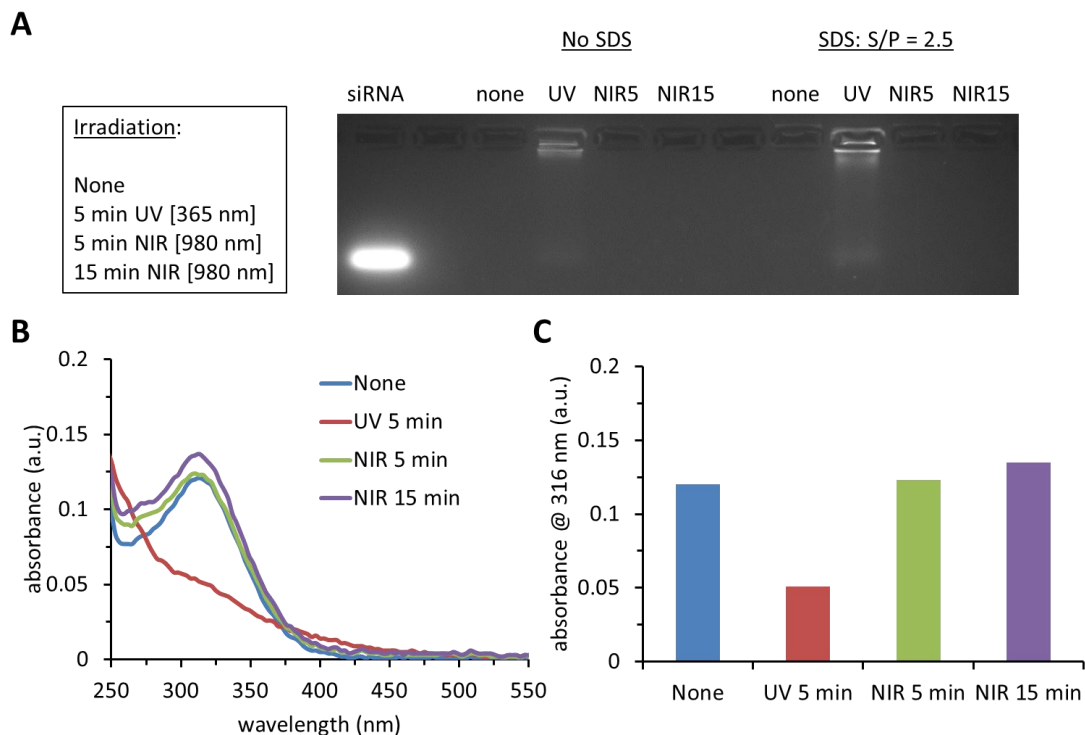


Figure 5.16: Light-induced siRNA release and mPEG-*b*-P(APNBMA) cleavage of UCNP-containing polyplexes. (A) Polyplexes were formulated with a UCNP/siRNA (w/w) ratio of 3 and incubated in solutions containing no SDS or SDS with an S/P ratio of 2.5 for 30 min. The polyplexes were then irradiated with either no light, 365 nm light for 5 min, 980 nm light for 5 min, or 980 nm light for 15 min. The solutions were analyzed *via* gel electrophoresis. (B) The solutions obtained from (A) also were measured using UV-Vis spectroscopy. (C) The peak absorbance of mPEG-*b*-P(APNBMA) at 316 nm was tracked to determine if polymer cleavage occurred.

5.4 Conclusions

The incorporation of PAA and QD excipients in photo-responsive complexes was systematically explored to enhance the utilization of siRNA. Wide ranges of PAA loading fractions and molecular weights were investigated, and the most efficient compositions were 30/70 PAA/siRNA with PAA molecular weights of 154 kDa and 240 kDa (~10-20 times that of siRNA). These nanocarriers mediated selective siRNA

release and improved the gene silencing efficiency by 100% relative to unmodified polyplexes. Moreover, the nanocarriers maintained full activity either when stored for one week or when transfected in serum-supplemented media. siRNA release studies enabled the generation of a predictive “heat map” that provided *a priori* insight into gene silencing efficiencies as a function of PAA loading fraction and molecular weight. These parameters governed polyplex activity on the basis of charge density and entanglement effects. QDs also were incorporated into polyplexes, and formulations containing 2 nM QDs enhanced gene silencing efficiency by 40% relative to unmodified polyplexes. Furthermore, the QD-containing polyplexes were able to self-report dynamic structural changes and nanocarrier disassembly through fluorescence-based analyses, and cryo-TEM analyses demonstrated that QDs enhanced the bioimaging potential of the nanocarriers. UCNPs also were incorporated into polyplexes, but their upconversion efficiency was much too low to induce polyplex disassembly with NIR light. Thus, this chapter highlights the ability of excipients to improve the efficiency of nucleic acid delivery vehicles and develop theranostics capable of self-reporting their disassembly. The insights gleaned from these results were used to increase siRNA release from polyplexes through the addition of anionic excipients and impart diagnostic capabilities into the nanocarriers.

REFERENCES

1. Gilleron, J.; Querbes, W.; Zeigerer, A.; Borodovsky, A.; Marsico, G.; Schubert, U.; Manygoats, K.; Seifert, S.; Andree, C.; Stoeter, M.; Epstein-Barash, H.; Zhang, L.; Kotliansky, V.; Fitzgerald, K.; Fava, E.; Bickle, M.; Kalaidzidis, Y.; Akinc, A.; Maier, M.; Zerial, M., Image-based analysis of lipid nanoparticle-mediated siRNA delivery, intracellular trafficking and endosomal escape. *Nat. Biotechnol.* **2013**, *31* (7), 638-646.
2. Wei, J.; Jones, J.; Kang, J.; Card, A.; Krimm, M.; Hancock, P.; Pei, Y.; Ason, B.; Payson, E.; Dubinina, N.; Cancilla, M.; Stroh, M.; Burchard, J.; Sachs, A. B.; Hochman, J. H.; Flanagan, W. M.; Kuklin, N. A., RNA-induced silencing complex-bound small interfering RNA is a determinant of RNA interference-mediated gene silencing in mice. *Mol. Pharmacol.* **2011**, *79* (6), 953-963.
3. de Fougerolles, A.; Vornlocher, H.-P.; Maraganore, J.; Lieberman, J., Interfering with disease: a progress report on siRNA-based therapeutics. *Nat. Rev. Drug Discov.* **2007**, *6* (6), 443-453.
4. Huang, Y.; Lin, D.; Jiang, Q.; Zhang, W.; Guo, S.; Xiao, P.; Zheng, S.; Wang, X.; Chen, H.; Zhang, H.-Y.; Deng, L.; Xing, J.; Du, Q.; Dong, A.; Liang, Z., Binary and ternary complexes based on polycaprolactone-graft-poly (N, N-dimethylaminoethyl methacrylate) for targeted siRNA delivery. *Biomaterials* **2012**, *33* (18), 4653-4664.
5. Dohmen, C.; Edinger, D.; Frohlich, T.; Schreiner, L.; Lachelt, U.; Troiber, C.; Radler, J.; Hadwiger, P.; Vornlocher, H. P.; Wagner, E., Nanosized multifunctional polyplexes for receptor-mediated siRNA delivery. *ACS Nano* **2012**, *6* (6), 5198-5208.
6. Zuckerman, J. E.; Davis, M. E., Clinical experiences with systemically administered siRNA-based therapeutics in cancer. *Nat. Rev. Drug Discov.* **2015**, *14* (12), 843-56.
7. Xu, H.; Gong, X.; Zhang, H. H.; Zhang, Q.; Zhao, D. D.; Peng, J. X., Targeting human telomerase reverse transcriptase by a simple siRNA expression cassette in HepG2 cells. *Hepat. Mon.* **2015**, *15* (3).

8. Li, H.-J.; Wang, H.-X.; Sun, C.-Y.; Du, J.-Z.; Wang, J., Shell-detachable nanoparticles based on a light-responsive amphiphile for enhanced siRNA delivery. *R. Soc. Chem. Adv.* **2014**, *4* (4), 1961-1964.
9. Greco, C. T.; Muir, V. G.; Epps, T. H., III; Sullivan, M. O., Efficient tuning of siRNA dose response by combining mixed polymer nanocarriers with simple kinetic modeling. *Acta Biomater.* **2017**, *50*, 407-416.
10. Johnson, R. N.; Chu, D. S. H.; Shi, J.; Schellinger, J. G.; Carlson, P. M.; Pun, S. H., HPMA-oligolysine copolymers for gene delivery: Optimization of peptide length and polymer molecular weight. *Journal of Controlled Release* **2011**, *155* (2), 303-311.
11. Liao, Z.-X.; Ho, Y.-C.; Chen, H.-L.; Peng, S.-F.; Hsiao, C.-W.; Sung, H.-W., Enhancement of efficiencies of the cellular uptake and gene silencing of chitosan/siRNA complexes via the inclusion of a negatively charged poly(γ -glutamic acid). *Biomaterials* **2010**, *31* (33), 8780-8788.
12. Kurosaki, T.; Kitahara, T.; Fumoto, S.; Nishida, K.; Nakamura, J.; Niidome, T.; Kodama, Y.; Nakagawa, H.; To, H.; Sasaki, H., Ternary complexes of pDNA, polyethylenimine, and γ -polyglutamic acid for gene delivery systems. *Biomaterials* **2009**, *30* (14), 2846-2853.
13. Syga, M.-I.; Nicoli, E.; Kohler, E.; Shastri, V. P., Albumin incorporation in polyethylenimine-DNA polyplexes influences transfection efficiency. *Biomacromolecules* **2016**, *17* (1), 200-207.
14. Tseng, S. J.; Zeng, Y.-F.; Deng, Y.-F.; Yang, P.-C.; Liu, J.-R.; Kempson, I. M., Switchable delivery of small interfering RNA using a negatively charged pH-responsive polyethylenimine-based polyelectrolyte complex. *Chem. Commun.* **2013**, *49* (26), 2670-2672.
15. Duceppe, N.; Tabrizian, M., Factors influencing the transfection efficiency of ultra low molecular weight chitosan/hyaluronic acid nanoparticles. *Biomaterials* **2009**, *30* (13), 2625-2631.
16. Liao, Z.-X.; Peng, S.-F.; Chiu, Y.-L.; Hsiao, C.-W.; Liu, H.-Y.; Lim, W.-H.; Lu, H.-M.; Sung, H.-W., Enhancement of efficiency of chitosan-based complexes for gene transfection with poly(γ -glutamic acid) by augmenting their cellular uptake and intracellular unpackage. *Journal of Controlled Release* **2014**, *193*, 304-315.

17. Han, L.; Tang, C.; Yin, C., Effect of binding affinity for siRNA on the in vivo antitumor efficacy of polyplexes. *Biomaterials* **2013**, *34* (21), 5317-5327.
18. Zhang, J.; He, C. B.; Tang, C.; Yin, C. H., Ternary polymeric nanoparticles for oral siRNA delivery. *Pharm. Res.* **2013**, *30* (5), 1228-1239.
19. Lee, J.; Ryoo, N. K.; Han, H.; Hong, H. K.; Park, J. Y.; Park, S. J.; Kim, Y. K.; Sim, C.; Kim, K.; Woo, S. J.; Park, K. H.; Kim, H., Anti-VEGF polysiRNA polyplex for the treatment of choroidal neovascularization. *Mol. Pharm.* **2016**, *13* (6), 1988-1995.
20. Hammond, P. T., Polyelectrolyte multilayered nanoparticles: using nanolayers for controlled and targeted systemic release. *Nanomedicine* **2012**, *7* (5), 619-622.
21. Chertok, B.; Langer, R.; Anderson, D. G., Spatial control of gene expression by nanocarriers using heparin masking and ultrasound-targeted microbubble destruction. *ACS Nano* **2016**, *10* (8), 7267-7278.
22. Kelkar, S. S.; Reineke, T. M., Theranostics: combining imaging and therapy. *Bioconjugate Chem.* **2011**, *22* (10), 1879-1903.
23. Ho, Y. P.; Chen, H. H.; Leong, K. W.; Wang, T. H., Evaluating the intracellular stability and unpacking of DNA nanocomplexes by quantum dots-FRET. *Journal of Controlled Release* **2006**, *116* (1), 83-89.
24. Derfus, A. M.; Chen, A. A.; Min, D. H.; Ruoslahti, E.; Bhatia, S. N., Targeted quantum dot conjugates for siRNA delivery. *Bioconjugate Chem.* **2007**, *18* (5), 1391-1396.
25. Foster, A. A.; Ross, N. L.; Sullivan, M. O., Fluorescent dye incorporation causes weakened gene association and intracellular aggregate formation in nonviral carriers. *Journal of Gene Medicine* **2015**, *17* (3-5), 69-79.
26. Burke, P. A.; Pun, S. H.; Reineke, T. M., Advancing polymeric delivery systems amidst a nucleic acid therapy renaissance. *ACS Macro Lett.* **2013**, *2* (10), 928-934.
27. Schlegel, A.; Largeau, C.; Bigey, P.; Bessodes, M.; Lebozec, K.; Scherman, D.; Escriou, V., Anionic polymers for decreased toxicity and enhanced in vivo delivery of siRNA complexed with cationic liposomes. *Journal of Controlled Release* **2011**, *152* (3), 393-401.

28. Wang, Y. L.; Kimura, K.; Dubin, P. L.; Jaeger, W., Polyelectrolyte-micelle coacervation: Effects of micelle surface charge density, polymer molecular weight, and polymer/surfactant ratio. *Macromolecules* **2000**, *33* (9), 3324-3331.
29. Hoffman, A. S., Stimuli-responsive polymers: Biomedical applications and challenges for clinical translation. *Adv. Drug Deliv. Rev.* **2013**, *65* (1), 10-16.
30. Chen, H. H.; Ho, Y.-P.; Jiang, X.; Mao, H.-Q.; Wang, T.-H.; Leong, K. W., Quantitative comparison of intracellular unpacking kinetics of polyplexes by a model constructed from quantum Dot-FRET. *Mol. Ther.* **2008**, *16* (2), 324-332.
31. Green, M. D.; Foster, A. A.; Greco, C. T.; Roy, R.; Lehr, R. M.; Epps, T. H., III; Sullivan, M. O., Catch and release: photocleavable cationic diblock copolymers as a potential platform for nucleic acid delivery. *Polym. Chem.* **2014**, *5* (19), 5535-5541.
32. Ross, N. L.; Munsell, E. V.; Sabanayagam, C.; Sullivan, M. O., Histone-targeted polyplexes avoid endosomal escape and enter the nucleus during postmitotic redistribution of ER membranes. *Mol. Ther. Nucleic Acids* **2015**, *4*, e226.
33. Foster, A. A.; Greco, C. T.; Green, M. D.; Epps, T. H., III; Sullivan, M. O., Light-mediated activation of siRNA release in diblock copolymer assemblies for controlled gene silencing. *Adv. Healthc. Mater.* **2015**, *4* (5), 760-770.
34. Braun, G. B.; Pallaoro, A.; Wu, G.; Missirlis, D.; Zasadzinski, J. A.; Tirrell, M.; Reich, N. O., Laser-activated gene silencing via gold nanoshell-siRNA conjugates. *ACS Nano* **2009**, *3* (7), 2007-2015.
35. Mahmoudi, M.; Lynch, I.; Ejtehadi, M. R.; Monopoli, M. P.; Bombelli, F. B.; Laurent, S., Protein-nanoparticle interactions: opportunities and challenges. *Chem. Rev.* **2011**, *111* (9), 5610-5637.
36. Sizovs, A.; Xue, L.; Tolstyka, Z. P.; Ingle, N. P.; Wu, Y.; Cortez, M.; Reineke, T. M., Poly(trehalose): sugar-coated nanocomplexes promote stabilization and effective polyplex-mediated siRNA delivery. *J. Am. Chem. Soc.* **2013**, *135* (41), 15417-15424.

37. Karmali, P. P.; Simberg, D., Interactions of nanoparticles with plasma proteins: implication on clearance and toxicity of drug delivery systems. *Expert Opin. Drug Deliv.* **2011**, *8* (3), 343-357.
38. Docter, D.; Westmeier, D.; Markiewicz, M.; Stolte, S.; Knauer, S. K.; Stauber, R. H., The nanoparticle biomolecule corona: lessons learned - challenge accepted? *Chem. Soc. Rev.* **2015**, *44* (17), 6094-6121.
39. Suzuki, Y.; Hyodo, K.; Tanaka, Y.; Ishihara, H., siRNA-lipid nanoparticles with long-term storage stability facilitate potent gene-silencing in vivo. *Journal of Controlled Release* **2015**, *220*, 44-50.
40. Ewe, A.; Schaper, A.; Barnert, S.; Schubert, R.; Temme, A.; Bakowsky, U.; Aigner, A., Storage stability of optimal liposome-polyethylenimine complexes (lipopolyplexes) for DNA or siRNA delivery. *Acta Biomaterialia* **2014**, *10* (6), 2663-2673.
41. Sarett, S. M.; Werfel, T. A.; Chandra, I.; Jackson, M. A.; Kavanaugh, T. E.; Hattaway, M. E.; Giorgio, T. D.; Duvall, C. L., Hydrophobic interactions between polymeric carrier and palmitic acid-conjugated siRNA improve PEGylated polyplex stability and enhance in vivo pharmacokinetics and tumor gene silencing. *Biomaterials* **2016**, *97*, 122-132.
42. Kim, H. J.; Miyata, K.; Nomoto, T.; Zheng, M.; Kim, A.; Liu, X.; Cabral, H.; Christie, R. J.; Nishiyama, N.; Kataoka, K., siRNA delivery from triblock copolymer micelles with spatially-ordered compartments of PEG shell, siRNA-loaded intermediate layer, and hydrophobic core. *Biomaterials* **2014**, *35* (15), 4548-4556.
43. Strand, S. P.; Lelu, S.; Reitan, N. K.; Davies, C. d. L.; Artursson, P.; Varum, K. M., Molecular design of chitosan gene delivery systems with an optimized balance between polyplex stability and polyplex unpacking. *Biomaterials* **2010**, *31* (5), 975-987.
44. Nelson, C. E.; Kintzing, J. R.; Hanna, A.; Shannon, J. M.; Gupta, M. K.; Duvall, C. L., Balancing cationic and hydrophobic content of PEGylated siRNA polyplexes enhances endosome escape, stability, blood circulation time, and bioactivity in vivo. *ACS Nano* **2013**, *7* (10), 8870-8880.
45. Zhou, J.; Liu, J.; Cheng, C. J.; Patel, T. R.; Weller, C. E.; Piepmeier, J. M.; Jiang, Z.; Saltzman, W. M., Biodegradable poly(amine-co-ester) terpolymers for targeted gene delivery. *Nature Materials* **2012**, *11* (1), 82-90.

46. Greco, C. T.; Epps, T. H., III; Sullivan, M. O., Mechanistic design of polymer nanocarriers to spatiotemporally control gene silencing. *ACS Biomater. Sci. Eng.* **2016**, *2* (9), 1582-1594.
47. Kim, Y. P.; Oh, Y. H.; Oh, E.; Ko, S.; Han, M. K.; Kim, H. S., Energy transfer-based multiplexed assay of proteases by using gold nanoparticle and quantum dot conjugates on a surface. *Analytical Chemistry* **2008**, *80* (12), 4634-4641.
48. Robin, M. P.; Osborne, S. A. M.; Pikrarnenou, Z.; Raymond, J. E.; O'Reilly, R. K., Fluorescent block copolymer micelles that can self-report on their assembly and small molecule encapsulation. *Macromolecules* **2016**, *49* (2), 653-662.
49. Endres, T.; Zheng, M. Y.; Kilic, A.; Turowska, A.; Beck-Broichsitter, M.; Renz, H.; Merkel, O. M.; Kissel, T., Amphiphilic biodegradable PEG-PCL-PEI triblock copolymers for FRET-capable in vitro and in vivo delivery of siRNA and quantum dots. *Mol. Pharm.* **2014**, *11* (4), 1273-1281.
50. Patterson, J. P.; Kelley, E. G.; Murphy, R. P.; Moughton, A. O.; Robin, M. P.; Lu, A.; Colombani, O.; Chassenieux, C.; Cheung, D.; Sullivan, M. O.; Epps, T. H., III; O'Reilly, R. K., Structural characterization of amphiphilic homopolymer micelles using light scattering, SANS, and cryo-TEM. *Macromolecules* **2013**, *46* (15), 6319-6325.
51. Kuntsche, J.; Horst, J. C.; Bunjes, H., Cryogenic transmission electron microscopy (cryo-TEM) for studying the morphology of colloidal drug delivery systems. *Int. J. Pharm.* **2011**, *417* (1-2), 120-137.
52. Weissman, H.; Rybtchinski, B., Noncovalent self-assembly in aqueous medium: Mechanistic insights from time-resolved cryogenic electron microscopy. *Curr. Opin. Colloid Interface Sci.* **2012**, *17* (6), 330-342.
53. Jayakumar, M. K. G.; Idris, N. M.; Zhang, Y., Remote activation of biomolecules in deep tissues using near-infrared-to-UV upconversion nanotransducers. *Proc. Natl. Acad. Sci. U.S.A.* **2012**, *109* (22), 8483-8488.
54. Zou, W. Q.; Visser, C.; Maduro, J. A.; Pshenichnikov, M. S.; Hummelen, J. C., Broadband dye-sensitized upconversion of near-infrared light. *Nat. Photon.* **2012**, *6* (8), 560-564.

Chapter 6

HYBRID FORMULATIONS FOR ATTENUATING MALADAPTIVE RESPONSES IN HUMAN AORTIC ADVENTITIAL FIBROBLASTS

This chapter describes the formulation of hybrid lipid-polymer nanocomplexes to enable efficient, on/off control over gene silencing in human primary AoAFs. Furthermore, the implementation of a dosing regimen allowed for the attenuation of maladaptive responses through the prolonged knockdown of two key functional genes. The text and figures in this chapter are adapted from a manuscript under review at *Advanced Biosystems*, written by Greco, C. T.; Epps, T. H., III; Sullivan, M. O., and entitled “Attenuation of Maladaptive Responses in Aortic Adventitial Fibroblasts through Stimuli-Triggered siRNA Release from Lipid-Polymer Nanocomplexes.”

6.1 Introduction

Cardiovascular disease is the leading cause of death worldwide,¹ and vascular reconstructive surgeries, including the placement of bypass grafts, have become routine procedures for treating these ailments.² Unfortunately, even standard treatments, such as autologous vein grafts from the leg or arterial grafts from the arm or thorax, commonly fail within a few years due to inappropriate vessel remodeling.³⁻⁶ These graft failures are primarily driven by maladaptive cellular responses elicited by tissue injury and hemodynamic stress.⁷ Anastomoses, the sites of surgical vessel connection, are at particular risk due to suture line scarring, stricture, and higher incidences of stenosis and fibrosis.⁸ Unfortunately, although drug eluting stents and externally applied films have shown promise in preventing complications, these

interventions provide inadequate spatial and temporal control over cell behaviors in the graft conduit.^{9, 10} Thus, new methods are needed that can locally target the key cell types involved in failure. Such approaches could enable improved healing responses by tuning the application and release of regulatory therapies according to the localized environment within the site of injury.¹¹

Adventitial fibroblasts (AF)s, which populate the outermost layer of arteries, are particularly important cellular mediators of normal and pathogenic vessel remodeling.^{12, 13} Specifically, AFs are the dominant cell type in the adventitium, and they regulate the structural integrity and growth of blood vessels through the production of extracellular matrix and the recruitment of the microvascular blood supply.^{13, 14} AFs contribute to the injury response through a variety of mechanisms, including their capacity to rapidly proliferate and differentiate into myofibroblasts, which have the ability to generate high contractile forces through the expression of alpha smooth muscle actin (α SMA) and the formation of multicellular networks.^{15, 16} Although such forces are necessary to induce vessel remodeling, this behavior is detrimental when it becomes excessive following reconstructive surgery.¹⁷ In particular, AF proliferation and differentiation directly control the progression of intimal hyperplasia and fibrosis, leading to the accumulation of fibrous connective tissue, vessel thickening and scarring, and ultimately, graft failure.^{11, 18} Therapeutic approaches geared toward the attenuation of AF-driven fibrosis would be extremely valuable.¹⁵

In addition to the local targeting of AFs, the control of genes that regulate maladaptive responses in AFs also is critical to promote healing at anastomotic sites. For example, recent studies have elucidated key proliferative effectors and phenotypic

modulators that likely play significant roles in the fibrotic response of AFs.^{19, 20} Two prominent genes noted in the above studies are interleukin 1 beta (IL1 β), a cytokine that mediates injury-induced inflammation,²¹ and cadherin 11 (CDH11), a cell-cell adhesion receptor that coordinates the contraction of fibroblast populations.²² It also is important to understand the differential effects of IL1 β and CDH11 on the signaling cascade initiated by transforming growth factor beta 1 (TGF- β 1), a potent activator of myofibroblasts that is produced by local inflammatory cells and overexpressed in diseased environments.²³ Although TGF- β 1-induced changes in both IL1 β and CDH11 expression have been correlated with myofibroblastic differentiation and inflammation in fibroblastic lineages, the functional relationship between IL1 β and CDH11 has not been explored in the context of adventitial remodeling.

In this chapter, lipid-small interfering RNA (siRNA) complexes (lipoplexes) were modified with stimuli-responsive polymers to gain spatiotemporal control over gene knockdown in human primary aortic adventitial fibroblasts (AoAF)s, which enabled the elucidation of the functional roles of IL1 β and CDH11 in improving vascular healing. These hybrid nanocomplexes were necessary because primary cells (e.g. AoAFs) tend to be refractory to transfection compared to immortalized cell lines.²⁴ Previous work established that the mPEG-*b*-poly(5-(3-(amino)propoxy)-2-nitrobenzyl methacrylate) [mPEG-*b*-P(APNBMA)] block copolymer system was capable of locally regulating the extent of protein silencing on cellular length scales,²⁵ making it an ideal candidate for spatially regulating gene expression in anastomoses. Additionally, the precisely controlled nature of the system allows for accurate predictions of siRNA dosing regimens that facilitate gene knockdown over clinically-relevant timescales associated with adventitial remodeling (one week).²⁶

These characteristics were exploited through the formulation of hybrid nanocarriers that mediated on-demand, spatially-controlled knockdown of IL1 β and CDH11 in AoAFs to $\leq 5\%$ of their initial levels following treatment with a photo-stimulus. The silencing of IL1 β on its own significantly reduced myofibroblast differentiation and proliferation, whereas CDH11 silencing on its own had only a moderate effect. Subsequently, kinetic modeling approaches were used to design dosing regimens that fully silenced IL1 β and/or CDH11 together, over sustained time periods. Complete attenuation of TGF- β 1-induced myofibroblast differentiation was achieved by simultaneously silencing IL1 β and CDH11 for one week, the timescale relevant to adventitial remodeling.²⁶ Thus, these studies uncovered synergistic functional roles of IL1 β and CDH11 in AoAFs and showed that sustained knockdown of these genes is a viable method for mitigating fibrotic responses. In the longer term, the photo-sensitive lipid-polymer nanocomplexes offer a unique opportunity to locally regulate fibrotic conditions in anastomoses and improve healing following cardiovascular surgery.

6.2 Materials and Methods

6.2.1 Materials

Lipofectamine RNAiMAX, anti-CDH11 siRNA, and rabbit IgG polyclonal antibody were purchased from Life Technologies (Carlsbad, CA). Non-targeted (universal negative control) siRNAs were purchased from Sigma-Aldrich (St. Louis, MO). Anti-IL1 β (human) siRNA and rabbit IgG polyclonal antibody were obtained from Santa Cruz Biotechnology (Dallas, TX). Poly(acrylic acid) [PAA] ($M_w = 240,000 \text{ g mol}^{-1}$) was obtained from Acros Organics (Waltham, MA). The mPEG-*b*-

P(APNBMA)_n polymers ($M_n = 7,900 \text{ g mol}^{-1}$, $n = 7.9$; $M_n = 13,100 \text{ g mol}^{-1}$, $n = 23.6$) were synthesized *via* atom-transfer radical polymerization as described previously.²⁷ Dulbecco's Modified Eagle Medium (DMEM) and Dulbecco's phosphate-buffered saline (DPBS, 150 mM NaCl, pH of 7.4) were obtained from Corning Life Sciences – Mediatech Inc. (Manassas, VA). Opti-MEM medium, SuperSignal West Dura Chemiluminescent Substrate, Phalloidin-660, Hoescht 33258, TRIzol Reagent, and AlamarBlue were purchased from Life Technologies (Carlsbad, CA). Antibodies (rabbit anti-GAPDH IgG polyclonal, rabbit anti- α SMA IgG polyclonal, secondary goat anti-rabbit IgG polyclonal-horseradish peroxidase (HRP), and secondary goat anti-rabbit IgG polyclonal-Alexa Fluor 488) and recombinant human TGF- β 1 were purchased from AbCam (Cambridge, MA). Bovine serum albumin (BSA) and a bicinchoninic acid (BCA) protein assay kit were purchased from Pierce (Rockford, IL). Primers were obtained from Eurofins MWG Operon (Huntsville, AL) with the following sequences: α SMA (human) forward 5' TATCCCCGGGACTAAGACGG 3'; α SMA (human) reverse 5' CACCATCACCCCCTGATGTC 3'; GAPDH (human) forward 5' CGGGTTCCTATAAATACGGACTGC 3'; GAPDH (human) reverse 5' CCCAATACGGCCAAATCCGT 3'; IL1 β (rabbit) forward 5' ACCAACAAGTGGTGTCTCCAT 3'; IL1 β (rabbit) reverse 5' ACGGTTGGGGTCTACTACTCT 3'; GAPDH (rabbit) forward 5' AGGTCGGAGTGAACGGATTT 3'; GAPDH (rabbit) reverse 5' TTCCCGTTCTCAGCCTTGAC 3'. The iTaq Universal SYBR Green One-Step Kit and optical flat 8-cap strips were purchased from Bio-Rad (Hercules, CA). Anti-IL1 β (rabbit) siRNAs were obtained from MilliporeSigma (Darmstadt, Germany). All other reagents were obtained from Thermo Fisher Scientific (Waltham, MA).

6.2.2 Formulation of siRNA nanocomplexes

The hybrid nanocomplexes were formed using a solution mixing self-assembly method. Solutions of siRNA and Lipofectamine RNAiMAX were prepared in Opti-MEM and mixed according to Life Technologies' protocol (to produce a final solution containing 0.2 μg siRNA and 3 μL Lipofectamine in a total volume of 96 μL). After a 5 min incubation period, 0.2 μg 240,000 g mol^{-1} PAA was added to the lipoplex solution. The solution was mixed *via* gentle vortexing and then incubated for 20 min. A separate polymer solution was prepared by adding equimolar amounts of mPEG-*b*-P(APNBMA)_{7,9} and mPEG-*b*-P(APNBMA)_{23,6}, on the basis of cationic amine groups. The polymer solution was mixed, *via* gentle vortexing, with the lipoplex/PAA solution to form hybrid complexes with an N:P ratio (N: cationic amine groups on polymer, P: anionic phosphate groups on siRNA) of 4. The hybrid complexes were incubated in a dark environment at room temperature for 30 min prior to further analysis. For the on/off photo-controlled protein silencing experiments, two separate control formulations were used: lipoplexes made with Lipofectamine RNAiMAX according to the manufacturer's protocol and polymer/siRNA complexes (polyplexes) formed as described previously.²⁸

6.2.3 Cell culture

Human aortic adventitial fibroblasts were obtained from Lonza (Walkersville, MD) and cultured following Lonza's protocol in stromal cell basal medium (SCBM) supplemented with the stromal cell growth medium (SCGM) SingleQuot Kit. Rabbit aortic fibroblasts were obtained from Cell Biologics (Chicago, IL) and cultured in the same media as the human AoAFs. The cells were cultured in a humid environment maintained at 37 °C and 5 vol% CO₂.

6.2.4 *In vitro* cell transfection

AoAFs were cultured in plates at a density of 15,000 cells cm⁻² for 24 h. Before transfection, the supplemented growth medium was removed, the cells were washed with DPBS, and Opti-MEM was added to the plates. The nanocomplex solutions were then added dropwise at a final siRNA concentration of 10 nM. Following a 3 h transfection period, the Opti-MEM was replaced with supplemented growth medium for a 30 min recovery period. The medium was replaced with phenol red-free Opti-MEM, and the cells were irradiated with 365 nm light at an intensity of 200 W m⁻² for 10 min on a 37 °C hotplate. Supplemented growth medium was added to the wells after irradiation. To stimulate cell differentiation in some samples, TGF-β1 was added to the growth medium at a concentration of 10 ng mL⁻¹. The growth medium and TGF-β1 were replenished every two days.

6.2.5 Protein knockdown analysis

Western blot analyses were used to measure IL1β and CDH11 protein silencing. In the single dose experiments, cells were transfected and lysed at the specified time points. The protein was extracted from the cells by adding a lysis solution composed of 0.5 vol% Triton X-100, 0.5% sodium deoxycholate, 150 mM NaCl, 5 mM Tris-HCl (pH 7.4), 5 mM EDTA, and 1x Halt Protease and Phosphatase Inhibitor cocktail. For the repeated dosing experiments, a second transfection of nanocomplexes was performed 72 h after the first transfection, and protein was extracted at the given time points. The total protein concentration of each sample was measured using the BCA Protein Assay Kit. The protein solutions were subjected to 4% - 20% sodium dodecyl sulfate polyacrylamide gel electrophoresis (SDS-PAGE) for 35 min at 150 V. The separated proteins then were transferred onto a

poly(vinylidene fluoride) membrane at 18 V for 75 min. The membrane was subsequently blocked in 5 vol % BSA in Tris–HCl-buffered saline (50 mM Tris–HCl, pH 7.4, 150 mM NaCl) containing 0.1 vol % Tween 20 (TBST) at room temperature for 1 h. The membrane was incubated overnight with IL1 β or CDH11 primary antibodies in TBST at 4 °C. The next day, the membrane was incubated in a solution of secondary antibody conjugated to HRP for 1 h. The SuperSignal West Dura Chemiluminescent Substrate was used to enable detection of the bands through chemiluminescent imaging in a FluorChem Q (ProteinSimple, San Jose, CA). To image the GAPDH bands, the membrane was stripped for 15 min with Restore PLUS Western Blot stripping buffer, blocked in BSA solution for 1 h, and subsequently incubated with GAPDH primary antibody overnight. The next day, after incubation in a solution of secondary goat anti-rabbit antibody conjugated to HRP, chemiluminescent imaging was used to detect the bands. The intensity of each target protein was analyzed with ImageJ software.

6.2.6 RNAi modeling

A set of equations (Equations 3.1-3.3 in section 3.3.3) was solved using differential equation solver ode45 in MATLAB.²⁵ Each siRNA dose was modeled by increasing the normalized siRNA concentration by 100 units following time points corresponding to light-triggered siRNA release. The siRNA turnover rate was estimated by determining the cell doubling time of AoAFs cultured in standard growth medium, which was measured to be ~38 h (Figure D.1). Protein degradation rate constants were computed on the basis of IL1 β and CDH11 half-lives, which were ~2.5 h and ~8 h, respectively, as reported in the literature.^{29,30} The mRNA degradation rate

constants were estimated by using a ~8 h half-life for both genes, as this is the approximate average mRNA turnover rate.³¹

6.2.7 Immunocytochemistry (ICC)

Cells were transfected with siRNAs. At the specified time points, the cells were washed with DPBS and fixed in 4% paraformaldehyde for 15 min. The cells were permeabilized with 0.1% (v/v) Triton X-100 in DPBS for 15 min and blocked with 5% bovine serum albumin in DPBS for 1 h. α SMA, a marker of myofibroblast differentiation, was detected by overnight incubation at 4 °C in an α SMA primary antibody solution [2 μ g mL⁻¹ in DPBS]. Alternatively, CDH11 protein expression was detected by overnight incubation at 4 °C in a CDH11 primary antibody solution [2 μ g mL⁻¹ in DPBS]. Samples were then incubated with a solution of secondary antibody labeled with AlexaFluor® 488 [4 μ g mL⁻¹ in DPBS] for 1 h. Cells were incubated in a solution of Phalloidin-660 [160 nM in DPBS] for 30 min to detect F-actin, and then the cells were incubated in a solution of Hoescht 33258 [0.5 μ g mL⁻¹ in DPBS] for 10 min to detect nuclear DNA. Cells were visualized using a 20x objective on an LSM META 510 confocal microscope (Zeiss, Germany) controlled by Image Pro Plus software (version 7.0; Media Cybernetics). The fluorescence intensities in zoomed-out (4x magnification) micrographs were quantified using ImageJ software. The fluorescence intensities of at least 1,000 cells from each channel were averaged through the quantification of total pixel intensity. Then, the signal from the protein of interest (α SMA or CDH11) was divided by the signal from the housekeeping protein (F-actin).

6.2.8 mRNA knockdown analysis

α SMA mRNA knockdown was measured using quantitative PCR (qPCR). Single and double transfections were carried out, and RNA was isolated by TRIzol Reagent according to the manufacturer's protocols. The iTaq Universal SYBR Green One-Step Kit was used to prepare samples for qPCR in triplicate, using the α SMA or GAPDH primers, as described in the manufacturer's protocols. cDNA synthesis and qPCR were conducted on a Bio-Rad CFX96TM using the following conditions: 10 min at 50 °C; 1 min at 95 °C; 40 cycles of 10 s at 95 °C and 30 s at 60 °C; and finally, a 65 °C to 95 °C ramp at a rate of 0.5 °C every 5 s. The $\Delta\Delta C_T$ method was used for analysis,³² and all sample data were normalized to data from untreated cell controls.

6.2.9 Cell Proliferation

Cell growth was evaluated using the AlamarBlue assay according to the manufacturer's protocols. Cells were transfected and grown in fully supplemented medium for 4 days or 7 days after the first transfection for the single dose and double dose experiments, respectively. Medium containing 10 vol% AlamarBlue was added to each well, and the cells were incubated for 6 h in a humid environment maintained at 37 °C and 5 vol% CO₂. Fluorescence was measured using a GloMax-multi detection system plate reader (Promega, Madison, WI). To determine the baseline fluorescence, medium containing 10 vol% AlamarBlue was added to a well without cells. *Note: All samples were treated with the photo-stimulus to isolate the effects of protein knockdown on cellular proliferation.*

6.3 Results and Discussion

6.3.1 Hybrid nanocomplexes enable on/off control over gene silencing

To achieve spatially-tailored and temporally-tuned gene silencing in AoAFs, various formulations of mPEG-*b*-P(APNBMA)/siRNA polyplexes were tested that had previously been shown to provide efficient, light-triggered siRNA delivery in murine embryonic fibroblasts.²⁸ None of the polyplex formulations were able to mediate efficient gene silencing in AoAFs (Figure 6.1). A lack of endosomal escape might be the limiting factor, based on prior evidence demonstrating that human primary cells often are refractory to transfection.²⁴ Lipoplexes comprised of Lipofectamine RNAiMAX were shown to transfect AoAFs efficiently (Figure 6.1), presumably because cationic lipids can interact with endosomal membranes and enhance cargo escape in primary cells.³³ However, these lipid solutions were not capable of mediating photo-controlled, spatiotemporal release. In contrast, hybrid nanocomplexes combining lipids and polymers remained dormant in the absence of a photo-trigger but rapidly released siRNA following the application of light, leading to efficient gene silencing in AoAFs (Figure 6.1). The model gene, IL1 β , was knocked down to ~5% of the protein expression levels measured in untreated controls, demonstrating that the hybrid siRNA nanocarrier system was vital to overcoming the shortcomings of the individual polyplex and lipoplex formulations. Moreover, the on/off control over siRNA activity afforded by the hybrid nanocomplexes can easily be extended to spatially regulate gene expression on the cellular length scale using previously described procedures.²⁵

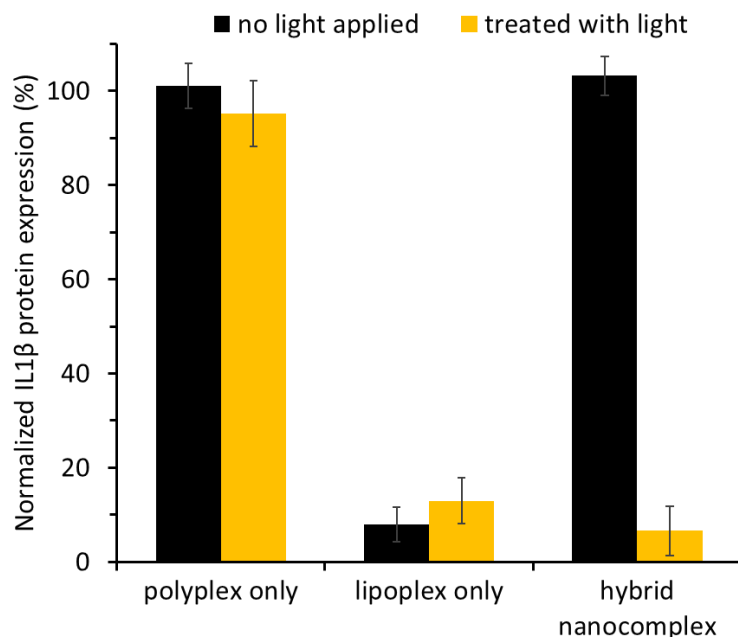


Figure 6.1: Photo-controlled IL1 β protein silencing with mPEG-*b*-P(APNBMA) polyplexes, Lipofectamine RNAiMAX lipoplexes, and hybrid nanocomplexes. AoAFs were treated with siRNA using the various carriers, irradiated with 365 nm light for either 0 min (black bars) or 10 min (gold bars), and lysed for western blot analysis at 48 h post-transfection. Data represent the IL1 β protein expression levels relative to the levels of the loading control glyceraldehyde 3-phosphate dehydrogenase (GAPDH), normalized to the protein levels in controls with no siRNA treatment. Results are shown as the mean \pm standard deviation of data obtained from three independent experiments.

The hybrid nanocomplexes were formulated according to the process depicted in Figure 6.2. First, siRNA was complexed with a cationic lipid, Lipofectamine RNAiMAX. Because these lipoplexes possessed a net positive charge and the mPEG-*b*-P(APNBMA) also was cationic, an anionic component was needed to facilitate electrostatic interactions. PAA, a polymer with a high anionic charge density,³⁴ was mixed with the lipoplexes to reverse the overall charge. Finally, the cationic mPEG-*b*-

P(APNBMA) was incorporated to impart photo-responsive characteristics (charge reversal) to the system.

The structural design and formulation process of the hybrid nanocomplexes share similarities with other lipid-polymer systems in the literature.^{35, 36} Generally, polymers are added to lipid-based carriers to impart a specific characteristic to the system. These features include reduced charge, stealthy behavior, biocompatibility, smaller sizes, and enhanced endosomal escape.³⁷ Although these modifications have proven to be effective, few stimuli-responsive components have been used to induce controlled siRNA release within hybrid lipid-polymer assemblies.³⁸ In this chapter, mPEG-*b*-P(APNBMA) was used to gain photo-responsive control over the disassembly of lipid-containing complexes. This favorable combination of behaviors (e.g. light-responsiveness and endosomal escape) presumably arose as a result of polymer shielding of the endosome-destabilizing cationic lipids prior to light-triggered polymer cleavage/charge reversal, which then initiated lipid-mediated endosome destabilization.³⁹ Thus, the nanocomplexes provide the benefits of both lipids and stimuli-sensitive polymers, enabling precisely tuned on/off control over nucleic acid activity in human primary AoAFs.

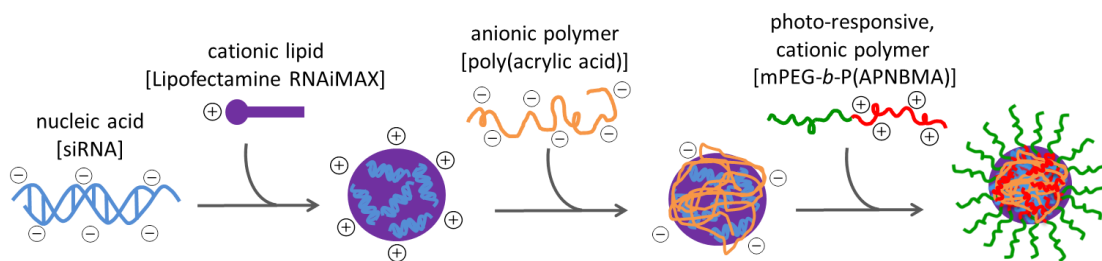


Figure 6.2: Schematic depicting the formulation of the hybrid nanocomplexes. First, nucleic acids (siRNA) were encapsulated in lipoplexes using cationic lipid (Lipofectamine RNAiMAX). Second, anionic polymer (PAA) was added to reverse the lipoplexes surface charge. Third, a mixture of photo-responsive cationic polymers (mPEG-*b*-P(APNBMA)_n with 50% n = 7.9 and 50% n = 23.6, on a molar basis of cationic amine groups) was incorporated into the formulation to form the hybrid nanocomplexes.

It is important to note that the composition of the nanocomplexes was optimized to transfect human AoAFs. Gene silencing experiments in other cell types demonstrated the cell specificity of the nanocomplexes, suggesting that the effects of protein knockdown would be minimal in other types of cells (e.g. smooth muscle cells) surrounding AoAFs on the adventitial side of vessels. Furthermore, future work involves the application of the nanocomplexes within hydrogels of ~1 mm thickness to the outside surface of vascular segments to enable modulation of adventitial cell behavior. These gel thicknesses allow for 365 nm light penetration.

6.3.2 Characterization of hybrid nanocomplexes

The hybrid lipid-polymer nanocomplexes were characterized to determine their fundamental physicochemical properties. As shown in Table D.1, the nanocarriers had an average diameter of 168 nm, which is within the size regime of nanoparticles that are able to undergo endocytosis and enter cells.⁴⁰ The nanocomplexes had a zeta potential of +3.1 mV (Table D.1), indicating that the nanocarrier surface was slightly

positively charged but very close to neutral. The relatively neutral zeta potential suggests that the mPEG-*b*-P(APNBMA) polymers were coating the lipoplexes and the PEG chains were forming an outer corona around the charged cores.⁴¹ The slight positive charge is favorable for inducing cellular uptake and minimizing interactions with serum-components.

Another important consideration in the formulation of new siRNA delivery vehicles is their cytotoxicity, especially when treating sensitive human primary cells such as AoAFs. As shown in previous work, mPEG-*b*-P(APNBMA)-only polyplexes did not lead to any significant change in cell viability relative to untreated cells (Figure 6.3). The hybrid nanocomplexes also possessed excellent biocompatibility (~98% cell viability), similar to the polyplexes. AoAFs that were treated with mPEG-*b*-P(APNBMA)-only polyplexes or the hybrid nanocomplexes combined with the photo-stimulus exhibited a modest (~20%) decrease in cell viability compared to untreated cells, indicating that 365 nm light was moderately cytotoxic. However, lipoplexes comprised of Lipofectamine RNAiMAX were significantly more cytotoxic than the polyplexes or the hybrid nanocomplexes, as treatment with lipoplexes reduced cell viability by ~18% and ~46% without and with 365 nm light, respectively (Figure 6.3). The lack of a significant cytotoxic response of the hybrid lipid-polymer nanocarriers suggests that the biocompatible mPEG-*b*-P(APNBMA) forms an outer corona that shields the cationic lipids from interacting with cells. This shielding feature and its resulting low cytotoxicity indicate that the hybrid nanocomplexes hold promise for use in therapeutic settings.

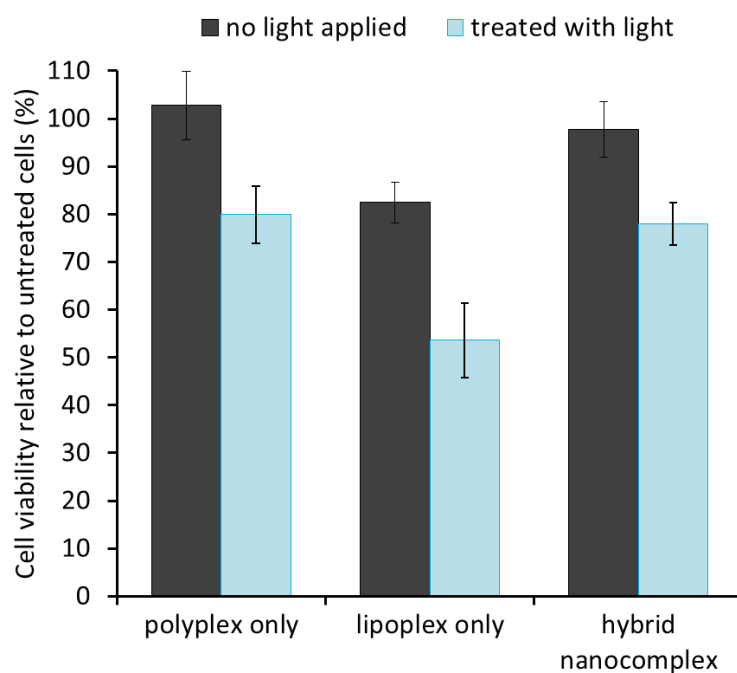


Figure 6.3: Aortic adventitial fibroblast (AoAF) cell viabilities following treatment with either polyplexes, lipoplexes, or hybrid nanocomplexes with without 365 nm light irradiation. 48 h following siRNA and light treatment, an Alamar Blue (AB) assay was used to measure cell viability relative to cells that were untreated. Results are reported as the mean \pm standard deviation of data obtained from three independent experiments.

Finally, the light-triggered siRNA release behavior of the nanocomplexes was explored to gain a better understanding of the on/off gene silencing response. As shown in Figure 6.4, nanocarriers that were not irradiated with light remained stable and encapsulated nearly 100% of the siRNA. Nanocomplexes that were treated with the photo-stimulus for increasing lengths of time exhibited increasing amounts of siRNA release. After 10 min of irradiation, which is the dosage of light used during transfections, ~56% of the siRNA was released. The high level of light-triggered

siRNA release helps explain the efficient, on/off gene silencing trends detected in cells, even when low concentrations of siRNA (10 nM) were used.

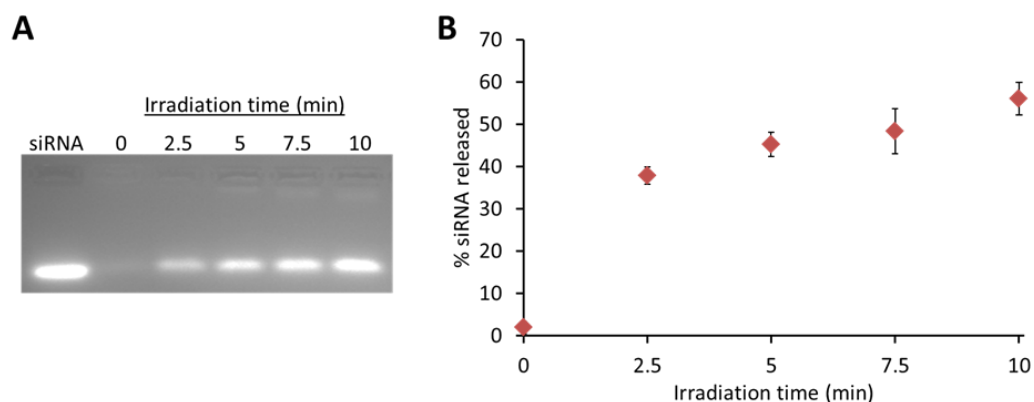


Figure 6.4: Light-triggered siRNA release from hybrid nanocomplexes. The nanocarriers were formulated, incubated in sodium dodecyl sulfate (SDS) solutions at an S/P ratio (S: sulfates on SDS, P: phosphates on siRNA) of 4 to simulate lipid-rich intracellular environments, and irradiated with 365 nm light for various lengths of time. (A) The solutions were analyzed by gel electrophoresis analyses, and (B) the amount of free siRNA was quantified on the basis of relative band intensities via ImageJ software. Results are reported as the mean \pm standard deviation of data obtained from three independent experiments.

6.3.3 Gene silencing dynamics following a single siRNA dose

Given the controlled release nature of the nanocomplexes, the dynamics of protein knockdown were investigated to determine how to appropriately dose siRNA in AoAFs. Two genes implicated in maladaptive responses, IL1 β and CDH11, were studied using a combination of experimental analyses and kinetic modeling. siRNAs targeting IL1 β or CDH11 were delivered to cells using the nanocomplexes, and siRNA release was induced upon application of a photo-stimulus at 3.5 h post-transfection. According to the model, protein expression for both genes was expected

to decrease immediately following photo-induced siRNA release (Figure 6.5A). However, the rate of change in protein concentrations varied between the two genes. IL1 β protein expression was forecasted to be almost fully knocked down ~16 h post-transfection, whereas complete CDH11 knockdown was not expected until ~27 h post-transfection. The proteins were predicted to be silenced to $\leq 5\%$ of their initial levels for ~47 h (IL1 β) or ~34 h (CDH11) before recovering. Experimental measurements of protein concentrations taken at various times validated these predictions and demonstrated that the model could accurately capture all three phases of the gene silencing process – e.g. initial knockdown, maximal silencing, and recovery of protein expression.

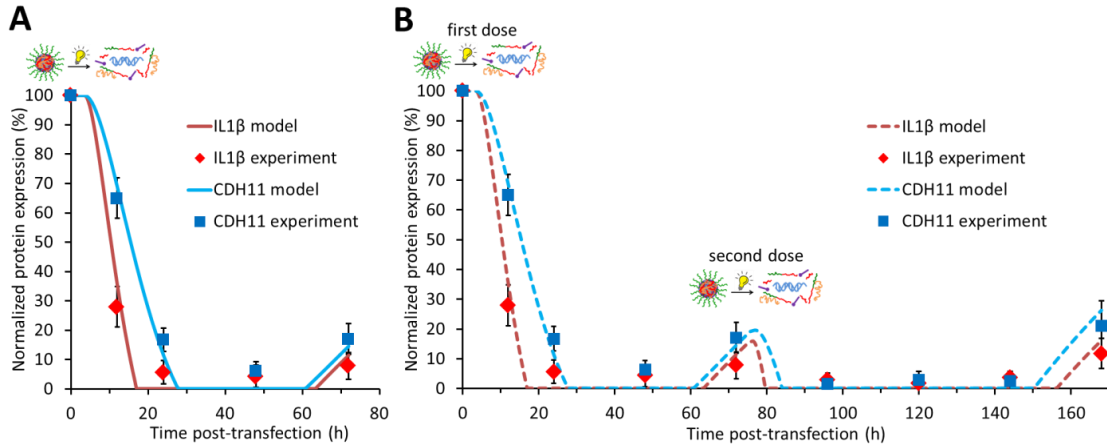


Figure 6.5: Dynamics of IL1 β and CDH11 protein silencing following a single dose (A) or double dose (B) of siRNA. Kinetic modeling was used to predict the temporal IL1 β (dashed red line) and CDH11 (dashed blue line) protein expression following doses of siRNA. Initial protein concentrations were normalized to 100, and the model predictions were verified experimentally using western blotting. Data points represent the normalized IL1 β (red diamonds) or CDH11 (blue squares) protein expression levels relative to the loading control. Experimental results are shown as the mean \pm standard deviation of data obtained from three independent samples. (A) AoAFs were transfected with the hybrid nanocomplexes at $t = 0$ h, irradiated with 365 nm light to release the siRNA 3.5 h post-transfection, and lysed at the times indicated by the data points. (B) AoAFs were transfected with the hybrid nanocomplexes at $t = 0$ h and $t = 72$ h, irradiated with 365 nm light 3.5 h after each transfection, and lysed at the times indicated by the data points.

The protein silencing dynamics for IL1 β and CDH11 followed the same overall trend, except that the rate of initial protein knockdown depended on the half-lives of the two proteins (IL1 β and CDH11 have protein half-lives of ~ 2.5 h and ~ 8 h, respectively).^{29,30} If sufficient amounts of siRNA are released to saturate the RNA-induced silencing complex machinery, the cleavage of targeted mRNAs rapidly occurs, and the translation of new protein is halted. The existing protein, translated before the onset of RNAi initiation, would then degrade in time according to its innate

turnover rate. Therefore, the concentration of IL1 β should decrease faster than CDH11 on the basis of its shorter protein half-life.

On the other hand, the duration of sustained maximal silencing depends more strongly on the doubling time of the cells, and to a much lesser extent, upon the stability of the siRNA.⁴² The intracellular siRNA is diluted in time due both to cell division and degradation from nucleases, and RNAi effects generally only last for a few days in growing cells, such as AoAFs. The concentration of IL1 β - and CDH11-targeted siRNA in the AoAFs decreased at approximately the same rate, and the protein levels start to recover at ~3 days post-transfection as detailed by the modeling and experimental data. Thus, these analyses elucidated the dynamics of IL1 β and CDH11 knockdown in AoAFs following a single dose of siRNA. These timescales are consistent with those for inflammation-mediated fibroblast proliferation,^{12, 43} providing further justification for the use of IL1 β - and CDH11-targeted siRNAs for the treatment of cardiovascular disease.

6.3.4 Gene silencing dynamics following a double dose of siRNA

Following severe injury, adventitial remodeling/myofibroblast differentiation occurs over a time period of ~7 days,²⁶ and thus, sustained gene silencing is needed in such cases. The kinetic modeling allowed the implementation of dosing schedules that enabled knockdown below a desired threshold over the one week duration. More specifically, using the framework established in Figure 6.5A, different dosing regimens were analyzed to predict the RNAi response following a second application of siRNA. As shown in Figure 6.5B, the second transfection was started at 72 h; i.e. near the time at which the protein levels were predicted to start recovering after the first transfection. The model forecasted that implementation of this dosing schedule

would allow the knockdown of both genes to be sustained for ~7 days at levels of < 20% relative to untreated controls. Experimental measurements of protein levels validated this dosing regimen model and demonstrated that the predictions accurately captured the prolonged knockdown and recovery phases. Thus, the modeling approach allowed us to accurately predict that only two doses were needed to achieve gene silencing of both genes over the clinically-relevant timescale of one week.⁴³ Specifically, recent work by Robinson *et al.* found that maladaptive tissue responses occur within 3 days of surgery and are sustained on the timescale of weeks.⁴³

One challenging aspect of implementing predictive siRNA dosing schedules is the effect of the silenced genes on cellular parameters governing responses to subsequent siRNA applications. Proliferation analyses (discussed later) determined that the knockdown of IL1 β slowed cellular growth rates by ~30% after each dose. Thus, the kinetic model was updated with this information to account for the change in siRNA dilution rate as a result of a longer cell doubling time. The updated model accurately predicted that IL1 β would remain knocked down longer than CDH11, which was verified by experiment measurements. Therefore, the combination of a double dosing regimen and simple kinetic modeling enabled the knockdown of both genes to be sustained for one week in a predictable manner.

6.3.5 Gene silencing affects myofibroblast differentiation (α SMA protein expression)

One of the primary hallmarks of fibrosis is the differentiation of fibroblasts into myofibroblasts, which is driven by the production of TGF- β 1 by local inflammatory cells.²¹ Accordingly, to simulate the inflammatory fibrotic responses in culture, recombinant TGF- β 1 protein was added to the growth medium of AoAFs.

The cells were treated with formulations of non-targeted siRNA, IL1 β siRNA, CDH11 siRNA, or combined IL1 β and CDH11 siRNAs *via* the single dosing schedule in Figure 6.5A. The extent of differentiation was determined by measuring changes in α SMA protein expression, the most widely used indicator of the myofibroblast phenotype.^{7, 12} As shown in the micrographs in Figure 6.6A, the addition of TGF- β 1 induced AoAFs to differentiate into myofibroblasts within 3 days, consistent with responses reported in the literature.⁴⁴ Specifically, AoAFs that were not treated with TGF- β 1 expressed low levels of α SMA protein relative to F-actin protein; however, cells treated with TGF- β 1 and either no siRNA or a single dose of non-targeted siRNA exhibited robust α SMA protein expression.

AoAFs treated with TGF- β 1 followed by application of functional siRNAs targeting IL1 β exhibited a significant reduction in α SMA staining, indicating that knocking down IL1 β blocks the differentiation cascade to a measurable extent. In contrast, TGF- β 1-treated cells with silenced CDH11 maintained robust α SMA protein expression. AoAFs that were treated with both IL1 β and CDH11 siRNAs also exhibited decreased α SMA staining. The quantification of protein expression based upon these ICC experiments is shown in Figure 6.6B and is presented as α SMA relative to F-actin. As can be noted from the micrographs, α SMA protein expression was only significantly attenuated when IL1 β was knocked down (either alone or in combination with CDH11) using the single dose regimen.

To determine how myofibroblast differentiation would be affected by the double dosing regimen, α SMA protein expression was analyzed on day 8. The differences in protein expression as a function of IL1 β and/or CDH11 knockdown were more prominent in the double dosing experiments, though the overall trends were

similar to the single dosing studies (comparison of Figures 6.6B and 6.6C). The delivery of IL1 β siRNA suppressed α SMA levels by ~45% at day 8 relative to treatment with non-targeting siRNA. However, CDH11 silencing alone provided no reduction in α SMA protein expression compared to treatment with non-targeting siRNA. This behavior most likely was exhibited because AoAFs that were treated with only CDH11 siRNA had differentiated to approximately the same extent as cells treated with non-targeting siRNA before application of the second dose (Figure 6.6B), and further CDH11 knockdown could not reverse the myofibroblast phenotype. A recent report demonstrated that the de-activation of myofibroblasts is difficult to control and that the restricted capacity of myofibroblasts to de-differentiate is a major cause of fibrotic disorders.⁴⁵

Regardless of dosing regimen, only cells treated with IL1 β siRNA exhibited a significant reduction in α SMA protein expression (Figure 6.6). In agreement with these findings, Guo *et al.* demonstrated that the neutralization of IL1 β *in vivo* attenuated fibrosis and was correlated with decreases in TGF- β 1 activity.⁴⁶ A number of recent studies also reported that increased IL1 β levels enhanced the severity of fibrosis *in vivo*.^{47, 48} In a related example, Chen and coworkers showed that IL1 β -stimulation of HO-8910PM and NIH3T3 cells increased the expression of α SMA and activated proteins involved in myofibroblast differentiation.⁴⁹ However, others have reported different impacts of IL1 β activity on α SMA expression in other cell types,^{21, 50, 51} and moreover, Dewald *et al.* found significant species-specific differences in cellular responses to inflammatory cytokines following myocardial infarction.⁵² The finding that IL1 β silencing effectively blocked TGF- β 1-induced α SMA protein

expression in AoAFs is likely applicable to fibroblasts derived from different organs but may not directly translate to all cell types or species.

CDH11 silencing in AoAFs did not attenuate α SMA protein expression compared to treatment with non-targeting siRNA, and the combination of CDH11 and IL1 β silencing also did not further reduce α SMA protein expression as compared with samples treated with IL1 β siRNA only (Figure 6.6). The knockdown of CDH11 has been shown to regulate the myofibroblast phenotype differently depending on the cell type.^{53,54} For example, Verhoekx *et al.* reported that α SMA expression remained unchanged in human dermal fibroblasts, but was reduced by ~50% in Dupuytren's myofibroblasts following CDH11 silencing.⁵⁴ Wang and coworkers also found that CDH11 knockdown did not affect differentiation when porcine valvular interstitial cells were treated with 5 ng mL⁻¹ of TGF- β 1.²³ Moreover, because the activity of CDH11 is dependent on the number of cell-cell contacts, differences in cell density also may contribute to the variations in cellular responses (discussed later).

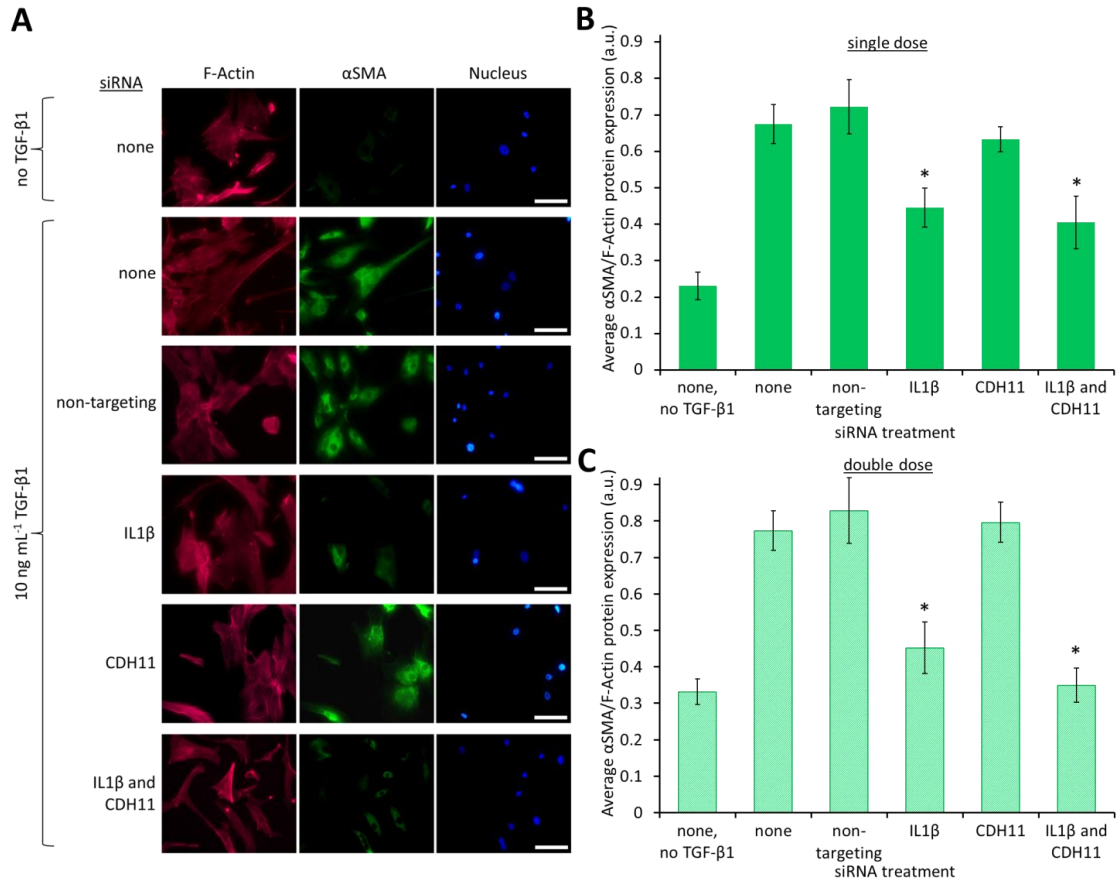


Figure 6.6: Attenuation of myofibroblast differentiation (α SMA protein expression) following siRNA dosing. AoAFs underwent transfection with different siRNA formulations and were treated with either 0 or 10 ng mL⁻¹ TGF- β 1 to induce differentiation. (A) Representative ICC micrographs of AoAFs 4 days post-transfection following a single dose of siRNA. AoAFs were stained for F-actin (magenta), α SMA (green), and nuclear DNA (blue). Scale bars = 50 μ m. *Note: A representative zoomed-in micrograph of F-actin staining that shows stress fibers is displayed in Figure D.2.* (B) Quantification of relative α SMA protein expression from single dose ICC micrographs in (A). (C) Quantification of relative α SMA protein expression from double dose ICC micrographs [not shown], characterized on day 8. The average total fluorescence intensity of α SMA relative to F-actin of at least 100 cells per sample was measured using ImageJ for both the single and double dose regimens. All results are shown as the mean \pm standard deviation of data obtained from three independent experiments. An asterisk indicates a statistically significant difference in α SMA protein expression in comparison to the no siRNA and 10 ng mL⁻¹ TGF- β 1 treatment control ($p < 0.05$).

6.3.6 Gene silencing affects myofibroblast differentiation (α SMA mRNA expression)

To gain a more quantitative understanding of temporal differences in myofibroblast differentiation, changes in the mRNA transcript levels also were analyzed. As shown in Figure 6.7A, the trends for the single dosing regimen were generally in agreement with the ICC data from Figure 6.6B. In particular, the addition of TGF- β 1 induced a six-fold increase in α SMA transcripts, and the knockdown of IL1 β provided a significant decrease in differentiation. The combined knockdown of IL1 β and CDH11 lead to a greater attenuation of α SMA mRNA expression than IL1 β knockdown alone, although the α SMA levels were still higher than the ‘no TGF- β 1’ control. CDH11 knockdown resulted in a minor, but statistically significant, reduction of α SMA transcript levels relative to cells not treated with siRNA. Despite slight differences, the measurements of α SMA mRNA (3 days) and α SMA protein expression (4 days) post-transfection, respectively, were in agreement.

α SMA transcript levels also were studied on day 7 of the double dosing schedule. AoAFs incubated in TGF- β 1 exhibited ~4.5 times more α SMA mRNA transcripts than untreated cells (Figure 6.7B), suggesting that untreated cells did not significantly alter their fibroblast phenotype on tissue culture plastic over 7 days (Figure D.3). The delivery of IL1 β siRNA significantly reduced α SMA mRNA levels relative to the delivery of non-targeting siRNA, whereas CDH11 silencing did not provide these effects. However, the combined knockdown of IL1 β and CDH11 attenuated α SMA mRNA expression to the same level as the no TGF- β 1 control, indicating that differentiation was completely halted over one week with the double dosing schedule.

Given the lack of response from CDH11 silencing alone, the significantly enhanced attenuation of differentiation from the combined delivery of IL1 β and CDH11 siRNA in comparison to IL1 β siRNA alone (combined effects were not simply additive) suggests that the two genes may cooperate synergistically. Little is known about the direct relationship between IL1 β and CDH11, but Yoshioka *et al.* recently found that the knockdown of CDH11 reduced IL1 β -induced proliferation by 42% in rheumatoid arthritis-derived synovial fibroblast cells.⁵⁵ The authors concluded that CDH11 is involved in IL1 β -mediated pathways, and that there is an indirect interplay between the two genes *via* β -catenin.⁵⁵ In a related study, CDH11 expression was found to be upregulated after addition of IL1 β in fibroblast-like synoviocytes.⁵⁶ These reports suggest that the two genes affect one another in other cell types. More work is needed to probe the intricate interactions between the downstream effectors of IL1 β and CDH11 in AoAFs; however, the data strongly suggest that the combined knockdown of the two genes provides a powerful synergistic method for attenuating TGF- β 1-induced myofibroblast differentiation.

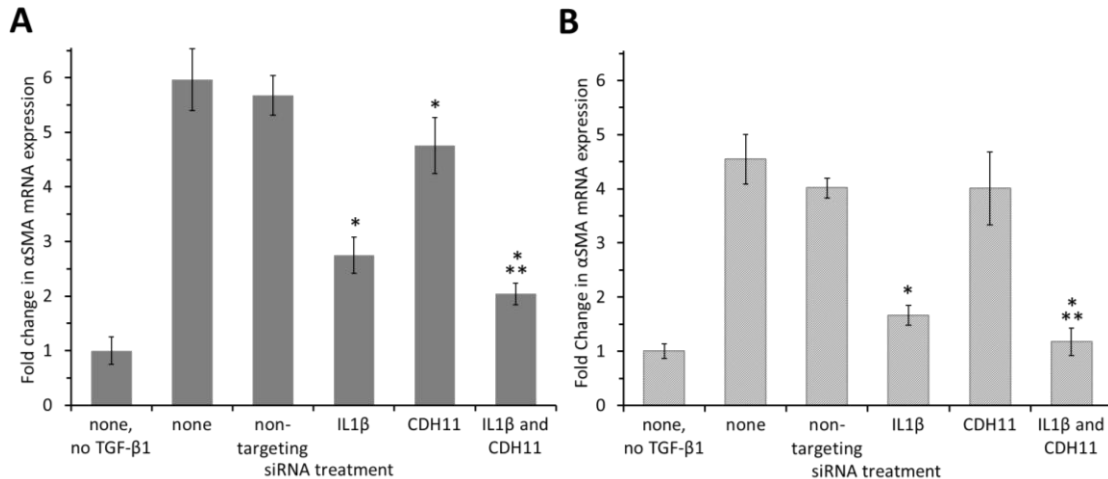


Figure 6.7: Attenuation of myofibroblast differentiation (α SMA mRNA expression) following the two different siRNA dosing schedules. AoAFs underwent transfection at either $t = 0$ h (A) or $t = 0$ h and $t = 72$ h (B) with various siRNA formulations and were treated with either 0 or 10 ng mL^{-1} TGF- β 1 to induce differentiation. (A) qPCR analyses of α SMA mRNA expression levels 3 days post-transfection in the single dose regimen. (B) qPCR analyses of α SMA mRNA expression levels 7 days after the first transfection [4 days after the second transfection] in the double dose regimen. qPCR values were normalized to the levels in the no siRNA and no TGF- β 1 treatment control for each dosing schedule. All results are shown as the mean \pm standard deviation of data obtained from three independent samples. A single asterisk indicates a statistically significant difference in α SMA mRNA expression in comparison to the no siRNA and 10 ng mL^{-1} TGF- β 1 treatment control, and a double asterisk indicates a statistically significant difference in α SMA mRNA expression in comparison to the IL1 β siRNA treatment formulation ($p < 0.05$).

6.3.7 Attenuation of cellular proliferation following gene silencing

In addition to myofibroblast differentiation, increased cellular proliferation is a classic hallmark of fibrosis. The reduction of fibroblast proliferation is a critical therapeutic goal to mitigate maladaptive responses and promote healing in cardiovascular tissues, particularly in the first week following vessel injury.^{12, 57} Changes in the growth rates of the AoAFs were analyzed to determine if the

knockdown of IL1 β and/or CDH11 affected proliferation. As shown in Figure 6.8, non-targeting siRNA did not significantly alter proliferation, which is indicative of the biocompatibility of the hybrid nanocomplexes. The knockdown of IL1 β reduced proliferation by ~30% and ~50% following a single and double dose, respectively. The delivery of only CDH11 siRNA provided a relatively minor reduction in proliferation rate in comparison to the untreated control samples. The combined knockdown of IL1 β and CDH11 reduced proliferation to the same extent as IL1 β alone. Thus, IL1 β , but not CDH11, appears to play a critical role in AoAF proliferation.

The findings in AoAFs are generally in agreement with most literature reports of IL1 β and CDH11 in other cell types.^{49, 55, 58} While IL1 β has been widely identified as playing a key role in fibroblast proliferation, few studies have implicated CDH11.⁵⁵ For example, Vesey *et al.* found that IL1 β was a potent inducer of proliferation with similar activities to those of TGF- β 1 in human cortical fibroblasts.⁵⁸ Consistent with these findings, the studies presented in this chapter indicated that the synergistic effects of knocking down IL1 β and CDH11 attenuated differentiation (Figure 6.7) but were not detected in the AoAF proliferation analyses.

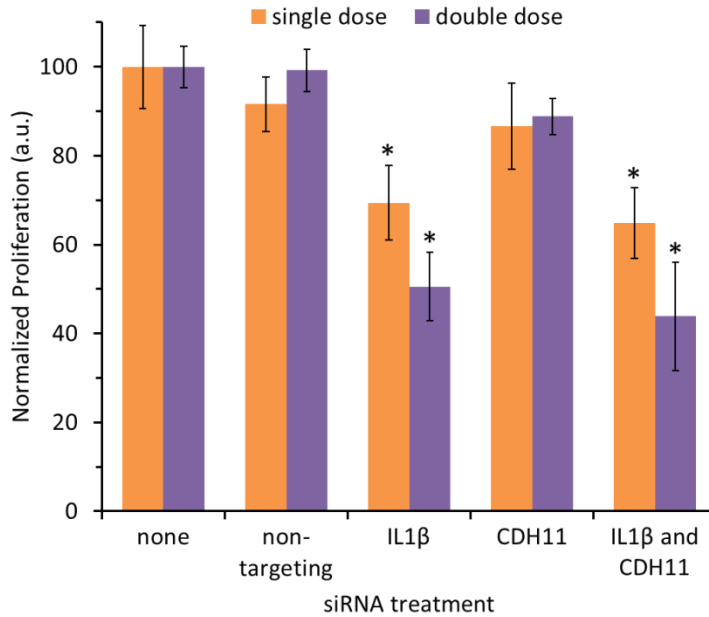


Figure 6.8: Proliferation of AoAFs following the single or double dose siRNA regimen. AoAFs were treated with different siRNA formulations and irradiated with 365 nm light for 10 min after each transfection. The change in the number of cells was measured using the AlamarBlue assay 4 days or 7 days after the first transfection for the single dose (orange bars) and double dose (purple bars) experiments, respectively. Data represent the normalized extents of cellular proliferation relative to cells that were not treated with siRNA, with 100 indicating no change relative to untreated cells. A value of 0 indicates no change in the absolute number of cells from the time of transfection. Results are shown as the mean \pm standard deviation of data obtained from three independent experiments. An asterisk indicates a statistically significant difference in proliferation in comparison to the no siRNA treatment controls ($p < 0.05$).

6.3.8 Cell density effects on CDH11 knockdown

In both the single dose and double dose studies, the knockdown of CDH11 provided only minor, if any, attenuation of myofibroblast differentiation. However, previous work identified CDH11 upregulation in inflamed AoAFs as a primary marker of myofibroblasts,^{19, 22} thus making it a promising target for mitigating differentiation.

One possible reason for this discrepancy is that CDH11 signaling requires cell-cell adhesion,²² which occurs at high cell densities,²³ yet under standard culturing conditions, cell-cell contacts are not made until confluency (3-4 d in this study). Within the context of Figure 6.5B, CDH11 may be a better target after day 3 when the cells are beginning to become more confluent. A second possible explanation is that CDH11 is simply a downstream effector of other proteins that govern the differentiation pathway, and the modulation of CDH11 does not impact upstream cascades.

To determine if silencing CDH11 has a significant impact on differentiation under other culturing conditions, cells were grown at different confluencies. As shown in Figure 6.9A, CDH11 siRNA was applied to low density and high density cells. There were almost no AoAFs with cell-cell contacts in the low density samples, but the majority of cells were in contact with other cells in the high density samples. AoAFs growing at the higher density expressed greater amounts of CDH11, as reported in the literature.²³ Both the low density and high density samples exhibited nearly complete knockdown when treated with CDH11 siRNA, despite the overexpression of CDH11 in the high density case. The α SMA protein expression of the cells was measured, and there was no difference in α SMA protein levels between the untreated samples and treated low density samples (Figure 6.9B). However, CDH11 siRNA treatment of the cells grown at high density was found to significantly reduce α SMA protein expression (Figure 6.9B), albeit to a lesser extent than IL1 β siRNA treatment (see also Figures 6.6 and 6.7). Therefore, CDH11 knockdown is a more promising strategy for attenuating differentiation when the number of AoAF cell-cell contacts is greater.

This finding is particularly important because the *in vivo* environment of the adventitium is crowded, and the cells are densely packed with many cell-cell interactions.¹² Recent reports in the literature also found CDH11 to be not merely a downstream effector of TGF- β 1, but also a factor able to regulate myofibroblast differentiation through multiple other pathways.²³ Moreover, the possible synergistic effects of CDH11 and IL1 β knockdown (see Figure 6.7B) and the role of CDH11 in the propagation *vs.* suppression of maladaptive responses in adventitial fibroblasts (e.g. by coordinating the contraction of fibroblast populations)^{15, 17, 19} justify further exploration of CDH11 as a possible therapeutic target. Taken together, CDH11 silencing may be a more promising strategy in clinical settings, especially if combined with the knockdown of IL1 β .

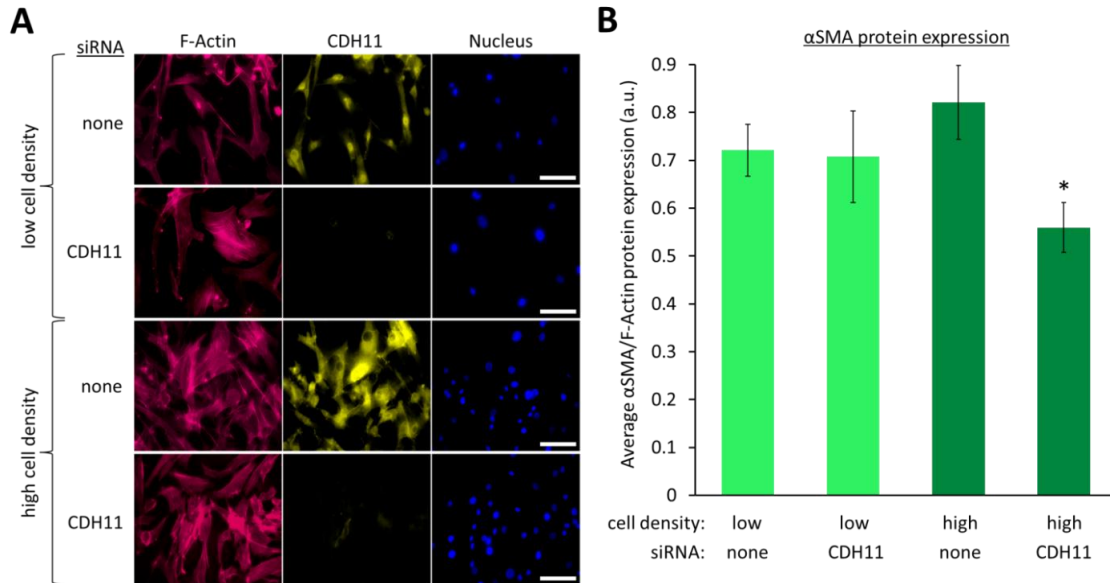


Figure 6.9: Effect of cell density on myofibroblast differentiation following CDH11 knockdown. AoAFs were plated at 10,000 cells cm^{-2} (low density) or 30,000 cells cm^{-2} (high density), transfected with CDH11 siRNA, and treated with 10 ng mL^{-1} TGF- β 1 to induce differentiation. ICC analyses were conducted to measure (A) CDH11 or (B) α SMA protein expression. (A) Representative ICC micrographs of AoAFs 2 days post-transfection. AoAFs were stained for F-actin (magenta), CDH11 (yellow), and nuclear DNA (blue). Scale bars = 50 μm . (B) Quantification of α SMA protein expression from ICC analyses. The average total fluorescence intensity of α SMA relative to F-actin of at least 100 cells per sample was measured using ImageJ. Results are shown as the mean \pm standard deviation of data obtained from three independent samples. An asterisk indicates a statistically significant difference in α SMA protein expression in comparison to the no siRNA treatment control at the appropriate cell density ($p < 0.05$).

6.3.9 Gene knockdown in rabbit aortic fibroblasts

The promising results obtained in human primary AoAFs justified more in-depth studies of the nanocomplexes in animal models. Recent work from Prof. Akins' lab at Nemours – Alfred I. duPont Hospital for Children (Wilmington, DE) demonstrated that the placement of hydrogels on skeletonized left common carotid

arteries in rabbits attenuated maladaptive responses following surgery.⁴³ Furthermore, the timescales of these cellular responses *in vivo* closely matched the timescales of the siRNA dosing regimens displayed in Figure 6.5. Thus, the rabbit surgical models represented a natural extension of the work reported in sections 6.3.1-6.3.8.

In preparation of the experiments in rabbits, new siRNA had to be designed to target rabbit IL1 β mRNA. Three custom-designed siRNAs (details in Table D.2 in Appendix D) were delivered to rabbit aortic fibroblasts separately and pooled together (1/3 each) using Lipofectamine lipoplexes. As shown in Figure 6.10, all three siRNAs significantly silenced IL1 β , and the pool of all three siRNAs was the most efficient.

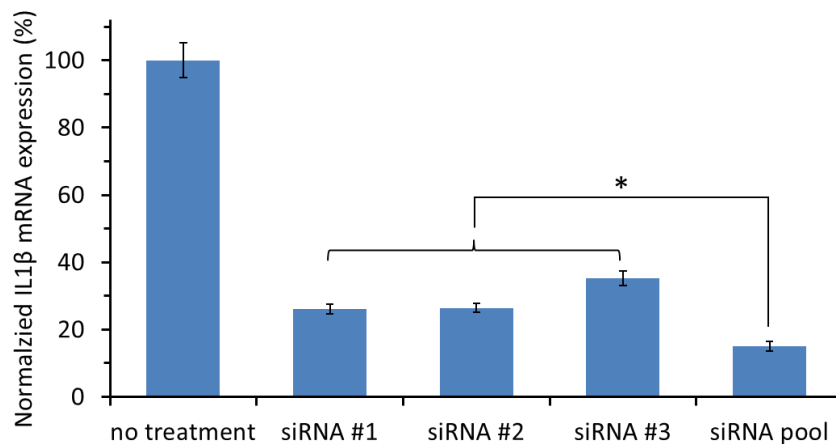


Figure 6.10: Gene silencing in rabbit aortic fibroblasts using different siRNAs. The siRNAs were encapsulated in Lipofectamine RNAiMAX lipoplexes separately or pooled in equal weight ratios (1/3 each) and delivered to rabbit aortic fibroblasts. qPCR analyses of IL1 β mRNA expression levels 24 h post-transfection were conducted, and the qPCR values were normalized to the levels in the no treatment control. All results are shown as the mean \pm standard deviation of data obtained from three independent samples. An asterisk indicates a statistically significant difference in IL1 β mRNA expression in comparison to the pooled siRNA treatment ($p < 0.05$).

Next, the efficacy of the hybrid nanocomplexes in rabbit aortic fibroblasts was examined. Cells were treated with the hybrid formulations (same composition as above) carrying the pooled IL1 β -targeting siRNA and either protected from or treated with 365 nm irradiation for 10 min. As shown in Figure 6.11, fibroblasts that were irradiated with light exhibited a significant decrease in IL1 β expression relative to cells that were not treated with the photo-stimulus. However, gene silencing still occurred in cells that were not exposed to 365 nm light, indicating that the nanocomplexes were not completely stable/dormant. The silencing efficiency following treatment with light also was lower than lipoplexes (Figure 6.10). These results were not too surprising, as the composition of the formulation was optimized to transfect a different cell type (human primary AoAFs). Future work should be aimed at modifying the nanocomplex composition to enable more efficient on/off gene silencing in rabbit aortic fibroblasts.

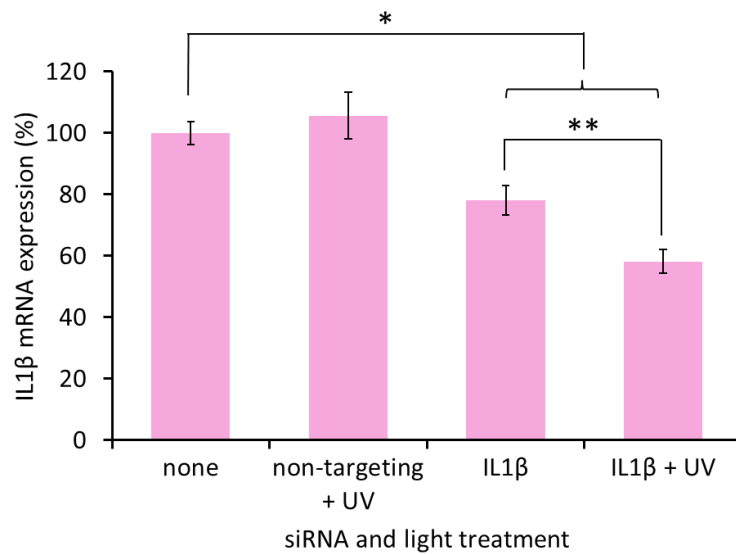


Figure 6.11: Gene silencing efficiency of hybrid nanocomplexes in rabbit aortic fibroblasts. Pooled siRNA was delivered using the hybrid nanocomplexes (same composition as used in human AoAFs), and the cells were protected from or irradiated with 365 nm light for 10 min. qPCR analyses of IL1 β mRNA expression levels 24 h post-transfection were conducted, and the qPCR values were normalized to the levels in the no treatment control. All results are shown as the mean \pm standard deviation of data obtained from three independent samples. A single asterisk indicates a statistically significant difference in IL1 β mRNA expression in comparison to the no treatment control, and a double asterisk indicates a statistically significant difference in IL1 β mRNA expression in comparison to cells treated with IL1 β -targeting siRNA but not light ($p < 0.05$).

6.4 Conclusions

A novel lipid-polymer hybrid formulation was developed to spatiotemporally control the knockdown of key genes implicated in maladaptive responses of human primary adventitial fibroblasts. The nanocarriers remained dormant in AoAFs until triggered and then silenced protein expression to $\leq 5\%$ of initial levels upon application of a photo stimulus. Additionally, the dynamics of protein turnover of two

functional genes, IL1 β and CDH11, were accurately predicted using simple kinetic modeling. This approach allowed the implementation of a double dosing regimen that sustained the knockdown of both genes for one week, which is the time period relevant for severely injured tissue to undergo adventitial remodeling. Cells with silenced IL1 β expression for one week exhibited attenuated differentiation and a ~50% reduction in proliferation. The effects of CDH11 knockdown alone were relatively minor, but were significantly enhanced at higher cell densities. However, the combined delivery of IL1 β and CDH11 siRNAs resulted in the complete halting of myofibroblast differentiation, as characterized by α SMA expression. siRNA also was designed to knockdown IL1 β in rabbit aortic fibroblasts, and preliminary work indicated that the hybrid nanocomplex composition should be tuned to enable on/off control over gene silencing in these different cell types. Thus, this chapter details a new formulation design for imparting stimuli-responsive features into materials capable of transfecting primary cells and elucidated the key functional roles of IL1 β and CDH11 in mediating fibrotic responses in AoAFs, both of which are critical for advancing therapies in the clinic to treat cardiovascular disease.

REFERENCES

1. Lloyd-Jones, D.; Adams, R. J.; Brown, T. M.; Carnethon, M.; Dai, S.; De Simone, G.; Ferguson, T. B.; Ford, E.; Furie, K.; Gillespie, C.; Go, A.; Greenlund, K.; Haase, N.; Hailpern, S.; Ho, P. M.; Howard, V.; Kissela, B.; Kittner, S.; Lackland, D.; Lisabeth, L.; Marelli, A.; McDermott, M. M.; Meigs, J.; Mozaffarian, D.; Mussolino, M.; Nichol, G.; Roger, V. L.; Rosamond, W.; Sacco, R.; Sorlie, P.; Stafford, R.; Thom, T.; Wasserthiel-Smoller, S.; Wong, N. D.; Wylie-Rosett, J., Heart disease and stroke statistics-2010 update a report from the American Heart Association. *Circulation* **2010**, *121* (7), e46-e215.
2. Motwani, J. G.; Topol, E. J., Aortocoronary saphenous vein graft disease - Pathogenesis, predisposition, and prevention. *Circulation* **1998**, *97* (9), 916-931.
3. Conte, M. S., Molecular engineering of vein bypass grafts. *J. Vasc. Surg.* **2007**, *45*, 74A-81A.
4. Deb, S.; Cohen, E. A.; Singh, S. K.; Une, D.; Laupacis, A.; Fremes, S. E.; Investigators, R., Radial artery and saphenous vein patency more than 5 years after coronary artery bypass surgery results from RAPS (radial artery patency study). *J. Am. Coll. Cardiol.* **2012**, *60* (1), 28-35.
5. Shavadia, J.; Norris, C. M.; Graham, M. M.; Verma, S.; Ali, I.; Baaney, K. R., Symptomatic graft failure and impact on clinical outcome after coronary artery bypass grafting surgery: Results from the Alberta Provincial Project for Outcome Assessment in Coronary Heart Disease registry. *Am. Heart J.* **2015**, *169* (6), 833-840.
6. Harskamp, R. E.; Alexander, J. H.; Ferguson, T. B.; Hager, R.; Mack, M. J.; Englum, B.; Wojdyla, D.; Schulte, P. J.; Kouchoukos, N. T.; de Winter, R. J.; Gibson, C. M.; Peterson, E. D.; Harrington, R. A.; Smith, P. K.; Lopes, R. D., Frequency and predictors of internal mammary artery graft failure and subsequent clinical outcomes insights from the project of ex-vivo vein graft engineering via transfection (PREVENT) IV trial. *Circulation* **2016**, *133* (2), 131-138.

7. Strauss, B. H.; Rabinovitch, M., Adventitial fibroblasts - Defining a role in vessel wall remodeling. *Am. J. Respir. Cell Mol. Biol.* **2000**, 22 (1), 1-3.
8. Fitzgibbon, G. M.; Kafka, H. P.; Leach, A. J.; Keon, W. J.; Hooper, G. D.; Burton, J. R., Coronary bypass graft fate and patient outcome: Angiographic follow-up of 5,065 grafts related to survival and reoperation in 1,388 patients during 25 years. *J. Am. Coll. Cardiol.* **1996**, 28 (3), 616-626.
9. Sousa, J. E.; Costa, M. A.; Abizaid, A. C.; Rensing, B. J.; Abizaid, A. S.; Tanajura, L. F.; Kozuma, K.; Van Langenhove, G.; Sousa, A.; Falotico, R.; Jaeger, J.; Popma, J. J.; Serruys, P. W., Sustained suppression of neointimal proliferation by sirolimus-eluting stents - One-year angiographic and intravascular ultrasound follow-up. *Circulation* **2001**, 104 (17), 2007-2011.
10. Kawatsu, S.; Oda, K.; Saiki, Y.; Tabata, Y.; Tabayashi, K., External application of rapamycin-eluting film at anastomotic sites inhibits neointimal hyperplasia in a canine model. *Ann. Thorac. Surg.* **2007**, 84 (2), 560-567.
11. Weman, S. M.; Salminen, U. S.; Penttila, A.; Mannikko, A.; Karhunen, P. J., Post-mortem cast angiography in the diagnostics of graft complications in patients with fatal outcome following coronary artery bypass grafting (CABG). *Int. J. Legal Med.* **1999**, 112 (2), 107-114.
12. Coen, M.; Gabbiani, G.; Bochaton-Piallat, M. L., Myofibroblast-mediated adventitial remodeling an underestimated player in arterial pathology. *Arterioscler. Thromb. Vasc. Biol.* **2011**, 31 (11), 2391-2396.
13. Sartore, S.; Chiavegato, A.; Faggini, E.; Franch, R.; Puato, M.; Ausoni, S.; Pauletto, P., Contribution of adventitial fibroblasts to neointima formation and vascular remodeling - From innocent bystander to active participant. *Circ. Res.* **2001**, 89 (12), 1111-1121.
14. Jiang, Z. H.; Yu, P.; Tao, M.; Fernandez, C.; Infantides, C.; Moloye, O.; Schultz, G. S.; Ozaki, C. K.; Berceci, S. A., TGF-beta- and CTGF-mediated fibroblast recruitment influences early outward vein graft remodeling. *Am. J. Physiol. Heart Circ. Physiol.* **2007**, 293 (1), H482-H488.
15. van den Borne, S. W. M.; Diez, J.; Blankesteyn, W. M.; Verjans, J.; Hofstra, L.; Narula, J., Myocardial remodeling after infarction: the role of myofibroblasts. *Nat. Rev. Cardiol.* **2010**, 7 (1), 30-37.

16. Hutcheson, J. D.; Chen, J.; Sewell-Loftin, M. K.; Ryzhova, L. M.; Fisher, C. I.; Su, Y. R.; Merryman, W. D., Cadherin-11 regulates cell-cell tension necessary for calcific nodule formation by valvular myofibroblasts. *Arterioscler. Thromb. Vasc. Biol.* **2013**, *33* (1), 114-120.
17. Hinz, B., Formation and function of the myofibroblast during tissue repair. *J. Invest. Dermatol.* **2007**, *127* (3), 526-537.
18. Braitsch, C. M.; Kanisicak, O.; van Berlo, J. H.; Molkentin, J. D.; Yutzey, K. E., Differential expression of embryonic epicardial progenitor markers and localization of cardiac fibrosis in adult ischemic injury and hypertensive heart disease. *J. Mol. Cell. Cardiol.* **2013**, *65*, 108-119.
19. Robinson, K. G.; Nie, T.; Baldwin, A. D.; Yang, E. C.; Kiick, K. L.; Akins, R. E., Jr., Differential effects of substrate modulus on human vascular endothelial, smooth muscle, and fibroblastic cells. *J Biomed. Mater. Res. A* **2012**, *100A* (5), 1356-1367.
20. Nie, T.; Akins, R. E., Jr.; Kiick, K. L., Production of heparin-containing hydrogels for modulating cell responses. *Acta Biomater.* **2009**, *5* (3), 865-875.
21. Mia, M. M.; Boersema, M.; Bank, R. A., Interleukin-1 beta attenuates myofibroblast formation and extracellular matrix production in dermal and lung fibroblasts exposed to transforming growth factor-beta 1. *PLoS One* **2014**, *9* (3), e91559.
22. Dallon, J. C.; Ehrlich, H. P., A review of fibroblast-populated collagen lattices. *Wound Repair Regen.* **2008**, *16* (4), 472-479.
23. Wang, H.; Leinwand, L. A.; Anseth, K. S., Roles of transforming growth factor-beta 1 and OB-cadherin in porcine cardiac valve myofibroblast differentiation. *FASEB J.* **2014**, *28* (10), 4551-4562.
24. Hamm, A.; Krott, N.; Breibach, I.; Blindt, R.; Bosserhoff, A. K., Efficient transfection method for primary cells. *Tissue Eng.* **2002**, *8* (2), 235-245.
25. Greco, C. T.; Epps, T. H., III; Sullivan, M. O., Mechanistic design of polymer nanocarriers to spatiotemporally control gene silencing. *ACS Biomater. Sci. Eng.* **2016**, *2* (9), 1582-1594.
26. Shi, Y.; O'Brien, J. E.; Fard, A.; Mannion, J. D.; Wang, D.; Zalewski, A., Adventitial myofibroblasts contribute to neointimal formation in injured porcine coronary arteries. *Circulation* **1996**, *94* (7), 1655-1664.

27. Green, M. D.; Foster, A. A.; Greco, C. T.; Roy, R.; Lehr, R. M.; Epps, T. H., III; Sullivan, M. O., Catch and release: photocleavable cationic diblock copolymers as a potential platform for nucleic acid delivery. *Polym. Chem.* **2014**, *5* (19), 5535-5541.
28. Greco, C. T.; Muir, V. G.; Epps, T. H., III; Sullivan, M. O., Efficient tuning of siRNA dose response by combining mixed polymer nanocarriers with simple kinetic modeling. *Acta Biomater.*, 2017; Vol. 50, pp 407-416.
29. Moors, M. A.; Mizel, S. B., Proteasome-mediated regulation of interleukin-1 beta turnover and export in human monocytes. *J. Leukoc. Biol.* **2000**, *68* (1), 131-136.
30. Niessen, C. M.; Leckband, D.; Yap, A. S., Tissue organization by cadherin adhesion molecules: dynamic molecular and cellular mechanisms of morphogenetic regulation. *Physiol. Rev.* **2011**, *91* (2), 691-731.
31. Schwanhausser, B.; Busse, D.; Li, N.; Dittmar, G.; Schuchhardt, J.; Wolf, J.; Chen, W.; Selbach, M., Global quantification of mammalian gene expression control. *Nature* **2011**, *473* (7347), 337-342.
32. Schmittgen, T. D.; Livak, K. J., Analyzing real-time PCR data by the comparative C-T method. *Nat. Protoc.* **2008**, *3* (6), 1101-1108.
33. Dominska, M.; Dykxhoorn, D. M., Breaking down the barriers: siRNA delivery and endosome escape. *J. Cell Sci.* **2010**, *123* (8), 1183-1189.
34. Schlegel, A.; Largeau, C.; Bigey, P.; Bessodes, M.; Lebozec, K.; Scherman, D.; Escriou, V., Anionic polymers for decreased toxicity and enhanced in vivo delivery of siRNA complexed with cationic liposomes. *J. Control. Release* **2011**, *152* (3), 393-401.
35. Jain, S.; Kumar, S.; Agrawal, A. K.; Thanki, K.; Banerjee, U. C., Enhanced transfection efficiency and reduced cytotoxicity of novel lipid-polymer hybrid nanoplexes. *Mol. Pharm.* **2013**, *10* (6), 2416-2425.
36. Aono, R.; Nomura, K.; Yuba, E.; Harada, A.; Kono, K., Gene expression of ternary complexes through the compaction of nanofiber-polyplexes by mixing with lipofectamine. *Biomater. Sci.* **2015**, *3* (5), 764-770.
37. Rezaee, M.; Oskuee, R. K.; Nassirli, H.; Malaekheh-Nikouei, B., Progress in the development of lipopolyplexes as efficient non-viral gene delivery systems. *J. Control. Release* **2016**, *236*, 1-14.

38. Goncalves, C.; Berchel, M.; Gosselin, M. P.; Malard, V.; Cheradame, H.; Jaffres, P. A.; Guegan, P.; Pichon, C.; Midoux, P., Lipopolyplexes comprising imidazolefimidazolium lipophosphoramidate, histidinylated polyethyleneimine and siRNA as efficient formulation for siRNA transfection. *Int. J. Pharm.* **2014**, *460* (1-2), 264-272.
39. Foster, A. A.; Greco, C. T.; Green, M. D.; Epps, T. H., III; Sullivan, M. O., Light-mediated activation of siRNA release in diblock copolymer assemblies for controlled gene silencing. *Adv. Healthc. Mater.* **2015**, *4* (5), 760-770.
40. Moller, K.; Muller, K.; Engelke, H.; Brauchle, C.; Wagner, E.; Bein, T., Highly efficient siRNA delivery from core-shell mesoporous silica nanoparticles with multifunctional polymer caps. *Nanoscale* **2016**, *8* (7), 4007-4019.
41. Germershaus, O.; Mao, S. R.; Sitterberg, J.; Bakowsky, U.; Kissel, T., Gene delivery using chitosan, trimethyl chitosan or polyethyleneglycol-graft-trimethyl chitosan block copolymers: Establishment of structure-activity relationships in vitro. *J. Control. Release* **2008**, *125* (2), 145-154.
42. Bartlett, D. W.; Davis, M. E., Insights into the kinetics of siRNA-mediated gene silencing from live-cell and live-animal bioluminescent imaging. *Nucleic Acids Res.* **2006**, *34* (1), 322-333.
43. Robinson, K. G.; Scott, R. A.; Heseck, A. M.; Woodford, E. J.; Amir, W.; Planchon, T. A.; Kiick, K. L.; Akins, R. E., Reduced arterial elasticity due to surgical skeletonization is ameliorated by abluminal PEG hydrogel. *Bioeng. Transl. Med.* **2017**.
44. Midgley, A. C.; Rogers, M.; Hallett, M. B.; Clayton, A.; Bowen, T.; Phillips, A. O.; Steadman, R., Transforming growth factor-beta 1 (TGF-beta 1)-stimulated fibroblast to myofibroblast differentiation is mediated by hyaluronan (HA)-facilitated epidermal growth factor receptor (EGFR) and CD44 co-localization in lipid rafts. *J. Biol. Chem.* **2013**, *288* (21), 14824-14838.
45. Hecker, L.; Jagirdar, R.; Jin, T.; Thannickal, V. J., Reversible differentiation of myofibroblasts by MyoD. *Exp. Cell. Res.* **2011**, *317* (13), 1914-1921.

46. Guo, J. L.; Gu, N. L.; Chen, J.; Shi, T. M.; Zhou, Y.; Rong, Y.; Zhou, T.; Yang, W. X.; Cui, X. Q.; Chen, W. H., Neutralization of interleukin-1 beta attenuates silica-induced lung inflammation and fibrosis in C57BL/6 mice. *Arch. Toxicol.* **2013**, *87* (11), 1963-1973.
47. Kolb, M.; Margetts, P. J.; Anthony, D. C.; Pitossi, F.; Gauldie, J., Transient expression of IL-1 beta induces acute lung injury and chronic repair leading to pulmonary fibrosis. *J. Clin. Invest.* **2001**, *107* (12), 1529-1536.
48. Wilson, M. S.; Madala, S. K.; Ramalingam, T. R.; Gochuico, B. R.; Rosas, I. O.; Cheever, A. W.; Wynn, T. A., Bleomycin and IL-1 beta-mediated pulmonary fibrosis is IL-17A dependent. *J. Exp. Med.* **2010**, *207* (3), 535-552.
49. Chen, H.; Yang, W. W.; Wen, Q. T.; Xu, L.; Chen, M., TGF-beta-induced fibroblast activation protein expression, fibroblast activation protein expression increases the proliferation, adhesion, and migration of HO-8910PM. *Exp. Mol. Pathol.* **2009**, *87* (3), 189-194.
50. Bronnum, H.; Eskildsen, T.; Andersen, D. C.; Schneider, M.; Sheikh, S. P., IL-1 beta suppresses TGF-beta-mediated myofibroblast differentiation in cardiac fibroblasts. *Growth Factors* **2013**, *31* (3), 81-89.
51. Saxena, A.; Chen, W.; Su, Y.; Rai, V.; Uche, O. U.; Li, N.; Frangogiannis, N. G., IL-1 induces proinflammatory leukocyte infiltration and regulates fibroblast phenotype in the infarcted myocardium. *J. Immunol.* **2013**, *191* (9), 4838-4848.
52. Dewald, O.; Ren, G. F.; Duerr, G. D.; Zoerlein, M.; Klemm, C.; Gersch, C.; Tincey, S.; Michael, L. H.; Entman, M. L.; Frangogiannis, N. G., Of mice and dogs: Species-specific differences in the inflammatory response following myocardial infarction. *Am. J. Pathol.* **2004**, *164* (2), 665-677.
53. Hinz, B.; Pittet, P.; Smith-Clerc, J.; Chaponnier, C.; Meister, J. J., Myofibroblast development is characterized by specific cell-cell adherens junctions. *Mol. Biol. Cell* **2004**, *15* (9), 4310-4320.
54. Verhoekx, J. S. N.; Verjee, L. S.; Izadi, D.; Chan, J. K. K.; Nicolaidou, V.; Davidson, D.; Midwood, K. S.; Nanchahal, J., Isometric contraction of Dupuytren's myofibroblasts is inhibited by blocking intercellular junctions. *J. Invest. Dermatol.* **2013**, *133* (12), 2664-2671.

55. Yoshioka, R.; Kita, Y.; Nagahira, A.; Manno, A.; Makita, N.; Tomita, U.; Murakawa, M., Quantitative analysis of cadherin-11 and -catenin signalling during proliferation of rheumatoid arthritis-derived synovial fibroblast cells. *J. Pharm. Pharmacol.* **2015**, *67* (8), 1075-1082.
56. Vandooren, B.; Cantaert, T.; ter Borg, M.; Noordenbos, T.; Kuhlman, R.; Gerlag, D.; Bongartz, T.; Reedquist, K.; Tak, P. P.; Baeten, D., Tumor necrosis factor alpha drives cadherin 11 expression in rheumatoid inflammation. *Arthritis Rheumatol.* **2008**, *58* (10), 3051-3062.
57. Dzau, V. J.; Braun-Dullaeus, R. C.; Sedding, D. G., Vascular proliferation and atherosclerosis: New perspectives and therapeutic strategies. *Nat. Med.* **2002**, *8* (11), 1249-1256.
58. Vesey, D. A.; Cheung, C.; Cuttle, L.; Endre, Z.; Gobe, G.; Johnson, D. W., Interleukin-1 beta stimulates human renal fibroblast proliferation and matrix protein production by means of a transforming growth factor-beta-dependent mechanism. *J. Lab. Clin. Med.* **2002**, *140* (5), 342-350.

Chapter 7

CONCLUSIONS AND FUTURE DIRECTIONS

7.1 Dissertation Summary

Overall, the work described in this dissertation provided insights that advanced our fundamental understanding of small interfering ribonucleic acid (siRNA) binding vs. release and enabled the development of new strategies for improving siRNA delivery to help facilitate translation into animal models. In Chapter 3, the mechanism of siRNA release in mPEG-*b*-poly(5-(3-(amino)propoxy)-2-nitrobenzyl methacrylate) [mPEG-*b*-P(APNBMA)] polyplexes was elucidated, which allowed for precise spatiotemporal control over protein knockdown and the development of a simple kinetic model to predict the dynamics of gene silencing. In Chapter 4, mixed polymer polyplexes were formulated that enhanced gene silencing efficiencies and provided controlled dose responses that could be predicted by kinetic modeling. In Chapter 5, the incorporation of anionic excipients into polyplexes facilitated greater siRNA and enabled Förster resonance energy transfer (FRET)-based monitoring of nanocarrier disassembly *in situ* while maintaining serum- and storage-stability. In Chapter 6, lipid-polymer hybrid formulations were used to gain on/off control over gene silencing in human primary cells and establish dosing regimens that could halt myofibroblast differentiation through the knockdown of two functional proteins. Taken together, this work exploited the tremendous versatility of mPEG-*b*-P(APNBMA) to elucidate key structure-function relationships related to nucleic acid delivery and develop formulation strategies to enhance the efficacy of siRNA delivery technologies that will

hopefully improve human health in the future. The following subsections provide more detailed motivations and synopses of the work presented in Chapters 3-6.

7.1.1 siRNA release: mechanistic understanding and spatiotemporal control (Chapter 3)

Current siRNA delivery systems lack the ability to precisely tune siRNA release and maximize gene silencing in a spatiotemporal manner. To overcome these challenges, photo-responsive block copolymer solution assemblies were developed, for which stimuli-triggered changes in polymer structure altered nanocarrier stability and defined siRNA activity. Uniquely, the biomaterial design enabled the development and validation of a simple kinetic model that accurately predicted the extent of intracellular nanocarrier disassembly and silencing. Moreover, the constructs showed that maximal gene silencing could be achieved using concentrations of siRNA five-fold lower than typical formulations due to the ability to rapidly release sufficient amounts of siRNA to saturate the cellular ribonucleic acid (RNA)-induced silencing complex (RISC) machinery. The ability of the nanocarriers to remain dormant prior to photo-triggered siRNA release allowed for the generation of cell patterns in gene expression with spatial control on cellular length scales and no detectable off-target effects. Furthermore, precisely tuned changes in nanocarrier structure enabled the modulation of protein and messenger RNA (mRNA) knockdown levels in murine fibroblasts and terminally differentiated human primary cells. These advances led to increased precision, potency, and utility relative to other recent spatiotemporally-controlled nucleic acid delivery vehicles reported in the literature. Moreover, the combination of experimental examination and kinetic modeling should

be applicable to a host of systems for which temporal control over nucleic acid delivery is a critical parameter in influencing cellular responses.

7.1.2 Mixed polymer nanocarriers and kinetic modeling to predict dosing (Chapter 4)

Two of the most prominent challenges that limit the clinical success of siRNA therapies are a lack of control over cargo release from the delivery vehicle and an incomplete understanding of the link between gene silencing dynamics and siRNA dosing. These obstacles were overcome through the formulation of siRNA polyplexes containing light-responsive polymer mixtures, whose varied compositions and triggered release behavior provide enhanced gene silencing and controlled dose responses that can be predicted by simple kinetic models. Through the straightforward mixing of two block copolymers, the level of gene knockdown was easily optimized to achieve the maximum level of glyceraldehyde 3-phosphate dehydrogenase (GAPDH) protein silencing in NIH/3T3 cells (~70%) using a single siRNA dose. The kinetic model was used to describe the dynamic changes in mRNA and protein concentrations in response to siRNA treatment. These predictions enabled the application of a second dose of siRNA to maximally suppress gene expression over multiple days, leading to a further 50% reduction in protein levels relative to those measured following a single dose. Furthermore, polyplexes remained dormant in cells until exposed to the photo-stimulus, demonstrating the complete control over siRNA activity as well as the stability of the nanocarriers. Thus, this work demonstrated that pairing advances in biomaterials design with simple kinetic modeling provided new insight into gene silencing dynamics and presents a powerful strategy to control gene expression through siRNA delivery.

7.1.3 Incorporation of anionic excipients for improved theranostics (Chapter 5)

The incorporation of anionic excipients into polyplexes is a promising strategy for modulating siRNA binding vs. release and integrating diagnostic capabilities; however, specific design criteria and structure-function relationships are needed to facilitate the development of nanocarrier-based theranostics. Poly(acrylic acid) (PAA) and quantum dot (QD) excipients were incorporated into photolabile siRNA polyplexes to increase gene silencing efficiencies by up to 100% and enable self-reporting of nanocarrier disassembly. The systematic approach identified the functional relationships between gene silencing and key parameters such as excipient loading fractions and molecular weights that facilitated the establishment of design rules for optimization of nanocarrier efficacy. For example, PAA molecular weights ~10-20 times greater than that of the co-encapsulated siRNA exhibited the most efficient release and silencing. Furthermore, siRNA release assays and RNAi modeling allowed us to generate a PAA “heat map” that predicted gene silencing *a priori* as a function of PAA molecular weight and loading fraction. QDs further promoted selective siRNA release and provided visual as well as FRET-based monitoring of the dynamic changes in nanostructure *in situ*. Moreover, even with the addition of anionic components, the formulations exhibited substantially improved stability and shelf-life relative to other polyplex formulations (e.g. PEI), with complete stability after a week of storage and full activity in the presence of serum. Taken together, these studies enabled synergistic improvements in siRNA release and diagnostic capabilities, along with the development of mechanistic insights that are critical for advancing the translation of nucleic acid theranostics into the clinic.

7.1.4 Hybrid formulations for attenuating maladaptive responses in human aortic adventitial fibroblasts (Chapter 6)

Lipid-siRNA assemblies were modified with photo-responsive polymers to enable spatiotemporally-controlled silencing of interleukin-1 beta (IL1 β) and cadherin 11 (CDH11), two genes that are essential drivers of maladaptive responses in human aortic adventitial fibroblasts (AoAF)s. These hybrid nanocomplexes addressed the critical challenge of locally mitigating fibrotic actions that lead to the high rates of vascular graft failures. In particular, the lipid-polymer formulations provided potent silencing of IL1 β and CDH11 that was precisely modulated by a photo-release stimulus, leading to knockdown of these genes to the desired extents between 100% and $\leq 5\%$ of their initial levels. Moreover, light-triggered gene silencing was combined with a dynamic modeling framework to design a multi-dose siRNA regimen that sustained knockdown of both genes over clinically-relevant timescales. Multi-dose suppression illuminated a cooperative role for IL1 β and CDH11 in pathogenic adventitial remodeling and was directly linked to desirable functional outcomes. Specifically, myofibroblast differentiation and cellular proliferation, two of the primary hallmarks of fibrosis, were significantly attenuated by IL1 β silencing. Meanwhile, the effects of CDH11 siRNA treatment on differentiation became more pronounced at higher cell densities characteristic of constrictive adventitial remodeling *in vivo*. Simultaneous knockdown of IL1 β and CDH11 for one week completely halted myofibroblast differentiation, indicating potentially synergistic roles for these proteins. Thus, this work offered a unique formulation design for photo-responsive gene suppression in human primary cells and established a new dosing method to satisfy the critical need for local attenuation of fibrotic responses in the adventitium surrounding vascular grafts.

7.2 Recommendations for Future Work

7.2.1 Direct extensions of recent work

There are two separate, but related, thrusts that build directly on recent work that is described in previous chapters. The first topic relates to translating the hybrid lipid-polymer formulations into *in vivo* rabbit models as preclinical analysis that would lead to a treatment strategy for coronary artery bypass graft interventions. Specifically, the formulations will be applied to arterial bypass grafts in rabbits in collaboration with Prof. Robert E. Akins' laboratory. The second thrust aims to make the polyplex formulations responsive to near infrared (NIR) light (as an alternative to ultraviolet (UV) light) through the incorporation of upconverting nanoparticles (UCNP)s. Changing the excitation wavelength from 365 nm to > 750 nm provides many benefits for biological applications and will aid in the translation of the polyplexes into new systems, especially *in vivo*.

7.2.1.1 *In vivo* rabbit models

In addition to veterinary medicine and the creation of research tools, one of the ultimate goals of biomedical technologies is translation into humans to improve health outcomes. A key step in the translational process is vigorous testing of the technology in various animal models. Given the encouraging *in vitro* gene silencing results in rabbit aortic fibroblasts presented in Chapter 6, future work should be designed to facilitate the translation into rabbit models. This project will be conducted in collaboration with Prof. Robert E. Akins' laboratory, which has expertise performing bypass grafting with surgically skeletonized arteries in New Zealand White rabbits.

In Chapter 6, a hybrid lipid-polymer formulation composition was identified that mediated efficient IL1 β transcript knockdown in rabbit aortic fibroblasts after

irradiation with 365 nm light but remained dormant without exposure to the photo-stimulus. These promising results suggest that the hybrid formulation may be useful in animal models when applied to rabbit aortic fibroblasts; however, it is likely that the native (*in vivo*) cells will have significant differences from the (*in vitro*) primary cells that will change the efficacy of the siRNA formulation.¹ Nevertheless, the current composition of the hybrid formulation represents a reasonable starting point that probably will need to be tuned for effective gene silencing *in vivo*.

Numerous other studies can be conducted prior to/in conjunction with gene silencing experiments, including cellular uptake and biocompatibility assays. Despite the fact that the skeletonization procedure will significantly reduce the number of barriers to cellular uptake, various extracellular proteins and tissue components may remain present in the animal model that could interact with the nanocarriers and alter cellular internalization (Figure 7.1).² Modifications to the hydrophilic PEG block (as detailed in section 7.2.2.2) or the implementation of strategies for improving endosomal escape (as detailed in section 7.2.3.2) may help overcome these delivery hurdles. Another important factor to consider is the duration of the transfection. Unlike *in vitro* experiments that have transfections last for a few hours, the time frame during surgery is on the order of minutes. To determine the time window necessary for sufficient internalization given the new rate of cellular uptake, the siRNA can be labeled with a fluorophore and tracked using fluorescence detection techniques.³ Alternatively, quantum dots could be incorporated into the formulations to enable monitoring with electron microscopy in addition to fluorescence assays.⁴ The biocompatibility of 365 nm light irradiation and nanocarrier treatment also should be

investigated using cell viability assays to determine the potential limitations related to undesired off-target (side) effects.

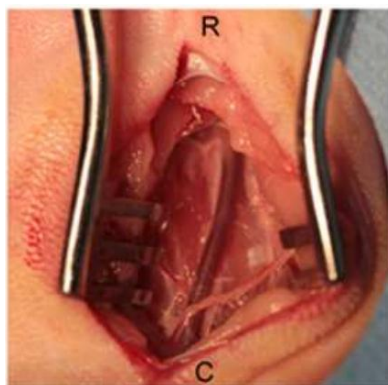


Figure 7.1: Representative view of the surgical field following skeletonization of the left common carotid artery in a rabbit (R = rostral, C = caudal). This figure was adapted with permission from Robinson, K. G.; Scott, R. A.; Heseck, A. M.; Woodford, E. J.; Amir, W.; Planchon, T. A.; Kiick, K. L.; Akins, R. E., Reduced arterial elasticity due to surgical skeletonization is ameliorated by abluminal PEG hydrogel. *Bioeng. Transl. Med.* 2017, Accepted Article.² Copyright 2017.

7.2.1.2 Incorporation of upconverting nanoparticles

Preliminary data was presented in Chapter 5 (section 5.3.9) that detailed the incorporation of UCNPs into polyplexes. The primary objective of this work was to enable light-triggered siRNA release from the nanocarriers using NIR light (> 750 nm) instead of UV light (365 nm) to avoid challenges related to penetration depth and cytotoxicity.⁵ Both types of tested UCNPs were acid-functionalized so that they would be negatively charged in water solutions and would electrostatically bind to mPEG-*b*-P(APNBMA). Similarly to the addition of quantum dots, the incorporation of anionic UCNPs resulted in polymer/siRNA/nanoparticle assemblies that were

relatively stable at low N/P ratios. However, the upconversion efficiency of the nanoparticles (emission wavelengths of ≤ 365 nm) was extremely low and not sufficient to induce polymer cleavage at the maximum irradiation intensity. This limitation is common, as most UCNPs suffer from very weak and narrowband NIR absorption.⁶ The major shortcoming of inefficient upconversion to 365 nm needs to be addressed before further progress can be made in the project.

There are reports of significantly more efficient UCNPs in the literature that were produced using fairly complicated and specialized synthetic procedures (that lie outside the expertise of our groups).^{7, 8} Thus, it is worthwhile to continue/form collaborations with groups that possess the technical expertise to carry out these synthetic protocols. Additionally, there have been recent advances in the field that have enhanced upconversion properties through multistep energy-cascaded transfer.⁹¹⁰ These breakthroughs rely on the conjugation of organic NIR-absorbing dyes, which can act as antennas to greatly improve upconversion efficiencies and broaden the absorption spectrum (Figure 7.2).^{6, 11} For example, Zou *et al.* found that their dye-sensitized nanoparticles enhanced upconversion by a factor of $\sim 3,300$ relative to unmodified UCNPs.⁶ Another report demonstrated that upconversion efficiencies of as high as 19% and significant absorption ranges spanning 150 nm in the NIR spectrum could be achieved.¹¹ The authors of these studies also speculated that optimization of the organic dye emission and nanoparticle absorption spectral overlap would further increase upconversion efficiencies. Therefore, a combination of higher quantum yield UCNPs and broadband dye-sensitization strategies may allow for the upconversion of NIR light to reach efficiencies sufficient enough to cleave the *o*-nitrobenzyl (*o*-NB) moiety of mPEG-*b*-P(APNBMA) and trigger siRNA release.

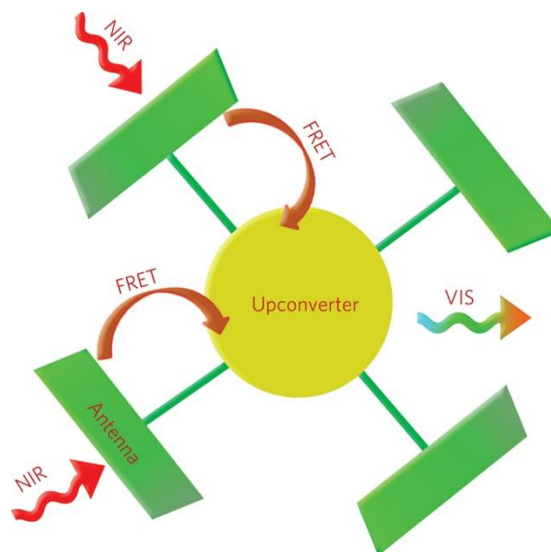


Figure 7.2: Antenna dyes (green) absorb NIR irradiation (red wavy arrows) and transfer it *via* FRET (brown arrows) to the UCNP core (yellow sphere). Upconversion is defined by a process in which the absorption of two or more low-energy (NIR) photons leads to the emission of a single photon with higher energy in the visible or UV regions (rainbow wavy arrow). This figure was adapted with permission from Zou, W. Q.; Visser, C.; Maduro, J. A.; Pshenichnikov, M. S.; Hummelen, J. C., Broadband dye-sensitized upconversion of near-infrared light. *Nat. Photon.* 2012, 6 (8), 560-564.⁶ Copyright 2012, Rights Managed by Nature Publishing Group.

7.2.2 Modifications to the polymer structure

The tailorability of mPEG-*b*-P(APNBMA) is one of the platform's greatest advantages, yet only the molecular weight of the cationic block was varied in this dissertation. Two additional approaches for imparting enhanced or new characteristics to the polymers are changing the chemical structure of the monomer unit or altering the molecular architecture of the hydrophilic block. The first strategy involves various aromatic substitutions and molecular group additions that can be made to the photocleavable *o*-NB moiety in the APNBMA monomer to increase the efficiency of the photo-reaction and/or shift the absorbance to higher wavelengths. The second

strategy involves changing the hydrophilic block to tune the shielding of the polyplex corona for applications that require different levels of solution stability and/or cellular uptake.

7.2.2.1 Altering the *o*-NB functional moiety in the monomer

In essentially all applications, it is desirable to have more rapid response times to the photo-stimulus and shorter irradiation times. These traits are particularly beneficial when working with sensitive cell types (e.g. human primary cells) that have low tolerances for high doses of 365 nm light or in *in vivo* settings when speed is critically important from a practicality standpoint. However, the photo-reactions of *o*-NB derivatives are quite inefficient, as the quantum yields are typically < 0.1 events photon⁻¹.^{12, 13} The most straightforward approach for addressing this concern is to increase the photolysis reaction efficiency by tuning the molecular structure of the *o*-NB group. As the photo-reaction is based on photons interacting with π -bonds and the subsequent transition of electrons (forming radicals and various excited electronic states), the addition of electron-donating or electron-withdrawing groups to the benzylic site of the aromatic ring should alter the quantum yield of the photolysis reaction and change the kinetics.¹² A proven strategy for enhancing the reaction efficiency is the incorporation of an α -methyl group onto the benzylic carbon, which can improve the relative cleavage rate by a factor of at least five.^{14, 15} In addition to electronic effects, the methyl group also provides increased steric hindrances that stabilize intermediates and enhance the total reaction efficiency.^{16, 17} The position of the α -methyl group on the benzylic carbon is depicted in Figure 7.3 as R_1 ($R_1 = \text{Me}$).

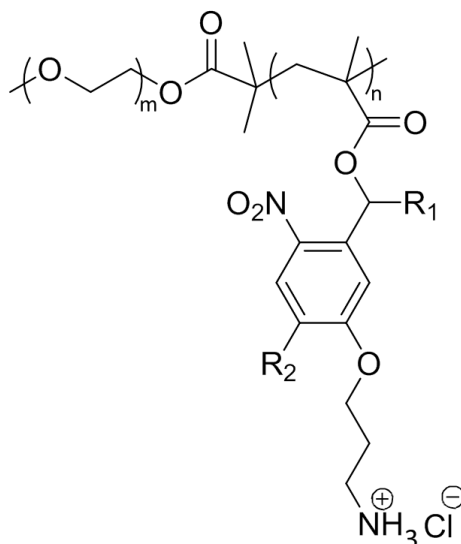


Figure 7.3: The generic form of the mPEG-*b*-P(APNBMA) polymers. Various alterations to the molecular structure of the APNBMA monomer unit could be made to tune the photo-responsive nature of the polymer. First, the α -group on the benzylic carbon, which is depicted as R_1 , can be modified. A methyl group is commonly substituted in this position to increase the quantum yield ($R_1 = \text{Me}$). Second, a hydrogen on the aromatic ring (R_2 position) can be substituted with a methoxy ($R_2 = \text{OMe}$) to provide a bathochromic shift in the excitation spectrum.

Another important factor to consider when designing the molecular structure of the photolabile *o*-NB moiety is the maximum excitation wavelength of the chromophore. Generally, biological systems are more susceptible to sustaining DNA mutations and cellular damage with shorter wavelength UV light ($< 365 \text{ nm}$).¹⁸ As shown in Figure 7.4, the absorbance spectrum of mPEG-*b*-P(APNBMA) exhibits an excitation maximum of $\sim 316 \text{ nm}$ prior to irradiation. Although the *o*-NB group in the polymer absorbs light up to $\sim 400 \text{ nm}$, the relative absorbance at 365 nm relative to the maximum absorbance at 316 nm is $< 25\%$. The inefficiency of the photo-reaction at higher wavelengths within the UV spectrum necessitates the use of fairly high doses of

light, which increases the likelihood of cellular damage, hinders the practical implementation of experimental procedures, and limits the stimulus response time.

To address these drawbacks, various alkoxy substituents have been incorporated into the aromatic rings of *o*-NB moieties to induce a bathochromic shift (towards lower energy absorbance).^{12, 19} Replacing hydrogen with electron withdrawing groups on the aromatic ring changes the electronic properties of the molecule and shifts the principle absorbance of the chromophore to higher wavelengths.²⁰ In particular, substituting a methoxy group for a proton significantly facilitates the photolytic cleavage reaction with > 350 nm light.¹⁵ A previous study demonstrated that the modification of *o*-NB with methoxy groups allowed the photolysis reaction to proceed at reasonable rates using 420 nm light.¹² This substitution to the aromatic ring is depicted in Figure 7.3 as R₂ (R₂ = OMe).

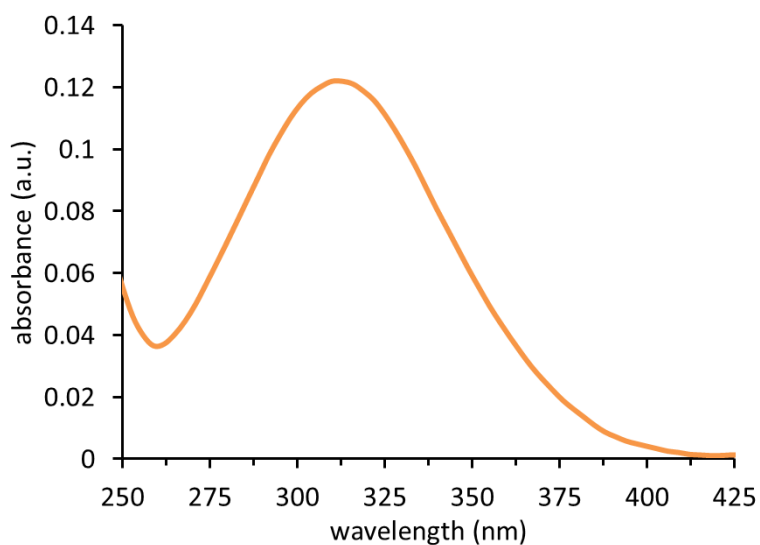


Figure 7.4: The absorbance spectrum of mPEG-*b*-P(APNBMA). The maximum excitation wavelength is ~316 nm, and the absorbance drops off rapidly at longer wavelengths (approaching no absorbance \geq 400 nm).

7.2.2.2 Changing the hydrophilic block

The chemical/physical composition of the polyplex surface is an extremely important determinant of the nanocarrier's solubility, biocompatibility, stability, behavior, and efficacy. For example, the nanocarrier corona may increase the delivery vehicle's solubility in water, reduce cytotoxicity, provide "stealthiness" and steric stability in the extracellular environment, influence cellular binding and the mode of internalization, and affect polyplex disassembly and siRNA release.²¹ The importance of each of these factors depends on the application (e.g. "stealthiness" is more critical for *in vivo* applications than *in vitro* applications). In many polyplex systems, the corona is comprised of a neutral hydrophilic block such as poly(ethylene glycol) (PEG) or N-(2-hydroxypropyl)methacrylamide (HPMA).²² PEGylation is the most common strategy for stabilizing nanocarriers and protecting the charged core from opsonization and nuclease-mediated degradation.²³ The hydrophilic PEG chains form a "shell" around the polyplex core that is necessary for reducing electrostatic interactions with the surrounding medium, especially intracellularly or in the body.

Although the ideal PEG molecular weight depends on the particular polyplex system, specific trends have emerged. For example, PEG blocks that are shorter than 2 kDa cannot effectively stabilize polyplexes in the extracellular environment.²⁴ Moreover, longer PEG blocks (e.g. 20 kDa) tend to provide more stability extracellularly but decrease cellular uptake.²⁵ A balance between these effects often is found to be optimal with PEG molecular weights of approximately 5-10 kDa.^{24, 25} PEG density also plays an important role in determining polyplex behavior. One method for varying the density of PEG is grafting PEG chains onto a cationic polymer (tuning the number of PEGs per cationic polymer).²⁶ Generally, increasing the PEG density increases stability but reduces cellular uptake, as was the case with increasing

PEG molecular weight. These tradeoffs suggest that PEG molecular weight and density should be systematically varied to determine the optimal combination for each polyplex system in the desired application; however, such studies may be tedious and expensive.²⁵ Alternatively, the use of mixed polymer nanocarriers would facilitate the rapid testing of multiple formulations from as few as two different polymers.²⁷ Therefore, only one or two modified polymers would need to be synthesized to explore a wide parameter space.

The mPEG-*b*-P(APNBMA) polymers contain a ~5 kDa PEG block on each polymer chain.²⁸ A number of modifications could be made to the “base” hydrophilic block, including a shorter/longer PEG block or the incorporation of a comb-like poly(ethylene glycol) methyl ether methacrylate (PEGMA) block. Depending on the application, more or less PEG shielding may be desirable. For example, shorter PEG blocks (e.g. 2 kDa) likely would be beneficial for *in vitro* applications where maximizing polyplex uptake is essential; whereas longer PEG blocks (e.g. 20 kDa) would be critical for *in vivo* applications such as injection into the bloodstream.²⁹ Analogously, the PEGMA block length could be varied to impart the desired shielding characteristics and a comb-like corona morphology.³⁰ Other groups have demonstrated that the incorporation of PEGMA (M_n ~300-2,000 Da) blocks ranging from ~8-33 kDa into cationic polymers produced polyplexes that enhanced the delivery of nucleic acids.^{31, 32} These reports suggest that synthesizing a polymer with a PEGMA block within these specifications may significantly improve the current polyplex system, particularly if mixed with “base” mPEG-*b*-P(APNBMA).

7.2.3 Endosomal escape: mechanistic understanding and strategies for enhancement

Endosomal escape is one of the primary intracellular barriers to siRNA delivery.²¹ Generally, polyplexes are internalized into cells through various endocytic pathways and become entrapped within endosomes. The siRNA nanocarriers must escape the endosomes to reach the cytoplasm (the site of RISC) before they are subjected to the degradative conditions in the acidifying endomembrane compartments and lysosomes. Despite extensive work in the literature, endosomal escape continues to hamper effective siRNA delivery and has been identified as the limiting step in many polyplex systems.³³ It is important to elucidate the endosomal escape mechanism and ultimate fate of the mPEG-*b*-P(APNBMA) polyplexes as well as provide a better understanding of endosomal escape that is pertinent to a wide variety of other delivery vehicles. Furthermore, strategies for enhancing the ability of the mPEG-*b*-P(APNBMA) polyplexes to escape endosomes may greatly benefit future work in a variety of applications.

7.2.3.1 Mechanistic understanding of cellular uptake, endosomal escape, and polyplex fate

Work presented in Chapters 1, 3, and 4 demonstrated that the polyplexes were rapidly internalized into NIH/3T3 cells. The polyplexes also mediated efficient gene silencing after exposure to the photo-stimulus, meaning that the polyplexes and/or siRNA must have escaped the endomembrane vesicular compartments and engaged the RISC.³⁴ NIH/3T3 cells that were not irradiated with 365 nm exhibited no gene silencing, suggesting that the polyplexes remained dormant and did not escape the endosome and/or did not release their siRNA payload. In Chapter 6, the incorporation of a cationic lipid (Lipofectamine) was necessary to enable on/off control over gene

knockdown in human primary cells, presumably due to challenges related to endosomal escape. In both cases, the on/off behavior was exploited to spatiotemporally control and tune the amount of protein knockdown; however, the specific endocytic pathway(s), mechanism of endosomal escape, and ultimate fate of the entrapped nanocarriers were not investigated in detail. Perhaps even more importantly, the unique on/off nature of the system provides a special opportunity to explore general siRNA delivery concepts such as endosomal escape mechanisms and the ideal location and timing of siRNA release that would be applicable to a host of other systems.

It is important to understand which specific endocytic pathways the polyplexes use to become internalized into cells. The most common pathways include clathrin (receptor)-mediated endocytosis, caveolae, macropinocytosis, and phagocytosis.³⁵ All of these pathways differ in where the cargo is trafficked, the rate of intracellular transport, and where the endosomes tend to accumulate. To study these modes of internalization, a number of chemical endocytic inhibitors can be used to block specific pathways before transfection.³⁶ A reduction in the amount of cellular uptake in the presence of a particular inhibitor would suggest that the corresponding endocytic pathway transports a significant proportion of the polyplexes into the cells. However, these chemical inhibitors tend to be non-specific and not completely reliable indicators of endocytic pathways.³⁷ An alternative/complementary approach involved the RNAi-induced knockdown of a protein that is specific and critical to a certain pathway. For example, Ross *et al.* silenced caveolin-1 in IBC SUM149 cells and found a significant reduction in gene transfection efficiency, which provided evidence that the polyplexes were internalized through the caveolin pathway.³⁸ These studies

are relatively simple and may provide crucial insights into the expected trafficking patterns and ultimate destinations of the polyplexes.

The dynamics and locations of intracellular polyplex trafficking also should be investigated. Extensive work has been conducted by Dr. Nikki Ross in the Sullivan group to study the trafficking patterns of histone-targeted polyethylenimine (PEI)/DNA polyplexes.³⁹ In particular, colocalization experiments with fluorescently labeled nucleic acids and cellular compartments as well as subcellular sucrose density gradient fractionation with radiolabeled nucleic acids elucidated detailed trafficking information. The insights gained from these experiments allowed for improved transfection efficiencies and suggested new opportunities in biomedical applications.

Another critical aspect to investigate is the mechanism of endosomal escape. A greater understanding of this mechanism would answer numerous system-specific questions and possibly shed light on new strategies that other polyplex systems could exploit. There are numerous experiments described in the literature to probe endosomal escape mechanisms, including lysosomal colocalization, endosomal pH-buffering, and electron microscopy approaches.⁴⁰⁻⁴² A particularly accessible and simple method involves labeling late endosomes/lysosomes with a stain and the siRNA with a fluorophore.⁴³ Detection of the colocalization of the two signals using confocal microscopy, in combination with quantification methods such as the Manders' coefficient,⁴⁴ provides information regarding endosomal escape at various points along the trafficking pathway.³⁹ In the mPEG-*b*-P(APNBMA) system, for example, the entrapment within late endosomes/lysosomes could be measured to study the effects of light irradiation and determine if polymer cleavage aids in endosomal escape, as hypothesized earlier.

Finally, it would be useful to know the ultimate fate of the polyplexes. The most likely destinations for dormant polyplexes are lysosomal degradation and exocytosis, neither of which allows the siRNA to engage with the RISC.³⁵ The final destination of the polyplexes also could be determined using colocalization experiments with labeled cellular compartment and nanocarrier components.

7.2.3.2 Strategies for overcoming limitations related to endosomal escape

As described in Chapter 5, the vast majority of the internalized siRNAs was not able to engage the RISC, even in the most efficient formulations that were able to release large amounts of siRNA, due to insufficient endosomal escape. Moreover, the lack of gene silencing in AoAFs without the addition of cationic lipids was presumably caused by inefficient endosomal escape. These results were not particularly surprising given that the mPEG-*b*-P(APNBMA) polymers do not contain any moieties that were explicitly designed for endosomal escape. Nevertheless, the packaged siRNA was able to escape the compartment and enter the cytoplasm when irradiated with 365 nm light in NIH/3T3 cells. I hypothesized that, following irradiation, the cleaved cationic groups from the polymer backbone interacted with the endosomal membrane and destabilized/ruptured the lipid bilayers to allow for endosomal escape. The liberated species may be free siRNA, partially disassembled polyplexes, and/or completely intact polyplexes. However, I speculated that this proposed mechanism did not occur in AoAFs, possibly due to different trafficking pathways or more stable endosomes. These findings suggested that the addition of new functional moieties that help induce endosomal escape to the polymer may enable more efficient gene silencing in NIH/3T3 cells and facilitate on/off control over siRNA activity with Lipofectamine-free systems in AoAFs.

A common strategy to trigger endosomal escape is the use of pH-responsive materials that can exploit the supposed proton-sponge effect, in which pH buffering of the endomembrane vesicle leads to an accumulation of ions within the compartment and an increase in osmotic pressure that bursts the endosome.⁴⁵ In fact, the excellent gene delivery efficiency of PEI, which possesses a high concentration of primary, secondary and tertiary amines, often is attributed to its pH buffering capabilities that aid in endosomal escape.^{39, 42} These reports suggest that the incorporation of PEI into the formulations may enhance endosomal escape in the mPEG-*b*-P(APNBMA) system. Alternatively, numerous pH-responsive chemical groups can be added to the polymer as a third block to take advantage of endosomal acidification during trafficking.⁴⁶ For example, fusogenic peptides, such as HA2 (derived from influenza virus hemagglutinin), have conformations that change in response to lower pH conditions.⁴⁷ The protonation of the acidic residues of the peptides induce the formation of hydrophobic faces that can strongly interact with the endosomal membrane, causing membrane destabilization and rupture.⁴⁷ Thus, the addition of endosomolytic reagents such as HA2 to the polymer offers a promising strategy for enhancing endosomal escape.

Other approaches for improving endosomal escape include formulating hybrid systems with cationic lipids (other than Lipofectamine), which are known to interact with endosomal membranes,⁴⁶ and the co-delivery of photosensitizers.⁴⁷ The most commonly employed fusogenic lipid is dioleoylphosphatidylethanolamine (DOPE),⁴⁶ which has been used to induce endosomal escape and enable efficient gene silencing with subpicomolar amounts of siRNA.⁴⁸ Moreover, the use of photosensitizers is particularly appealing from an application standpoint because the mPEG-*b*-

P(APNBMA) system already utilizes light. There are numerous photosensitizers that have successfully improved endosomal membrane disruption through the generation of highly reactive oxygen species upon application with a photo-stimulus.⁴⁹ For example, Oliveira *et al.* demonstrated that the inclusion of a photosensitizer, meso-tetraphenylporphine with two sulfonate groups on adjacent phenyl rings (TPPS_{2a}), into lipoplexes enhanced gene silencing by a factor of 10 relative to lipoplex treatment alone.⁵⁰ The photosensitizer was stimulated using 375–450 nm light, which is close to the wavelengths that are relevant for *o*-NB cleavage. Therefore, the addition of photosensitizer agents represents a potentially straightforward method for enhancing endosomal escape and gene silencing efficiencies.

7.2.4 Co-cultures and other anionic theranostic cargo

The polyplexes and hybrid formulations have been used to successfully deliver siRNA to cell monocultures; however, there are other cell culture models and therapeutic/diagnostic payloads for which the mPEG-*b*-P(APNBMA) platform could be beneficially employed. The first possible extension of the platform is the application of polyplexes to co-culture cell systems that are more representative of an *in vivo* environment. The second possible extension of the platform is the delivery of other anionic cargos, alone or in combination with siRNA.

7.2.4.1 Cell co-cultures

There are hundreds of different cell types in the human body that perform their own specialized functions. Moreover, target cells are typically not isolated in the body but instead are surrounded by many other types of cells, and almost all health problems are carried out by multiple cell types that play key roles in the disease

progression in the given tissue(s). To better mimic the complicated disease environment in animals, cell co-cultures may be implemented during *in vitro* experiments.³⁸

The choice of the co-culture depends on the particular application. For example, there are three cell types that are particularly relevant to coronary artery bypass grafting – fibroblasts, endothelial cells, and smooth muscle cells.⁵¹ If the therapeutic is intended to be used in only one of these cell types (e.g. fibroblasts), it would be appropriate to determine if the nanocarriers could be designed to target only that specific cell type and avoid off-target effects in the other cells (e.g. endothelial and smooth muscle cells). A co-culture system would be useful for investigating whether this goal is even feasible. To implement such an experiment, the composition of the hybrid lipid-polymer formulations possibly could be tuned to allow for efficient gene silencing in one cell type but no silencing in the others at a given irradiation dosage.

Macrophages also play a critical role in many applications, as they are present in nearly all tissues.⁵² These cells engulf cellular debris, foreign substances, cancer cells, and other components that are not recognized to be associated with the host's healthy body (including nanocarriers). Furthermore, macrophages play critical roles in the immune system and are extremely active during inflammation, both of which are important components to the body's response to many diseases.⁵² Therefore, co-culture systems involving macrophages would be useful for determining the propensity of macrophages to uptake the nanocarriers relative to the target cells and investigating how macrophages influence disease progression.

7.2.4.2 Anionic cargos

The work outlined in this dissertation primarily focused on the delivery of siRNA as well as diagnostic quantum dot nanoparticles using mPEG-*b*-P(APNBMA). The polymer also is able to encapsulate DNA, mRNA, and gold nanoparticles into polyplexes. The cationic block of mPEG-*b*-P(APNBMA) should be able to electrostatically bind essentially all negatively charged molecules, including multivalent anionic small molecules and negatively charged peptides/proteins. For example, other cationic copolymers have been shown to solubilize anionic small molecule drugs, such as mefenamic acid and indomethacin,⁵³ and anionic antimicrobial peptides/proteins (AAMP)s have garnered interest for medical applications.⁵⁴ It is likely that the polyplex system could be adapted to deliver these other anionic cargo for therapeutic and/or diagnostic purposes. Generally, the strength of electrostatic binding increases as the charge density and molecular weight increase; thus, smaller molecules with low charge densities will likely be the most difficult to encapsulate but the easiest to release.²² The N/P ratio, mixed polymer composition, and incorporation of anionic excipients could be varied to optimize the balance between binding *vs.* release for any cargo. It also would be interesting to explore the co-delivery of various combinations of these cargos, which may be practical for specific applications and may enable staggered release profiles with different dosages of light. Ultimately, the modularity of the system offers numerous directions that may prove to be fruitful for both fundamental science and biomedical therapeutic standpoints.

7.2.5 Summary of recommended future directions

There are four main categories for future work: direct extensions of recent work (*in vivo* applications and incorporation of UCNPs), modifications to the polymer structure, mechanistic understanding and strategies for enhancing endosomal escape, and co-culture systems and anionic theranostic cargo. Initially, I recommend continuing the recent work related to translating the technology into rabbit models so that the primary hurdles can be identified early and subsequently addressed. For example, the results may indicate that stability and/or cellular uptake is an issue, meaning that a modification to the hydrophilic (PEG) block may be necessary before further progress can be made *in vivo*. Perhaps the UV light causes severe cytotoxicity or cannot penetrate far enough into the tissue, which would suggest accelerating the UCNP work and the synthesis of a new monomer unit that undergoes the photo-reaction more efficiently and at higher wavelengths. It also is possible that endosomal escape is a major challenge *in vivo*, indicating that one of the strategies described in section 7.2.3.2 may be critical for overcoming this barrier. Due to the complex nature of animal models, it is difficult to predict which combination of these potential hurdles will be the most pressing; however, the ideas detailed in this chapter should provide a good starting point for addressing these possible challenges.

REFERENCES

1. Zuckerman, J. E.; Davis, M. E., Clinical experiences with systemically administered siRNA-based therapeutics in cancer. *Nat. Rev. Drug Discov.* **2015**, *14* (12), 843-856.
2. Robinson, K. G.; Scott, R. A.; Heseck, A. M.; Woodford, E. J.; Amir, W.; Planchon, T. A.; Kiick, K. L.; Akins, R. E., Reduced arterial elasticity due to surgical skeletonization is ameliorated by abluminal PEG hydrogel. *Bioeng. Transl. Med.* **2017**, *Accepted Article*.
3. Greco, C. T.; Epps, T. H., III; Sullivan, M. O., Mechanistic design of polymer nanocarriers to spatiotemporally control gene silencing. *ACS Biomater. Sci. Eng.* **2016**, *2* (9), 1582-1594.
4. Chen, H. H.; Ho, Y.-P.; Jiang, X.; Mao, H.-Q.; Wang, T.-H.; Leong, K. W., Quantitative comparison of intracellular unpacking kinetics of polyplexes by a model constructed from quantum dot-FRET. *Mol. Ther.* **2008**, *16* (2), 324-332.
5. Jayakumar, M. K. G.; Idris, N. M.; Zhang, Y., Remote activation of biomolecules in deep tissues using near-infrared-to-UV upconversion nanotransducers. *Proc. Natl. Acad. Sci. U.S.A.* **2012**, *109* (22), 8483-8488.
6. Zou, W. Q.; Visser, C.; Maduro, J. A.; Pshenichnikov, M. S.; Hummelen, J. C., Broadband dye-sensitized upconversion of near-infrared light. *Nat. Photon.* **2012**, *6* (8), 560-564.
7. Wang, F.; Liu, X. G., Recent advances in the chemistry of lanthanide-doped upconversion nanocrystals. *Chem. Soc. Rev.* **2009**, *38* (4), 976-989.
8. Liu, N.; Qin, W. P.; Qin, G. S.; Jiang, T.; Zhao, D., Highly plasmon-enhanced upconversion emissions from Au@beta-NaYF₄:Yb,Tm hybrid nanostructures. *Chem. Commun.* **2011**, *47* (27), 7671-7673.
9. Chen, G. Y.; Agren, H.; Ohulchanskyy, T. Y.; Prasad, P. N., Light upconverting core-shell nanostructures: nanophotonic control for emerging applications. *Chem. Soc. Rev.* **2015**, *44* (6), 1680-1713.

10. Wu, X.; Zhang, Y. W.; Takle, K.; Bilsel, O.; Li, Z. J.; Lee, H.; Zhang, Z. J.; Li, D. S.; Fan, W.; Duan, C. Y.; Chan, E. M.; Lois, C.; Xiang, Y.; Han, G., Dye-sensitized core/active shell upconversion nanoparticles for optogenetics and bioimaging applications. *ACS Nano* **2016**, *10* (1), 1060-1066.
11. Chen, G. Y.; Damasco, J.; Qiu, H. L.; Shao, W.; Ohulchanskyy, T. Y.; Valiev, R. R.; Wu, X.; Han, G.; Wang, Y.; Yang, C. H.; Agren, H.; Prasad, P. N., Energy-cascaded upconversion in an organic dye-sensitized core/shell fluoride nanocrystal. *Nano Lett.* **2015**, *15* (11), 7400-7407.
12. Klan, P.; Solomek, T.; Bochet, C. G.; Blanc, A.; Givens, R.; Rubina, M.; Popik, V.; Kostikov, A.; Wirz, J., Photoremovable protecting groups in chemistry and biology: reaction mechanisms and efficacy. *Chem. Rev.* **2013**, *113* (1), 119-191.
13. Kloxin, A. M.; Kasko, A. M.; Salinas, C. N.; Anseth, K. S., Photodegradable hydrogels for dynamic tuning of physical and chemical properties. *Science* **2009**, *324* (5923), 59-63.
14. Kim, M. S.; Diamond, S. L., Photocleavage of o-nitrobenzyl ether derivatives for rapid biomedical release applications. *Bioorg. Med. Chem. Lett.* **2006**, *16* (15), 4007-4010.
15. Holmes, C. P., Model studies for new o-nitrobenzyl photolabile linkers: Substituent effects on the rates of photochemical cleavage. *J. Org. Chem.* **1997**, *62* (8), 2370-2380.
16. Reichmanis, E.; Smith, B. C.; Gooden, R., Ortho-nitrobenzyl photochemistry - solution vs solid-state behavior. *J. Polym. Sci. A Polym. Chem.* **1985**, *23* (1), 1-8.
17. Cameron, J. F.; Frechet, J. M. J., Photogeneration of organic-bases from ortho-nitrobenzyl-derived carbamates. *J. Am. Chem. Soc.* **1991**, *113* (11), 4303-4313.
18. Matsumura, Y.; Ananthaswamy, H. N., Toxic effects of ultraviolet radiation on the skin. *Toxicol. Appl. Pharmacol.* **2004**, *195* (3), 298-308.
19. Aujard, I.; Benbrahim, C.; Gouget, M.; Ruel, O.; Baudin, J. B.; Neveu, P.; Jullien, L., o-Nitrobenzyl photolabile protecting groups with red-shifted absorption: Syntheses and uncaging cross-sections for one- and two-photon excitation. *Chem. Eur. J.* **2006**, *12* (26), 6865-6879.

20. Zhao, H.; Sterner, E. S.; Coughlin, E. B.; Theato, P., o-Nitrobenzyl alcohol derivatives: opportunities in polymer and materials science. *Macromolecules* **2012**, *45* (4), 1723-1736.
21. Burke, P. A.; Pun, S. H.; Reineke, T. M., Advancing polymeric delivery systems amidst a nucleic acid therapy renaissance. *ACS Macro Lett.* **2013**, *2* (10), 928-934.
22. Johnson, R. N.; Chu, D. S. H.; Shi, J.; Schellinger, J. G.; Carlson, P. M.; Pun, S. H., HPMA-oligolysine copolymers for gene delivery: Optimization of peptide length and polymer molecular weight. *J. Control. Release* **2011**, *155* (2), 303-311.
23. Millili, P. G.; Selekman, J. A.; Blocker, K. M.; Johnson, D. A.; Naik, U. P.; Sullivan, M. O., Structural and functional consequences of pPoly(ethylene glycol) inclusion on DNA condensation for gene delivery. *Microsc. Res. Tech.* **2010**, *73* (9), 866-877.
24. Mao, S.; Neu, M.; Germershaus, O.; Merkel, O.; Sitterberg, J.; Bakowsky, U.; Kissel, T., Influence of polyethylene glycol chain length on the physicochemical and biological properties of poly(ethylene imine)-graft-poly(ethylene glycol) block copolymer/siRNA polyplexes. *Bioconjugate Chem.* **2006**, *17* (5), 1209-1218.
25. Miteva, M.; Kirkbride, K. C.; Kilchrist, K. V.; Werfel, T. A.; Li, H.; Nelson, C. E.; Gupta, M. K.; Giorgio, T. D.; Duvall, C. L., Tuning PEGylation of mixed micelles to overcome intracellular and systemic siRNA delivery barriers. *Biomaterials* **2015**, *38*, 97-107.
26. Kunath, K.; von Harpe, A.; Petersen, H.; Fischer, D.; Voigt, K.; Kissel, T.; Bickel, U., The structure of PEG-modified poly(ethylene imines) influences biodistribution and pharmacokinetics of their complexes with NF-kappa B decoy in mice. *Pharm. Res.* **2002**, *19* (6), 810-817.
27. Greco, C. T.; Muir, V. G.; Epps, T. H., III; Sullivan, M. O., Efficient tuning of siRNA dose response by combining mixed polymer nanocarriers with simple kinetic modeling. *Acta Biomater.* **2017**, *50*, 407-416.
28. Green, M. D.; Foster, A. A.; Greco, C. T.; Roy, R.; Lehr, R. M.; Epps, T. H., III; Sullivan, M. O., Catch and release: photocleavable cationic diblock copolymers as a potential platform for nucleic acid delivery. *Polym. Chem.* **2014**, *5* (19), 5535-5541.

29. Kunath, K.; von Harpe, A.; Fischer, D.; Peterson, H.; Bickel, U.; Voigt, K.; Kissel, T., Low-molecular-weight polyethylenimine as a non-viral vector for DNA delivery: comparison of physicochemical properties, transfection efficiency and in vivo distribution with high-molecular-weight polyethylenimine. *J. Control. Release* **2003**, *89* (1), 113-125.
30. Zhou, G. Y.; Xu, Y. M.; Chen, M. W.; Cheng, D.; Shuai, X. T., Tumor-penetrating peptide modified and pH-sensitive polyplexes for tumor targeted siRNA delivery. *Polym. Chem.* **2016**, *7* (23), 3857-3863.
31. Cheng, C.; Convertine, A. J.; Stayton, P. S.; Bryers, J. D., Multifunctional triblock copolymers for intracellular messenger RNA delivery. *Biomaterials* **2012**, *33* (28), 6868-6876.
32. Cho, H. Y.; Srinivasan, A.; Hong, J.; Hsu, E.; Liu, S. G.; Shrivats, A.; Kwak, D.; Bohaty, A. K.; Paik, H. J.; Hollinger, J. O.; Matyjaszewski, K., Synthesis of biocompatible PEG-based star polymers with cationic and degradable core for siRNA delivery. *Biomacromolecules* **2011**, *12* (10), 3478-3486.
33. Kwon, Y. J., Before and after endosomal escape: roles of stimuli-converting siRNA/polymer interactions in determining gene silencing efficiency. *Acc. Chem. Res.* **2012**, *45* (7), 1077-1088.
34. Foster, A. A.; Greco, C. T.; Green, M. D.; Epps, T. H., III; Sullivan, M. O., Light-mediated activation of siRNA release in diblock copolymer assemblies for controlled gene silencing. *Adv. Healthc. Mater.* **2015**, *4* (5), 760-770.
35. Munsell, E. V.; Ross, N. L.; Sullivan, M. O., Journey to the center of the cell: current nanocarrier design strategies targeting biopharmaceuticals to the cytoplasm and nucleus. *Curr. Pharm. Des.* **2016**, *22* (9), 1227-1244.
36. Reilly, M. J.; Larsen, J. D.; Sullivan, M. O., Polyplexes traffic through caveolae to the golgi and endoplasmic reticulum en route to the nucleus. *Mol. Pharm.* **2012**, *9* (5), 1280-1290.
37. Al Soraj, M.; He, L.; Peynshaert, K.; Cousaert, J.; Vercauteren, D.; Braeckmans, K.; De Smedt, S. C.; Jones, A. T., siRNA and pharmacological inhibition of endocytic pathways to characterize the differential role of macropinocytosis and the actin cytoskeleton on cellular uptake of dextran and cationic cell penetrating peptides octaarginine (R8) and HIV-Tat. *J. Control. Release* **2012**, *161* (1), 132-141.

38. Ross, N. L.; Sullivan, M. O., Overexpression of caveolin-1 in inflammatory breast cancer cells enables IBC-specific gene delivery and prodrug conversion using histone-targeted polyplexes. *Biotechnol. Bioeng.* **2016**, *113* (12), 2686-2697.
39. Ross, N. L.; Munsell, E. V.; Sabanayagam, C.; Sullivan, M. O., Histone-targeted polyplexes avoid endosomal escape and enter the nucleus during postmitotic redistribution of ER membranes. *Mol. Ther. Nucleic Acids* **2015**, *4*, e226.
40. Gilleron, J.; Querbes, W.; Zeigerer, A.; Borodovsky, A.; Marsico, G.; Schubert, U.; Manygoats, K.; Seifert, S.; Andree, C.; Stoeter, M.; Epstein-Barash, H.; Zhang, L.; Kotliansky, V.; Fitzgerald, K.; Fava, E.; Bickle, M.; Kalaidzidis, Y.; Akinc, A.; Maier, M.; Zerial, M., Image-based analysis of lipid nanoparticle-mediated siRNA delivery, intracellular trafficking and endosomal escape. *Nat. Biotechnol.* **2013**, *31* (7), 638-646.
41. Wittrup, A.; Ai, A.; Liu, X.; Hamar, P.; Trifonova, R.; Charisse, K.; Manoharan, M.; Kirchhausen, T.; Lieberman, J., Visualizing lipid-formulated siRNA release from endosomes and target gene knockdown. *Nat. Biotechnol.* **2015**, *33* (8), 870-876.
42. Benjaminsen, R. V.; Matthebjerg, M. A.; Henriksen, J. R.; Moghimi, S. M.; Andresen, T. L., The possible "proton sponge" effect of polyethylenimine (PEI) does not include change in lysosomal pH. *Mol. Ther.* **2013**, *21* (1), 149-157.
43. Zhang, T. B.; Song, X. Y.; Kang, D.; Zhang, L.; Zhang, C. Q.; Jin, S. B.; Wang, C. X.; Tian, J. H.; Xing, J. F.; Liang, X. J., Modified bovine serum albumin as an effective charge-reversal platform for simultaneously improving the transfection efficiency and biocompatibility of polyplexes. *Journal of Materials Chemistry B* **2015**, *3* (23), 4698-4706.
44. Manders, E. M. M.; Verbeek, F. J.; Aten, J. A., Measurement of colocalization of objects in dual-color confocal images. *J. Microsc-Oxford* **1993**, *169*, 375-382.
45. Varkouhi, A. K.; Scholte, M.; Storm, G.; Haisma, H. J., Endosomal escape pathways for delivery of biologicals. *J. Control. Release* **2011**, *151* (3), 220-228.
46. Dominska, M.; Dykxhoorn, D. M., Breaking down the barriers: siRNA delivery and endosome escape. *J. Cell Sci.* **2010**, *123* (8), 1183-1189.

47. Endoh, T.; Ohtsuki, T., Cellular siRNA delivery using cell-penetrating peptides modified for endosomal escape. *Adv. Drug Deliv. Rev.* **2009**, *61* (9), 704-709.
48. Hassani, Z.; Lemkine, G. F.; Erbacher, P.; Palmier, K.; Alfama, G.; Giovannangeli, C.; Behr, J. P.; Demeneix, B. A., Lipid-mediated siRNA delivery down-regulates exogenous gene expression in the mouse brain at picomolar levels. *J. Gene Med.* **2005**, *7* (2), 198-207.
49. Hogset, A.; Prasmickaite, L.; Selbo, P. K.; Hellum, M.; Engesaeter, B. O.; Bonsted, A.; Berg, K., Photochemical internalisation in drug and gene delivery. *Adv. Drug Deliv. Rev.* **2004**, *56* (1), 95-115.
50. Oliveira, S.; Fretz, M. M.; Hogset, A.; Storm, G.; Schiffelers, R. M., Photochemical internalization enhances silencing of epidermal growth factor receptor through improved endosomal escape of siRNA. *Biochim. Biophys. Acta - Biomembranes* **2007**, *1768* (5), 1211-1217.
51. Robinson, K. G.; Nie, T.; Baldwin, A. D.; Yang, E. C.; Kiick, K. L.; Akins, R. E., Jr., Differential effects of substrate modulus on human vascular endothelial, smooth muscle, and fibroblastic cells. *J Biomed. Mater. Res. A* **2012**, *100A* (5), 1356-1367.
52. Ovchinnikov, D. A., Macrophages in the embryo and beyond: Much more than just giant phagocytes. *Genesis* **2008**, *46* (9), 447-462.
53. Saal, W.; Ross, A.; Wyttenbach, N.; Alsenz, J.; Kuentz, M., A systematic study of molecular interactions of anionic drugs with a dimethylaminoethyl methacrylate copolymer regarding solubility enhancement. *Mol. Pharm.* **2017**, *14*, 1243-1250.
54. Harris, F.; Dennison, S. R.; Phoenix, D. A., Anionic antimicrobial peptides from eukaryotic organisms. *Curr. Protein Pept. Sci.* **2009**, *10* (6), 585-606.

Appendix A

SUPPORTING INFORMATION FOR CHAPTER 3

Table A.1: Representative calculation of the normalized mRNA expression level (m) of a test sample relative to the untreated control. The values were computed using Equations 2.12 and 2.13, as described in detail in Chapter 2 (section 2.7).

	C_q target gene	C_q housekeeping gene	[target] - [housekeeping]	d	m
untreated sample	17.1	12.5	4.6	0	100%
test sample	18.9	12.7	6.2	1.6	33.0%

Table A.2: The raw values of the ratios between the intensities of the acceptor and donor peaks (I_{665}/I_{560}) of three independent samples from Figure 3.9B (prior to normalization).

Irradiation time (min)	Sample #1	Sample #2	Sample #3	Average	Standard Deviation
0	1.12	1.11	1.19	1.14	0.044
2.5	0.53	0.43	0.53	0.50	0.058
5	0.3	0.36	0.36	0.34	0.035
10	0.28	0.24	0.21	0.24	0.035
20	0.14	0.18	0.17	0.16	0.021
40	0.09	0.08	0.12	0.10	0.021

Compensation matrix for 0 min

	APC	PE	PE-Texas Red
APC	100.0%	0.1%	2.45%
PE	0.0%	100.0%	33.8%
PE-Texas Red	0.0%	24.4%	100.0%

Compensation matrix for 5 min

	APC	PE	PE-Texas Red
APC	100.0%	0.1%	2.65%
PE	0.0%	100.0%	34.1%
PE-Texas Red	0.0%	24.4%	100.0%

Compensation matrix for 20 min

	APC	PE	PE-Texas Red
APC	100.0%	0.1%	2.50%
PE	0.0%	100.0%	35.6%
PE-Texas Red	0.0%	24.4%	100.0%

Figure A.1: Compensation matrices used to correct for signal spillover in Figure 3.10. The APC and PE channels primarily detected signals from individual fluorophores (control samples) and the PE-Texas Red channel primarily detected the signal attributed to FRET.

Appendix B

SUPPORTING INFORMATION FOR CHAPTER 4

Table B.1: Raw values of polyplex diameters and the calculation of the average and standard deviation for each mixed polymer formulation. These values are plotted in Figure 4.5.

	0/100	25/75	50/50	75/25	100/0
Sample #1	120.1	103.8	44.5	24.2	21.9
Sample #2	113.3	87.0	38.4	27.0	22.3
Sample #3	124.9	94.1	35.6	30.4	24.5
Average diameter (nm)	119.4	95.0	39.5	27.2	22.9
Standard deviation (nm)	5.8	8.4	4.6	3.1	1.4

Table B.2: Raw values of polyplex zeta potentials and the calculation of the average and standard deviation for each mixed polymer formulation. These values are plotted in Figure 4.5.

	0/100	25/75	50/50	75/25	100/0
Sample #1	10.9	11.1	8.3	6.4	6.2
Sample #2	12.7	12.6	10.2	7.7	5.6
Sample #3	12.3	12.8	9.9	6.8	6.2
Average zeta potential (mV)	12.0	12.2	9.5	6.9	6.0
Standard deviation (mV)	0.98	0.96	0.99	0.68	0.34

Appendix C

SUPPORTING INFORMATION FOR CHAPTER 5

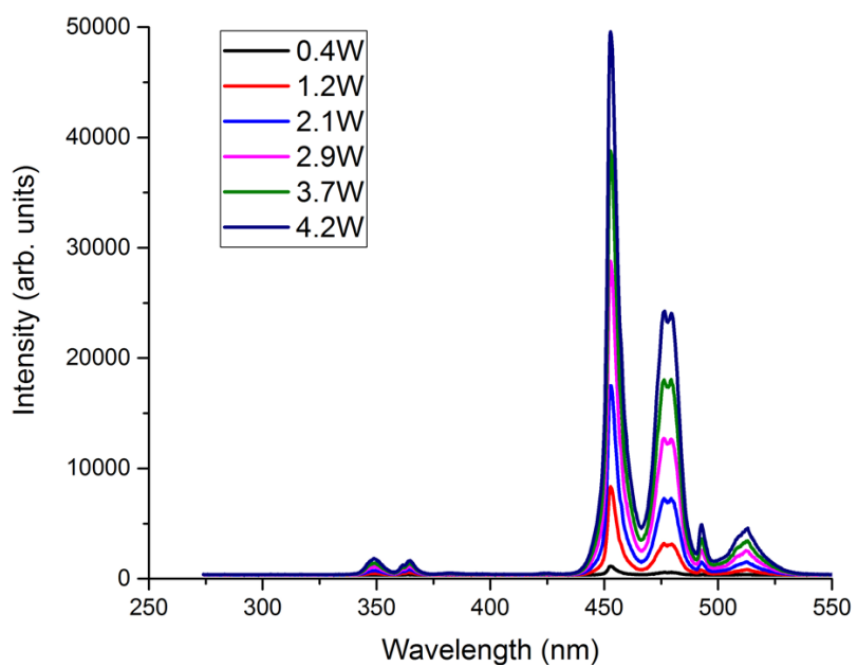


Figure C.1: Emission spectra of lanthanide atom doped NaYF_4 upconverting nanoparticles (UCNP)s as a function of irradiation intensity. The UCNPs were excited with 980 nm light, and the resulting emission was characterized. These measurements were performed by Eric Chen from the Doty lab at the University of Delaware.

Discussion for Figure C.1: The UCNPs exhibited a very weak emission peak around 365 nm.

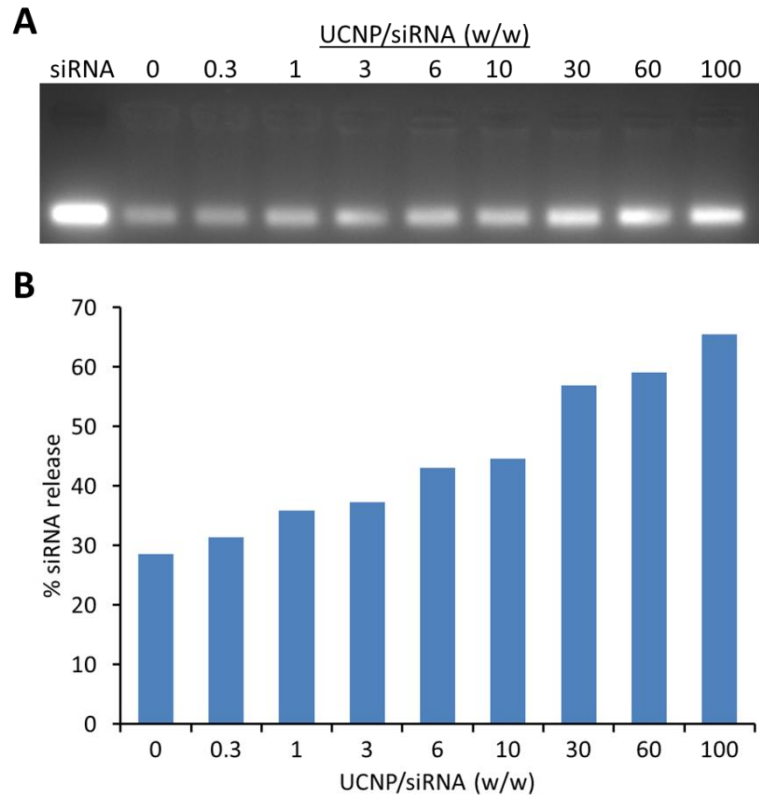


Figure C.2: Polyplex formation and siRNA release as a function of the UCNP loading ratio. (A) Acid-functionalized UCNPs were added to the polyplex formulations at various loading ratios (UCNP/siRNA [w/w]), and heparin was added (heparin/siRNA [w/w] of 5) to induce siRNA release. Then, the solutions were subjected to gel electrophoresis. (B) The free siRNA bands in the gel in (A) were quantified using ImageJ analyses.

Discussion for Figure C.2: As the UCNP/siRNA (w/w) loading ratio increased, the amount of heparin-induced siRNA release also increased, indicating that the UCNPs were influencing polyplex stability.

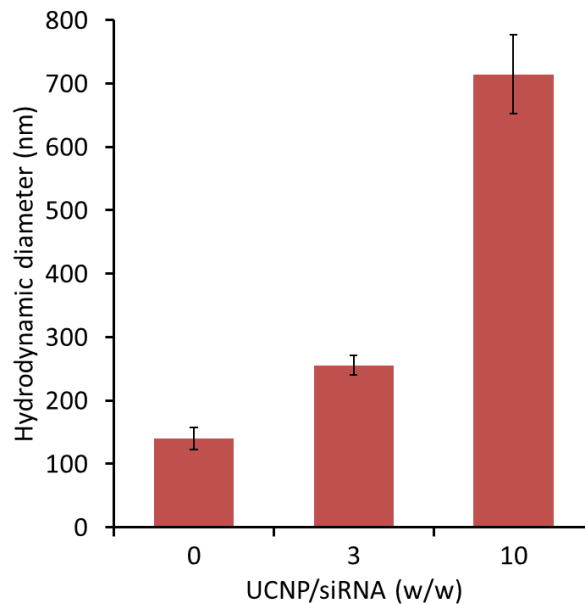


Figure C.3: Average polyplex size as a function of UCNP loading ratio. Polyplexes were formulated with various loading ratios of UCNP/siRNA (w/w) and analyzed using dynamic light scattering (DLS).

Discussion for Figure C.3: The average hydrodynamic diameter increased significantly upon the addition of UCNPs, and the sizes surpassed 200 nm at UCNP/siRNA ratios ≥ 3 . Only one population was detected using DLS, further suggesting that the UCNPs were incorporated into the polyplexes.

Appendix D

SUPPORTING INFORMATION FOR CHAPTER 6

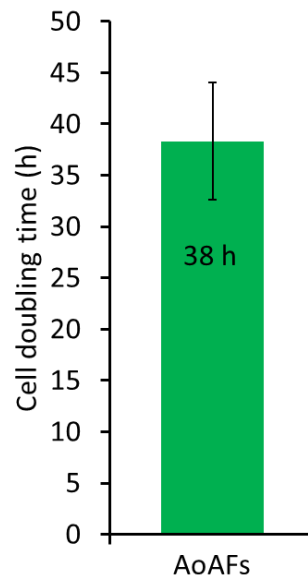


Figure D.1: Cell doubling time of AoAFs, as evaluated by the AlamarBlue assay. Results are reported as the mean \pm standard deviation of data obtained from three independent samples.

Methods for Figure D.1: Cells were cultured in plates at a density of 20,000 cells cm^{-2} and grown for 72 h. Medium containing 10 vol% AlamarBlue was added to the plates,

and the cells were incubated for 2 h in a humid environment maintained at 37 °C and 5 vol% CO₂. Fluorescence was measured using a GloMax-multi detection system plate reader (Promega, Madison, WI). To determine the baseline fluorescence, medium containing 10 vol% AlamarBlue was added to a well without cells.

Discussion for Figure D.1: The AoAFs had a doubling time of ~38 h, which was incorporated into the $k_{s,deg}$ rate constant estimate for the kinetic modeling predications.

Table D.1: Average size and zeta potential of the hybrid lipid-polymer nanocomplexes. The average nanocomplex diameter was determined using fluorescence correlation spectroscopy (FCS). The average zeta potential was determined using a Brookhaven Instruments (Brookhaven, CT) ZetaPALS, and each sample was measured with 3 runs of 10 cycles. Results are reported as the mean and standard deviation of data obtained from three independent experiments.

	average	standard deviation
diameter (nm)	168	11
zeta potential (mV)	+3.1	2.8

Methods for Table D.1: Nanocomplexes were formulated with Dy547-labeled small interfering RNA (siRNA) and analyzed on cover slips. FCS measurements were carried out on an LSM 780 confocal microscope (Carl Zeiss, Oberkochen, Germany) using a 561 nm laser and a 40x (numerical aperture = 1.2) water immersion apochromat objective. Thirty measurements, each lasting 8 s, were taken for each sample, and data analysis was performed with ZEN 2010 software (Carl Zeiss). A solution of free Alexa Fluor 555 dye, with an assumed diffusion coefficient of $340 \mu\text{m}^2 \text{s}^{-1}$,¹ was used to determine the structural and measurement parameters.

Discussion for Table D.1: The nanocomplexes had an average diameter of 168 nm. The nanocarriers had a zeta potential of +3.1 mV, which is very close to neutral.

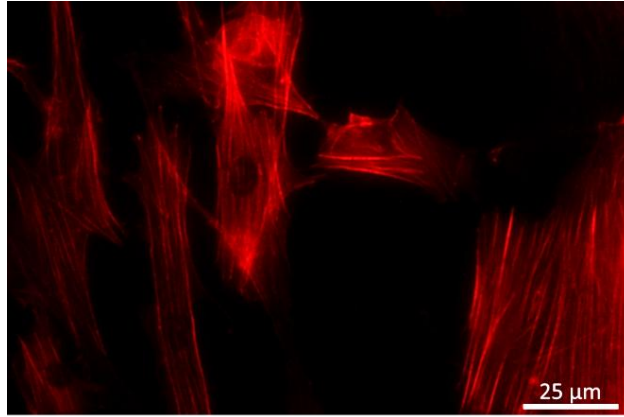


Figure D.2: Representative micrograph showing F-actin stress fibers at a higher magnification. The scale bar represents 25 μm .

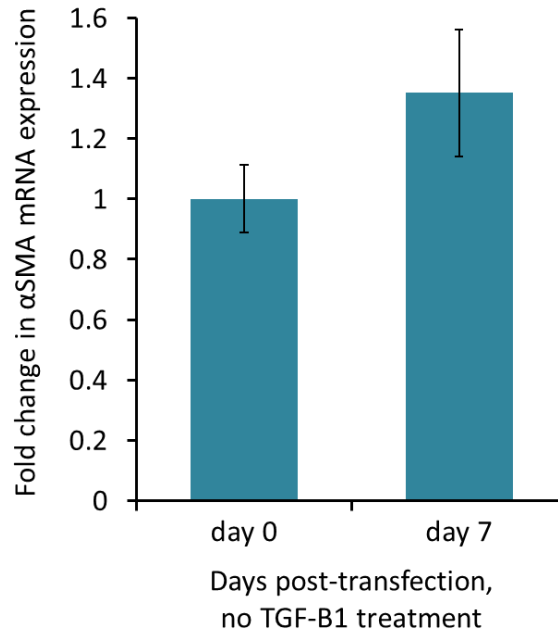


Figure D.3: Changes in alpha smooth muscle actin (α SMA) mRNA expression (marker of myofibroblast differentiation) over the course of one week without transforming growth factor beta 1 (TGF- β 1) treatment. Quantitative PCR (qPCR) analyses compared the α SMA mRNA expression levels on day 7 relative to day 0.² Results are shown as the mean \pm standard deviation of data obtained from three independent samples. The samples were not significantly different from each other at a significance level of 0.05.

Discussion for Figure D.3: The α SMA mRNA expression levels in AoAFs did not significantly change over the course of one week (significance level of 0.05). This suggests that the AoAFs primarily maintained their fibroblast phenotype over 7 days when seeded on tissue culture plastic.

Table D.2: Sequences of custom-designed siRNA sequences that target IL1 β in rabbits. The siRNA was purchased in duplex form from MilliporeSigma (Darmstadt, Germany).

siRNA	Sequence (Sense) 5' to 3'	Sequence (Antisense) 5' to 3'
#1	CAGAGAAUCUGAACCAACA dTdT	UGUUGGUUCAGAUUCUCUG dTdT
#2	CUGUACCUGUCCUGCGUGA dTdT	UCACGCAGGACAGGUACAG dTdT
#3	GAGUGUGAUGCAGUACGAU dTdT	AUCGUACUGCAUCACACUC dTdT

REFERENCES

1. Ross, N. L.; Munsell, E. V.; Sabanayagam, C.; Sullivan, M. O., Histone-targeted polyplexes avoid endosomal escape and enter the nucleus during postmitotic redistribution of ER membranes. *Mol. Ther. Nucleic Acids* **2015**, *4*, e226.
2. Schmittgen, T. D.; Livak, K. J., Analyzing real-time PCR data by the comparative C-T method. *Nat. Protoc.* **2008**, *3* (6), 1101-1108.

Appendix E

TEXT AND FIGURE REPRINT PERMISSIONS



Thank you for your order!

Dear Chad Greco,

Thank you for placing your order through Copyright Clearance Center's RightsLink® service.

Order Summary

Order Date: Mar 10, 2017
Order Number: 4065370431509
Publication: Journal of Controlled Release
Title: Stimuli-responsive nanomaterials for therapeutic protein delivery
Type of Use: reuse in a thesis/dissertation
Order Total: 0.00 USD

View or print complete [details](#) of your order and the publisher's terms and conditions.



Thank you for your order!

Dear Chad Greco,

Thank you for placing your order through Copyright Clearance Center's RightsLink® service.

Order Summary

Order Date:	Mar 10, 2017
Order Number:	4065370555037
Publication:	Nature Reviews Drug Discovery
Title:	Knocking down barriers: advances in siRNA delivery
Type of Use:	reuse in a dissertation / thesis
Order Total:	0.00 USD

View or print complete [details](#) of your order and the publisher's terms and conditions.

WILEY

Thank you for your order!

Dear Chad Greco,

Thank you for placing your order through Copyright Clearance Center's RightsLink® service.

Order Summary

Order Date: Mar 10, 2017
Order Number: 4065390395675
Publication: Advanced Healthcare Materials
Title: Light-Mediated Activation of siRNA Release in Diblock Copolymer
Assemblies for Controlled Gene Silencing
Type of Use: Dissertation/Thesis
Order Total: 0.00 USD

View or print complete [details](#) of your order and the publisher's terms and conditions.

Sincerely,

Copyright Clearance Center

Catch and release: photocleavable cationic diblock copolymers as a potential platform for nucleic acid delivery

M. D. Green, A. A. Foster, C. T. Greco, R. Roy, R. M. Lehr, T. H. Epps, III and M. O. Sullivan, *Polym. Chem.*, 2014, 5, 5535

DOI: 10.1039/C4PY00638K

This article is licensed under a [Creative Commons Attribution 3.0 Unported Licence](#). Material from this article can be used in other publications provided that the correct acknowledgement is given with the reproduced material.

Reproduced material should be attributed as follows:

- > For reproduction of material from NJC:
[Original citation] - Published by The Royal Society of Chemistry (RSC) on behalf of the Centre National de la Recherche Scientifique (CNRS) and the RSC.
- > For reproduction of material from PCCP:
[Original citation] - Published by the PCCP Owner Societies.
- > For reproduction of material from PPS:
[Original citation] - Published by The Royal Society of Chemistry (RSC) on behalf of the European Society for Photobiology, the European Photochemistry Association, and RSC.
- > For reproduction of material from all other RSC journals:
[Original citation] - Published by The Royal Society of Chemistry.

Information about reproducing material from RSC articles with different licences is available on our [Permission Requests page](#).



RightsLink®

Home

Create Account

Help



ACS Publications
Most Trusted. Most Cited. Most Read.

Title: Mechanistic Design of Polymer Nanocarriers to Spatiotemporally Control Gene Silencing
Author: Chad T. Greco, Thomas H. Epps, Millicent O. Sullivan
Publication: ACS Biomaterials Science & Engineering
Publisher: American Chemical Society
Date: Sep 1, 2016

Copyright © 2016, American Chemical Society

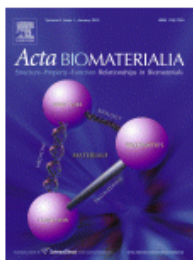
LOGIN

If you're a [copyright.com](#) user, you can login to RightsLink using your [copyright.com](#) credentials. Already a RightsLink user or want to [learn more?](#)

PERMISSION/LICENSE IS GRANTED FOR YOUR ORDER AT NO CHARGE

This type of permission/license, instead of the standard Terms & Conditions, is sent to you because no fee is being charged for your order. Please note the following:

- Permission is granted for your request in both print and electronic formats, and translations.
- If figures and/or tables were requested, they may be adapted or used in part.
- Please print this page for your records and send a copy of it to your publisher/graduate school.
- Appropriate credit for the requested material should be given as follows: "Reprinted (adapted) with permission from (COMPLETE REFERENCE CITATION). Copyright (YEAR) American Chemical Society." Insert appropriate information in place of the capitalized words.
- One-time permission is granted only for the use specified in your request. No additional uses are granted (such as derivative works or other editions). For any other uses, please submit a new request.



Thank you for your order!

Dear Chad Greco,

Thank you for placing your order through Copyright Clearance Center's RightsLink® service.

Order Summary

Order Date: Mar 16, 2017
Order Number: 4070920144588
Publication: Acta Biomaterialia
Title: Efficient tuning of siRNA dose response by combining mixed polymer nanocarriers with simple kinetic modeling
Type of Use: reuse in a thesis/dissertation
Order Total: 0.00 USD



Thank you for your order!

Dear Chad Greco,

Thank you for placing your order through Copyright Clearance Center's RightsLink® service.

Order Summary

Order Date:	Mar 27, 2017
Order Number:	4077111333019
Publication:	Nature Photonics
Title:	Broadband dye-sensitized upconversion of near-infrared light
Type of Use:	reuse in a dissertation / thesis
Order Total:	0.00 USD

View or print complete [details](#) of your order and the publisher's terms and conditions.



RightsLink®

Home Account Info Help

WILEY

Title: Letter from the Editor
Author: Samir Mitragotri
Publication: Bioengineering & Translational Medicine
Publisher: John Wiley and Sons
Date: Jun 3, 2016

Logged in as:
Chad Greco
Account #:
3001123511
[LOGOUT](#)

© 2016 The Authors. Bioengineering & Translational Medicine is published by Wiley Periodicals, Inc. on behalf of The American Institute of Chemical Engineers

Welcome to RightsLink

This article is available under the terms of the Creative Commons Attribution License (CC BY) (which may be updated from time to time) and permits use, distribution and reproduction in any medium, provided that the Contribution is properly cited.

For an understanding of what is meant by the terms of the Creative Commons License, please refer to [Wiley's Open Access Terms and Conditions](#).

Permission is not required for this type of reuse.

Wiley offers a professional reprint service for high quality reproduction of articles from over 1400 scientific and medical journals. Wiley's reprint service offers:

- Peer reviewed research or reviews
- Tailored collections of articles
- A professional high quality finish
- Glossy journal style color covers
- Company or brand customisation
- Language translations
- Prompt turnaround times and delivery directly to your office, warehouse or congress.

Please contact our Reprints department for a quotation. Email corporatesaleseurope@wiley.com or corporatesalesusa@wiley.com or corporatesalesDE@wiley.com.



RightsLink®

Home

Create Account

Help



ACS Publications
Most Trusted. Most Cited. Most Read.

Title:

Anionic Polymer and Quantum Dot Excipients to Facilitate siRNA Release and Self-Reporting of Disassembly in Stimuli-Responsive Nanocarrier Formulations

Author:

Chad T. Greco, Jason C. Andrechak, Thomas H. Epps, et al

Publication: Biomacromolecules

Publisher: American Chemical Society

Date: Jun 1, 2017

Copyright © 2017, American Chemical Society

LOGIN

If you're a copyright.com user, you can login to RightsLink using your copyright.com credentials. Already a RightsLink user or want to [learn more?](#)

PERMISSION/LICENSE IS GRANTED FOR YOUR ORDER AT NO CHARGE

This type of permission/license, instead of the standard Terms & Conditions, is sent to you because no fee is being charged for your order. Please note the following:

- Permission is granted for your request in both print and electronic formats, and translations.
- If figures and/or tables were requested, they may be adapted or used in part.
- Please print this page for your records and send a copy of it to your publisher/graduate school.
- Appropriate credit for the requested material should be given as follows: "Reprinted (adapted) with permission from (COMPLETE REFERENCE CITATION). Copyright (YEAR) American Chemical Society." Insert appropriate information in place of the capitalized words.
- One-time permission is granted only for the use specified in your request. No additional uses are granted (such as derivative works or other editions). For any other uses, please submit a new request.